Towards a Computational Model of the Colonic Crypt with a Realistic, Deformable Geometry

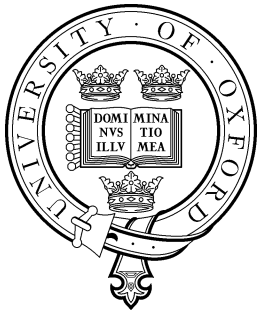

Sara-Jane Dunn

The Queen's College

University of Oxford

A thesis submitted for the degree of

Doctor of Philosophy

Michaelmas 2011

Acknowledgements

It's likely that there are only two parts of this thesis which anyone other than my supervisors and examiners will read: the abstract and the acknowledgements. The abstract mostly takes care of itself, so given this, it's important not to forget anyone who might turn on me if they don't find their name here, furnished with a number of carefully chosen superlatives. Further difficulties present themselves when actually composing the words themselves – one wants to avoid creeping too far down the sentimental route, where you thank the world, your primary school teachers and the pet goldfish that lost its tail when you were 8 years old. However, it's also important to take advantage of an opportunity to publicly thank those who have made a difference to your research and time as a D.Phil. student. So here we go. But I'll start with this caveat: if you're not mentioned here, it's your own fault.

Firstly, thanks must go to my supervisors: Dave, Ozzy, Helen and Jon. Advice, encouragement, proof-reading, support and your good humour have all been appreciated. Particular thanks go to (Dumble)Dave for making it possible for me to embark on this topic when it wasn't proposed in the big book of DTC short projects, and for his faultless optimism. Ozzy, for answering inane questions, and for never being too busy to help me – you made this a lot of fun. I would also like to thank our biological collaborators – Inke, Paul and Scott – who have been patient with our mathematical musings, and gentle with their biological corrections.

There have also been a number of key people who have provided help along the way. If there was a phrase for an unofficial supervisor role analogous to a godparent, then Alex, that would be you. Your ability to debug Chaste across Gchat is impressive, and so far, unmatched. And, not forgetting the rest of the Chaste team, all of whom at some point have answered an oddly-posed question about seg faults, boost errors and broken builds. I'm sorry I broke the build.

The foundation of these years was laid by my experience as an EPSRC-funded student of the Life Sciences Interface Doctoral Training Centre. When you can explain to someone what the Leucine Zipper is through the medium of interpretive dance, or you've faced a 5000 word essay of original research in one afternoon (just before Christmas) you know you're ready to set off on independent research. This year was invaluable to my experience as a D.Phil. student, and undoubtedly, provided the best foundation for what was to come. A mention must go to all DTC students from my year – good luck, and thanks for a great first year.

One of the main reasons I've enjoyed my D.Phil. so much is that I got to do it in a great research group. It just wouldn't have been as enjoyable without all of my office mates. In particular: Gaa, Raf, Liya, Matt and Mikael. You all get a special mention. In a similar vein, life at Queen's has contributed towards keeping me here and happy. So thanks to all who have entertained me, and who fed me in the final throes of writing up.

As part of this research experience, I've been fortunate enough to travel to conferences in far-flung locations (fortunate, but don't get me wrong, I knew exactly what I was doing). Funding for these trips is gratefully acknowledged from The Queen's College, the Department of Computer Science (*cough*comlab*cough*), the LSI DTC, and Prof. Philip Maini.

Finally, thank you to my family. Encouragement to keep going has never failed, and support has never faltered. Dad, for correcting my split-infinitives and providing endless deadpan humour (often, in French); mum, for keeping me sane, and always putting me before herself; Lise-Anne and Andy, for unbelievable generosity in the face of poor studentdom; Jols, for answering all my ridiculous medical queries and his too-kind words; and, Gran and Uncle, for providing a nearby refuge and for feeding me too much. To uncle especially, I wish you were here to see me finish.

Now, I think you should all read this from cover to cover.

Abstract

Colorectal cancer (CRC) is one of the most prevalent and deadly forms of cancer. Its high mortality rate is associated with difficulties in early detection, which is crucial to survival. The onset of CRC is marked by macroscopic changes in intestinal tissue, originating from a deviation in the healthy cell dynamics of glands known as the crypts of Lieberkühn. It is believed that accumulated genetic alterations confer on mutated cells the ability to persist in the crypts, which can lead to the formation of a benign tumour through localised proliferation. Stress on the crypt walls can lead to buckling, or crypt fission, and the further spread of mutant cells. Elucidating the initial perturbations in crypt dynamics is not possible experimentally, but such investigations could be made using a predictive, computational model. This thesis proposes a new discrete crypt model, which focuses on the interaction between cell- and tissue-level behaviour, while incorporating key subcellular components. The model contains a novel description of the role of the surrounding tissue and musculature, which allows the shape of the crypt to evolve and deform. A two-dimensional (2D) cross-sectional geometry is considered. Simulation results reveal how the shape of the crypt base may contribute mechanically to the asymmetric division events typically associated with the stem cells in this region. The model predicts that epithelial cell migration may arise due to feedback between cell loss at the crypt collar and density-dependent cell division, an hypothesis which can be investigated in a wet lab. Further, *in silico* experiments illustrate how this framework can be used to investigate the spread of mutations, and conclude that a reduction in cell migration is key to confer persistence on mutant cell populations. A three-dimensional (3D) model is proposed to remove the spatial restrictions imposed on cell migration in 2D, and preliminary simulation results agree with the hypotheses generated in 2D. Computational limitations that currently restrict extension to a realistic 3D geometry are discussed. These models enable investigation of the role that mechanical forces play in regulating tissue homeostasis, and make a significant contribution to the theoretical study of the onset of crypt deformation under pre-cancerous conditions.

Contents

List of Figures

Glossary

The following acronyms are used in this thesis. Page numbers indicate where each acronym is first introduced.

- **CRC**: Colorectal cancer 1
- **2D**: Two-dimensional 3
- **3D**: Three-dimensional 3
- **PCFS**: Pericryptal fibroblast sheath 9
- **DNA**: Deoxyribonucleic acid 11
- **Cdks**: Cyclin-dependent kinases 16
- **TCF**: Transcription factor 16
- *Apc* / **APC**: Adenomatous polyposis coli 18
- **NICD**: Notch intracellular domain 20
- **PCP**: Planar cell polarity 22
- **ACF**: Aberrant crypt foci 25
- **CA**: Cellular automaton 33
- **CPM**: Cellular potts model 36
- **GUI**: Graphical user interface 36
- **1D**: One-dimensional 46
- **OS**: Overlapping spheres 47
- **DCIS**: Ductal carcinoma in situ 59
- **IFE**: Interfollicular epidermis 59
- **OE**: Olfactory epithelium 59
- **ORNs**: Primary olfactory receptor neurons 59

- **XP**: eXtreme programming 66
- **ODE**: Ordinary differential equation 74
- **PDE**: Partial differential equation 74
- **PETSc**: Portable extensible toolkit for scientific computation 74
- **MPI**: Message passing interface 74
- **CPU**: Central processing unit 117

Chapter 1

Introduction

Colorectal cancer (CRC) is the third most prevalent form of cancer, and the second most common cause of cancer-related death worldwide[1]. This demands a response from scientists and clinicians alike to understand its aetiology and develop effective treatments. Over 90% of cases arise from adenocarcinomas, malignant growths that form in the glandular tissue of the intestine, which is punctuated by regularly-spaced invaginations known as the crypts of Lieberkühn. Specifically, these tumours are believed to originate via genetic alterations which affect the normal dynamics of the crypt, accumulate and confer persistence to mutated cells, allowing unchecked proliferation that eventually leads to the formation of a tumour. The pathobiology of this particular disease is such that symptoms often present very late in development, which makes the cancer hard to detect without preemptive screening. However, if detected early enough, it remains curable.

The crypts of Lieberkühn are test-tube shaped glands that completely cover the surface of the small and large intestine, which are lined with a monolayer of columnar epithelial cells. The crypts function to renew the intestinal surface every few days, enabling the organ to manage the damage caused by the harsh digestive environment, and the passing of food and waste. This is coordinated by a delicate balance of cell division, migration and death, and the continuous upward migration and removal of cells from the crypt provides a frontline defense mechanism against mutant cell populations, which are prevented from remaining in the crypt long enough to cause significant damage. However, if cells accumulate genetic mutations that alter their migration velocity or provide resistance to apoptosis cues, then these cells may persist and multiply in the crypts. This alone can increase stress on the walls of the crypts, causing buckling, but the problem will be aggravated if such cells acquire additional mutations which increase the rate of cell proliferation, or alter cell-cell

[1]Statistics provided by Cancer Research UK, `www.cancerresearchuk.org`.

or cell-substrate adhesion. Dysplastic crypts – which are colonised by mutated cells – can allow the formation of a benign tumour, known as an adenoma, if the mutant cells do not leave the crypt as they should, but rather persist and proliferate in a localised area. Over time and via accumulated mutations, these growths can spread to adjacent crypts, and progress to a malignant lesion that can break through to the underlying tissue stroma. Once a tumour gains access to the bloodstream, metastases can follow, which are secondary tumours that grow in different locations of the body.

The dynamic cell properties which are required to alter crypt homeostasis sufficiently to aggravate growth of a lesion via crypt budding (also referred to as buckling) and fission (the splitting of one crypt into two) are poorly understood, as it is difficult for biologists to observe experimentally, either *in vivo* or *in vitro*, the initial changes in this sequence of events. Rather, the downstream effects can be observed after the initial mutations have spread and altered the normal dynamics of the system. Performing *in silico* experiments using an accurate, predictive, computational model of the crypt will highlight the conditions required for this breakdown to occur, and so provide valuable insight into the tissue-level effects of genetic mutations that lead to CRC. Further, accurate modelling can be utilised to investigate the administration of drugs that are designed to target specific aspects of subcellular and cellular dynamics, and how drug delivery is affected by abnormal cell migration, division and apoptosis.

While the crypt is an intense focus of research within the scientific community, there are still gaps in the biological understanding of how tissue homeostasis is maintained. In particular, the mechanisms of cell removal and apoptosis within the crypt are still unknown, as well as the typical number and location of stem cells, which are the immortal cells thought to give rise to all cell lineages. These are examples of unknown elements of crypt biology that could be addressed by targeted investigation using a mathematical model of an individual crypt, and it is suggested here that such a predictive model could also be employed to advance understanding of the system as it functions under normal conditions.

The normal dynamics of the crypt arise as a consequence of events that are coupled across the different spatial scales. For example, the nature of stem cell number and the incidence of cell death at the collar is likely to be intimately linked to the geometry of the crypt, and its shape could influence cell behaviour as the cells move position. Also, it is thought that signalling gradients along the crypt axis influence cell proliferation and differentiation. Moreover, the progression of CRC is a multiscale process, arising from genetic mutations which alter the normal cell-level behaviour, compromising the structure of the crypt and ultimately manifesting as a growth at the tissue level. This emphasises that to investigate

accurately the breakdown of the system dynamics, it is necessary to adopt a multiscale approach: to achieve accurate, reliable predictions, a model of the crypt must link processes occurring at the subcellular, cellular and tissue levels. Given the need to visualise macroscopic changes at the tissue level, and to address the influence of crypt shape on cell behaviour, the model must also be based on a realistic, deformable geometry. This will necessitate incorporating detail of the stability and structure of the surrounding tissue stroma, which supports the crypt, and that the crypts themselves are very tightly packed. It is also necessary to consider the system in three dimensions, so as to reproduce accurately the degrees of freedom that are afforded to cells throughout migration. Such a model does not yet exist.

Presented in this thesis is a new computational model of the colonic crypt, which focuses on mechanical effects and seeks to remove the imposition of a fixed geometry to enable investigation of the deformation of the epithelium that can occur as a consequence of abnormal cellular behaviour. A discrete modelling approach is used, and the computational code is developed within an open-source numerical library, designed and developed primarily within the University of Oxford Computational Biology group to tackle computationally intensive problems in biology and physiology: Chaste [94]. This open-source approach, which facilitates future research based upon current work, is unusual in academia, and is one of the innovative aspects of this research.

Model development is undertaken in iterative stages, by firstly presenting a two-dimensional (2D) model of a healthy, growing, deformable epithelial monolayer. By extending this to a 2D cross-sectional representation of the crypt, and despite the inherent spatial limitations of such a model, insight is provided into a possible mechanism of cell migration, which is currently unknown. Further, results also suggest that crypt shape may be a factor in the cellular decision of asymmetric or symmetric division, as well as cell death at the crypt collar. Preliminary results which focus on the spread of mutant cell populations throughout the crypt suggest that a reduction in cell migration is key to confer persistence, but it is necessary to consider the third spatial dimension to prevent unnecessary restrictions on cell movement. A three-dimensional (3D) extension is presented, and the building blocks for a complete realisation of the crypt structure are presented. As this is computationally intensive, full use of the 3D model is currently infeasible, and necessitates parallelisation of the Chaste framework or a new model definition that removes dependence on a mesh-based cell model. This marks out the direction for future work, which is discussed in Chapter 8.

The justification and the potential for developing a 3D model of the colonic crypt with a deformable geometry lies in the predictive power of *in silico* investigations, which can

contribute to the understanding of interactions across the spatial scales involved. Increasingly, scientists within the field of cancer research are recognising the usefulness of, and moreover the need for, mathematical modelling as a tool for providing further insight into the mechanisms of carcinogenesis [6]. Cancer biologists have realised that comprehensive models are needed to maximise the information content of existing data and to identify key system parameters [49]. Feedback within the physical and life sciences is essential to drive research forward: communication and collaboration are vital to ensure accuracy and to push consistently the boundary of knowledge forward. Such dependency, therefore, is necessary in this work, to produce qualitative results that identify parameters, or parameter balances, that are crucial to the behaviour of the system and which cannot at present be obtained for ethical, financial or viability reasons.

In order to generate a realistic tool, a collaboration has been established for this work with Prof. Inke Näthke, Dr. Paul Appleton and Dr. Scott Nelson, based at the College of Life Sciences, University of Dundee. The purpose of this collaboration is to generate an accurate and realistic crypt model, with which to perform informed *in silico* experiments, and to that end, the biological foundation of the model has been established via *in vitro* experiments, presented in Section 2.1.1. Where possible, experimental data has been used to evaluate model output, but the extent of such comparison is limited at this early stage of model development. However, hypotheses that arise from initial *in silico* investigations will initiate a feedback loop of experimental and computational investigations that will advance the fundamental understanding of the system.

1.1 Overview of Thesis

The content of this thesis is as follows. The biological background is presented in Chapter 2, which introduces the relevant aspects of crypt biology that are applied within existing mathematical models as well as the new models that are proposed in this thesis. An investigation of current and relevant mathematical literature is given in Chapter 3, to lay the foundation and justify the direction for new modelling work. The off-lattice cell-centre model, which forms the basis for the new crypt model, is introduced in Chapter 4, together with the Chaste framework that has been used and, by necessity, extended. Chapter 5 introduces and develops a discrete, deformable model of the epithelial monolayer that lines the crypt, which incorporates a novel representation of the role of the surrounding tissue stroma and musculature. In Chapter 6, this model is incorporated into a 2D cross-sectional crypt geometry and simple experiments are conducted to investigate the spread of a mutant

cell population. In Chapter 7 the model is extended to 3D space, where preliminary results support those already found in the 2D models. Chapter 7 also discusses the computational challenges faced throughout the model development described in Chapters 4, 5, 6 and 7, and the limitations which currently prevent the extension of this 3D model to adopt a realistic crypt geometry. The key results from Chapters 5, 6 and 7 are summarised and discussed in Chapter 8, where suggestions for future work are also included.

Chapter 2

Biological Background

This chapter presents the biological background of the function and dynamics of the crypts of Lieberkühn. Firstly, experimental results that characterise the tissue structure of the crypts and surrounding musculature are presented, which have been collected and provided by our experimental collaborators. Cellular dynamics and the established proliferative hierarchy within the crypt are discussed, with focus given to the role of the Wnt and Notch signalling pathways which are key in determining cell proliferation and differentiation. The components of cell dynamics which are presented here are later incorporated in the crypt models proposed in this thesis, as well as in existing models that are discussed in the literature review provided in Chapter 3.

Section 2.2 discusses what is currently understood about the progression from a healthy crypt epithelium through to the formation of a malignant tumour, and how changes at the subcellular level manifest as cell-level properties which disturb the normal behaviour of the crypts. While it is possible for biologists to observe changes at the tissue level, it is not currently possible to elucidate the initial stages in carcinoma development, and hence conclude the necessary and sufficient conditions for CRC to arise. Therefore the biology presented here provides the basis for the development of a computational model of the crypt, which can be used as an *in silico* tool to test hypotheses and investigate the destabilisation of the crypt structure which precedes tumour growth.

2.1 The Colorectal Crypt

The main function of the intestine is to digest food and absorb the nutrients released by the digestion processes [2]. The small intestine carries out most of this work, while the large intestine acts mainly to absorb excess water and salts from solid waste. To maximise

efficiency of absorption, an epithelial layer with a large surface area is required, and this layer must also be equipped with a level of protection from the harsh environment created by the digestive enzymes, and from the repeated contraction of the gut which aids the transport of solid waste through the system. To accomplish this, the intestine is covered by millions of regularly spaced invaginations – the crypts of Lieberkühn – which, in addition to secreting enzymes and a protective layer of mucus, also continuously replenish the epithelial layer. In the small intestine, villi that project from the surface are surrounded by a number of crypts, which increases the surface area available, as this is where the majority of nutrient absorption takes place.

To maintain a healthy system, the body must balance the need for epithelial renewal (to protect against damage caused by the contents of the gut) with the need to prevent over-proliferation, which would use excessive amounts of energy and could lead to further complications by disrupting the regular crypt function. Specific mechanisms, such as controlled cell death and volume-dependent cell division, exist to regulate these cellular processes and maintain normal crypt dynamics. These are employed and managed by the crypts at the subcellular, cellular and tissue levels. These mechanisms are outlined in detail here.

2.1.1 Structure of the Colonic Mucosa

Individual crypts are closely packed units that are surrounded and separated by loose connective tissue, the lamina propria. Each crypt consists of contiguous epithelial cells anchored to a basement membrane, which forms a physical barrier to the surrounding tissue stroma. The lamina propria has two functions: immunological, due to the presence of immunocompetent and cytokine-producing cells, and structural, to provide support for the epithelial layer. Immediately beneath the crypts lies a thin layer of smooth muscle, known as the muscularis mucosae, that forms the boundary between the mucosa and submucosa, as shown in Figure 2.1. These images of murine gut tissue were obtained using fluorescent microscopy of sectioned gut tissue following the methods described in Appleton et al. [5].

In the murine small intestine, the muscularis mucosae is only one or two cells thick, forming a network that follows the contours of the crypt bases. Examination of intact mouse tissue in 3D shows that, contrary to the reported structure of human gut tissue, the smooth muscle cells of the small intestinal muscularis mucosae are mostly oriented parallel to the longitudinal muscle layer of the muscularis externa, as indicated in Figure 2.1(A), (B) and

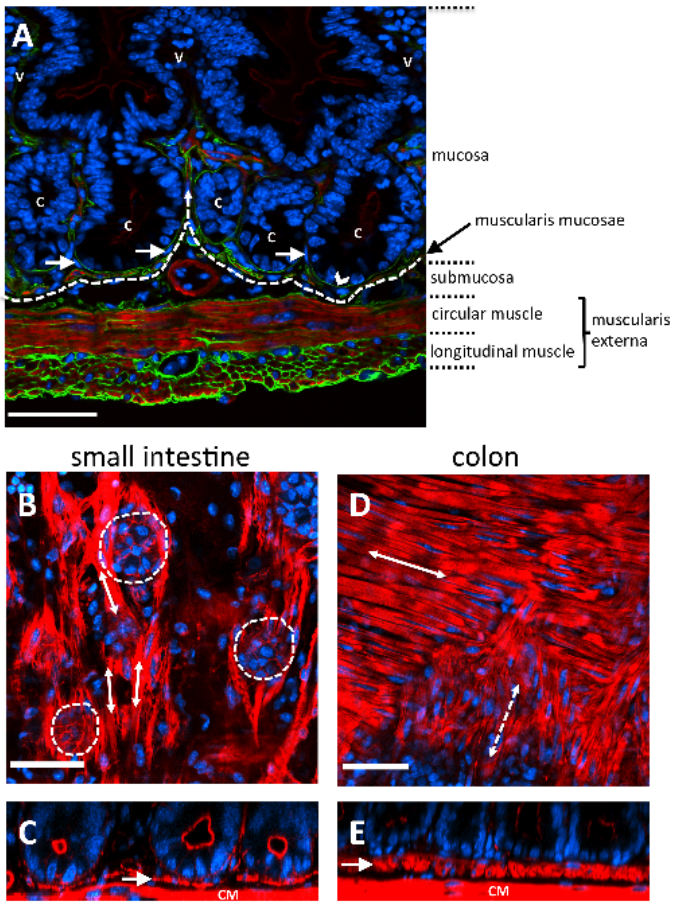

Figure 2.1: Musculature of the murine intestinal wall. (A) A section through the wall of the small intestine, fluorescently labelled and visualised by widefield fluorescence microscopy. Nuclei (blue) are stained with DAPI, F-actin (red) highlights the smooth muscle cells and apical surface of the gut epithelium. The gut epithelium is continuous from the crypts (marked 'C') and over the villi (marked 'V'). Basement membranes (green) are stained with an anti-laminin antibody. Pericryptal fibroblasts surround the crypt epithelium, and these are indicated by the arrows. (B) A longitudinal section through the small intestine shows the base of crypts (outlined by dashed circles). Smooth muscle fibres of the muscularis mucosae are oriented parallel (arrows) to the longitudinal muscle. (C) A transverse section of small intestine shows the muscularis mucosae (arrow). It is comprised of a single cell layer that forms an incomplete meshwork beneath crypts, just above the circular muscle. (D) A longitudinal section through the colon shows the outer (solid arrow) and inner (dashed arrow) more disorganised layers of the muscularis mucosae. The outer layer is oriented parallel to the longitudinal muscle and the inner layer parallel with the circular muscle, as indicated by double headed arrows. (E) A transverse section through the colon shows the muscularis mucosae (arrow) at the base of the crypts, which is much thicker than that found in the small intestine. Scale bars = 50 μm.

(C). In the small intestine, the smooth muscle fibres of the muscularis mucosae extend upwards into the villi. It is thought that the role of the muscularis mucosae is to agitate the

epithelium gently and constantly to help expel secretions from crypts and enhance contact between epithelium and luminal contents [45].

When viewed in transverse section (Figure 2.1(A)), the muscularis mucosae appears to follow closely the outline of the base of each crypt. When viewed in longitudinal section (Figure 2.1(B)), the muscularis mucosae appears to form individual baskets beneath each crypt, analogous to an egg box which contains each crypt base as a single egg. The muscularis mucosae of the colon is composed of two distinct layers of smooth muscle fibres, the outer layer being oriented parallel to the longitudinal muscularis externa, the inner layer being more disorganised, but generally oriented parallel with the circular muscularis externa, as shown in Figures 2.1(D) and (E).

The laminin-rich basement membrane that is directly attached to the basal surface of gut epithelial cells, indicated in Figure 2.1(A), is comprised of a basal lamina and a reticular lamina; the former is a thin mat composed primarily of Type IV collagen that is attached to the basal side of the epithelial cells, and also by collagen fibrils to the reticular lamina, which is attached to the connective tissue. The basement membrane itself, when compared to cells, is much stiffer [46]. Evidence suggests that the interactions between the epithelium and basement membrane promote cell adhesion, induce expression of differentiated cell functions (such as mucosal protection) via the extracellular component Laminin-1 [81], initiate and maintain cell polarity, participate in the regulation of morphogenesis and promote cell migration [20, 119].

Just below the basement membrane, surrounding each crypt, is a pericryptal fibroblast sheath (PCFS), comprising a highly organised system of fibroblasts, collagen and mucopolysaccharide ground substance [88]. By scoring sections of gut tissue, Neal and Potten [84] found that there are 38 PCFS cells per mouse small intestinal crypt and 124 per colonic crypt, and also observed that there is no migration of these stromal cells. PCFS cells produce signalling factors, such as Wnt signals, that are involved in the growth and maintenance of the crypt [132] and which are described in Section 2.1.3.

Beneath the muscularis mucosae lies the submucosa, which consists of loose connective tissue rich in collagen and elastic fibres. Embedded in this material are larger blood vessels, lymphatics and nerves. The submucosa is enclosed by the muscular wall of the gut, called the muscularis. It consists of outer longitudinal and inner circular layers of smooth muscle. The muscularis is responsible for peristalsis, the contractile movements involved in advancing intestinal contents.

The detail of the tissue structure of the crypt is relevant when developing a theoretical model which seeks to track deformation of the epithelial monolayer and examine the influence of the shape on cell behaviour, as this shape is influenced by elements such as the PCFS. The detail described above is thus applied in Chapters 5, 6 and 7, where the new model is defined and investigated.

2.1.2 Crypt Dynamics

The crypts of Lieberkühn coordinate the renewal of the epithelium via synchronised cell proliferation, migration, differentiation and apoptosis. As shown in Figure 2.2, within the crypts there is believed to be a proliferative hierarchy of cells, beginning with a stem cell niche at the base [55]. On average, these stem cells divide asymmetrically to produce one stem cell and one transit-amplifying cell [9]. Transit-amplifying cells, occupying the lower two-thirds of the crypt, then perform several symmetric divisions before undergoing terminal differentiation into one of four cell types [2]:

- **Colonocytes**: these are absorptive columnar epithelial cells, which are also responsible for secreting the hydrolytic enzymes that carry out digestion. (These are known as enterocytes in the small intestine.)
- **Goblet cells**: these secrete mucus to facilitate movement of the contents of the gut and provide protection against damage.
- **Enteroendocrine cells**: these release hormones to regulate the secretion of digestive enzymes.
- **Paneth cells**: these are found primarily in the small intestine; they respond to the presence of bacteria by secreting antimicrobial molecules [83].

Apart from the Paneth cells of the small intestine, all differentiated cell types are found in the upper third of the crypt. Other cell types found in the crypts include caveolated cells, which have an unknown function, and M cells, which function in the transportation of antigens to present to the immune cells, but these are very few in number by comparison [28].

Stem Cells

By definition, "a stem cell is a primitive, undifferentiated cell that has the capacity for both self-renewal and the production of daughter cells that are committed to the formation of

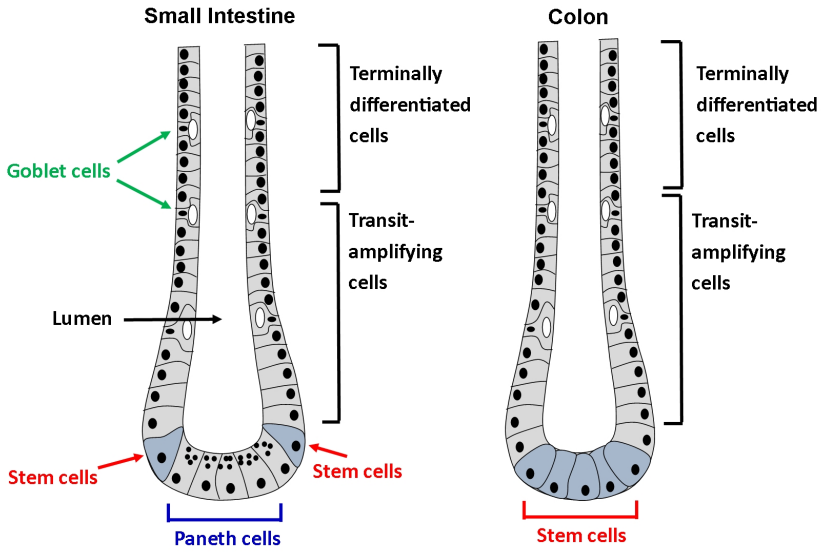

Figure 2.2: The overall structure of a crypt from the small intestine and large intestine indicating the location and position of the different cell types and proliferative states. This schematic is based on a figure from McDonald et al. [75].

every adult cell lineage within their tissue of origin" [28]. Consequently, stem cells play a key role in the dynamics of the crypt, functioning to regulate the overall rate of cell production. Stem cells demonstrate the capacity both to divide asymmetrically, to produce one stem cell and one transit-amplifying cell, and symmetrically, to produce two stem cells. In 1975, Cairns [22] proposed that throughout asymmetric division, stem cells retain the original set of chromosomes, while the newly synthesized DNA is passed to the progenitor cell which is committed to differentiation. Subsequently referred to as Cairns' hypothesis, this has the effect of minimising mutations introduced by replication errors and is discussed in further detail in Section 2.2.

Currently the stem cell niche, maintained by supporting mesenchymal cells [55], is believed to reside at the base of the crypts in the large intestine, with some stem cells identified to sit above the Paneth cells in the small intestine, as shown in Figure 2.2 [103]. The absence of reliable stem cell markers means that the number of stem cells is unknown and is a current area of interest for investigation. It has been suggested that there are between 4 - 16 stem cells in the small intestine, compared with only 3 - 4 in the large intestine [132].

In 2007, Barker et al. [9] found cells at the crypt base expressing the LGR5$^+$ gene (leucine-rich-repeat-containing G-protein-coupled receptor 5), which displayed the two hallmark properties of stem cells: multipotency, the ability to generate all the observable differentiated lineages of the crypt, and self-renewal, the ability to maintain population number.

(Together these characterise the *stemness* of a cell [110].) Consequently, LGR5$^+$ has been identified as a valid marker gene for crypt stem cells in both the small and large intestine, and further results revealed that stem cells in the small intestine crypts cycle more quickly than those in the large intestine, which explains the more rapid epithelial turnover in the small intestine.

In 2008, Sangiorgi and Capecchi [103] identified the BMI1 gene as an intestinal stem cell marker, but contrary to Barker et al. [9], located stem cells at the +4 position, *i.e.* four cells above the crypt base. More recently, it has been found that BMI1 expression is highest in LGR5$^+$ cells, which indicates that this work may simply overlap that of Barker et al. [9], such that in both cases the marked cells derive from the same cells at the crypt base [110]. Indeed, recent experiments by Quyn et al. [99] using the LGR5$^+$ marker validate the Barker et al. [9] results and identify stem cells up to position 7. It is possible that either the BMI1 and LGR5$^+$ studies identify different stem cell pools, or that the stem cells can migrate from one niche to the other. Alternatively, it might be that these markers identify two distinct subpopulations which differ according to their state of proliferation – one which is actively cycling (identified by LGR5$^+$), and one which is quiescent (identified by BMI1) – as such subpopulations have been found to exist in other tissues [132].

Despite efforts to determine stem cell numbers in the crypts, it is understood that the stem cells cycle approximately once a day, which is slower than the transit amplifying cells positioned directly above [8, 75]. The stem cells also respond to the general needs of the tissue, and indeed are capable of regenerating the tissue following injury, which is known as stem cell plasticity [19, 28]. This is achieved via clonal growth that repopulates the tissue [96].

Cell Migration

As the epithelial cells divide and differentiate, directed migration occurs towards the crypt collar. One exception to this is the movement of the Paneth cells of the small intestinal crypts, which instead migrate towards the crypt base [48]. Mechanisms proposed to describe the general upward motion include passive mechanisms such as mitotic pressure, negative pressure due to cell loss at the villus tip, global movement of the components of the extracellular matrix, and a 'conveyor belt' action of the basement membrane [63]. Movement induced by the extracellular matrix has been rejected based on the asynchronous behaviour of the PCFS and epithelium [84], and because the basement membrane does not renew itself sufficiently rapidly, nor is it strong enough to carry epithelial cells upwards.

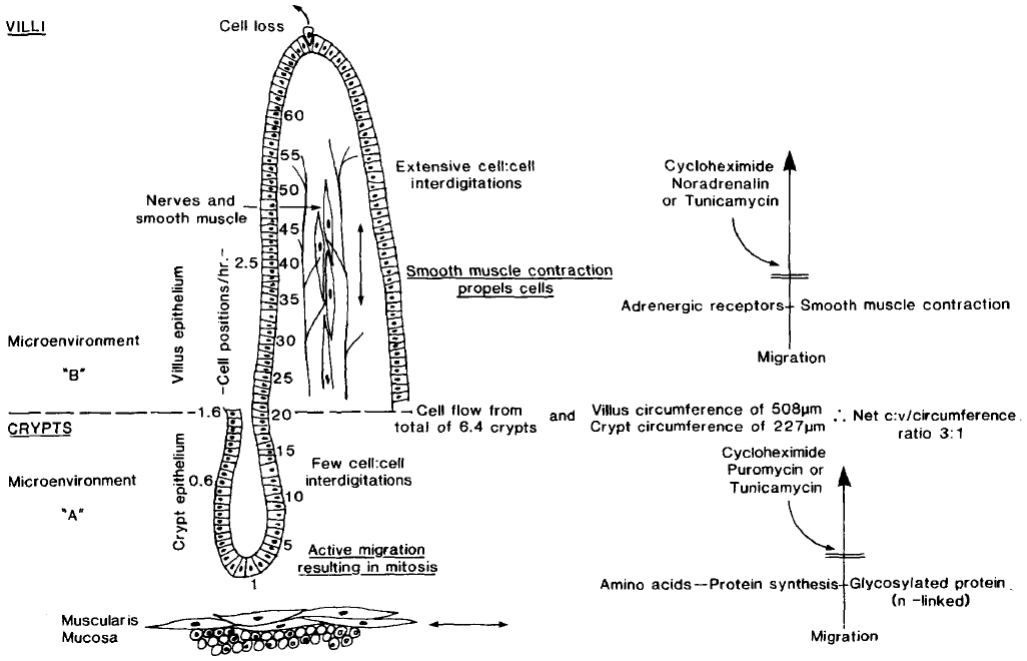

Figure 2.3: A model for cell migration proposed by Kaur and Potten [63]. This model suggests that active migration occurs in the crypt as a consequence of protein synthesis and glycosylation, whereas motion on the small intestinal villus is driven by the contraction of smooth muscle in the underlying connective tissue. Reprinted with permission from Kaur and Potten [63].

In 1986, by eliminating cell division using radiation and toxic agents, Kaur and Potten [61] demonstrated that migration can occur in the absence of mitotic activity, and therefore dismissed both passive motion due to mitotic pressure, and also the negative pressure theory, but without justification.

Active mechanisms that have been proposed include basal feet on migrating cells, active motion along the basement membrane, amoeboid-type movement and protein synthesis of 'motility molecules'. The first three of these can be rejected on the basis of existing biological understanding of the epithelium, but the action of protein synthesis was investigated by Kaur and Potten [63] in a study of small intestinal crypts and villi. This investigation focused on the response to the application of different drugs – puromycin and cycloheximide, which both inhibit protein synthesis, and noradrenaline, which smooths muscle contraction. The experimental results suggest that inhibition of protein synthesis can reduce (but not halt) cell migration in the crypts, whereas inhibition of smooth muscle contraction only reduces migration on the villus. This suggests that there are two migration mechanisms at work in the small intestine – one within the crypts, and one on the villus. These mechanisms are summarised in Figure 2.3.

In the experiments that eliminate mitosis, Kaur and Potten [63] monitored crypts for a maximum of 24 hours post interference, a relatively short period. It is plausible that the observed migration is a consequence of the relaxation of the crypt following irradiation, as cells readjust to form a mechanical equilibrium. In general, the turnover of epithelial cells in the crypt suggests a good comparison between cell migration and birth rate, which does indicate that cell division influences movement. Thus, to confirm the hypotheses of Kaur and Potten [63], experimental investigation is required to verify the existence of the proposed 'motility molecules' in the epithelial cells. Further, within their experiments, it may be the case that the elimination of protein synthesis could have further implications for cellular dynamics, such that reduced motility is a secondary effect, and this must be proven otherwise. This remains an open question which modelling may lend insight into, and indeed the mechanism of cell migration in the crypt is addressed in Chapter 5.

Cell Death

Two control mechanisms are known to trigger cell death in the crypt. Firstly, terminally differentiated epithelial cells that reach the extrusion zone at the crypt collar and intercrypt table undergo apoptosis and/or are shed into the lumen. The toxic environment of the colon and the process of solid material being forced past the crypt openings is likely to be at least one of the causes of the cell shedding events that occur – cells are literally swept away. However, while experimentally, apoptotic cells are found on the intercrypt table (for example, [111]) and towards the crypt collar, the cause of apoptosis is not known. It is possible that apoptosis is induced when a cell exceeds a certain age, a consequence of it having simply 'run its course'. Alternatively, there may be a spatial gradient in a signalling molecule which triggers apoptosis at a certain physical location or at a specific point in the life cycle of a differentiated cell. Support for this is given by the distribution of adhesion molecules observed in the basement membrane, and how this changes moving up the crypt axis [107]. Alternatively, apoptosis may simply be a consequence of cell compression that arises due to pressure from migrating cells below.

In addition, a form of programmed cell death, termed anoikis, is triggered when there is inadequate adhesion of the epithelial cells to the extracellular matrix [44], with detachment inducing apoptosis within three hours for healthy cells [128]. Functioning correctly, this maintains tissue homeostasis by restricting proliferation to the monolayer, thereby averting dysplasia, and by preventing cells from re-attaching in another location and resuming growth. Anoikis events are common at the crypt collar, where the crowding induced by the curvature of the layer in this region may render cells particularly vulnerable to

extrusion. Due to the negative curvature of the epithelial layer at the crypt collar, cells in this region can have a reduced basal contact area, and so incur a loss of substrate adhesion, which may contribute further to detachment. Apoptosis has been found to follow such extrusion events, observed for epithelial cells at the villus tip in the small intestine, and along the surface epithelium of the colon [64].

Disruption of anoikis has relevance to pre-cancerous epithelial cells, aiding colonisation of secondary sites following detachment from the extracellular matrix – a concept known as anchorage-independent growth. As such, the failure of anoikis is key in tumorigenesis and metastasis. The anchorage of cells to the underlying extracellular matrix is sustained and mediated largely by the action of integrins, but some cancerous cells can resist anoikis, prolonging survival in the absence of matrix attachment [52]. Studies have suggested that resistance to anoikis can arise in several ways: activated oncogenes such as Src and Ras, over expression of the Focal Adhesion Kinase (FAK) protein and activation of growth factor receptors; many of these transformations occur during the development of a colon tumour [128].

While apoptosis events are taking place, maintenance of epithelial barrier function is essential for the integrity of the layer – failure could result in leakage and the formation of gaps in the epithelium. However, in simple epithelia – those that are one cell thick – it has been found that the barrier of the epithelium is maintained even when there is a high incidence of apoptosis, mediated by a process of cell extrusion. Coordination of this process is summarised in the following model proposed by Rosenblatt et al. [102]: an apoptotic cell signals neighbouring cells to form an actin and myosin cable ring at the apical interface between cells. Contraction of this ring by the neighbours squeezes the dead cell out of the epithelium, while simultaneously closing the gap. Alternative hypotheses focus on the role of phagocytosis, whereby the apoptotic cell is engulfed by macrophages. However, this leads to gaps in the epithelium, disrupting barrier function.

2.1.3 Cell Division

As described thus far, within each crypt, stem cells reside at the base and divide continuously to produce transit-amplifying cells, which go on to divide several times before terminally differentiating. Differentiated cells undergo apoptosis and/or are shed from the epithelial layer. For homeostasis and to maintain 'normal' crypt dynamics, it is crucial that cell production balances with cell removal, and it has been proposed that these processes

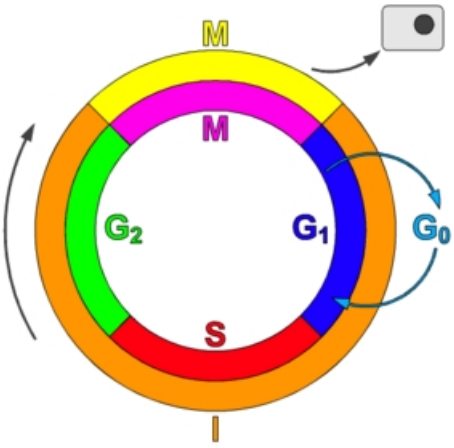

Figure 2.4: The stages of the cell cycle. Reprinted with permission from Alberts et al. [2].

are controlled by extracellular factors such as the Wnt signalling pathway. The key regulators of cell division, the Wnt and Notch pathways and cell polarity, are discussed below, as well as the mechanism of cell adhesion.

The Cell Cycle

Cell division occurs as a consequence of progression through the cell cycle, which has four distinct stages: S, G_2, M and G_1 (see Figure 2.4). S-phase refers to the synthesis stage, where the cell DNA is duplicated. Typically, this takes half of the total cell cycle time in a mammalian cell, which is approximately 10 – 12 hours [2]. Cell division occurs during the mitosis stage, referred to as M-phase. This has a shorter duration than S-phase, requiring less than an hour in a mammalian cell. Gap phases are inserted into the cycle to account for the time required for a cell to grow and double its mass, as well as to allow it to monitor its environment and ensure that it is ready to enter the next phase [2]. G_1 is the gap between M-phase and S-phase, and G_2 is the gap between S-phase and M-phase. There is also a resting stage in the cycle known as G_0, in which cells may reside to delay progress through G_1 if extracellular conditions are unfavourable.

Cyclin-dependent kinases (Cdks) and their regulatory cyclin proteins form the central machinery of the cell cycle control system. Unless Cdks are tightly bound to a cyclin, they have no activity, and it is the cyclical change in Cdk activity that regulates the phosphorylation of intracellular proteins which control events in the cell cycle [2]. Cyclin D proteins are recognised as crucial to the G_1 phase of the cell cycle [50], and the G_1/S transition [123], and in particular as one of the targets of β-catenin, a transcription factor (TCF) for D-type

cyclins in colorectal tissue [116]. Further to this, the duration of each of the S, G_2 and M phases is thought to be independent of Cyclin D.

Density-Dependent Inhibition of Mitosis

Checkpoints exist in the cell cycle before the G_1/S and G_2/M transitions, to ensure the successful completion of the respective synthesis and mitosis phases [114]. These checkpoints allow for cells to respond to extracellular influences – signals that promote or inhibit cell proliferation by regulating progression through the checkpoint. Continuation through to the next phase is granted when certain proteins exceed a particular threshold concentration, and if not, the cycle can be arrested if necessary [2]. An example of this is density-dependent inhibition of mitosis (also known as contact inhibition), which arises as a consequence of the limited availability of mitogens, growth and survival factors for cells [2]. Under normal circumstances, this prevents over-proliferation of cells once a state of confluence has been reached, and experimental results indicate that growth arrest is actively induced in the G0/G1 phase of the cell cycle [67]. This is relevant in the context of cancer, as cancerous cells have been shown to divide despite excess compression [2].

The Wnt Signalling Pathway

Expression of D-type cyclins is induced by extracellular growth factors. An important example is the Wnt/Wingless signalling pathway, whose activity is mediated by the β-catenin protein, which is normally localised in the cytoplasm when Wnt signalling is 'off'. Evidence shows that the Wnt signalling pathway is required to maintain the stem cell compartment in the crypt, and so is crucial to epithelial cell renewal and differentiation [66]. Moreover, it has been observed that cells closest to the crypt base accumulate β-catenin in the nucleus, and that levels of nuclear β-catenin decrease upwards along the vertical crypt axis [120]. This suggests a localised source of diffusible Wnt factors in the stroma that surrounds the crypt base, and leads to the hypothesis that a spatial gradient in Wnt may be responsible for the proliferative hierarchy observed in the crypt. This is illustrated in Figure 2.5, which also highlights the decreasing 'stemness' of the epithelial cells up the crypt [48].

A measure of Wnt signalling activity is the amount and location of β-catenin, which can stabilise in either the nucleus or on the cell membrane, where it has a role in cell adhesion. The canonical Wnt pathway, which is generally accepted to be most relevant to the

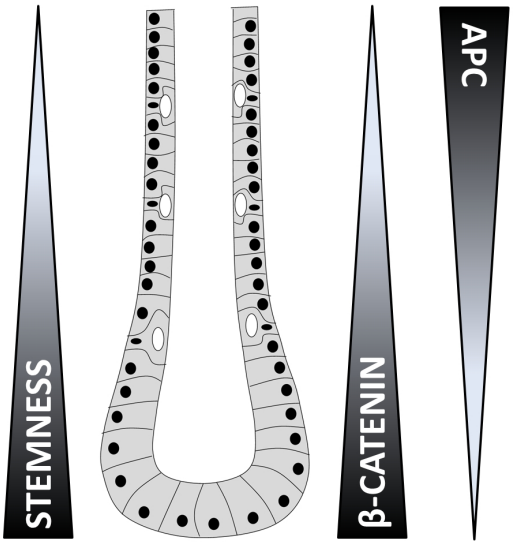

Figure 2.5: Cells closest to the crypt base accumulate nuclear β-catenin, and this expression of β-catenin has a decreasing gradient up the vertical crypt axis, which indicates a decreasing cell 'stemness'. The APC tumour suppressor gene is a key component of the destruction complex that acts to maintain low levels of β-catenin, and this demonstrates an inverse gradient. Drawn according to Gaspar and Fodde [48].

development of CRC, is shown in Figure 2.6. This pathway controls the level of nuclear β-catenin and exists in either the 'on' or 'off' state.

In the 'on' state, the Wnt ligands bind to the Frizzled receptors on the cell surface. A series of reactions is initiated, which eventually inhibit and destabilise the β-catenin destruction complex via the Dishevelled protein. Destabilisation and failure of the complex to phosphorylate β-catenin leads to an increase in cytoplasmic β-catenin, which then travels to the nucleus. In the nucleus, it binds to a transcription factor from the TCF/LEF family and induces transcription of proteins that control the cell-cycle, cell migration and apoptosis [56].

Conversely, in the absence of an external Wnt stimulus, the 'off' state, a destruction complex containing the Adenomatous Polyposis Coli (*Apc*) tumour suppressor gene, Axin and GSK3β proteins, maintains low levels of β-catenin [56]. This is achieved by phosphorylation of β-catenin, which is subsequently destroyed. Thus, β-catenin is prevented from translocating to the nucleus, but rather the Groucho transcriptional repressor is able to bind to the TCF/LEF transcription factors, which prevents activation of the Wnt target genes. The role of the Wnt signalling pathway is considered in a number of mathematical models of the crypt [21, 87, 123], as well as in the new crypt model proposed in Chapter 6.

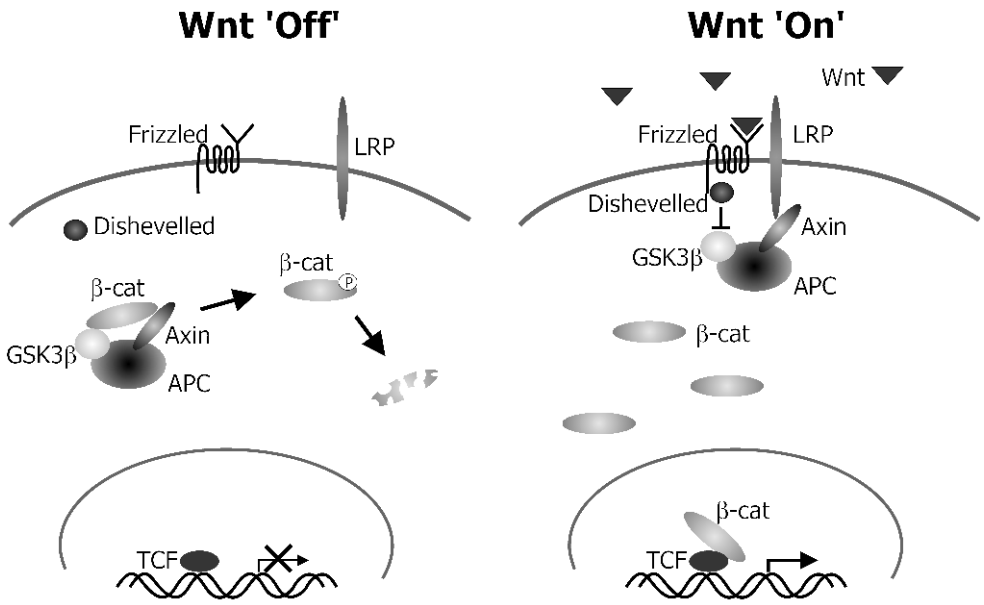

Figure 2.6: The canonical Wnt pathway. *Left*: In the absence of Wnt, the destruction complex maintains low levels of β-catenin. Transcription of Wnt target genes is suppressed. *Right*: Wnt factors bind to receptors on the cell surface, initiating the destabilisation of the destruction complex. Thus, β-catenin accumulates in the cytoplasm and travels to the nucleus where it binds to TCF and induces transcription of proteins that control the cell-cycle. Reprinted with permission from Mirams [78].

The Notch Signalling Pathway

A second signalling pathway that has been found to be crucial to the maintenance of the proliferating cell population in the crypt is the Notch signalling pathway [43]. This pathway is considered in existing mathematical models of crypt dynamics, such as that due to Buske et al. [21] which is introduced in Section 3.1.4, and so detail is provided here. Notch proteins are largely expressed towards the crypt base, in the stem cell region [26]. In particular, this pathway is implicated in influencing the fate of the crypt progenitor cells, in the self-renewal of stem cells and in cell differentiation [60]. The Notch protein itself spans the cell membrane, and so consists of an extracellular and intracellular domain. Activation is achieved via cell-cell contacts, through binding with a transmembrane ligand on a neighbouring cell, and in this way, this signalling pathway is responsible for communication between neighbouring cells. The canonical and non-canonical Notch signalling pathways are illustrated in Figure 2.7.

Specifically, the canonical Notch pathway is activated when a Notch transmembrane receptor (one of Notch1, Notch2, Notch3, Notch4) binds to a Notch transmembrane ligand (Jagged1, Jagged3, or the delta homologs DLL1, DLL3, DLL4) on an adjacent cell, which

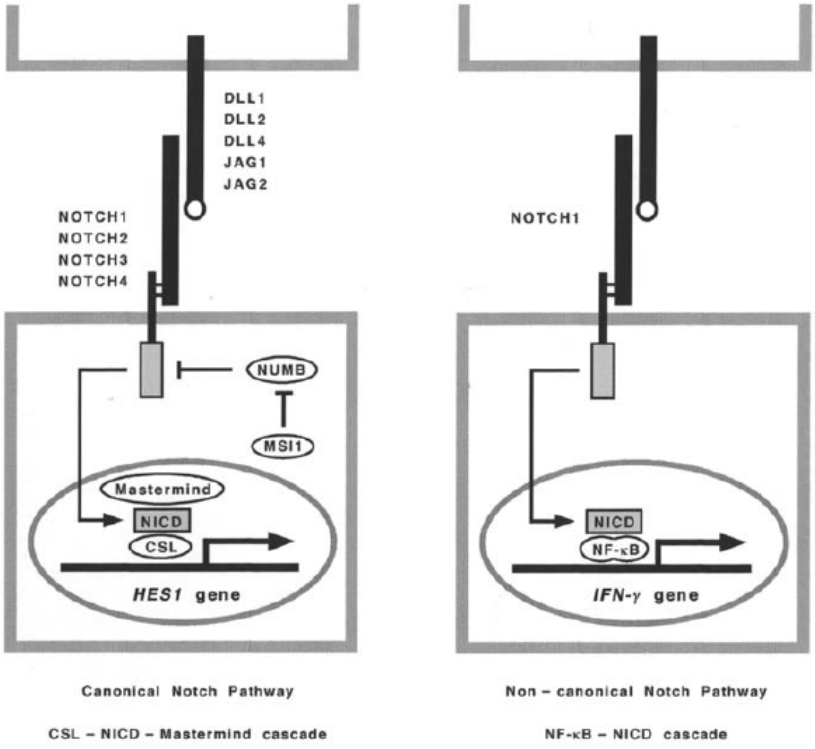

Figure 2.7: *Left*: The canonical Notch signalling pathway. Notch ligands bind to Notch receptors, activating cleavage of the receptor, which translocates to the nucleus and forms a complex with one of the transcriptional regulators (Mastermind and CSL), subsequently activating Notch target genes such as Hes-1. *Right*: An example of the non-canonical pathway. Here, the NICD can also form a complex with NF-κB, activating transcription of the IFN-γ gene. Reprinted with permission from Katoh and Katoh [60].

causes proteolytic cleavage of the receptor. This then triggers the release of the Notch intracellular domain (NICD) which translocates to the nucleus, whereupon it forms a complex with a transcriptional regulator and initiates transcription of Notch target genes. Typically, and as illustrated in Figure 2.7, Notch signals are transduced to the CSL-NICD-Mastermind complex to coordinate maintenance of the stem and transit-amplifying cell populations by inhibiting differentiation. The non-canonical Notch pathway differs in that activation can occur through binding to a non-canonical ligand, or may not require cleavage of the Notch receptor [4].

It has been shown that inactivation of the Notch pathway leads to an increase in the number of goblet and enteroendocrine cells. Conversely, increased activation leads to a reduction in the number of these secretory cell types. Hence, in healthy tissue, cells achieve a secretory fate by avoiding Notch activation, and because these cells also express Delta proteins, Notch is subsequently activated in their neighbours, preventing them from differentiating

to a secretory cell type, but rather securing an absorptive fate. This is known as lateral inhibition, and is such that Notch signalling induces a binary cell fate decision between the two lineage types [101]. Maintenance of the proliferative compartment is attributed to Notch signalling because of complementary loss- and gain-of-function studies, which identify that Notch inactivation reduces the size of the proliferative compartment, whilst expression of NICD inhibits cell differentiation. The Wnt and Notch signalling pathways are not recognised as having distinct functions in the crypt, but rather there is established crosstalk which implies that stem cells require both signals in combination to maintain a proliferative state [26].

The Adenomatous Polyposis Coli Gene

While the best-characterised role of *Apc* is as part of the destruction complex modulated by Wnt signalling, the multifunctional nature of *Apc* must be highlighted, given that it is vital to understanding numerous basic cellular processes, as well as the disregulation of the balance of these processes that occurs at the onset of CRC [48]. Studies in *C. elegans* and *Drosophila* have identified a role in cytoskeletal organisation, through regulation of migration, division and differentiation of cells. Further, through interaction with microtubules, *Apc* affects cell polarity and directed cell division (discussed below), and also supports nuclear shuttling of β-catenin [83]. Given the importance of the *Apc* gene, especially in the intestinal crypts, current and active research is seeking to understand more about the hierarchy of function, and the implications this may have for treatment in CRC.

Cell Adhesion

Lateral adhesion and diffusion between the epithelial cells in the crypt arises due to adherens junctions, tight junctions and desmosomes [20]. In particular, the adherens junctions form a continuous adhesion belt which encircles all of the cells, close to the apical surface, which comprises actin filaments that reside on the cytoplasmic surface, connected from cell to cell by transmembrane adhesion proteins known as cadherins [2]. β-catenin is one of the anchor proteins that bind the cadherins to the actin filaments, and so this adhesion is dependent on the amount of stable, membrane-bound β-catenin, which is directed from the cytoplasmic pool of β-catenin [56]. Hence, membrane-bound β-catenin is unavailable to take part in the canonical Wnt pathway, and be translocated to the nucleus. However, evidence shows that there is a switch that can divert β-catenin from the membrane to the nucleus and thus a switch from cell adhesion to Wnt signalling [13]. Currently, it is not

believed that the influence for this switch comes from Wnt signalling itself, so activation of the canonical Wnt pathway does not correspond to decreased adhesion between cells.

Cell Polarity

The epithelial cells in the crypt exhibit apico-basal cell polarity, whereby the apical membrane of each cell points towards the crypt lumen, and the basal surface remains in contact with the basement membrane. In addition to this, planar cell polarity (PCP) controls cell shape, division, movement and differentiation, and overall, regulates tissue expansion orthogonal to the apico-basal axis [20]. During division, this is coordinated through the regulated positioning of the mitotic spindles relative to the tissue layer [40]. PCP is modulated by the Wnt/planar cell polarity pathway, which is one of the three pathways activated by Wnt[1] [56, 121].

Symmetric and Asymmetric Division

During symmetric division, the mitotic spindles align parallel to the tissue stroma, whereas in asymmetric division, the spindles align perpendicularly such that one daughter cell sits above the other, positioned towards the lumen. This is illustrated in Figure 2.8. In each case, the spindles are displaced close to the apical surface, with the cell itself being rounded and compressed at the base by neighbouring cells, such that it appears tethered to the underlying basement membrane by a stalk. The apically displaced daughter cell is ultimately placed back into the epithelial layer – the mechanism for this is currently unknown for asymmetric division – and the monolayer is maintained throughout growth.

Recently, Quyn et al. [99] (2010) demonstrated that asymmetric division occurs preferentially in the stem cell compartment using 3D images of whole-mount intestinal tissue. In agreement with Fleming et al. [40], it was also shown that divisions which occur in the transit-amplifying cells do so symmetrically. Evidence for Cairns' hypothesis was found in the mechanism of asymmetric division, whereby the unreplicated DNA strands are asymmetrically segregated towards the basal end of the dividing cells [22]. This may also shed light on the fate of cells born out of asymmetric division in the stem cell niche – the positioning of one daughter cell atop another places these cells in different environments, and may commit the upper cell to differentiation [99].

[1]The third pathway is the Wnt/calcium (Wnt/Ca^{2+}) pathway, which acts to increase intracellular calcium and activation of protein kinase C. The function of this pathway is not known [56].

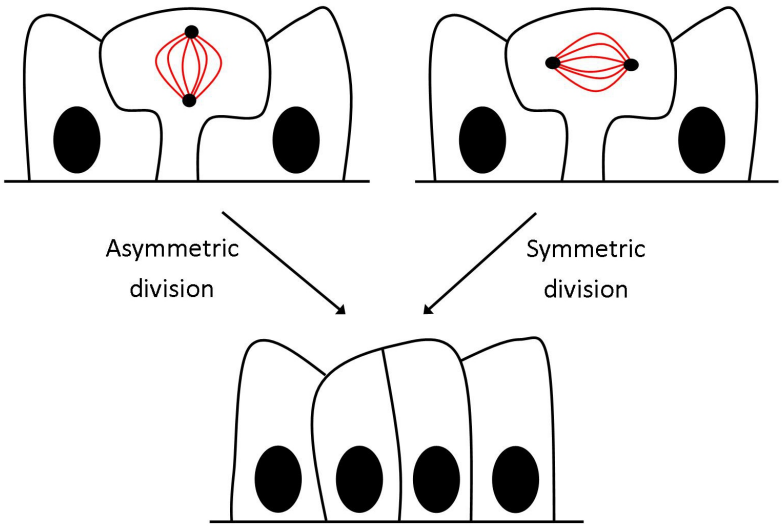

Figure 2.8: A cartoon diagram indicating the difference between asymmetric (left) and symmetric (right) division. In asymmetric division, the mitotic spindles align perpendicular to the tissue stroma, such that the transit daughter cell sits atop the stem daughter cell before cytokinesis. In symmetric division, the spindles align parallel to the basement membrane. In each case, the two daughter cells ultimately sit beside each other, within the plane of the epithelial monolayer.

Cell shape may also play a role in restricting spindle alignment, such that the more compressed apical region of stem cells at the crypt base actually forces the spindles to align perpendicularly to the tissue stroma. In contrast, the spindles in less compressed transit cells further up the crypt can align parallel to the stroma. This is an interesting hypothesis which proposes that the crypt geometry and structure, mechanically, may influence cell division and fate. Indeed, experimental results demonstrate that epithelial cells do respond to their mechanical environment, and moreover that cytokinesis is a mechanical process [36], and it has been suggested that the shape of cells and tissues can influence cell division via cortical tension heterogeneity which guides spindle orientation [117]. Such influence is investigated using the new model proposed in Chapters 5 and 6.

APC is vital in the regulation of cell polarity during mitosis by localising to the plus ends of kinetochore microtubules, and it has been demonstrated that loss of function of this tumour suppressor alters spindle stability and positioning [40, 59]. This is relevant in the context of colorectal carcinogenesis, as inactivation of *Apc* is generally accepted to be one of the initial events in the progression of CRC, which is now discussed.

2.2 Colorectal Carcinogenesis

The upward migration and regular clearance of cells from the crypts (every 3-5 days in the murine intestine) equips the gut with a level of protection that ensures that cells which acquire oncogenic mutations often cannot remain long enough to do significant damage. The implication of this control is that for a mutation to remain in the crypt, it must alter the normal migratory pattern, either by changing its direction and/or rate of movement, or by ignoring the cues for apoptosis, or by over-proliferating beyond the extent of apoptosis [83].

Further, given that stem cells do remain in the crypt longer than their differentiated progeny, indeed for the lifetime of the crypt, there are protective measures which specifically deal with mutations that originate in the stem cell niche. In the small intestine, Paneth cells, which are located next to the stem cells, secrete antimicrobial peptides. More generally, however, when a stem cell divides asymmetrically, if Cairn's hypothesis holds then the original template DNA remains in the stem cell. Thus any replication errors that arise are passed into daughter cells which have a finite lifespan in the crypt [28, 83]. Despite this, and because stem cells can and do divide symmetrically, it is not yet known whether the mutations that lead to CRC originate in the stem or transit-amplifying cells.

2.2.1 The Adenoma-Carcinoma Sequence

Under normal circumstances, the cellular processes governing epithelial renewal in the intestine are regulated by biochemical and biomechanical signals, such as cell-cell contacts and via the Wnt signalling pathway [122]. However, the delicate balance of division, migration and apoptosis leaves the tissue vulnerable to carcinogenesis. CRC is thought to originate via disruption to the cellular dynamics within the crypts, following a progression known as the adenoma-carcinoma sequence, first described by Fearon and Vogelstein [37] (1990). This genetic model proposes that stages of development in CRC correspond to the accumulation of mutations in certain genes, as shown in Figure 2.9. The intestinal metaplasia that follows is not restricted to the epithelium itself, but also affects the surrounding connective tissue [81].

Inactivation of the *Apc* tumour suppressor gene is generally accepted to be the initiating event in CRC [41, 55, 104]. Indeed, a germline mutation in *Apc* is responsible for the heritable condition Familial Adenomatous Polyposis (FAP), in which numerous benign growths form in normal-appearing colonic mucosa, which predisposes a patient to developing

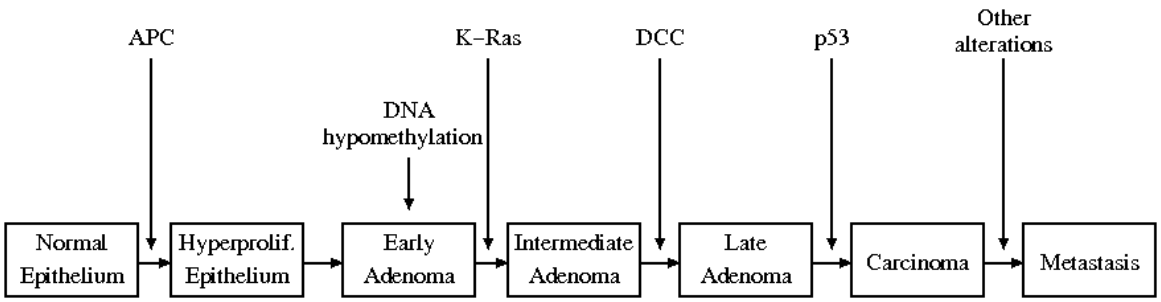

Figure 2.9: The adenoma-carcinoma sequence proposed by Fearon and Vogelstein [37]. The arrows indicate the genes for which alterations are suspected to occur in at the progressive stages of tumour development. Drawn according to Fearon and Vogelstein [37].

CRC, and usually earlier than in sporadic cases [2, 18]. The accompanying genetic model proposes that, given its role as a scaffold protein within the destruction complex, loss of APC activates the canonical Wnt pathway by the translocation of β-catenin to the nucleus [42]. This leads to abnormal or even halted migration of a cell, increased proliferation and a failure to differentiate [104]. Such mutant cells then produce progeny that also exhibit these premalignant cell properties.

Further to this, *Apc* regulates cell polarity during mitosis by interacting with the microtubules, and it has been demonstrated that loss of function alters mitotic spindle positioning [40, 99]. In particular, Quyn et al. [99] showed that preferential asymmetric division in the stem cell compartment is absent following the loss of APC. Deregulation of spindle organisation in both the stem and transit compartments could result in cells losing contact with the basement membrane, triggering cell apoptosis or shedding to the lumen. If a cell does not undergo apoptosis then hypertrophy – an increase in size – can result, disrupting the tissue architecture.

Given the consequences of inactivation of *Apc*, it is possible that cells which acquire this mutation can persist in the crypt, and the balance of cell proliferation with cell loss is disturbed. Disrupting the dynamics of the crypts in this way has a further consequence: placing the structure under additional stress that can cause the walls to buckle. How these mutations manifest at the tissue level is discussed below.

Tissue Dysplasia: Bottom Up vs. Top Down

The first observable deviation from a healthy epithelium in the intestine are aberrant crypt foci (ACF), which are clusters of one or more crypts that appear raised above the epithelial surface. First discovered by Bird in 1987 [14, 95, 126], these aberrant crypts appear larger, with slit-like lumens and a thicker epithelial lining than healthy crypts, and are thought

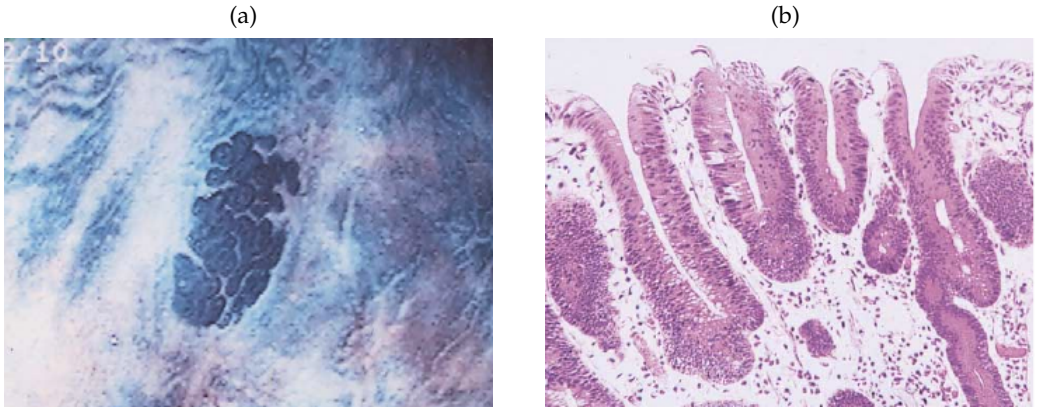

Figure 2.10: (a) A large aberrant crypt focus, imaged using an endoscope with methylene blue staining, (b) a closer look at the crypts from this focus. Each crypt exhibits a thickened epithelial layer with compressed lumen. Reprinted with permission from Takayama et al. [115].

to increase in size as a result of crypt fission [24]. Figure 2.10 shows a representative endoscopic and histologic example of a large focus that exhibits dysplasia.

ACFs are the putative precursors to fully developed adenomas – benign growths with a glandular organisation – which often occur as protrusions into the gut lumen, known as polyps [2]. Preston et al. [98] (2003) propose that the initial dysplastic ACF is the monocryptal adenoma: a single crypt filled completely with adenomatous cells, and this is the first lesion that is detectable [98]. Such crypts are monoclonal, *i.e.* believed to be the result of a single mutated stem cell that colonizes the entire epithelial surface.

Two arguments have been proposed for the spread of such mutations. Firstly, a "bottom-up" progression, which suggests that the initial mutation occurs in a stem cell at the crypt base and spreads upwards throughout the crypt. The abnormal behaviour exhibited by the mutant cells (characteristics such as excess proliferation, arrested apoptosis, misdirected migration) leads to the formation of an adenoma by crypt fission and budding events, which are followed by the invasion and subsequent colonisation of mutant cells into neighbouring crypts. Adenomatous crypts are demonstrably elongated and deformed, exhibiting multiple branching events, but maintain a monolayer of epithelial cells [122]. Examples of monocryptal adenomas are shown in Figure 2.11.

The "bottom-up" theory is contradicted by a "top-down morphogenesis" approach, which also states that the mutation originates in a stem cell, but instead asserts that invasion occurs from the surface of the colonic mucosa, and spreads downwards into healthy crypts [108]. Supporting examples for these two contrasting theories are shown in Figure 2.12. This hypothesis is motivated by the observation of the authors that dysplastic cells reside in the region of the crypt towards the collar, and in contrast, those cells at the base of the

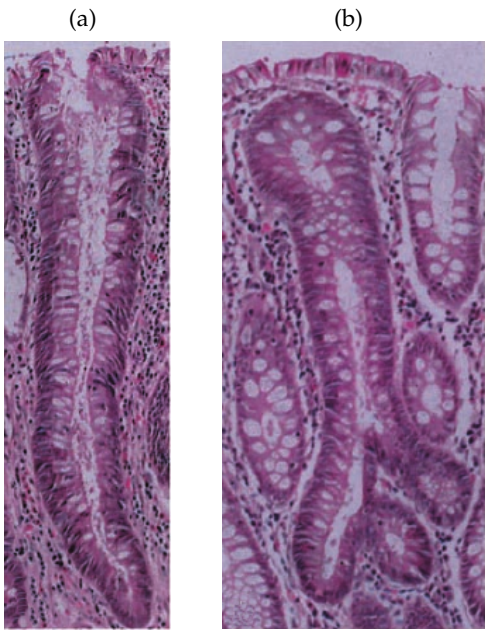

Figure 2.11: Examples of monocryptal adenomas with staining of nuclear β-catenin: (a) showing the extension of the adenomatous epithelium towards the crypt collar, (b) illustrating the multiple budding events that can occur in a more developed adenoma. Reprinted with permission from Preston et al. [98].

crypt appear normal. Further, these two distinct subsets of cells are not clonally related, and so generate a polyclonal lesion. While Preston et al. [98] observe such downward growth into adjacent crypts, this is in more developed sporadic adenomas.

An implication of the "top down" hypothesis is that a dividing cell must be located on the intercrypt table, or that the aberrant transformation only manifests towards the crypt collar, or for such a cell to ignore the cues to differentiate. The first of these contradicts the substantial body of evidence which restricts dividing cells to the base of the crypt; for example, both of the stem cell investigations carried out by Sangiorgi and Capecchi [103] and Barker et al. [9] support the "bottom-up" hypothesis, by identifying stem cells towards the base of the crypt. Barker et al. [8] have also shown that the growth of an adenoma arising through loss of APC in the stem cell population is aggressive in comparison with that induced by loss of APC in the transit-amplifying region. This suggests that persistent adenomas formed in the transit-amplifying region, while possible, require additional mutations. It also implies that a "bottom up" progression is the more likely initiation of an adenomatous growth. In reality, it is possible that both hypotheses are correct, and occur at different stages of adenoma development, and increasingly it is accepted that crypt fission is the predominant mode of growth of an adenomatous crypt [55].

Another gene thought to be involved in the adenoma-carcinoma sequence, and included

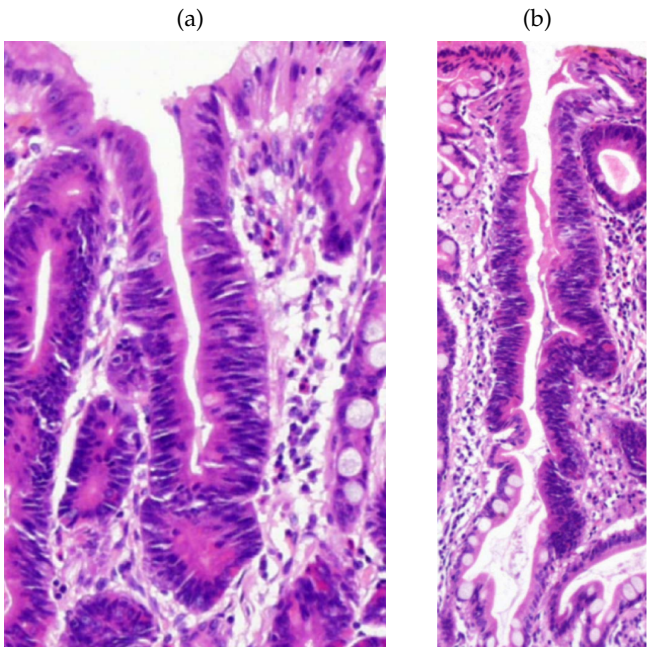

Figure 2.12: (a) An example of a crypt justifying the "bottom-up" hypothesis – this crypt has dysplastic cells at the base, which exhibit larger nuclei and pseudo-stratification (the nuclei are positioned at different levels), (b) an example justifying the "top-down" hypothesis – this crypt has dysplastic cells towards the top, with normal appearing cells at the base. Reprinted with permission from Deheragoda and Wright [28].

in Figure 2.9, is the oncogene KRAS. Once mutated, oncogenes prompt cells to divide continuously, irrespective of growth signals, and it is the activation of KRAS that permits overgrowth of cells so that the adenoma can increase in size [129]. Recent experimental work has found that activation of KRAS is essential for the translocation of β-catenin to the nucleus, and consequently that loss of APC is insufficient to achieve this in itself [92]. These results show that the only downstream effect of APC loss is a failure of cells to differentiate, and that it does not prompt increased cell proliferation; rather, additional activation of KRAS is required. However, while loss of APC is incapable of driving the translocation of β-catenin to the nucleus, there is evidence to show that loss of APC is sufficient for Wnt signalling activation [118]. Further, Tomlinson and Fodde [118] also argue that failure of some studies to observe nuclear β-catenin may be attributed to inconsistency in experimental protocols and reagents. It must also be taken into consideration that nuclear accumulation of β-catenin is not consistent throughout the tissue environment of a tumour [83]. Hence, to fully understand the complexities of the genetic mutations that drive the formation and growth of an adenoma, it is likely that experiments will have to use additional markers to that of nuclear β-catenin. This highlights the complexity of understanding and categorising the initial stages of the adenoma-carcinoma sequence.

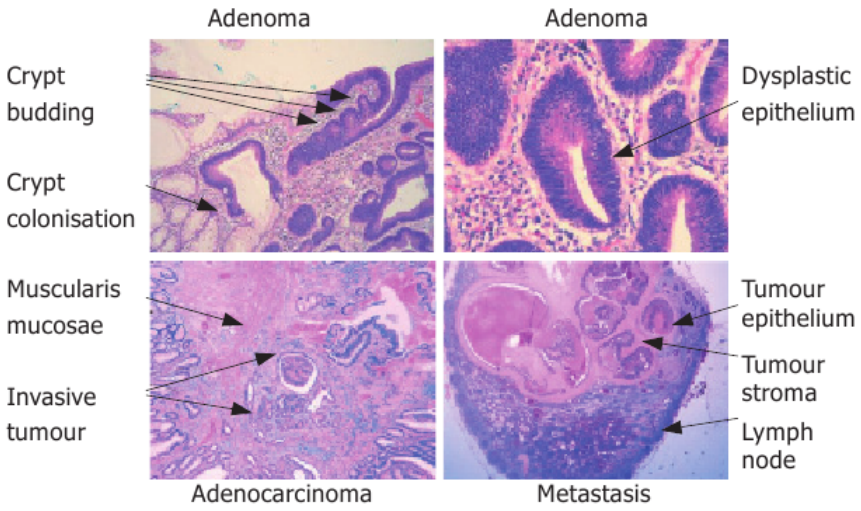

Figure 2.13: The stages of adenoma development showing the progression from adenoma to carcinoma and metastasis. Manifested as a dysplastic epithelium, adenomas grow by crypt branching and colonisation of additional crypts (top). Further mutations result in tumour cells invading the basement membrane (bottom left), so that the adenoma has become a carcinoma. At this stage, tumour cells can grow and metastasis to other sites are possible (bottom right). Reprinted with permission from Van Leeuwen et al. [122].

Carcinomas

Adenomas are the precursors to carcinomas, malignant tumours that can break through the basement membrane to gain access to the blood stream. Loss of further tumour suppressor genes, such as DCC, DPC4 and JV18-1/MADR2, allow the adenoma to progress and the loss of p53 drives the change from adenoma to carcinoma, as shown in Figure 2.13. Carcinomas are able to invade the surrounding tissue stroma and metastasise following the further loss of suppressor genes, and this is the last stage of the adenoma-carcinoma sequence (see Figure 2.9).

2.3 Summary

In this chapter, the biological background of the intestinal crypt and the current understanding of the progression of CRC has been presented. This exposition has highlighted how the subcellular and cellular dynamics of the crypts are influenced by, and respond to, cues from the tissue environment. This is evident in the influence of the Wnt and Notch signalling pathways, which coordinate changes in cell proliferation and the switch to terminal differentiation along the crypt axis, as well as the planar cell polarity exhibited by the epithelial monolayer. Cells make decisions to differentiate into one particular cell type

over another, to undergo apoptosis appropriately, and to migrate in a certain direction. It is also hypothesised that the geometry of the crypt determines cell shape, leading to preferential asymmetric division in the stem cell compartment, and symmetric division for the transit-amplifying compartment [99]. In turn, the tissue environment is influenced by the decisions that cells make, and the downstream effects of aberrant genetic mutations that prompt incorrect decisions include buckling of the crypt structure, the formation and growth of adenomas, and eventually carcinomas.

To accurately model the colonic crypt, it is important to understand the factors that influence and control cell behaviour. Further, an understanding of the dynamics of the crypts is vital to making advances in the knowledge, aetiology and treatment of CRC. Statistically, CRC is the third most common type of cancer and the second most deadly, with around 110 new cases diagnosed every day in the UK, and the incidence is increasing throughout Europe [23]. The motivation for research into this form of cancer is clear, and requires a combined effort from both the physical and life sciences, for the following reasons.

- Experiments in a wet lab are limited by the organisation of the intestinal tissue structure; individual crypt size and depth, as well as the tight packing of neighbouring crypts, make accessibility a challenge, and ultimately 2D histological slices yield incomplete information [99].

- Inevitably, there are experiments which cannot be carried out easily, accurately, ethically or inexpensively. In particular, it is not possible to dynamically visualise the first stages of the adenoma-carcinoma sequence *in vivo*, and achieving this *in vitro* is limited by the accurate reproduction of the complex tissue organisation described above. It has been demonstrated that crypt-like organoids can be grown in matrigel in the presence of growth factors distributed uniformly throughout the gel, which appear similar to crypts in tissue. That additional forces do play a significant role *in vivo* is illustrated by the fact that crypts which are mutant in *Apc* form apparently normal shapes in whole tissue, but do not in matrigel [105]. Therefore, at this stage, it is not yet possible to state decisively how crypt organoids could be used to test hypotheses generated by theoretical models.

A comprehensive, accurate, 3D computational model of the crypt could address some of these limitations, and enable *in silico* experiments to test hypotheses, investigate malignant behaviour and direct future experiments. In particular, such a model could investigate directly the role of the crypt structure in influencing cell decisions, and isolate the key characteristics of mutated cells that translate to the tissue level properties observed in adenomas. As a specific example, the competing "top-down" and "bottom-up" theories

for the spread of dysplastic cells could be simulated and compared. This kind of model would also prove invaluable for investigating drug delivery in CRC – by linking the effect of a drug to the dynamics of the crypt, questions of timing, dosage and efficacy can be addressed.

Such a model must address the crypt geometry and tissue structure, and how each influences cell decisions and responses. This will enable investigation of possible mechanical contributions to cell dynamics. Accuracy and reliability for predictive experiments and model inference necessitate collaboration with biologists, for the application of real data and realistic assumptions.

The detail provided in this chapter is intended to establish a comprehensive and rigorous background to this biological system, so as to justify model components that are defined in existing and new work. Given this, the following chapter discusses existing mathematical and computational models which have been proposed to explain both healthy and unhealthy crypt dynamics. These models are assessed both for the understanding they have brought to the field, and the possible limitations which prevent complete and accurate investigation of the questions outlined above.

Chapter 3

Literature Review

The biological background provided in Chapter 2 introduces and describes the function and dynamics of the crypts of Lieberkühn, the tightly packed intestinal glands responsible for the renewal of the intestinal epithelium, which are implicated in the origin of CRC. The crypts are regulated functional units, which not only consist of a small number of cells, but also possess well-characterised properties that make the system amenable to mathematical modelling. These properties include controlled cell division, differentiation, polarity and apoptosis. The processes that govern crypt dynamics are intrinsically coupled across spatial and temporal scales, and crucially, the tissue-level behaviour both influences, and is influenced by, subcellular and cellular-level events.

Chapter 2 also highlights that the current understanding of adenoma and carcinoma development is incomplete, and in particular, that the initial stages in the breakdown of crypt homeostasis and architecture are difficult for biologists to observe experimentally, either *in vivo* or *in vitro*. This problem represents a good example of the usefulness and need for mathematical and computational modelling, which increasingly are providing insights into the interplay between the different subsystems that control cell decision-making, as well as how these mechanisms can break down. Performing *in silico* experiments using an accurate, predictive, computational model of the crypt will highlight the conditions required for sufficient destabilisation to occur, and so provide crucial insight into the tissue-level effects of genetic mutations that lead to CRC. Such a model will facilitate investigation which is not possible in an experimental setting, and complement biological research when developed in collaboration and founded on valid data.

This chapter explores the impact of the most influential of the mathematical and computational models of the crypt, as well as highlighting their current limitations and scope for future research. Emphasis is given to models that track the spatial location of cells, and so

compartmental models of crypt dynamics (*e.g.* Boman et al. [16], Paulus et al. [91]) will not be reviewed here. As each modelling paradigm is considered, it is explained in the context of the full model proposed by its authors: how cells are instructed to divide, migrate and differentiate. However, in the light of the focus of this thesis, a detailed investigation of subcellular and cell cycle models is not included. Where such models have informed the understanding of crypt function this is discussed, and each model is considered with respect to concepts that are applicable for future work. Where comparison is feasible, the models are distinguished.

The chapter is organised as follows. Models of healthy crypt dynamics are discussed in Section 3.1, which presents the two main types of discrete cell-level modelling approach: on-lattice and off-lattice models. Recent publications which have applied these frameworks to multiscale models are then introduced. Section 3.2 discusses models of the buckling of epithelial monolayers, in particular those which address the breakdown of crypt dynamics and structure. This section details both discrete and continuum models that have been proposed. A brief discussion on modelling generic monolayer epithelia, as well as specific non-crypt biological exemplars, is given in Section 3.3 – this highlights the scope and influence of research in epithelial tissue modelling. The theoretical motivation for the work contained in this thesis is presented in Section 3.4, which, in consideration of the biological background already given, completes the introduction to this topic and research initiative.

3.1 Models of Cellular Crypt Dynamics

Mathematical models that focus on the cell-level behaviour of the crypts can be characterised into one of two different approaches: those based on a lattice representation such as the cellular automaton (CA) framework; and those which encompass an off-lattice description of cell movement. These cell-level models have also been embedded within multiscale frameworks to inform understanding of interactions across spatial scales. This section considers each approach in turn, highlighting their respective advantages and disadvantages. There then follows a discussion of two recent multiscale models of the crypt.

3.1.1 Lattice-Based Models of the Crypt

First proposed by Loeffler et al. [72] (1986), and subsequently extended for later work [71, 90], the earliest models of the dynamics of the crypt were based on CA. These models

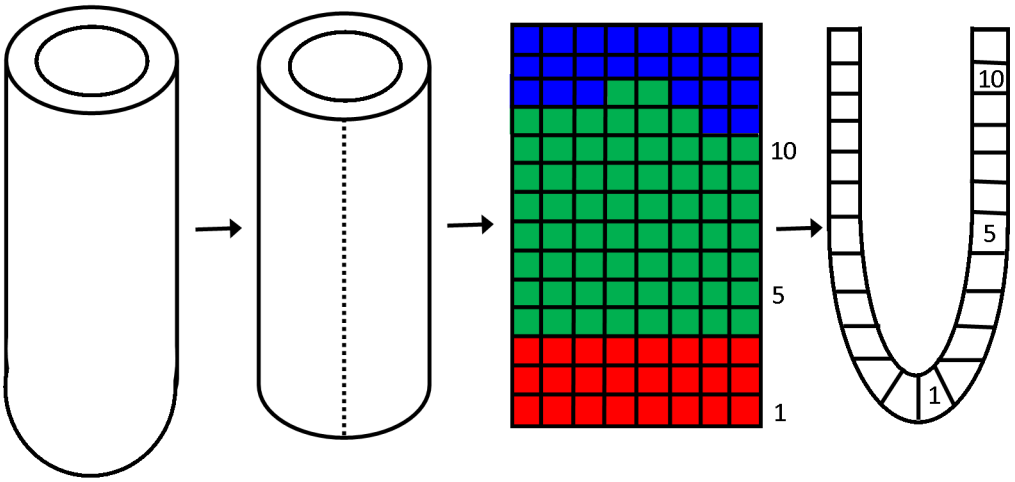

Figure 3.1: The test-tube shape of the crypt is approximated as a cylinder, which is cut open down the long axis and rolled out to form a rectangle. CA models are defined on a lattice constrained by this rectangle. Cells occupy individual rectangular positions on the grid, and are restricted to move within the rows and columns.

consider a cylindrical approximation of the crypt geometry, which is cut open and rolled out to become a rectangle, upon which the lattice is defined, with periodic boundary conditions imposed on the vertical edges (see Figure 3.1). Cells occupy individual, equally-sized positions on the grid, with division and displacement governed by rules designed to mimic the known confinement of proliferative cells to the lower portion of the crypt, as described in Section 2.1.2.

The first investigations based on this type of model compared possible insertion rules for newly created daughter cells with data from tritiated thymidine labelling experiments, which marks proliferative cells [71, 72]. By defining three proliferative states – stem, transit and differentiated cells – eight models for cell displacement were compared, the models differing in how each accounts for random, age-dependent and long-range rearrangement. The experimental data produced from the labelling experiments was used to identify the distribution of labelled cell positions in the crypt, and facilitated comparison with the different displacement paradigms[1]. The results revealed that age-dependent movement, whereby the newly created daughter cell displaces the oldest nearest neighbour, correlated well with the experimental data, and suggested that cells sense the maturity or age of local neighbours when undergoing division. By comparing the different displacement rules, the

[1]The labelling index corresponds to the proportion of cells in a cell population which are currently in S-phase. The name derives from the visible molecules / stains which are incorporated into newly synthesized DNA [2].

authors also concluded that lateral displacement can occur in the crypt, rather than solely vertical insertions.

In a follow-up paper, Loeffler et al. [71] verified and extended this model through comparison with mitotic index data and proposed the following hypothesis concerning cell migration: the frequent, lateral insertions of newly created daughter cells stabilise the circumference of the crypt, which also experiences pressure due to elastic contracting forces. In the absence of mitosis, and hence in the absence of such lateral insertions, the contracting forces dominate, causing the vertical columns of cells to merge, which ultimately forces upward migration. This is proposed to explain the experimental observation that cell migration continues in the absence of mitosis [61]. This hypothesis was not investigated further, nor was a source suggested for the proposed elastic forces.

The CA framework has also been implemented and extended to include goblet cell maturation [90]. The results from this work compared well with experimental data concerning goblet cell positioning in the crypt and by assuming that these differentiated cells arise from the transit-amplifying population, the model was able to explain the observed distribution of goblet cells. Indeed it was later proven experimentally, using clonal analysis, that goblet and columnar cells arise from a common ancestor [15]. Further models which also employ CA include Finney et al. [39], Isele and Meinzer [57], Meinzer et al. [77].

Model Limitations

The use of CA models, while computationally simple and inexpensive, limits accurate investigation of crypt dynamics due to certain unrealistic simplifications associated with the confinement of cells to the lattice structure. Firstly, cells are uniform in size, shape and arrangement. The discrete nature of cell movement, which occurs on the scale of cell-sized steps, prevents replication of continuous cell movement. Cell division forces disruption of the grid by moving an entire column upwards to enable insertion of the daughter cell, and in so doing, breaks many cell-cell contacts. Such long-range effects of cell division are biologically unrealistic, and further, local age-dependent migration is necessary to counteract these effects, rendering these conclusions and hypotheses redundant. Long-distance effects also occur if a cell undergoes apoptosis, which leaves a hole in the lattice that must be filled. Lastly, migration is driven solely by mitosis, and ceases immediately in the absence of cell proliferation, which is contrary to experimental observation [61].

The Cellular Potts Model

Another lattice-based model, the cellular Potts model (CPM), overcomes some of these limitations by defining a single cell using multiple adjacent lattice sites that are each assigned a spin or cell id, σ [51]. Cell movement is determined by choosing lattice sites at random, and changing the associated spin to that of a neighbouring cell, σ', only if it is energetically favourable to do so. However, the Monte Carlo probability that is used to determine whether or not to change the spin is dependent on a temperature parameter, which has no biological basis, is key to the model behaviour, influencing cell coalescence or dissociation. The Potts model has been applied to the crypt to examine differential adhesion and its role in cell sorting and migration [130]. These results concluded that cell migration speed increases moving up the crypt, such that the differentiated cells move faster than the proliferating cells below, and that differential adhesion helps to increase migration speeds.

CompuCell3D[2] is a widely used open-source computational tool which implements the CPM. The code is written in C++ with a python wrapper, but usefully, simulations can be run using the CompuCell player graphical user interface (GUI), enabling model simulations to be quickly designed and visualised. Unlike the Chaste library, which is described in Chapter 4, CompuCell3D is restricted to simulating the CPM and cannot currently be used for models that incorporate alternative cell-level modelling frameworks, such as the cell-centre or cell-vertex models described below.

3.1.2 Lattice-Free Models of the Crypt

A Cell-Centre Model

The first cell-centre model of a 2D cylindrical crypt was proposed in 2001, and introduced by Meineke et al. [76]. This model overcomes many of the structural problems associated with the earlier CA models by implementing a lattice-free structure, which assigns individual nodes to cells, and so allows continuous, rather than discrete, movement. Given that this model forms the basis for the new crypt model proposed in this thesis, a detailed mathematical description is reserved for Chapter 4.

Cell centres are defined as points in space, with connections between cells determined using a Delaunay triangulation, and the corresponding cell shapes subsequently defined by the dual Voronoi tessellation, as shown in Figure 3.2. This replicates the polygonal

[2] `http://www.compucell3d.org`

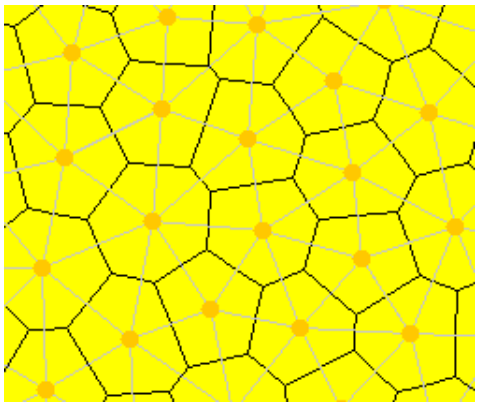

Figure 3.2: An example of a Delaunay triangulation and dual Voronoi tessellation for a given set of nodes. The triangulation (grey) is defined such that the circumcircle of each triangle does not contain any nodes. The Voronoi tessellation (black) partitions the plane into polygonal boundary regions, so that each region contains only those points that are closer to a particular node than any other.

packing of cells [54], with neighbouring cells sharing a common boundary edge, thereby preventing cell overlap as well as major disruption to the structure when a cell undergoes division.

Again, the model crypt is approximated as an unfolded cylinder, with periodic boundary conditions on the two long edges. Four types of cells are considered: Paneth, stem, transit and differentiated cells. Of these, only the stem and transit cells undergo division, and the Paneth and stem cells remain stationary. A pedigree concept is applied to define progressive proliferative generations and subsequent mature, non-dividing populations. As such, each cell belongs to a particular generation: stem cells are generation 0, and are fixed in number. They divide asymmetrically, producing one stem cell and one transit cell (generation 1) whereas transit cells perform a given number of symmetric divisions before differentiating and becoming non-dividing cells. Cell flux is driven by the resulting mitotic pressure – division propels migration up the crypt, with cells removed once they reach the collar to model the sloughing that occurs in this region. A snapshot of the crypt model proposed by Meineke et al. [76] is shown in Figure 3.3.

Interactive forces between cells are modelled as linear springs, with fixed spring constant, μ. The overall force acting on each cell is subject to a drag term, η, which is applied to model the friction due to cells migrating over the surface of the extracellular matrix.

The purpose of the original model was to investigate whether more realistic assumptions regarding cell movement and cell packing could reproduce experimental data published by Kaur and Potten [62] more accurately. These data describe the percentage of labelled and mitotic cells at each cell position, as well as cell velocities and run changes, which

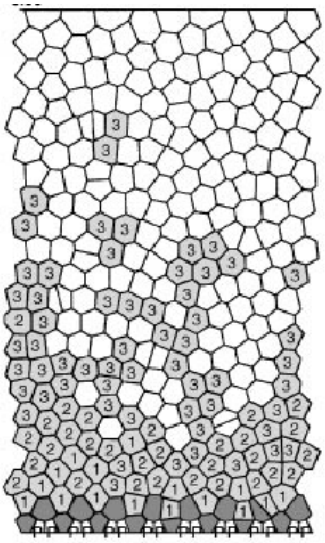

Figure 3.3: A snapshot of a cylindrical crypt simulation reprinted with permission from Meineke et al. [76]. Stem cells are coloured dark grey, transit cells of indicated generation are coloured light grey, and non-differentiating cells are white.

give the number of changes between labelled and unlabelled cells within each section. In particular, the comparison of model simulations with experimental data indicates that cell rearrangement according to age or type following division is not required. This result is in contrast to the conclusions made by Loeffler et al. [71] using the CA model, as discussed in Section 3.1.1.

Model Limitations

While the off-lattice cell-centre model captures realistic cell shapes and local cell rearrangement, and also removes the unrealistic discrete, stepwise movement, it still has limitations. Some of these limitations have been addressed in more recent, extended models. The assumption that the spring constant, μ, is equal for all neighbouring cells gives rise to a strong attraction between distant neighbours, even if the contact edge is very short [123]. Allowing μ to depend on cell-cell contact length would yield different and more realistic attractions, and this was addressed by Walter [125]. Further to this, cell adhesion to the basement membrane, η, is assumed constant and equal for all cells. An improvement to this model would be to set this parameter to be dependent on, and so increase with, the contact surface area, as considered by Van Leeuwen et al. [123].

In general, the cell-centre model has a subtle relationship between cell size and cell-cell adhesion. Increased cell adhesion is achieved by increasing the spring constant, however this will result in increased repulsion should the cells be closer than the equilibrium distance

apart. This must be taken into account when choosing a suitable model framework for cell-level interactions, and indeed the cell-centre approach may not be appropriate, at all, for implementing detailed models of cell adhesion. Pathmanathan et al. [89] considered a number of different force laws within the cell-centre framework, such as linear, linear-exponential and nonlinear force laws. These laws were applied to compare the mechanical behaviour of a block of tissue which is subject to compression, stretching or shearing. The results of these *in silico* experiments, which also compared the Voronoi tessellation with an overlapping spheres model, found that the bulk behaviour of the model does not change with the application of different cell-cell interaction laws. Despite these results, there are alternative models which address cell adhesion in a more realistic manner, such as the cell-vertex model discussed below.

There are also limitations in the implementation of this framework to define the crypt model proposed by Meineke et al. [76]. The removal of cells from the crypt collar is purely phenomenological, and hence is not regulated by a biological mechanism (cells are simply removed from the simulation above a certain height), and other forms of apoptosis (such as anoikis) are not considered, although the Voronoi tessellation would prevent any holes from arising should cell death occur. The progression of a cell through the cell cycle is determined at birth, when the length of the G_1 phase is assigned from a uniform distribution. Thus division is not regulated by positional cues, such as Wnt factors and cell-cell contacts [66, 120]. The cylindrical geometry which is assumed overestimates the number of (stem) cells at the crypt base, and these are pinned, yet there is no evidence for the stem cells being immotile in the crypt. Finally, as a simplification, the stabilising presence of the connective tissue surrounding the crypt, and indeed the influence of the neighbouring crypts, is ignored. Recent works have addressed a number of these limitations with some success, and two such examples are discussed below [21, 123].

A Cell-Vertex Based Model

Vertex models are lattice-free models in which cell size and shape are determined by the movement and arrangement of the shared vertices. An example of this is shown in Figure 3.4(a). First proposed by Weliky and Oster [127] to describe epithelial morphogenesis, the model has since been applied by Nagai and Honda [82] (2001) to describe a general monolayer epithelium, where cells are assumed to have equal height. More recently, the vertex model was employed as the cell-level component of a multiscale model of the colonic crypt, and compared with the cell-centre model described above [87]. The computational simulations carried out by Nagai and Honda [82] demonstrated that over time, given

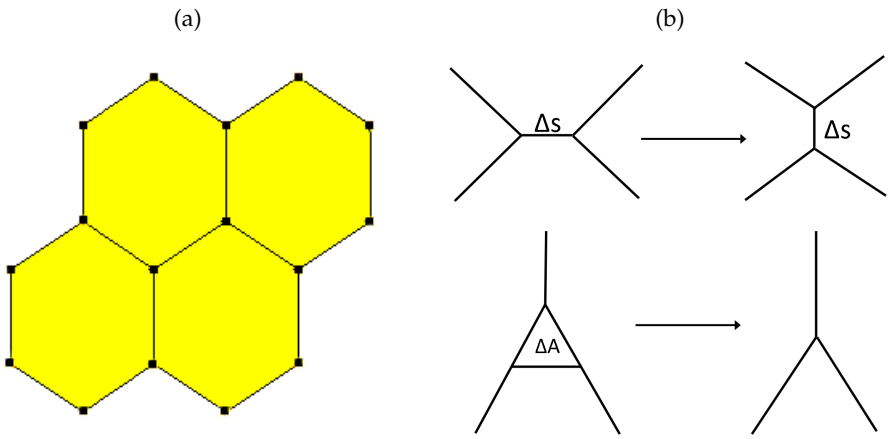

Figure 3.4: (a) Cell-cell connectivity and movement in the cell-vertex framework are determined by shared vertices and edges. (b) Topological changes are governed by vertex-swapping rules. A T1 swap (top) occurs when an edge is sufficiently small (Δs). The edge is rotated by 90°, which creates to new neighbours whilst separating two existing neighbours. A T2 swap (bottom) occurs when a triangular element has sufficiently small area (ΔA). This triangle shrinks to form a single vertex.

irregular initial patterns, the local dynamics of this mechanical model produce regular polygonal packing characteristic of epithelial tissue. This arises as the cells equilibrate and balance resistance to deformation with the tension of the cell boundaries. Such cell packing also occurs in the cell-centre model via the Voronoi tessellation, however implementing the Delaunay triangulation and subsequent tessellation becomes computationally expensive for large numbers of cells.

A free energy, U, is associated with each cell and is used to update cell locations at every timestep. This is defined as the sum of energy contributions from all cells which act at a particular vertex. The gradient of this energy defines the force acting on each vertex, and it is balanced with a viscous drag term that is assumed to be proportional to the velocity of the vertex. Under the additional assumption that inertial effects are negligible, the equations of motion can be written as:

$$\begin{aligned} \eta_i \frac{d\mathbf{r}_i}{dt} &= -\nabla U \\ &= -\nabla_i \sum_{j=1}^{n} (U_D^j + U_S^j + U_A^j)\,. \end{aligned} \tag{3.1}$$

Here, $\mathbf{r}_i$ is the location of vertex i and η_i is the balancing drag coefficient, which is averaged over the values assigned to each cell that contains vertex i. For each cell j, U_D^j is the deformation energy, which works to maintain a target volume for all cells; U_S^j is the membrane surface tension energy, which conserves membrane length and encourages circular cell shapes; and U_A^j is the cell-cell adhesion energy, which acts in proportion to the

contact area between neighbouring cells. The total number of cells in the system is defined as n. Equation (3.1) ensures that all cell movements result in a decrease in the total energy, U.

Topological changes arise according to rules for switching neighbouring vertices, and for controlling cell division, as shown in Figure 3.4(b). For example, if two vertices connected by an edge move to within a sufficiently small distance of one another, this edge is rotated by 90° (this is known as a T1 swap). The vertices assigned to the cells in the local area of this swap are rearranged. A T2 swap occurs if a triangular element exists which has a sufficiently small area – the element shrinks to form a single vertex. T2 swaps are commonly used to prevent holes appearing after apoptosis events.

Cells are assigned a target volume which increases linearly over the G_1 phase of the cell cycle, and once a cell divides, it splits into two daughter cells of equal volume. The division is conducted along the shortest axis of the cell, and if the cell is perfectly symmetrical, an axis is chosen at random. Two new vertices are defined where the dividing axis meets the cell perimeter.

Cell-Centre Vs. Cell-Vertex

In a study of the cylindrical crypt model, Osborne et al. [87] concluded that simulations of the cell-centre and cell-vertex models produce similar results, an example of which is shown in Figure 3.5. Despite this, there are advantages and disadvantages unique to each cell-level description, and so the implementation of either framework must be chosen to suit the problem at hand. In particular, however, it should be noted that the vertex model provides a more natural representation of cell adhesion, as it is defined to be dependent on the contact area between cells, preventing the ambiguity in the cell-centre model that merges the concept of cell adhesion with cell size. However, computationally, the cell-vertex model runs more slowly, as it requires a smaller timestep to ensure stability and there are multiple nodes corresponding to each cell for which forces must be calculated. This is in contrast to the single node characterising the cells in the cell-centre model, and despite the Delaunay triangulation that must be defined at each timestep, which becomes more of a burden for larger numbers of cells.

3.1.3 A Multiscale Model of the Crypt

Recently, Van Leeuwen et al. [123] proposed a multiscale model of regular crypt dynamics that links processes occurring at the subcellular, cellular and tissue levels of organisation.

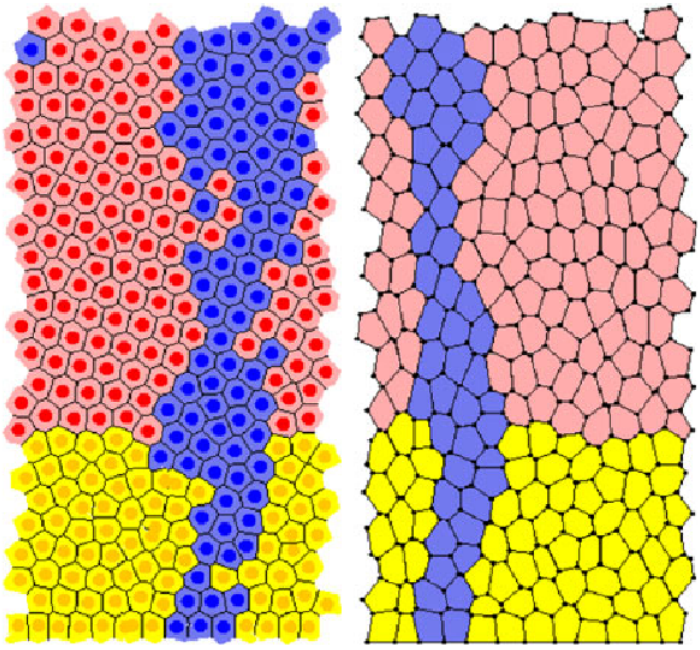

Figure 3.5: A comparison of the cell-centre (left) and cell-vertex (right) frameworks being implemented in the cylindrical model of the crypt. These snapshots are taken from a clonality experiment simulation, where the marked blue cells are all derived from the same cell lineage. Each model produces a wavy ribbon of marked cells. Transit cells are coloured yellow, and differentiated cells are coloured pink. Reprinted with permission from Osborne et al. [87].

This is currently being extended within the computational framework of the Chaste project [94], which is discussed in detail in Section 4.2. Through virtual microdissection and labelling-index experiments, this model has been used to investigate clonal expansion and the disruption of crypt homeostasis which forms the first step in colorectal carcinogenesis.

The model consists of three modules, with the crypt still approximated as an unfolded cylinder with periodic boundary conditions imposed on the long edges. At the lowest level, deterministic models describe the molecular networks governing the cell cycle and Wnt signalling, and hence determine cellular responses and behaviour. A decreasing Wnt-factor profile is imposed up the vertical axis of the crypt. Each cell samples the local Wnt level at its cell centre, and passes this value to the Wnt model (a nonlinear system of ODEs). The output of the Wnt model, which also quantifies the Wnt dependent adhesion complexes used in the definition of cell mechanics, is then linked to a cell cycle model first proposed by Swat et al. [114]. The cell cycle model is defined such that cells exposed to high levels of Wnt can progress through the cell cycle rapidly, and in this way, the spatially varying Wnt profile generates position-dependent proliferation. Differentiated cells are those in the regions where Wnt levels are low, and such cells never progress beyond the G_1/S checkpoint. At the cellular level, individual cell mechanics are defined by

the interactive forces proposed by Meineke et al. [76]. Simulations monitor proliferation, differentiation and migration events to update the configuration at each timestep.

The *in silico* experiments conducted by Van Leeuwen et al. [123] suggest that the incorporation of a decreasing extracellular Wnt profile to the crypt can explain the observed position-dependent rates of cell proliferation and adhesion. The spatial variation in nuclear β-catenin which is observed experimentally [120] has been reproduced, in this model, by extracellular Wnt factors located solely at the base of the crypt. Further, the results also show that clonal expansion and niche succession (the progeny of one stem cell taking over the entire stem cell pool) can occur if the stem cells are motile, and not fixed in position. This has implications for monoclonal conversion, and the hypothesis that the monocryptal adenoma constitutes the first identifiable lesion in the progression to CRC. A major benefit of this work is that it is possible to track all cells individually and to repeat and reproduce experiments using this model within the Chaste framework. As discussed in Chapter 4, this framework facilitates comparison of different modelling paradigms, and the code itself is rigorously tested to ensure accuracy and reliability. Such *in silico* experiments are invaluable in gaining a better understanding of crypt dynamics.

Model Limitations

Despite the insight that it has provided, this model cannot, at present, be used to examine the evolution of the tissue structure of the crypt if the shape and geometry change due to abberant cell properties. An issue common to the earlier CA models, and to the Meineke et al. [76] crypt model, is that the cylindrical approximation (shown in Figure 3.1) still overestimates the number of cells at the crypt base. That the walls of the crypt are assumed to be rigid prevents investigation of the deformation that can occur when dysplastic cells colonise the crypt, leading to crypt budding and fission. Further, the surrounding connective tissue and the influence of neighbouring crypts is overlooked.

3.1.4 A Three-Dimensional Model of the Crypt

In 2011, Buske et al. [21] proposed a 3D multiscale, agent-based crypt model, which defines lineage specification and cell differentiation according to threshold-dependent rules that correspond to the effects of Wnt and Notch signalling. This is the first 3D representation of the crypt structure, and snapshots from simulations are shown in Figure 3.6(a).

The authors employ a lattice-free cell-level model in which cells are treated as elastic spheres, characterised by an internal state vector, Ω, which determines the properties of

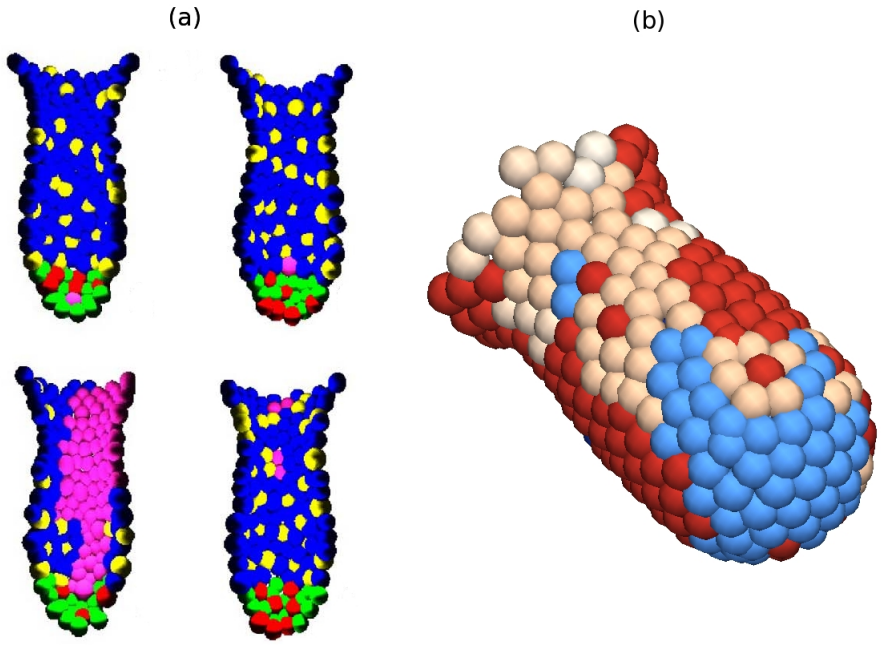

Figure 3.6: (a) Snapshots of the 3D crypt model proposed by Buske et al. [21]. Cells are colour-coded according to type: undifferentiated cells (red), paneth cells (green), enterocyte progenitors (blue), goblet cells (yellow), labelled cells (pink). Reprinted with permission from Buske et al. [21]. (b) A snapshot of this model, as reproduced using Chaste, where cells are coloured by lineage.

each cell. Ω is dependent on both cell shape and cell contacts, which relate to Wnt and Notch signalling respectively. Wnt signalling is assumed to depend on the local curvature of the basement membrane. Notch signalling is mediated by cell-cell contacts, being controlled by the number of neighbouring cells which express sufficient Notch ligands. In this way, lineage specification and cell differentiation are governed by rules which employ Wnt and Notch thresholds to determine whether a cell follows a secretory (Paneth or Goblet) / non-secretory, differentiated / undifferentiated fate. For example, Paneth cells, typically found at the base of the small intestinal crypts, are defined in the model as being undifferentiated, having high Wnt signalling and low Notch signalling. Such decisions are inherently reversible in this model, however there is a terminal differentiation state which occurs when Wnt signalling drops below a defined threshold. These Wnt and Notch signals are manipulated for each cell according to its current position in the crypt.

Active movement is applied to each cell using a migration force, in addition to the passive motion which results from events such as cell division. As is the case in reality, the migration force pushes Paneth cells downwards, and all other cell types upwards. The basement membrane is explicitly modelled as an artificial fibre network, with a defined

local radius for each cell position, which thereby prescribes a fixed crypt geometry. The basement membrane interacts with individual cells, but is fixed in position, and cells undergo anoikis upon losing contact with the membrane.

In silico experiments using this model were shown to reproduce the typical crypt cell proliferation patterns under steady state conditions, and the parameter values chosen for the model were obtained through a fit to experimental data. Subsequently, *in silico* experiments were shown to be in agreement with *in vitro* experiments that examine clonal dynamics, deregulated Wnt and Notch signalling and deletion of the crypt base stem cell population which corresponds to the Lgr5+ cells discovered by Barker et al. [9]. Crucially, however, these results were obtained without assuming an explicit stem cell population, and without the hitherto assumed pedigree concept of cell division.

Model Limitations

In common with the earlier models already discussed, this model still uses a fixed crypt geometry. This simplification prevents full examination of self-organisation of the tissue structure. Detailed subcellular pathways are neglected in favour of threshold-dependent rules governing cell fate, but the inclusion of these models would increase the scope of the multiscale framework employed and enable more detailed investigation of the coupling of the different spatial scales. Such subcellular models already exist within the Chaste framework, as demonstrated by Van Leeuwen et al. [123], and could be incorporated into a similar model as required. A snapshot of this model, as produced using the Chaste framework, is shown in Figure 3.6(b). These simulations were easily reproduced, and this presents a good example of the benefit of employing an open-source code framework for these types of models. This is discussed further in Section 4.2.

3.2 Models of Crypt Buckling and Fission

While the models discussed thus far have informed understanding of clonal expansion, definition of the stem cell population and the role of Wnt signalling, these tools commonly do not permit full examination of the evolution of the tissue structure under normal and adenomatous conditions. Models that have addressed this challenge are now discussed with attention focussing on those concepts and results which are particularly relevant to the research undertaken in this D.Phil. thesis.

The following models have been used to investigate the cause and aggravation of folding and buckling in simple epithelia, and, in light of the deformation of the crypt that can occur in adenoma formation which was discussed in Section 2.2, are of interest within the context of colorectal carcinogenesis. The objective for each model is to simulate growth in an epithelial monolayer, and investigate the destabilising effect that proliferation can have.

Two approaches have been employed in this context: discrete, agent-based models, and continuum models. As shown in Section 3.1, discrete models characterise cell behaviour at the individual level, and permit observation of the tissue level behaviour that arises as an emergent property through *in silico* experiments. The second approach is relevant at the tissue level, and manipulation of the resulting equations of motion may lead to the identification of regions of parameter space in which particular behaviours occur, without the need to run multiple simulations.

Despite differences in the modelling approaches, however, results from all of these models reveal that excessive proliferation, which can arise through an enlarged proliferative compartment or reduced cell cycle time, must be balanced by a bending stiffness in the layer in order to maintain a stable crypt configuration [29, 31, 35]. Further, it is hypothesised that during development, colonic crypts form as a consequence of buckling of an initially smooth intestinal surface, this process being facilitated by localised softening of the epithelial layer.

3.2.1 Buckling of One-Dimensional Cell Chains

In a pair of publications, Drasdo and Forgacs [29] and Drasdo and Loeffler [31] implemented a stochastic growth model to examine whether folding in a single-layer tissue sheet could be attributed to abnormal cell proliferation, or the presence of a stabilising bending force. In the first instance, the model is applied to an epithelial cell layer folding during gastrulation in early morphogenesis, for which the first stage of embryonic development is a hollow, one-cell thick sphere which grows by cell division, known as a *blastula* [29]. In the second paper, attention initially focuses on the crypts of Lieberkühn, where a 2D vertical section of the crypt is represented by a U-shaped chain of deformable, growing circles (see Figure 3.7(a)), but the authors also consider the original topic of blastula growth [31]. In each case, the focus is on a one-dimensional (1D) cell chain represented in 2D space, where cells move to decrease the total energy of the configuration. Specific details of the crypt model are discussed below.

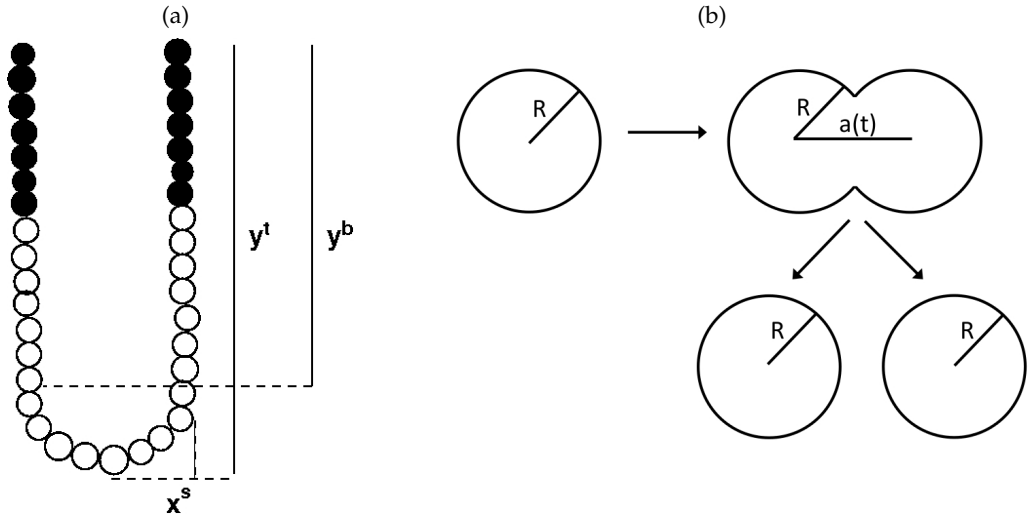

Figure 3.7: (a) A 2D representation of the colonic crypt as a U-shaped chain of deformable, growing circles. Black cells are assumed to be differentiated and so do not undergo division. y^t is the height of the crypt, and y^b is the height of the cylindrical portion, neglecting the semi-spherical base. x^s is the width of half of the crypt, *i.e.* the distance from the centre to the wall of the crypt. Reprinted with permission from Drasdo and Loeffler [31]. (b) The process of mitosis. A cell grows and deforms into a dumbbell shape before separating into two daughter cells, which each have half the mass of the parent cell. Drawn according to Drasdo and Forgacs [29].

Cell-cell connectivity is defined using the overlapping spheres (OS) method. Each cell is modelled as an elastic sphere, and interaction is dependent on the separation distance between neighbouring cells – two cells are assumed to be connected if their spheres overlap. During mitosis, a cell doubles its mass over the course of interphase before deforming into a dumbbell shape and subsequently splitting to form two separate, spherical daughter cells (as shown in Figure 3.7(b)). Only those cells in the lower two-thirds of the crypt are capable of division to mimic the confinement of the proliferative compartment to this region.

The position, $\mathbf{r}_i$, of cell i is updated at each timestep, neglecting inertial effects due to the strong friction opposing cell movements provided by the extracellular components. By appealing to Newton's second law, and by balancing the total force acting on the cell with a drag term, gives

$$\gamma \frac{d\mathbf{r}_i}{dt} = \mathbf{F}_i \,, \tag{3.2}$$

where γ is the friction constant (here estimated by a cellular Einstein relation: $\gamma = D/F_T$, where $D = 4.6 \times 10^{-16}$ m^{2}s^{-1} is the cell diffusion constant and $F_T \approx 10^{-16}$ J is a reference energy [12]).

The total force that acts on each cell combines the adhesive forces between neighbouring cells, and stabilising forces that are introduced to model the stiffness of connective and

surrounding tissue. It is thus defined as:

$$\mathbf{F}_i = \mathbf{F}_i^{\mathrm{NN}} + \mathbf{F}_i^{\mathrm{bend}} + \mathbf{F}_i^{\mathrm{bott}} + \mathbf{F}_i^{\mathrm{s}} \,. \tag{3.3}$$

Here $\mathbf{F}_i^{\mathrm{NN}}$ denotes the elastic force acting between neighbouring cells due to adhesive bonds, $\mathbf{F}_i^{\mathrm{bend}}$ is a bending force, $\mathbf{F}_i^{\mathrm{bott}}$ is the force from the tissue below the crypt, assumed to act only on cells in the semi-spherical bottom, and $\mathbf{F}_i^{\mathrm{s}}$ comprises a number of additional stabilising terms: shear forces, as well as forces from the surrounding connective tissue and a force that anchors the collar in the intestinal lumen, which declines towards the base of the crypt.

Similarly to the cell-centre framework proposed by Meineke et al. [76], the attractive and repulsive adhesive forces acting on cell i due to its nearest neighbours are modelled as linear springs:

$$\mathbf{F}_i^{\mathrm{NN}} = \sum_{jNNi} \mathbf{F}_{ij}^{\mathrm{NN}} = -k_{NN} \sum_{jNNi} \left(d_{ij} - d_{ij}^{(0)} \right) \frac{\mathbf{r}_j - \mathbf{r}_i}{d_{ij}} \,. \tag{3.4}$$

Here d_{ij} is the distance between the centre of the two cells, and $d_{ij}^{(0)}$ is the equilibrium distance, or rest length of the spring. The spring constant k_{NN} is a measure of the strength of this force, characterised by the Young's modulus of the cells, which is taken to be $E = 400$ Pa.

The bending force, $\mathbf{F}_i^{\mathrm{bend}}$, models the cell chain as a membrane, which is justified by cell polarity. The expression for this force is derived following Allen and Tildesley [3] using the chain rule, and is defined as

$$\mathbf{F}_i^{\mathrm{bend}} = \sum_{j=i}^{i+2} -\frac{dv_{\beta_j}(\beta_j)}{d\cos(\beta_j)} \frac{d\cos(\beta_j)}{d\mathbf{r}_i} \,, \tag{3.5}$$

where

$$v_{\beta_j}(\beta_j) = \frac{k_b}{2} \left(\beta_j - \beta_j^{(0)} \right)^2 \,, \tag{3.6}$$

is the bending potential between neighbouring cell centres. Here, β_j is the local deviation, or curvature, angle and the angle $\beta_j^{(0)}$ corresponds to the spontaneous curvature, which is the curvature that the configuration would adopt if allowed to bend freely and independently of constraints [70] (the authors do not provide a value for this parameter). The constant $k_b = \kappa/l$, where κ is the bending rigidity and l is the diameter of the cell, quantifies the extent to which the cell has deviated from its spontaneous curvature.

A further consequence of cell polarity, introduced in Section 2.1.3, is that cell division occurs within the plane. In this model, orientational changes act to maintain the integrity of the monolayer during cell division events. Each cell attempts to orientate its axis along the

tangent to the local radius of curvature at its position, which is determined by the relative positions of the two nearest neighbours, and is also updated for each cell at each timestep. This condition acts to maintain the crypt shape.

The components of the model for blastula growth are similar to those implemented for the crypt. The principal difference between the two systems is the magnitude of cell displacements that occur, these being much smaller during blastula formation, so that noise cannot be neglected. To model this, Drasdo and Forgacs [29] implemented the Metropolis algorithm, and assigned a total energy to each configuration of cells. Preferred cell configurations exist due to cell polarity and cell-cell contacts, and these correspond to minima in the energy, V^{tot}, associated with each cell. As in Equation (3.3), the total energy is the sum of that due to nearest-neighbour interactions, a bending energy to model cell polarity and a rotational energy associated with optimal cell orientation during division. Displacements, orientational changes and compressions which alter these configurations increase the energy, and so it is assumed that cells move or adjust their orientation in order to minimise V^{tot}. Thus, the probability of accepting a randomly chosen translation, axis re–orientation or growth step is dependent on whether it is energetically favourable.

Results

The computational simulations carried out by Drasdo and Loeffler [31] verify that under normal conditions – estimated biological parameters and realistic cell cycle times – the crypt model maintains the single-layered, test-tube geometry. Indeed, the size of the crypt and the turnover time of cells is stable. Further investigations examined the effect of reducing the cell stiffness, a term absorbed into the nearest neighbour interactions, as well as changing the cell cycle time. A buckling instability was observed that also was found in the growing blastula, namely that excess cell division cannot be sufficiently balanced by cell migration if the bending stiffness in the layer is too small, or if the growth rate is too large. Buckling is observed at the base of the crypt, as shown in Figure 3.8, as the bending rigidity is reduced.

Figure 3.9 shows the analogous results for the growing circular configuration that models blastula formation. Lowering the bending rigidity decreases resistance to bending within the layer, whilst a reduced cell cycle time shortens the period over which cells are able to fix undesirable transverse movements, which ultimately are compounded.

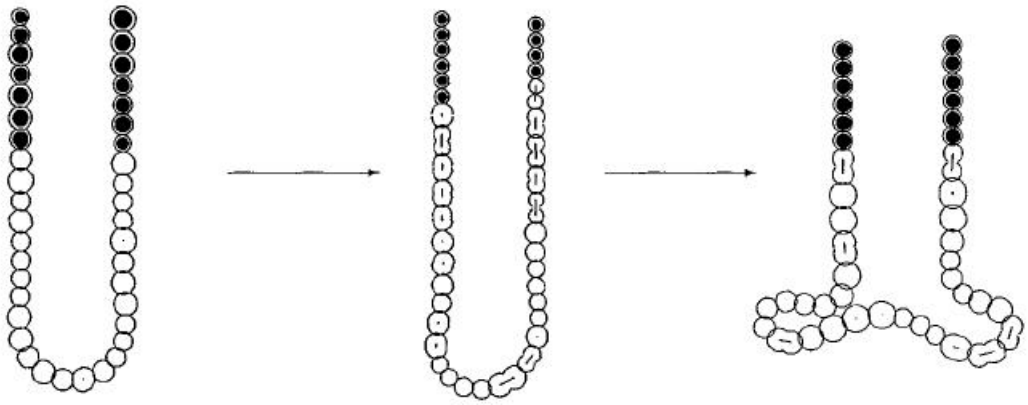

Figure 3.8: Crypt fission occurring in the 1D cell chain model. The progression to the state of crypt fission evolves as the bending rigidity is reduced to half the initial value. Reprinted from Drasdo and Loeffler [31].

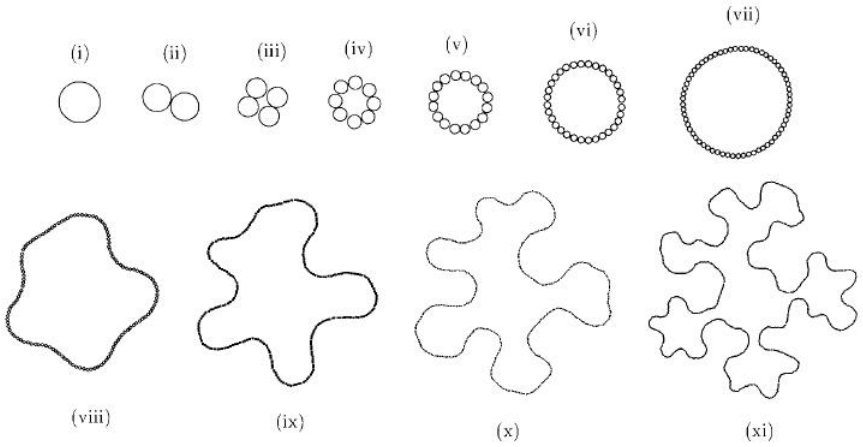

Figure 3.9: Simulations of the blastula formation model demonstrating the buckling instability of a growing, circular configuration of cells. Instability arises at stage (viii), when undulations form, and (ix)–(xi) show that buckling becomes more pronounced with time. Once the layer folds, gastrulation will take place. Reprinted with permission from Drasdo and Forgacs [29].

Model Limitations

Biological validation is not provided for either of these studies in the form of explicit comparison of the analytic and *in silico* results with experimental observation; rather the context of folding and buckling epithelial layers is discussed. The authors do not address whether buckling could occur further up the vertical crypt axis, as has been found experimentally [28] and which is shown in Figure 2.12. Such a result may be compromised by the application of the anchoring force imposed at the crypt collar. A further limitation of this work is that the connective tissue, and the influence of neighbouring crypts, are not modelled explicitly. In reality, the connective tissue will be deformed and drawn up with

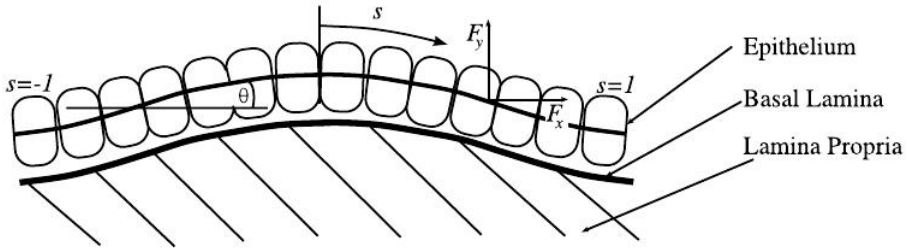

Figure 3.10: Schematic diagram of an unfolded crypt that has buckled, where the epithelium is modelled as a beam. Arc length, s, is measured from the centre, θ is the angle the beam makes with the horizontal and F_x and F_y are forces in the x and y direction, respectively. Reprinted with permission from Edwards and Chapman [35].

the buckling layer, and the neighbouring crypts may influence, or be influenced by, the spread of mutated cells. Lastly, the authors do not state how apoptosis is executed within the model, nor is the role of anoikis considered.

3.2.2 A Continuum Model of the Crypt

In 2007, Edwards and Chapman [35] adopted a continuum approach to investigate crypt buckling and fission as a consequence of downstream effects brought about by an activating mutation in the Wnt cascade. The epithelial layer in the crypt is unfolded, stretched out and modelled as a beam attached to the underlying mucosa, so that each end of the beam corresponds to the crypt collar, with cell-substrate attachments generating stress in the beam as it grows. These attachments are modelled using viscoelastic springs, to allow cells to detach and reattach as they move along the crypt. A schematic representation of the epithelial layer is given in Figure 3.10. The authors examine two causes of buckling: the application of an external force, and the effect of growth within the layer.

The steady-state configuration of the crypt is assumed to be a flat tissue layer, modelled using the non-dimensional beam equation

$$\frac{d^2\theta}{ds^2} + \lambda_0(F_y \cos\theta - F_x \sin\theta) = 0\,. \tag{3.7}$$

Here θ denotes the angle the beam makes with the horizontal, s is the arc length along the beam from the centre and F_x and F_y are the forces acting in the x and y directions respectively. The parameter $\lambda_0 = kL^4/B$ – where k is the spring constant of the cellular attachments, L is the crypt depth and B is the bending stiffness – gives a measure of the importance of spring strength against bending stiffness. Variables are non-dimensionalised

by scaling the arc length with the crypt depth, and the forces F_x and F_y with kL^2. The forces are obtained by considering the force balance of the tension generated in the springs

$$\frac{dF_x}{ds} = T_x, \qquad \frac{dF_y}{ds} = T_y\,, \tag{3.8}$$

where T_x, T_y are the x and y components of tension respectively, given by

$$T_x = \int_0^s \cos\theta\,\mathrm{d}s - f(s), \qquad T_y = \int_{-1}^s \sin\theta\,\mathrm{d}s\,. \tag{3.9}$$

The function $f(s)$ is the map from the deformed configuration back to the steady state configuration: $(X, Y) = (f(s), 0)$.

By linearising the model about its initial flat state, an eigenvalue problem is obtained for the deflection of the beam from the steady state. This assumes that the transverse displacement, $y(x)$, is small compared to the length of the beam, so that $\theta \sim dy/dx \ll 1$, and thus

$$\sin\theta \sim \frac{dy}{dx} \text{ and } \cos\theta \sim 1\,. \tag{3.10}$$

Under this assumption, (3.7) and (3.8) become

$$\frac{d^4y}{dx^4} - \lambda_0\left(F_x\frac{d^2y}{dx^2} + \frac{dF_x}{dx}\frac{dy}{dx} - y\right) = 0\,, \tag{3.11}$$

$$\frac{dF_x}{dx} = x - f(x)\,. \tag{3.12}$$

By implementing appropriate boundary conditions, which model the application of an externally applied force, the authors use this model to describe quantitatively the conditions under which the crypt will buckle: seeking the eigenvalue relationship between F_0 and λ_0 that corresponds to non-zero solutions. In this way, it is possible to consider the balance between spring strength and bending stiffness, and the effect that these parameters have on the stability of the beam.

In order to model buckling of the crypt that can arise through excess growth within the epithelial layer, this model is adapted to include the cell movement that occurs as cells detach from and reattach to the basement membrane during migration. This introduces a new parameter, λ_T, which quantifies the competition between the rates of cell growth and cell movement, and so describes the rate at which cells can move their bonds. To close the system a growth rate, $\gamma(x)$, is introduced, which is defined to restrict proliferation to a compartment at the centre of the beam as it lies flat.

As before, an eigenvalue problem is constructed for the linearised model, where non-zero solutions, if they exist, correspond to buckling of the tissue. It is then investigated whether changes in parameters, which correspond to specific changes in crypt dynamics, destabilise the flat, steady state solution.

Results

Three parameter groupings, λ_0, λ_T and λ_p, quantify the relationship between spring strength and bending stiffness, the competition between cell growth and cell movement, and the size of the proliferative compartment, respectively. By varying these parameters it is possible to investigate the effects of a mutation in the Wnt cascade – increasing the net proliferation rate (decreasing λ_T), changes to cell adhesion and motility (changing λ_0 and λ_T) and increasing the size of the proliferative compartment (decreasing λ_p).

The results, obtained using spectral methods, show that the effects of a mutation in the Wnt cascade will destabilise the steady state solution. More specifically, decreasing λ_T, which increases the net proliferation rate or the time taken for a cell to move its attachments, will initiate buckling independently of the other parameters. Also, provided λ_0 is large enough, decreasing λ_p from a particular point on the solution surface changes from the stable region to the unstable region and so buckling will occur. This translates to a larger spring strength, or smaller bending stiffness, combined with a larger proliferative compartment.

Model Limitations

The continuum model due to Edwards and Chapman [35] suggests fundamental mechanisms that may be responsible for the breakdown of the crypt structure. Failed differentiation, increased proliferation, decreased apoptosis and altered motility and adhesion are defined as consequences of changes in the three parameters described above. Analysis of the characteristic dynamics of adenomas is in agreement with these results [18, 55]. This continuum model enables general conclusions to be made, such as the consequence of failed apoptosis, and insight to be gained into the underlying system. However, it cannot account for cell heterogeneity, and in this current form, it does not allow stochasticity or noise. In common with Drasdo and Loeffler [31], this model does not explicitly account for deformation of the underlying connective tissue, which is required to fully understand crypt buckling beyond these initial stages.

3.2.3 Growth-Induced Buckling in Colonic Crypt Formation

In 2010, the model of Edwards and Chapman [35] was extended to investigate whether growth-induced buckling could drive colonic crypt formation [85]. In addition to the 'supported-monolayer model' due to Edwards and Chapman [35], the analysis was combined with a second mathematical model, the 'bilayer model', and complementary *in vitro*

(a)

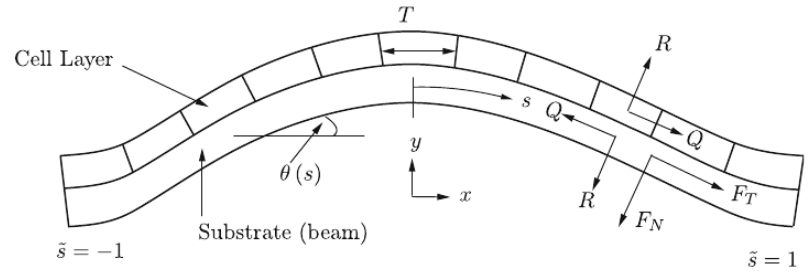

(b)

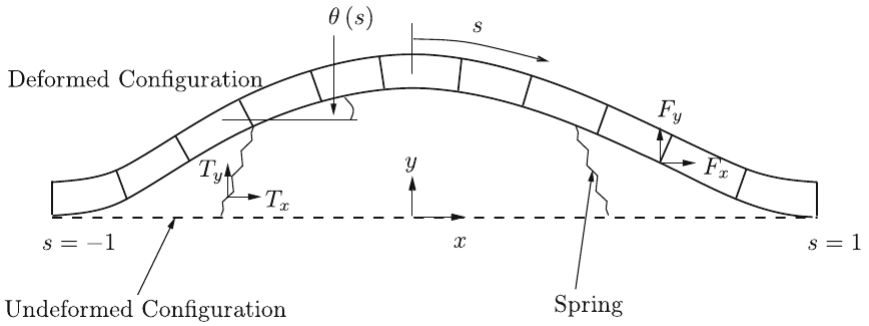

Figure 3.11: (a) Schematic diagram of the Bilayer model proposed by Nelson et al. [85], where the epithelium is modelled as a beam atop a flexible substrate. Arc length, s, is measured from the centre, $\tilde{s}$ is the Lagrangian arc length, θ is the angle the beam makes with the horizontal and F_N and F_T are forces in the normal and tangential directions, respectively. Q is the friction that acts between the two layers, and R is the normal reaction. Lastly, T is the in-plane tension that is generated. (b) The supported monolayer model, as for Edwards and Chapman [35]. Reprinted with permission from Nelson et al. [85].

experimental investigation to simulate and understand growth of an epithelial layer on an elastic substrate, and the subsequent incidence of buckling in this configuration. The authors propose that these experimental investigations form the basis for *in vitro* tools for research into colonic crypt function and destabilisation.

The experimental data used in this study were obtained by culturing rat intestinal cells beyond confluence on a thin, deformable silicon membrane. Deflections of this membrane were measured from marked reference points using light microscopy and image analysis software. Excess cell proliferation was induced by exposing the cells to a growth-factor, and the experimental results revealed membrane deformation resulting purely from cell growth, indicating that proliferating cells can generate a sufficient force to deform the underlying substrate.

To accompany this experimental work, two mathematical models were developed and anal-

ysed to identify parameter dependencies required to generate different buckling modes. The bilayer model is defined to be the theoretical equivalent of the experimental setup described above, and hence considers a monolayer of epithelial cells, defined as springs, adhered to a thin, extensible beam, which models the substrate, as shown in Figure 3.11(a). Solutions to the linearised model are characterised by two dimensionless parameters: α_1, which defines the balance of the resistance of cells to extension, to the resistance of the substrate to bending; and α_2, which defines the balance of the resistance of cells to extension, to the resistance of the substrate to extension. A discrete representation of the cell layer is used to derive homogenised force-balance equations, and it is subsequently assumed that deformations of the beam satisfy the Euler-Bernoulli relation. Two particular cases are explored: firstly, when cells are strongly adherent to the substrate, and secondly, when the adhesion is weak so that cells can easily slide along the beam. Boundary conditions fix the ends of the beam.

The authors perform a linear stability analysis to identify necessary conditions for buckling. The results show that there is no significant difference in the post-buckled states for the two extreme adhesion cases that were investigated and so the authors concluded that the strength of cell-substrate adhesion is not important. Indeed, the shape of the buckled layer is more sensitive to net cell growth, rather than local or non-uniform growth, but the extent of compressibility of the underlying substrate demonstrates an effect even at small amplitudes, and separates the different modes of bifurcation, which characterise the maximum deviation of the beam from its initial flat state.

Secondly, through nondimensionalisation, the supported-monolayer model due to Edwards and Chapman [35], discussed in Section 3.2.2, yields two key parameters: β_0, which characterises the force needed to extend the tethering springs relative to that required to bend the beam; and β_T, the ratio of the growth and viscous relaxation timescales. Analysis of the linearised model shows that β_0 is crucial to the onset of buckling. Allowing rapid viscous relaxation of the springs gives rise to major buckling of the layer and the formation of a geometric state resembling that of the crypt. Further, when non-uniform growth is investigated to replicate the localisation of the proliferative compartment in the crypt, the resulting crypt shapes are found to be more realistic, as shown in Figure 3.12. Despite this, as predicted using the Bilayer model, the final buckled state is more sensitive to the local bending stiffness of the beam rather than the pattern of growth.

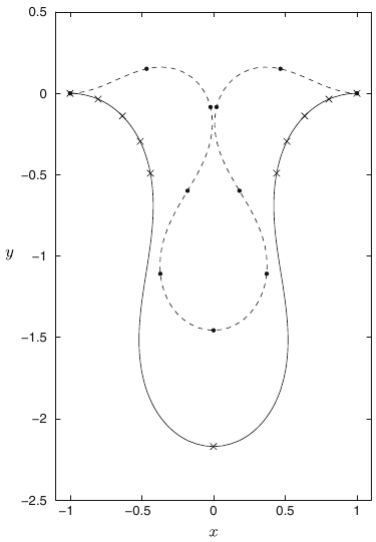

Figure 3.12: A comparison of the buckling profile obtained when proliferation is uniform throughout the layer (dashed line) and restricted proliferation (solid line). Reprinted with permission from Nelson et al. [85].

Model Limitations

This study forms the basis of understanding how growth of an epithelial monolayer constrained to a flexible substrate can recapitulate the geometry of the colorectal crypt. It is hypothesised that the formation of crypts is due to buckling of the epithelial layer during development, and this study suggests that such buckling arises as a consequence of softening of the cell layer rather than strictly through excess growth. This work, however, does not address the phenomenon of crypt fission, as explored by Drasdo and Loeffler [31], during which crypts grow and divide [55]. Such an investigation would not be possible in this model without assuming a post-buckled state to model the crypt shape, nor without considering neighbouring crypts.

3.3 General Applications of Cell-Based Models

Also relevant to the work presented in this thesis are those cell-based models which consider, for example, generic as well as (non-crypt) specific biological epithelia, and tumour growth in different parts of the body. Some additional models are discussed here to put this D.Phil. work in the context of the wider research efforts within the field.

In earlier work which lays the groundwork for the 3D crypt model proposed by Buske et al. [21], Galle et al. [47] present a 3D overlapping spheres model to examine growth

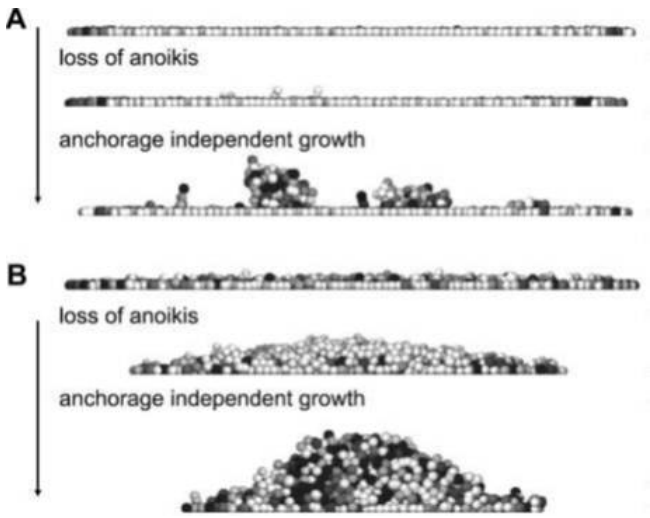

Figure 3.13: Vertical cross-sections through the 3D cell populations. (A) A cell-substrate anchorage of 600 μN/m, (B) 200 μN/m. Each example demonstrates the effect of loss of anoikis, as well as anchorage-independent growth. The combined failure of these two growth control mechanisms causes an accumulation of cells and loss of the monolayer structure. Reprinted with permission from Galle et al. [47].

regulation in epithelial layers *in vitro*. Cell deformation is calculated using the Hertz force law [68], while cell-cell and cell-substrate adhesion is defined to increase with contact area. The model considers a growing layer of epithelial cells, with infinite proliferative capacity, and imposes density-dependent inhibition of mitosis, whereby cell division can only occur above a threshold volume of $0.99V_0$, where V_0 is the equilibrium cell volume. Provided cell-substrate anchorage is greater than cell-cell anchorage, simulations demonstrate that confluent cell monolayers form.

As illustrated in Fig. 3.13, model simulations examine the role of two growth control mechanisms – anoikis and anchorage-dependent growth – for varying cell-substrate adhesion. It is found that if the cell-substrate adhesion is strong, only a small number of cells pop out of the layer, which remain only under failed anoikis. If anchorage-dependent growth is also lost, those cells which are not in contact with the substrate will continue to proliferate (Fig. 3.13(A)). If the cell-substrate adhesion is weak, then a greater number of cells will be vulnerable to detaching from the substrate. Subsequently, the loss of anoikis allows cell aggregates to form, which continue to increase in size if anchorage-dependent growth is also lost (Fig. 3.13(B)).

A 3D deformable spheres model is also implemented by Schaller and Meyer-Hermann [106] to investigate the growth of tumour spheroids, where in contrast to Galle et al. [47], the neighbour interactions are determined by a weighted Delaunay triangulation between cell centres. The dual Voronoi tessellation is applied to provide a more realistic definition

of the contact surface between neighbouring cells, which is subsequently used throughout the calculations instead of the sphere contact surface. Drasdo *et al.* (2007) [30] also consider the growth of monolayers on a substrate and multi-cellular spheroids, and revisit single-layered tissues such as the blastula during development (considered in [31]) to examine the mechanical influence of contact inhibition on the growth of the cell population.

Assuming the same parameter values as Galle et al. [47], the 3D overlapping spheres model is also implemented by Ramis-Conde et al. [100] within a multiscale model that incorporates a sub-cellular model of cell-cell adhesion, which is dependent on intracellular β-catenin and its interaction with E-cadherin at the cell membrane. The total E-cadherin concentration is composed of three different states: $[E_c]$, catenin-free within the cytoplasm; $[E_m]$, catenin-free at the cell membrane; and $[E/\beta]$, the E-cadherin-β-catenin complex at the cell membrane.

Simple chemical reactions are defined to model the intracellular dynamics, which are dependent on the contact area between a cell and its local neighbours as shown below.

$$
\begin{aligned}
&[E_c] \xrightarrow{\text{contact}} [E_m]\,, \\
&[\beta] + [E_m] \xrightarrow{\nu} [E/\beta]\,, \\
&[E/\beta] \xrightarrow{\text{detachment}} [E_c] + [\beta]\,.
\end{aligned}
$$

Specifically, it is assumed that the amount of cadherin that is stimulated to move from the cytoplasm towards the membrane is proportional to the contact area between neighbouring cells. The E-cadherin-β-catenin complex is produced at a rate ν, and ruptured upon cell detachment. Cell-cell contact is determined by coupling this intracellular model to the overlapping spheres model, such that the contact area approximates the bonds formed by physical contact between cells.

This multiscale model is then used to investigate the upregulation of β-catenin that occurs following the break of E-cadherin bonds upon cell detachment. In particular, detachment waves are observed in epithelial layers by inserting a single cell within a 2D monolayer that has no β-catenin regulation activity, and tracking the induced detachment in its neighbours. Further, an effect similar to the epithelial-mesenchymal transition is observed by simulating a constant source of chemoattractant within a 2D layer of cells with a fixed boundary, in 3D space. Cells detach and migrate away from the fixed boundary. This effect is also observed in a 2D cross section of a 3D tumour mass: cells migrate towards the source of a chemoattractant, detaching from the main tumour mass, causing the boundary cells to lose some E-cadherin bonds, upregulate β-catenin and thereby enhance migration and invasion.

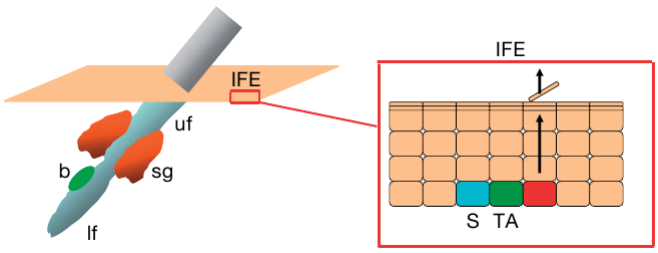

Figure 3.14: A schematic illustration of the hair follicle and IFE. Stem cells are located at the base of the follicle, in the bulge labelled *b*. These stem cells generate the lower and upper hair follicles (*lf* and *uf*), as well as the IFE itself. Within the basal layer of the IFE, there are stem cells (blue), transit cells (green) and post-mitotic basal cells that migrate upwards whilst differentiating, as indicated by the arrow. Reprinted with permission from Clayton et al. [25].

These modelling examples demonstrate the usefulness of individual-based models to investigate the growth dynamics of epithelial cell populations, and how a multiscale approach can be utilised to investigate behaviour across the spatial scales.

3.3.1 Other Biological Exemplars

Thus far, this chapter has focused specifically on models of the intestinal epithelium, as well as generic epithelial monolayers and tumour spheroids. Three non-crypt biological exemplars are considered here briefly: the interfollicular epidermis (IFE), the olfactory epithelium (OE), and the ductal carcinoma in situ (DCIS).

In the same way that the intestinal epithelial layer is maintained by the cells that line the crypts of Lieberkühn, skin tissue itself is replenished by a population of stem and transit-amplifying cells. The hair follicles in the skin are surrounded by the IFE, shown in Figure 3.14, which comprises a basal layer of proliferating cells that produce cells committed to differentiation, and which migrate towards the upper cell layers. Clayton et al. [25] propose a stem/transit-amplifying cell hypothesis for the IFE, much like the hierarchy observed in the crypt, and a comparison of experimental results reveals that a model for a single stem cell compartment is compatible with the data recorded.

A second example is that of the OE, self-renewing neural tissue lining the nasal cavity, which is responsible for transmitting odour information to the brain (see Figure 3.15) [69]. This particular epithelium sits above the Bowman glands, which are similar to the intestinal crypts. Research into the OE has concentrated on understanding the relationship between growth control and cell lineages – like the crypt, the OE maintains a stable size through continuous replacement of dying cells, such as the primary olfactory receptor neurons (ORNs), which can be killed by pathogens entering the nose [32]. Research is seeking to

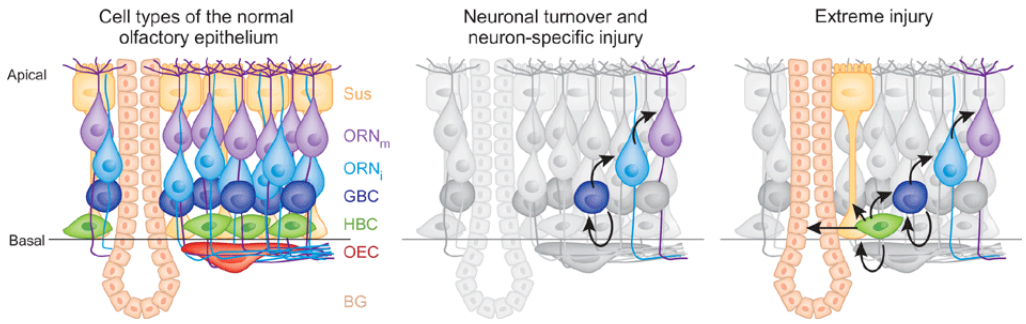

Figure 3.15: Schematic illustration of the OE and cell lineage relationships. Reprinted with permission from Duggan and Ngai [32].

define a population of stem cells which generates all of the cell lineages, and which is responsible for replenishing the epithelium following injury. Direct parallels can be drawn to the cell lineage model in the crypt, and the strict control exerted to maintain a stable population throughout regular cell turnover.

Lander et al. [69] propose a feedback model that characterises growth control in the olfactory epithelium managed by the cell lineage pathways, and the results of this study suggest that there is no cell type distinction between stem and transit-amplifying cells, but rather two types of observable behaviour. The behaviour exhibited by cells is dependent on that exhibited by other cells, environmental cues and geometric positioning. This result is consistent with the increasingly accepted idea of reversible stem cell fate, which is an emerging concept in crypt biology, as proposed by Buske et al. [21] for the 3D crypt model discussed in Section 3.1.4.

DCIS is a type of breast cancer that is localised to the milk ducts – tubes lined with a columnar epithelium – which arises as a precursor to an invasive tumour. In common with CRC, detection of DCIS is difficult, and in particular it is hard to estimate the full extent of the tumour from patient imaging alone. Macklin et al. [73] use an agent-based model to simulate the cross-sectional structure of a DCIS tumour. Cells are modelled as deformable spheres, with fixed volume, located within a defined lumen that represents the intraductal space. The basement membrane is modelled as an impermeable boundary using level set functions. Example simulation snapshots are illustrated in Fig. 3.16. The forces acting on cells are determined by cell-cell, cell-matrix and cell-basement membrane adhesion, as well as cell-cell repulsion, modelled by potential functions as for Galle et al. [47], Ramis-Conde et al. [100]. A novel feature of the DCIS model is that it accounts for cell necrosis moving from the basement membrane towards the duct centre, leading eventually to calcification, and a patient-specific model calibration protocol is described in which single time-point

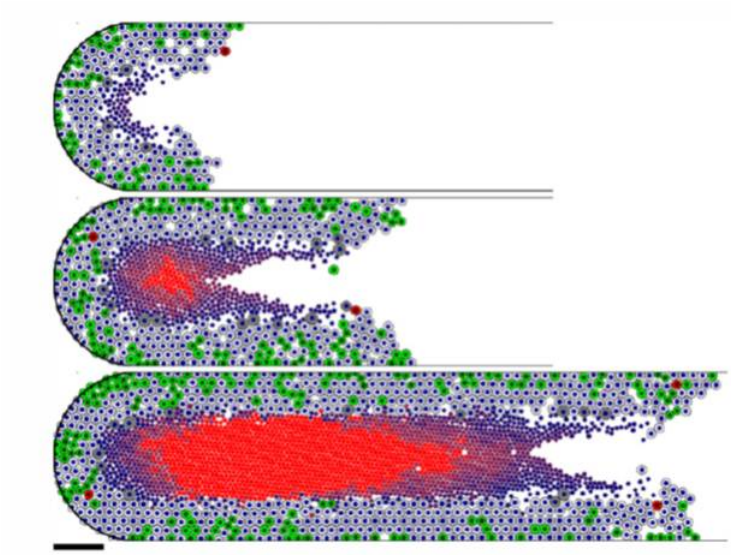

Figure 3.16: Snapshots of the DCIS model simulations for a 1mm length of duct, taken after 11, 24 and 45 days. The basement membrane is indicated by the black boundary, and cells are coloured as follows: quiescent cells (pale blue), proliferating cells (green), apoptotic cells (red, shaded according to the degree of calcification), necrotic cells (grey), lysed cells (dark circles in the centre of the duct). The scale bar corresponds to 100 μm. Reprinted with permission from Macklin et al. [73].

measurements are used to simulate the growth of cancer in a patient. This demonstrates the possibility of applying agent-based modelling approaches tailored to individual cases within the clinic.

These examples demonstrate that there is overlap between areas of research in crypt dynamics and that of other biological epithelia. In addition to the examples that have been discussed here, there is ongoing work in epithelial tissue modelling both in a general context [124], and also within developmental biology [1] and wound healing [113]. This emphasises the need to be aware of research that is ongoing in the wider field, both to yield more advanced and insightful modelling approaches, and perhaps to supplant concepts that have persisted in crypt modelling which have already been identified as redundant in these areas.

3.4 Summary

As outlined in Chapter 2, the adenoma-carcinoma sequence is a multiscale process. The gap in the current knowledge of this process is a firm understanding of how the genetic mutations identified in the sequence, which correspond to changes in specific cell properties, manifest at the tissue level. In particular, the question remains of whether a single mutation

is sufficient, or rather a combination of aberrant cell properties is necessary to sufficiently destabilise the regular crypt dynamics and provoke permanent changes. To address this problem mathematically or computationally necessitates a multiscale modelling approach.

Given that this problem is inherently concerned with architecture and structural integrity, it is necessary to take account of the geometry of the crypt, and the influence of the surrounding connective tissue and neighbouring crypts. Cell decisions arise as a consequence of choices made relating to cell division, polarity, adhesion – both to nearest neighbours and to the underlying substrate – and differentiation. Thus appropriate forces must be applied to model these influences, and essential signalling factors incorporated. By discussing existing work, this chapter has introduced the building blocks for constructing a realistic computational model of the crypt that takes account of such requisite influences and components of the system. However, the models that have been proposed thus far are not suitable to explore fully crypt budding, fission and adenoma development.

A common feature of the cylindrical crypt models discussed in Section 3.1 is that they all impose an unrealistic, rigid crypt shape, and do not permit investigation of the role of the surrounding connective tissue, or neighbouring crypts. This geometric simplification overestimates the number of cells at the crypt base, the location of the stem cell population. The 2D models, whilst simple to implement and computationally inexpensive, do not capture all of the degrees of freedom that can be exploited by cells, and which may add a robustness to the structure, delaying or even preventing colonisation of mutant cells. However, the crypt model recently proposed by Buske et al. [21], while capturing the crypt geometry and 3D cell movement, still imposes a rigid crypt structure.

The models of crypt buckling and fission discussed in Section 3.2 characterise the epithelial cell layer in 2D, assigning a bending stiffness to the monolayer and examining the destabilising effect of growth. The bending stiffness acts to conserve the favoured cell configuration, and this term is crucial in determining the stability of the layer. The continuum model due to Edwards and Chapman [35], unlike the discrete models, accounts for cellular attachment to the underlying matrix using viscoelastic springs, and considers the ratio of the bending stiffness to the strength of these attachments. Model analysis reveals that the connections to the tissue matrix play a crucial role – combined with an increase in proliferation, increasing the strength of the attachments can generate buckling. A consequence of the continuum approach undertaken in this case is that cell heterogeneity is neglected, and so individual cell properties, such as polarity, are not included in the model. Such components were included in the discrete models due to Drasdo and Forgacs [29] and Drasdo and Loeffler [31]. As a consequence, there are particular downstream effects of individual

mutations that cannot be considered within a continuum model, which manifest as local changes which harbour the potential to achieve colonisation following proliferation.

Nelson et al. [85] hypothesize that crypt formation is a consequence of local buckling arising in an initially flat epithelium during development, but deduce that such buckling requires softening of the cell layer in addition to excess growth. In its current form, and in addition to the reasons outlined above, this continuum model is not applicable for studying buckling in the test-tube shaped geometry of the crypt. It would be of interest, however, to examine how a similar softening of the cell layer might manifest in the fully-formed structure, and whether such tissue properties might compound or prevent crypt buckling.

Together with Chapter 2, the background to the problem that is considered in this thesis is now complete. Biologically, to move towards an accurate, predictive computational model of the crypt, cellular influences such as polarity, cell-substrate contacts and extracellular signalling gradients must still be taken into account. To improve on existing theoretical work, this model must also allow and track the effects of deformation on the lamina propria. As outlined already, ideally a 3D, multiscale framework is needed, one which permits the inclusion of subcellular models that determine division events, and mechanical models that control migration, cell-cell and cell-matrix adhesion. As shown in this literature review, all of these elements have yet to be combined in any single model of the colonic crypt.

To develop a computational model of the crypt with a realistic, deformable geometry, seeking to incorporate elements of cell dynamics such as anoikis, cell polarity and adhesion to the basement membrane, it is necessary to work in a discrete framework. The first stage of model development is to define the cell-level model that will be implemented. The off-lattice cell-centre model of cell-level behaviour is applied given the advantages over alternative models of cell mechanics which were discussed in Section 3.1.2, as well as speed of computation, which becomes very important as additional factors and forces are taken into consideration. This is discussed in more detail in Chapter 4, where Chaste, the computational framework used for model development and simulation, is introduced.

The model must include the role of forces on the epithelial monolayer which act to maintain the integrity of the organ in the absence of genetic alterations. It is desirable, therefore, to focus specifically on the mechanical forces that exist between cells and the underlying lamina propria. In particular, the composition of the surrounding connective tissue must be considered, in light of the support afforded to the crypt base by the muscularis mucosae, and the general stabilising effect of the basement membrane and PCFS. This represents the primary challenge to any model of a growing, deformable epithelium. By firstly approaching this challenge in a general geometric framework, such a model will not be

specific to the crypt itself, but rather applicable in similar modelling approaches for other biological epithelia, such as those outlined in Section 3.3.1.

Chapter 5 introduces a new model to address these issues. Following this, the next step is to define a realistic geometry, which is achieved in two steps. A 2D cross-sectional representation of the crypt is considered in Chapter 6, which is subsequently extended to 3D in Chapter 7.

Chapter 4

An Off-Lattice Cell Centre Model of the Colorectal Crypt

Thus far, the motivation for developing a comprehensive model of the colorectal crypt has been discussed from both a biological and theoretical perspective. In particular, it has been noted that a computational model of the crypt can lend insight into, and generate predictions for, the mechanisms of this system. Given the limitations of existing mathematical models discussed in Chapter 3, and the nature of the biological problem discussed in Chapter 2, it is proposed that to advance understanding of the crypt system under healthy conditions, as well as how a breakdown in cell dynamics can lead to the development of CRC, a computational model which enables full examination of tissue-level behaviour is required. The development of such a model is the main aim of this D.Phil. thesis.

This chapter describes one of the main building blocks for the new crypt model: the off-lattice cell-centre model, which is applied to model interactions at the cellular level. This framework is employed to define a new model of a growing, deformable epithelial monolayer in Chapter 5, which is incorporated into a 2D crypt geometry in Chapter 6 and then to a 3D model in Chapter 7. Cell centres are defined as nodes (these terms can be used interchangeably) which are free to move in space. Cell shapes are prescribed using a Voronoi tessellation, and cell movement is governed by summing the attractive and repulsive forces that act on a particular cell.

This agent-based model, first introduced and applied to the colorectal crypt by Meineke et al. [76], is simple and computationally inexpensive to implement for the small number of cells in the system. The advantages over the earlier CA models include continuous, geometrically-unconstrained movement and realistic polygonal cell packing that arises from the Voronoi tessellation. Further, cell division does not lead to unrealistic,

far-reaching cell movements which are required to accommodate newly created cells in CA. The individual components of the cell-centre model are introduced in Section 4.1.

The second half of this chapter is concerned with the computational framework that is used to implement and develop the new model of the colorectal crypt: Chaste (the 'Cancer, Heart And Soft Tissue Environment') [94]. Chaste is an open source software library, written in object-oriented C++ and constructed using agile programming techniques according to the principles of 'eXtreme programming' (XP) [11]. It is designed as a general purpose simulation package aimed at computationally-demanding multiscale problems arising in biology and physiology, and has been in continuous development since 2005.

Section 4.2 describes the Chaste ethos, and motivates the need for high-quality software to address such problems, rather than individual code developed by a single user in academia. The software engineering practices employed to achieve this are explained, and an outline for the code structure is given. An example of the code used to generate a typical cell-based simulation of the cylindrical crypt model illustrates how Chaste is designed such that simple changes control and alter fundamental model components, and enable comparison of different modelling paradigms.

4.1 The Cell-Centre Model

The components of the cell-centre model are now introduced: the definition of cell-cell connectivity, how interactive forces are modelled to influence cell movement, and the mechanical execution of cell division. The specific geometry, boundary conditions and cell cycle model applied by Meineke et al. [76] are discussed in Section 3.1.2 and so are omitted at this stage. In addition, the manner in which such model components are adapted or extended for this work is discussed in Chapter 5.

4.1.1 Delaunay Triangulation and Voronoi Tessellation

To describe the spatial connectivity of nodes in the off-lattice cell-centre model, the following definitions are required [38, 86]:

Definition 4.1.1 *Let $P = \{p_1, p_2, \ldots, p_n\}$ be a set of points in the two-dimensional Euclidean plane. These are called the sites. Partition the plane by assigning every point in the plane to its nearest site. All those points assigned to p_i form the Voronoi region $V(p_i)$. $V(p_i)$ consists of all the points*

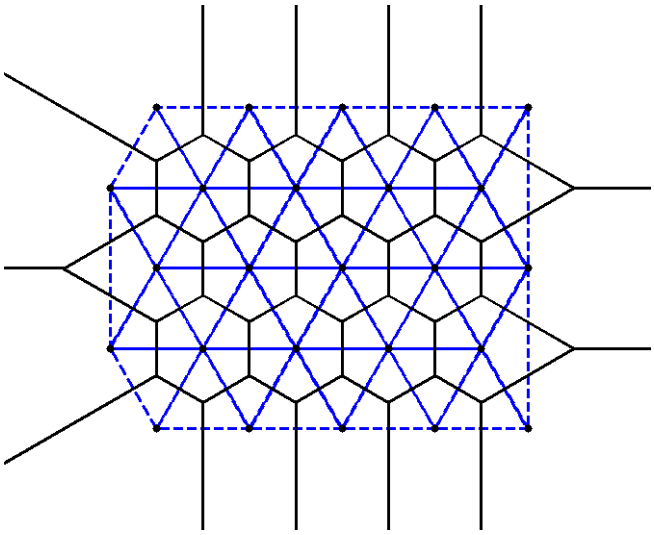

Figure 4.1: An example of the Delaunay triangulation (blue dashed lines) and the dual Voronoi tessellation (black solid lines) for a set of evenly spaced nodes.

in space at least as close to p_i as to any other site:

$$V(p_i) = \{x : |p_i - x| \leq |p_j - x| \forall j \neq i\}\,. \tag{4.1}$$

Definition 4.1.2 *Let $P = \{p_1, p_2, \ldots, p_n\}$ be a set of points in the two-dimensional Euclidean plane. The Delaunay triangulation $\mathcal{D}(P)$ is the straight line dual graph of $\mathcal{V}(P)$, such that the nodes of $\mathcal{D}(P)$ are the sites of $\mathcal{V}(P)$, and two nodes are connected by a straight arc if their corresponding Voronoi polygons share a Voronoi edge.*

An example of a Delaunay triangulation for a given set of nodes is shown in Figure 4.1, together with the corresponding Voronoi tessellation of these nodes. This figure shows a triangulation that is fully relaxed, such that equilateral triangle elements are shared by neighbouring nodes, save those on the boundary.

By assigning cell centres to nodes, the cell-centre model defines cell connectivity and assigns nearest neighbours according to the Delaunay triangulation. Cell shapes are defined by the Voronoi tessellation of these centres, and give rise to polygonal regions that have been demonstrated to resemble epithelial cell shapes, as shown in Figure 4.2 [54, 76].

4.1.2 Ghost Nodes

The convex hull of a given set of points in a plane can be informally described as the shape taken by a rubber band stretched around nails hammered into the plane at each point, which in 3D extends to the concept of a plastic wrap around the points [86]. Unless a mesh

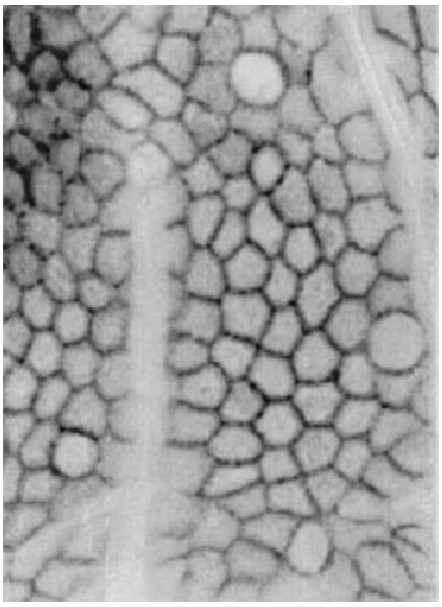

Figure 4.2: An image obtained using light microscopy, where β-catenin staining highlights the cell borders. This reveals the polygonal packing of epithelial cells in a monolayer, and can be compared with the internal elements of the Voronoi tessellation shown in Figure 4.1. Reprinted with permission from Meineke et al. [76].

of nodes forms a convex hull, the resulting Delaunay triangulation will have some very long connections at the edges, which lead to large, unrealistic forces acting on the cells, and semi-infinite Voronoi tessellations which disrupt visualisation, as shown for the boundary nodes in Figure 4.1. To avoid this problem, a layer of 'ghost nodes' can be included around the edges of the mesh, as shown in Figure 4.3. These nodes are labelled as such because, while real nodes will exert a force on ghost nodes causing them to move throughout the simulation, ghost nodes will not exert any forces on real nodes. The presence of these nodes prevents long connections from forming between real nodes, and only the ghost nodes have infinite tessellations, which enables visualisation of the Voronoi regions of the real nodes.

4.1.3 Interactive Cell Forces

The interactive forces between neighbouring cells, which correspond to the adhesion and repulsion that exist due to cell-cell contacts and limited compressibility, are modelled by a network of linear, overdamped springs that connect cell centres along the Delaunay triangulation mesh. This is defined such that a steady state distribution of cells is reached in the absence of proliferation (as is the case in Figure 4.1). Each spring is assigned a rest length, $s_{i,j}(t)$, and spring constant, μ, and it is assumed that cell-cell adhesion bonds have

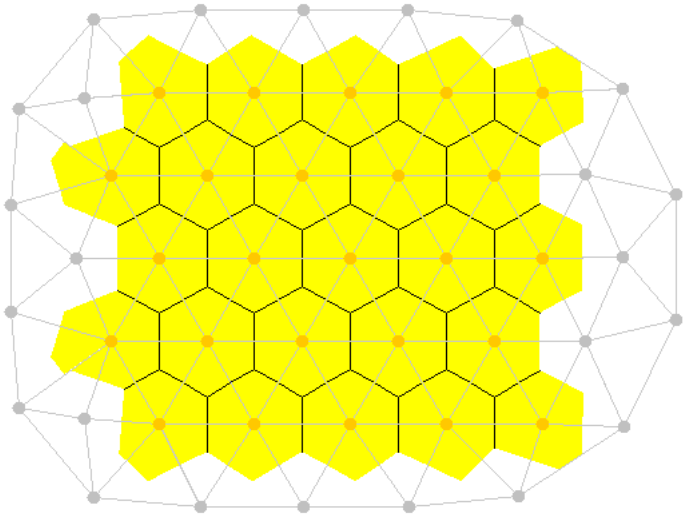

Figure 4.3: A block of real cells (yellow) surrounded by ghost nodes (grey). The triangulation (grey) connects all nodes, whereas the Voronoi tessellation (black) only defines regions around real nodes.

the same strength for any pair of neighbouring cells, so μ is constant and equal for all cells.

The total force acting on each cell is found by calculating the sum of the contributing forces from the springs connecting all neighbouring cells, according to Hooke's law:

$$\mathbf{F}_i(t) = \mu \sum_{\forall j(t)} \hat{\mathbf{r}}_{i,j}(t)(s_{i,j}(t) - |\mathbf{r}_{i,j}(t)|)\,. \tag{4.2}$$

Here, $\mathbf{r}_{i,j}(t)$ is the vector from cell centre i to cell centre j, with $\hat{\mathbf{r}}_{i,j}(t)$ the corresponding unit vector, $s_{i,j}(t)$ is the spring rest length, which is equal for all connections, save those between cells that have just undergone division, as explained below.

By neglecting inertial terms relative to dissipative terms (a valid assumption due to the small estimated Reynold's number for cell movement through aqueous medium [27]), the velocity of node i is given by

$$\eta_i \frac{d\mathbf{r}_i}{dt} = \mathbf{F}_i(t)\,, \tag{4.3}$$

where $\mathbf{r}_i$ is the position of node i. The constant η_i is a drag coefficient modelling the strength of epithelial cell adhesion to the basement membrane in the cylindrical crypt framework, which can depend on cell type, but is kept constant unless stated otherwise. By iterating in small time intervals, cell positions are updated at each timestep using the Forward Euler method [7].

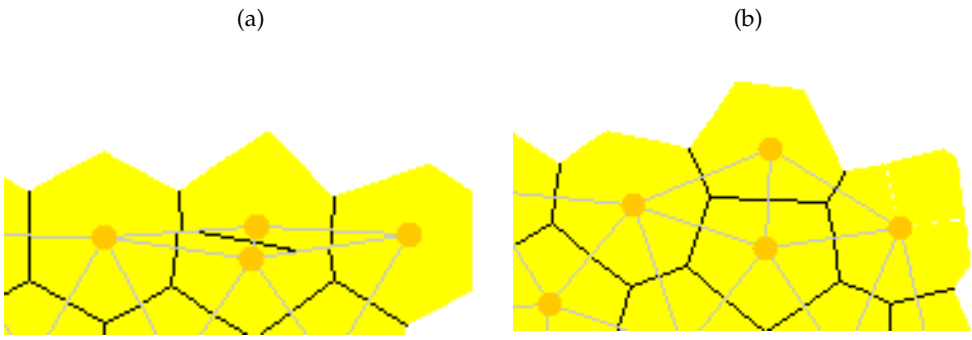

Figure 4.4: Simulation snapshots showing a division event. (a) Just after the cell has divided, there are two newly created cell centres with a short connecting spring, (b) after M phase, the connecting spring has grown and the cells are starting to equilibrate.

4.1.4 Cell Division

In the absence of mitotic activity, neighbouring cells tend to reach a state of equilibrium, where inter-cell distances are equal and take the constant value of the mature spring rest length, s, which is scaled to a single cell width (10 μm [2, 109]). When a cell divides, two daughter nodes are created in place of the original parent node, connected by a new spring, and positioned a small distance of $0.05s$ away on either side of the parent node position. The new connecting spring is assigned a rest length, $s_{i,j}(t)$, which increases linearly from $0.1s$ to s over the course of M phase (1 hour). This models the growth of a cell before division occurs (albeit the two cells are already distinguished in the simulation). This also acts to prevent cells from springing apart too abruptly after division. This is illustrated in Figure 4.4.

4.1.5 Cylindrical Geometry

Meineke et al. [76] model the crypt as an unwrapped cylinder, such that the geometry is equivalent to the implementation of periodic boundary conditions on the vertical edges of a rectangular domain. These boundary conditions are utilised in Chapter 5 to model the presence of neighbouring crypts, and so the details are provided here. Figure 4.5 accompanies this description.

Firstly, a rectangular mesh of nodes is defined, as shown in Figure 4.5(a). To construct periodic boundary conditions and to maintain a convex hull for the real nodes, ghost nodes are placed at the top and bottom of the mesh and image nodes are created from the real nodes on either side of the vertical edges (Figure 4.5(b) and (c)). If the width of the mesh of real nodes is defined as w, then images of those nodes in $0 \leq x < w/2$ are

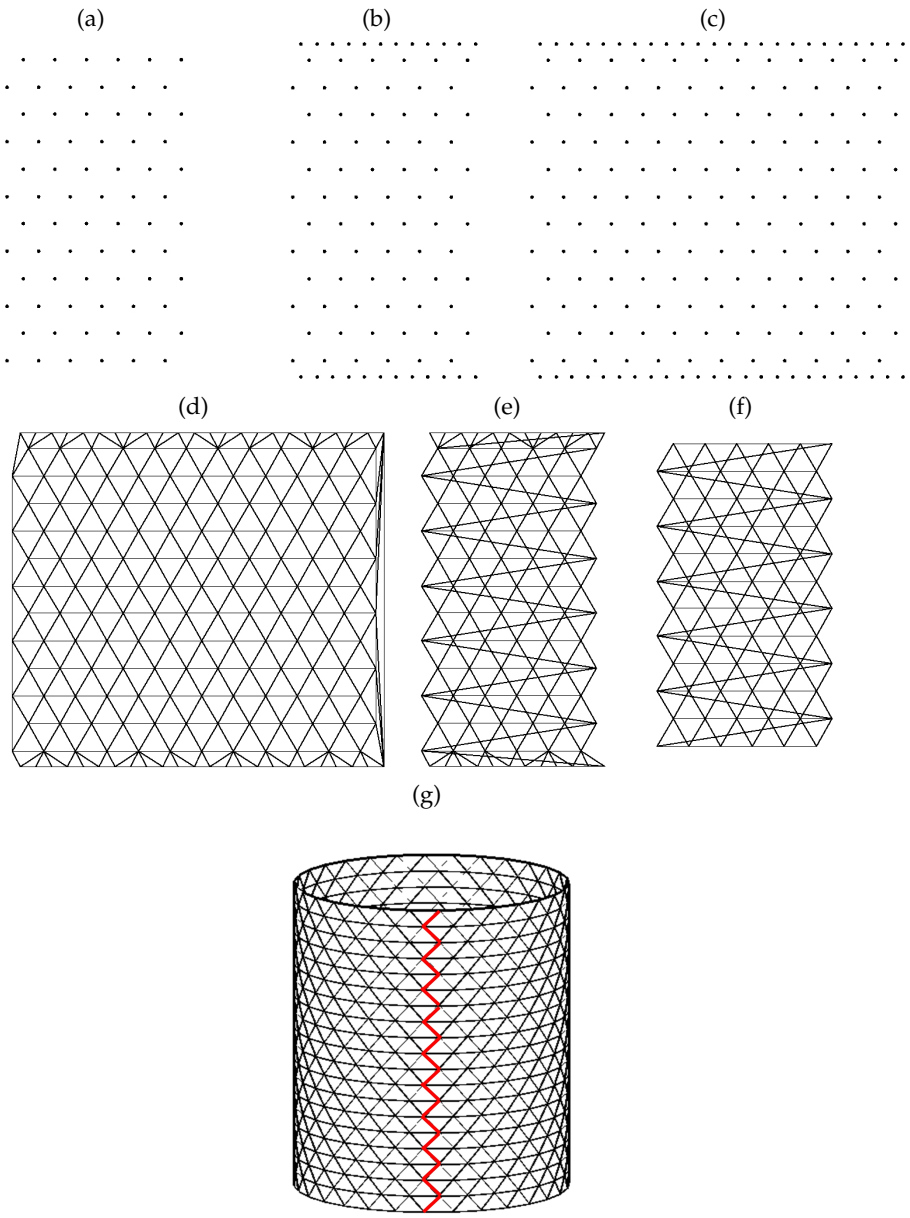

Figure 4.5: (a) The initial mesh of real nodes, (b) including a layer of ghost nodes above and below the mesh of real nodes, (c) including the image nodes of on either side of the mesh of real nodes, (d) forming the Delaunay triangulation of the ghost, image and real nodes, (e) replacing image nodes with real counterparts in elements containing a single image node, and removing those elements that contain more than one image node, (f) tracking only the connectivity of the real nodes, (g) an example of how such a triangulation sits on the surface of a cylinder, where the red line indicates the boundaries that are stitched together from (f). Reprinted with permission from Mirams [78].

placed in $w \leq x < 3w/2$, and similarly images of those nodes in $w/2 \leq x < w$ are placed in $-w/2 \leq x < 0$. By keeping a record of the associated real and image nodes, the Delaunay triangulation is constructed from the new mesh (Figure 4.5(d)). Following this, elements that contain only one image node have this node replaced by the associated real node, and

elements that contain more than one image node are removed, in addition to the image nodes themselves (Figure 4.5(e)). The simulation then follows only the real nodes, and this defines the cylindrical mesh (Figure 4.5(f)). Figure 4.5(g) illustrates how the mesh sits on the surface of a cylinder, where the red line indicates the boundaries that are stitched together from Figure 4.5(f). For visualisation purposes, boundaries are assigned to each periodic mesh such that cells that move beyond the boundaries are transferred to the opposite edge.

4.1.6 Summary

This section has outlined the general components of the off-lattice cell centre model, which is chosen to characterise behaviour at the cellular level in the multiscale crypt model that is defined and investigated in Chapters 5 and 6. Extensions to this framework are outlined in these chapters, which include variable cell adhesion between cells of different proliferative and mutation state, and a novel model of the role of the surrounding musculature, basement membrane and PCFS. To complete the background for this work, the computational environment used for model development is now introduced.

4.2 Chaste

Within academia, it is the norm for individual researchers to develop specialised code aimed at a specific problem, which is inherently limited by the computational experience and style of that specific researcher and often difficult for other programmers / researchers to understand, implement and, ultimately, extend. It is also becoming more evident that as models of biological problems increase in complexity and in the amount of data that is applied, the efficiency of the computational tools used plays an increasing role in the research initiative. Further, when individual code is used to investigate model behaviour, accurate comparison of different modelling paradigms becomes impossible, as the distinction between the model components, when combined with a unique computational implementation, is not feasible. Moreover, at present it is not the convention within this field to routinely publish code, and it is up to the individual researcher to ensure that it is fully tested and correct.

The Chaste project was originally conceived and initiated to challenge this convention, and to produce high-quality code within a development framework established to ensure long-term maintenance and extensibility. The code is written in object-oriented C++ and

is designed to be robust, fast and accurate, implementing state-of-the-art numerical techniques [94]. Whilst Chaste is designed to be a generic library, the focus of the code initially supported the modelling of two specific biological problems: cardiac electrophysiology (cardiac Chaste) and discrete modelling of cell populations (cell-based Chaste). More recently, the cell-based side of Chaste has evolved to incorporate a number of different models at each of the three main spatial scales (subcellular, cellular and tissue level) which directly enables comparison of model behaviours. For example, the model proposed by Buske et al. [21] has been programmed within Chaste with relative ease (see Figure 3.6(b)), and it is now possible to compare the behaviour of this model with alternatives, in the knowledge that differences which may emerge in cell behaviours arise due to differences in the models, and not due to errors or differences in the code. Released under the BSD open source license, Chaste is available as a resource to the research community[1].

The following section outlines the principles behind the Chaste code structure and development ethos, and describes some biological applications currently being investigated. Given the biological background for this D.Phil. work, focus is given to the cell-based side of Chaste, rather than the cardiac applications. Unless stated otherwise, simulation snapshots that are presented in this, and subsequent, chapters have been produced using a graphics visualisation tool created purposely in Java for Chaste.

4.2.1 eXtreme Programming

Extreme programming refers to a particular software development methodology, which employs agile programming techniques to ensure good software engineering principles that result in high-quality code. The elements of this approach which have been employed in designing the Chaste framework include the following [93].

- **Collective code ownership**: Chaste is advanced simultaneously by a core team of developers who can contribute to all aspects of the code. This ensures that no one person assumes responsibility for the overall direction or design, and all developers are familiar with the entire framework.
- **Iterations**: Code development advances through a series of planned day or week-long iterations, attended by the team of developers, in which specific updates or new functionality are defined, and subsequently implemented.
- **Pair programming**: At each iteration, work is undertaken in pairs, with one person assuming the position of the "driver", who types, whilst the second reviews the

[1] `http://www.cs.ox.ac.uk/chaste`

code. The pair discuss and strategise, and alternate the driving position at regular intervals. Throughout the iteration, the pairs swap so that different developers work together on different targets. This particular methodology maintains collective code ownership.

- **Test-driven development**: Before adding new functionality, the developer writes a failing unit test, which incorporates, and so tests the use of, the desired new component. Once this test is defined, the component functionality is added to the main trunk of code. This has the benefit of guiding the design of the code that is required, and development does not continue unless all tests pass. A second type of test, acceptance tests, are used to check the behaviour of the whole system. This particular methodology ensures that every line of code is tested.
- **Refactoring**: This refers to the redesign of the code to remove unnecessary duplication, without altering the existing functionality. Refactoring is undertaken as necessary.

4.2.2 Code Structure

The cardiac and cell-based libraries in Chaste both depend on four core libraries: `mesh`, `pde`, `linalg` and `ode`. This highlights the shared functionality of these two biological applications – a reliance on mesh-constructed geometries, ordinary differential equation (ODE) and partial differential equation (PDE) solvers, and solvers for large linear and nonlinear systems – and the generic design of the framework itself. In turn, these four libraries depend on two low-level libraries: `global` and `io`, which are responsible for initialisation, exceptions, input and output. The code architecture is illustrated in Figure 4.6, which indicates the library dependencies, including the `Crypt` class, which inherits functionality from the `cell-based` class, and which is used to run the cylindrical crypt simulations defined by Meineke et al. [76], Van Leeuwen et al. [123] and Osborne et al. [87]. Two established libraries are implemented to handle large-scale linear algebra and parallelisation, PETSc (Portable Extensible Toolkit for Scientific Computation) and MPI (Message Passing Interface), whilst the `C++` Boost libraries are used for serialization, which allows simulations to be saved, reloaded and then restarted.

The class structure for the cell-based Chaste library is shown in Figure 4.7. Individual classes are assigned to different biological elements of the multiscale framework, such as cell cycle models, cell killers and interactive cell forces. This schematic illustrates how cell-based simulations are constructed, and the relevant class dependencies. The individual

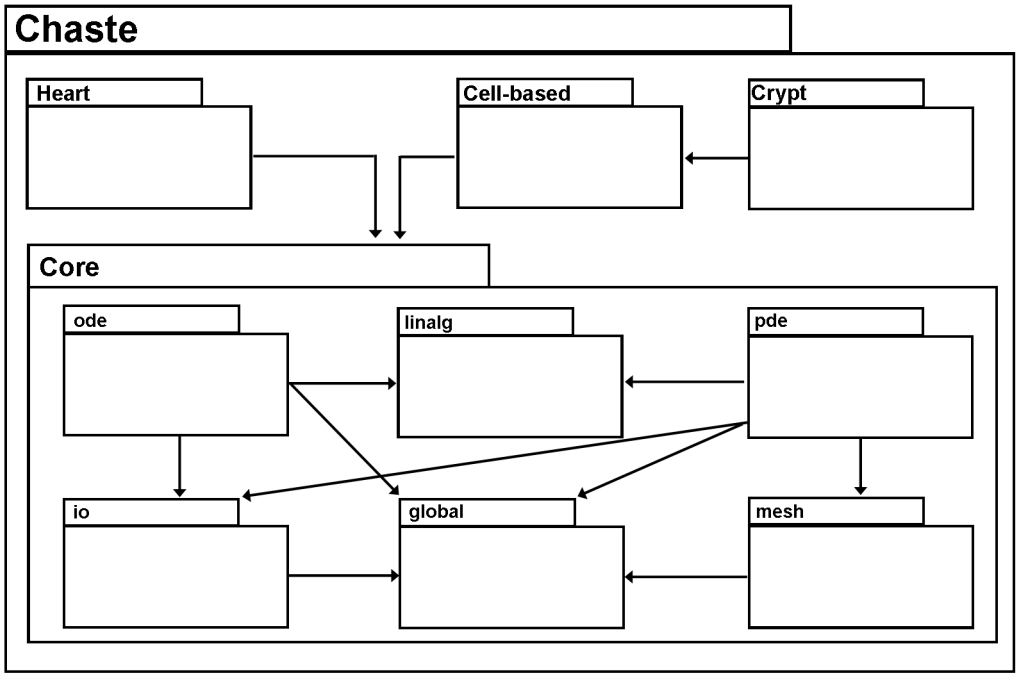

Figure 4.6: The Chaste architecture indicating the six core libraries and dependencies. Drawn according to Pitt-Francis et al. [94].

component folders in this figure also list some examples of the different types of models that can be implemented at each stage.

Constructing a Cell-based Simulation

Following the practice of test-driven development, as outlined above, tests are written for all methods of each class in Chaste to ensure accuracy, and these tests are run nightly to check that any new functionality does not break existing code. As a consequence, simulations themselves are constructed as tests, and in this way future development is made easier for new users and developers by providing a working starting point from which to build extensions. Each cell-based simulation test is composed of the following elements:

1. **A mesh.** Spatial information is stored as a mesh, which is defined subject to the geometry and cell-level model that is required. For example, the `Cylindrical2dMesh` class, which inherits from the general `MutableMesh` class, implements the cylindrical geometry with periodic boundary conditions described in Section 4.1.5. Similarly, `Cylindrical2dVertexMesh` generates the equivalent for the cell-vertex

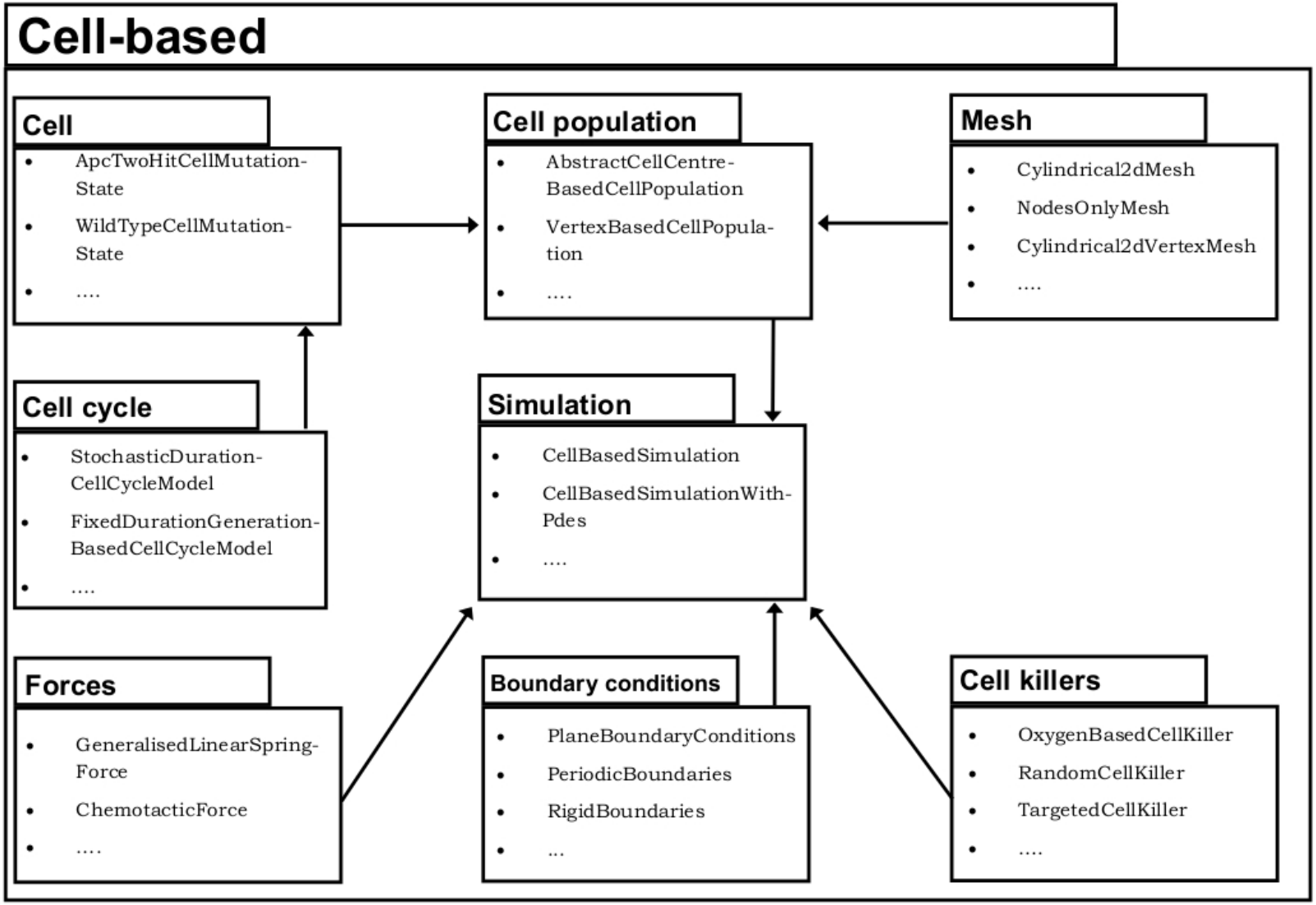

Figure 4.7: The class hierarchy in the cell-based library of Chaste. This illustrates the class dependencies, and gives examples of the different types of cell cycle models, forces, cell killers *etc.* that currently exist within Chaste. The naming convention adopted for all classes within Chaste is designed to be descriptive of what each class does, which helps both users and developers.

model, and inherits functionality from `MutableVertexMesh`. Helper classes exist to generate generic mesh geometries, such as `HoneycombMeshGenerator` and `HoneycombVertexMeshGenerator`.

2. **A collection of cells.** Individual cells are assigned to the real nodes in the mesh, and are allocated a proliferative state, as well as a cell cycle model common to the collection as a whole. Additional cell properties, such as a `WildTypeCellMutationState` or `ApcTwoHitCellMutationState` can be assigned as necessary for the simulation to distinguish between different cell types. Each cell has an associated cell cycle model.

3. **A cell cycle model.** Different cell cycle models exist within the Chaste framework, which range from very simple constant or stochastic time models, such as `FixedDurationGenerationBasedCellCycleModel` and `StochasticDurationGenerationBasedCellCycleModel`, to ODE models that are dependent on spatially varying Wnt profiles, like `StochasticWntCellCycleModel` (which prescribes a threshold below which cells are proliferative, and the cell cycle duration varies stochastically) or `SingleOdeWntCellCycleModel`.

4. **A cell population.** Each cell population is composed of the spatial mesh and collection of individual cells, and is characterised again by the cell-level model. As such, there are separate cell population classes, such as `MeshBasedCellPopulation`, `VertexBasedCellPopulation` and `NodeBasedCellPopulation`. If ghost nodes are included in the simulation, then a `MeshBasedCellPopulationWithGhostNodes` is defined.

5. **A simulation class.** Each simulation class takes the cell population as input, and updates the correspondence between cells at each timestep throughout cell division, movement and apoptosis. Boundary conditions, force laws and cell killer objects are all passed to the simulation. The general `OffLatticeSimulation` class will run an off-lattice 2D or 3D simulation for a cell-centre or cell-vertex population.

6. **Cell forces.** One or more different cell force classes can be passed to the simulation class, which prescribe the mechanical properties of the collection of cells. Examples of force classes that exist within the Chaste framework include `GeneralisedLinearSpringForce` (described in Section 4.1.3), for cell-centre simulations, and `NagaiHondaForce` for cell-vertex simulations (described in Section 3.1.2).

7. **Cell Killers.** The cell killer classes specify conditions under which cells undergo apoptosis. Examples include `OxygenBasedCellKiller`, `TargetedCellKiller` and `RandomCellKiller`.

8. **Boundary conditions.** One or more different boundary condition classes can be passed to the simulation class, such as `PlaneBoundaryCondition`. These allow the specification of various conditions, such as rigid boundaries that cells cannot pass through.

4.2.3 User Projects

Within Chaste, there are individual user projects which inherit functionality from the main trunk of code and enable individual researchers to conduct original research on specific problems. These user projects are not extended throughout the main code iterations, and are not accessed or edited by other members of the Chaste team. In this way, programming within the Chaste framework deviates slightly from the traditional XP approach, which demands pair-programming in all instances of code development. This, however, is not always suitable for the scientific research field which must attribute work to individuals or small groups, for example, to work on a journal article, or for a thesis. Provided users are familiar with the existing code, in this way, Chaste enables such research to be conducted more efficiently, by preventing a researcher from spending time deciphering 'hand-me-down' code (in contrast to an established framework that is well documented), or having to write new code for standard computational problems, such as ODE solvers.

The model development carried out for this thesis has been conducted within a single user project created by the author, with specific details provided in Section 5.2.2. The numerical parameters are discussed in Section 5.5. Specific challenges that were met throughout model development, with regard to interfacing new and existing code in Chaste, are discussed in Section 7.4.1.

4.2.4 A Cylindrical Crypt Simulation

To run a model simulation, the user creates a test which prescribes the requisite elements described in Section 4.2.2. An example of a simple test that can be used to generate the cylindrical crypt model implemented by Van Leeuwen et al. [123] is given in Figure 4.8, which also shows a simulation snapshot from running this test. Firstly, the size of a `Cylindrical2dMesh` is defined, and cells are created accordingly, subject to a `WntCellCycleModel`. This is an ODE-based cell cycle model, with constant M phase duration, which is dependent on a linearly decreasing β-catenin concentration gradient. A threshold is defined at one third of the crypt length, such that cells below this threshold are in the region of sufficient β-catenin, and so are defined to be proliferative (coloured

```
void Test2dCylindricalCryptModel() throw (Exception)
{
    SimulationTime::Instance()->SetStartTime(0.0);
    RandomNumberGenerator::Instance()->Reseed(0);

    // Create mesh
    double crypt_length = 22.0;
    unsigned cells_across = 6;
    unsigned cells_up = 12;
    unsigned thickness_of_ghost_layer = 1;

    CylindricalHoneycombMeshGenerator generator(cells_across, cells_up, thickness_of_ghost_layer);
    Cylindrical2dMesh* p_mesh = generator.GetCylindricalMesh();

    // Get location indices corresponding to real cells
    std::vector<unsigned> location_indices = generator.GetCellLocationIndices();

    // Create cells
    std::vector<CellPtr> cells;
    CryptCellsGenerator<WntCellCycleModel> cells_generator;
    cells_generator.Generate(cells, p_mesh, location_indices, true);

    // Create cell population
    MeshBasedCellPopulationWithGhostNodes<2> cell_population(*p_mesh, cells, location_indices);

    // Create an instance of a Wnt concentration
    WntConcentration<2>::Instance()->SetType(LINEAR);
    WntConcentration<2>::Instance()->SetCellPopulation(cell_population);
    WntConcentration<2>::Instance()->SetCryptLength(crypt_length/3.0);

    // Create crypt simulation from the cell population
    CryptSimulation2d simulator(cell_population);
    simulator.SetOutputDirectory("2dCylindricalCrypt");
    simulator.SetEndTime(100.0);

    // Create a force law and pass it to the simulation
    MAKE_PTR(GeneralisedLinearSpringForce<2>, p_linear_force);
    simulator.AddForce(p_linear_force);

    // Create cell killer and pass it to the simulation
    MAKE_PTR_ARGS(SloughingCellKiller<2>, p_killer, (&cell_population, crypt_length));
    simulator.AddCellKiller(p_killer);

    // Run simulation
    simulator.Solve();

    // Tidy up
    WntConcentration<2>::Destroy();
    SimulationTime::Destroy();
}
```

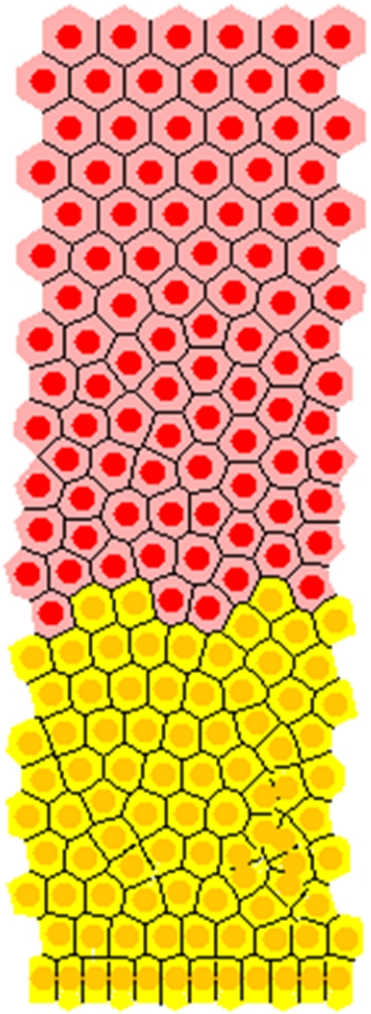

Figure 4.8: An example of a simple crypt simulation in Chaste, and a simulation snapshot showing the cell population after a short time.

yellow in the simulations). Those cells above this threshold do not have sufficient nuclear β-catenin to progress through the cell cycle, and so are defined to be terminally differentiated (coloured pink). A simple cell killer is implemented to remove cells above a certain height, to model the cell sloughing that occurs at the crypt collar.

By changing specific elements of this test, it is possible to vary individual model components and so compare different modelling paradigms. For example, a different cell cycle model could be applied, or a different cell killer could be exchanged or added. In this way, the existing tests which run in Chaste can be used as the foundation for future work, and enable new researchers or developers to quickly and easily incorporate new functionality. For example, a similar test can be used to generate a cell-vertex based simulation. To do this, a `HoneycombVertexMeshGenerator` is used instead of a `HoneycombMeshGenerator`, and a `VertexBasedCellPopulation` would be generated rather than a `MeshBasedCellPopulationWithGhostNodes`.

The structure of tests used to generate simulations of the crypt model proposed in this thesis follow the pattern of those described here. However, it is necessary to define additional forces, and implement alternative models for apoptosis, anoikis and the cell cycle. Changes to the code structure are discussed as appropriate.

4.3 Summary

This chapter has introduced the final building blocks for the new crypt model that is proposed in this thesis: the existing off-lattice cell-centre model which is implemented to govern cell-level behaviour, and Chaste, the computational framework used for model development.

The cell-centre model describes the mechanics of individual interactions between cells – to this, a model of the cell cycle, cell death and a geometry for the cell population must be defined, and with these additional components it is possible to reconstruct the cylindrical crypt model due to Meineke et al. [76] or Van Leeuwen et al. [123]. However, to accomplish the aim of modelling the tissue structure of the crypt more realistically, the role of the surrounding musculature, basement membrane and PCFS must be accounted for. This is considered in the following chapter, which presents a model for a growing, deformable epithelial monolayer. As specified in Section 4.2.3, extensions to the existing Chaste code base have been written in a single user project, and details of this code are also given in Chapter 5. The challenges associated with model development in Chaste are discussed in Chapter 7.

Chapter 5

A Model for a Growing, Deformable Epithelial Monolayer

The goal for this D.Phil. research is to develop a new computational model of the colorectal crypt which incorporates detail at the tissue level, and so accounts for the mechanical influence of the surrounding environment on cell level behaviour, and vice versa. This has been motivated thus far by describing the composition of the connective tissue surrounding the crypts, by demonstrating the interplay between events occurring at the different spatial scales, and by discussing the importance of various environmental factors in cell decision-making. Whilst it is important to understand these interactions under healthy conditions, a full knowledge of this interplay is crucial to understanding the development of CRC, and further, to identify mechanisms that could be targeted to halt the progression of this disease.

The muscularis mucosae, basement membrane and pericryptal fibroblast sheath, introduced in Section 2.1.1, are vital in maintaining the integrity and structure of the epithelial layer that lines the crypt. While the muscularis mucosae appears to follow closely the outline of the base of each crypt, providing support to the base in a manner analogous to an egg in an egg box, the basement membrane functions as both a mechanical support and a physical interface between epithelial cells and the surrounding connective tissue. Beneath this lies the PCFS, a highly organised system of stromal cells thought to be responsible for maintenance of the stem cell niche [132]. To model the tissue structure of the crypts accurately, the combined role of the musculature, PCFS and basement membrane must be taken into account, and this is explored in this chapter in the context of a growing epithelium in a simplified 2D geometry. Once this model is understood fully in a simple geometric framework that permits quantitative analysis, it can be incorporated and extended into the glandular shape of the crypt.

Collectively, the support provided by the muscularis mucosae and the basement membrane is modelled here by an additional force (subsequently referred to as the basement membrane force) that is applied within an off-lattice cell-centre model of cell-cell connectivity, which is described in detail in Chapter 4. An epithelial monolayer is constrained to lie on a bed of stromal cells which approximate the PCFS and loose connective tissue, and the basement membrane is defined to reside between these two regions. *In silico* simulations are conducted in two stages, which focus firstly on the simple, slightly more general, case equivalent to the flat vertical walls of the crypt. These results reveal that the basement membrane force is crucial in maintaining the stability of a monolayer of proliferating cells, and moreover, that cell migration is promoted over cell death provided the basement membrane is sufficiently rigid.

The second stage of investigations focus on the role of the basement membrane and musculature beneath the curved base of the crypt, and results reveal a feedback process by which apoptosis and density-dependent inhibition of mitosis together promote cell migration, which is a new hypothesis of the mechanism of cell movement in this field. Details of the computational intensity of these simulations, as well as simulation movies that are provided on the attached cd, are described in Section 5.5.

The model definition and implementation presented in Sections 5.1 and 5.2, as well as the results shown in Section 5.3, have been published in the Journal of Theoretical Biology [34]. The results presented in Section 5.4 have been published in PLoS Computational Biology, in addition to those presented in Chapter 6, in collaboration with Prof. Inke Näthke, Dr. Paul Appleton and Dr. Scott Nelson at the University of Dundee [33]. In each case, permission has been granted to duplicate the results figures also printed in each of these publications, which were originally generated for this thesis.

5.1 A Model for the Basement Membrane

The model for the basement membrane is defined in this section as a component of a discrete cell-centre model of an epithelial monolayer constrained to grow along a bed of stromal cells, which approximate the connective tissue. Firstly, the geometric domain and accompanying boundary conditions are defined, followed by the mechanisms that govern cell division and apoptosis. These mechanisms are grounded in the biology reviewed in Chapter 2. Two development iterations are considered – firstly, a region where the basement membrane seeks to remain flat, for example along the vertical wall of the crypt, and secondly where the basement membrane is curved, and where the muscularis mucosae

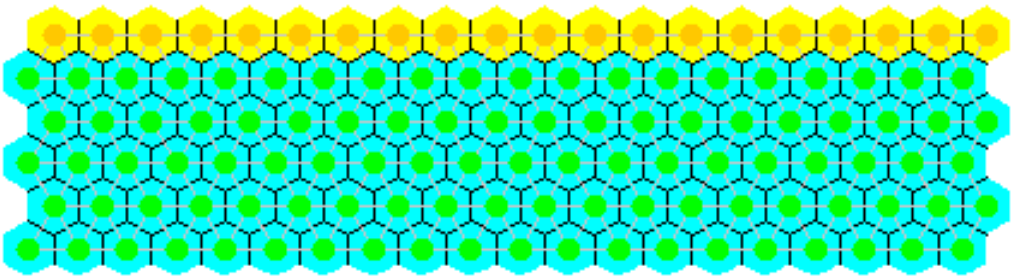

Figure 5.1: The simple 2D configuration defined to investigate growth of a monolayer of proliferating epithelial cells (yellow) attached to a bed of non-proliferating stromal cells (green), which represents a small section of the vertical crypt wall. The Voronoi tessellation, which defines the cell shapes, is indicated in black, whilst the Delaunay triangulation is shown in grey.

extends support at the base of the crypt. Simulation results are presented for both situations, and used to inform parameter estimates for a 2D cross-sectional crypt geometry.

5.1.1 Geometry and Boundary Conditions

Cell centres are defined as nodes which move according to the off-lattice cell-centre model, as described in Section 4.1 [76]. As such, spatial connectivity is determined by a Delaunay triangulation of cell centres, and the corresponding cell shapes are subsequently defined by the dual Voronoi tessellation.

The simple geometry considered at this stage is shown in Figure 5.1, where a section of the crypt wall is represented by a single layer of proliferating cells (yellow) atop a bed of non-proliferating stromal cells (green). As such, the crypt lumen is the space above the layer of proliferating cells, and the connective tissue is approximated as a collection of cells that are connected as described above. The structural properties of the stroma can be altered by varying the interactive cell forces, which in turn define the rigidity and density of the collection of cells. This geometry is chosen to inform understanding of the basement membrane force, and is not yet intended to replicate the crypt geometry itself.

The initial mesh is a block of 20 x 6 nodes, chosen to ensure that there is a sufficient volume of stroma, should major deformation of the epithelial layer occur. This is constructed using a simple, rectangular honeycomb mesh surrounded by a layer of ghost nodes. Rigid boundary conditions are imposed on the vertical walls of the stroma, and the bottom row of nodes – those at the base of the tissue stroma – are held pinned.

5.1.2 Cell Division

The epithelial cells in the monolayer are all proliferative, and divide according to a simple stochastic cell cycle model, which assigns a G_1 phase duration to each cell that is sampled from a Uniform $X \sim U(1,3)$ distribution, following Meineke *et al.* [76]. The remaining phases of the cell cycle are held constant and assigned the following durations so that the cell cycle duration for each proliferating cell is between 11-13 hours [8]: G_2 phase of 4 hours, S phase of 5 hours and M phase of 1 hour. For the purposes of this investigation, the epithelial cells are assigned unlimited proliferative capacity to consider a continuously growing monolayer, whilst stromal cells are assumed to be terminally differentiated, and so do not divide.

To model the directed cell division that arises from planar cell polarity, which was discussed in Section 2.1.3, each cell is instructed to divide according to the relative position of the nearest epithelial neighbours. Two new nodes are created when a parent cell divides, as described in Section 4.1.4, but now these nodes are connected by a spring that lies parallel to the vector that connects the nearest epithelial neighbours of the parent node. In the event that the monolayer is corrupted, which will occur if the epithelial cells do not undergo apoptosis due to a mutant cell property, a dividing cell may have more than two epithelial neighbours. In this situation, the spring that connects the two daughter nodes is assigned a randomly chosen axis.

5.1.3 Anoikis and Cell Sloughing

Anoikis is implemented in the top layer, with an epithelial cell undergoing apoptosis should it lose all connections to the basement membrane, retaining only connections to other epithelial cells in the monolayer. This is determined using the Delaunay triangulation of the cell centres, and an example of two cells undergoing anoikis is shown in Figure 5.2. Once a cell is apoptotic, it is removed from the simulation. Given that, by definition, the epithelial cells connected to an apoptotic cell are also connected to one another, no holes will appear in the monolayer. The implementation of anoikis here is similar to that defined by Galle *et al.* [47], where anoikis is dependent on the contact area between epithelial cells and the substrate below, and cells are removed once the contact area reaches zero.

Further, to model cell sloughing at the crypt collar, epithelial cells that move beyond the ends of the vertical walls of stromal cells are removed from the simulation. These two mechanisms of cell removal are subsequently referred to as anoikis and sloughing respectively.

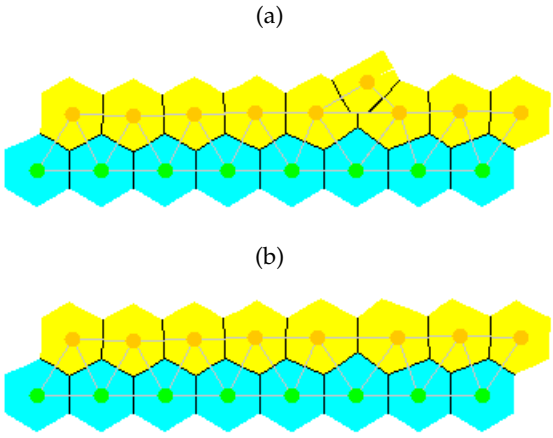

Figure 5.2: An illustrative 'before and after' example of how the Delaunay triangulation is implemented to determine when a cell has lost contact with the underlying basement membrane. (a) An epithelial cell has moved up and out of the monolayer – the Delaunay triangulation (grey) determines that this cell retains connections only to other epithelial cells, and so has lost contact with the basement membrane. (b) After anoikis has been applied, this cell is removed from the simulation and the cell centres are re-meshed.

5.1.4 Cell-Cell Forces

Interactive forces between cells are modelled as linear springs that act along the edges of the triangulation as detailed in Section 4.1.3; consequently, a steady-state distribution of cells is reached in the absence of proliferation. Each spring has rest length s and spring constant μ.

By modifying the spring constant, μ, the magnitude of cell-cell adhesion or repulsion is varied. In reality, both epithelial cells and stromal cells are adherent to the basement membrane, but have no direct connections to each other. However, it is the case that the surrounding tissue implicitly provides support to the epithelial layer, and resists deformation and invasion. In order to invade the surrounding tissue stroma, epithelial cells must secrete digestive enzymes to first break through the basement membrane. To model this, the spring connections between epithelial and stromal cells are defined to exert a force only under repulsion and hence the basement membrane is a physical barrier. In this way, stromal cells do not pull on epithelial cells and the epithelial cells are tightly adherent to the basement membrane by applying a strong force, which is described in Section 5.1.5. The spring constant applied between different types of cells can be varied, and values are chosen to maintain the stability of the layer, as discussed in Section 5.2.

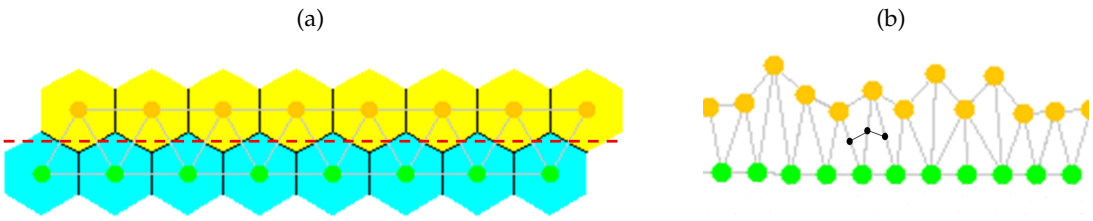

Figure 5.3: (a) The red dashed line indicates the location of the basement membrane, which is defined to pass through the midpoints of the springs connecting neighbouring epithelial and stromal cells. (b) How to calculate the local curvature of the basement membrane: for each epithelial node, the triangulation is used to identify which elements of the mesh are shared between an epithelial and stromal node pair, and the midpoints of the neighbouring springs are taken to form a piecewise linear curve defined by three points. An example is indicated by the lines connecting the three points marked by black circles.

5.1.5 The Basement Membrane Force

The Delaunay triangulation requires that each epithelial cell has at least one connection to the stromal cells surrounding the crypt (otherwise it would be removed from the simulation by anoikis), and each connection is modelled as a spring. The basement membrane, to which both epithelial and stromal cells are connected, is modelled as a piecewise linear curve that passes through the midpoints of these springs, as shown in Figure 5.3(a), which magnifies a portion of the epithelial layer and the top layer of stromal cells. This membrane is not dependent on the Voronoi regions of the individual cells, which are used for visualisation purposes only.

The walls of the crypt column are assumed to remain flat under normal conditions, while the base remains curved, and the epithelial monolayer is maintained. Accordingly, the region of the basement membrane beneath the crypt walls will be flat, which for a smooth, continuous curve corresponds to a curvature of zero. Beneath the crypt base, where additional support is provided by the muscularis mucosae, the basement membrane will be curved, which corresponds to a non-zero curvature.

As the basement membrane is modelled here as a piecewise linear interpolation of the spring midpoints, the discrete equivalent is sought for the curvature, which is hereafter referred to as the discrete curvature. A force is applied which is dependent on the local discrete curvature of the membrane, which acts to maintain the appropriate spontaneous curvature (introduced in Section 3.2.1, this is the curvature that the layer will adopt if allowed to bend freely and independently of any constraints).

For each spring that connects an epithelial cell to a stromal cell, there will be a force acting along that spring according to the signed curvature of the membrane at the spring

midpoint. The discrete curvature is calculated locally, using the Delaunay triangulation to identify which elements of the mesh are shared between an epithelial and stromal node pair, and the midpoints of the neighbouring springs are taken to form a piecewise linear curve defined by three points, as shown in Figure 5.3(b). These points are then used to calculate the discrete curvature parametrically according to the method below, and the restoring force is proportional to this curvature and acts in the direction from the stromal cell centre towards the epithelial cell centre.

The application of this force is similar to the stabilising bending force of Drasdo and Loeffler [31], which is applied to the epithelial cell chain directly to correct for the deviation of a cell away from its spontaneous curvature, to model cell polarity. It is also similar to the bending stiffness considered in the continuum model of Edwards and Chapman [35]. However, these earlier models applied a bending stiffness directly to the epithelial monolayer, rather than modelling the basement membrane explicitly, as is the case here.

Curvature Calculation

The definition of curvature for a smooth, continuous curve is as follows.

Definition 5.1.1 *Let C be a curve defined parametrically by $\mathbf{r}(s) = (x(s), y(s))$, where s is arc length. The signed curvature, $\kappa(s)$, at a point P on C measures the rate of change, $\mathbf{u}'(s)$, of the unit tangent vector, $\mathbf{u}(s)$, at P. Now, $\mathbf{u}(s) = \mathbf{r}'(s)$ and thus*

$$\kappa(s) = \mathbf{u}'(s) = \mathbf{r}''(s)\,. \tag{5.1}$$

In the (x, y) coordinate framework, Equation (5.1) corresponds to

$$\kappa(s) = \frac{x'y'' - y'x''}{(x'^2 + y'^2)^{3/2}}\,, \tag{5.2}$$

where $'$ denotes d/ds. The sign of the curvature indicates in which direction the unit tangent vector rotates as a function of the parameter along the curve. If $\kappa > 0$, then the unit tangent vector rotates anticlockwise, and conversely if $\kappa < 0$, it rotates clockwise.

Equation (5.2) can be used to calculate the local curvature of the basement membrane, and hence to quantify deviation from a spatially-varying spontaneous curvature. This deviation can then be used to determine the restoring force due to the basement membrane. For example, in a model of the crypt, a spontaneous curvature of zero is to be maintained on the vertical walls, such that if an epithelial node moves towards the crypt lumen, then the local signed curvature will be negative and the basement membrane force will act to

pull the node towards the tissue stroma. Conversely, if an epithelial cell moves towards the stroma, then the local signed curvature will be positive and it will be pushed away by the same force. For the curved base of the crypt, a positive spontaneous curvature is applied and the value of the force changes accordingly (this is investigated in Section 5.4).

For the purposes of this model, it is necessary to approximate Equation (5.2) to calculate the discrete curvature at a point $(x_i, y_i) = (x(s_i), y(s_i))$ on a piecewise linear curve defined using the two neighbouring points, (x_{i-1}, y_{i-1}) and (x_{i+1}, y_{i+1}). Now, defining

$$(\Delta s_i)^2 = (x_i - x_{i-1})^2 + (y_i - y_{i-1})^2 \,, \tag{5.3}$$

the positive square root is taken so that

$$s_i = \sum_{j=0}^{i} \Delta s_j \tag{5.4}$$

is strictly increasing. The first and second derivatives are approximated using central differences [112] so that

$$x'(s_i) \approx \frac{x_{i+1} - x_{i-1}}{\Delta s_i + \Delta s_{i+1}} \,, \tag{5.5}$$

$$x''(s_i) \approx 2\left[\frac{\Delta s_i x_{i+1} - (\Delta s_i + \Delta s_{i+1})x_i + \Delta s_{i+1} x_{i-1}}{\Delta s_i \Delta s_{i+1}(\Delta s_i + \Delta s_{i+1})}\right] , \tag{5.6}$$

with similar formulae for $y'(s_i)$ and $y''(s_i)$.

These approximations are substituted into Equation (5.2) to calculate the discrete curvature at a particular spring midpoint. The discrete curvature is then used to calculate a restoring force acting on each epithelial node i subject to each cell j in the set of neighbouring stromal cells N_i:

$$\mathbf{F_i} = \beta \sum_{\forall j \in N_i} (\kappa_{ij} - \kappa_S)\hat{\mathbf{u}}_{\mathbf{ij}} \,. \tag{5.7}$$

Here β is the basement membrane force parameter, which characterises the strength of adhesion of the epithelial layer to the basement membrane and the stiffness of the membrane itself, $\hat{\mathbf{u}}_{\mathbf{ij}}$ is the unit vector from the stromal node j to the epithelial node i, and κ_{ij} is the calculated local discrete curvature for this cell pair. The value of the spontaneous curvature, κ_S, depends on where a particular epithelial cell lies. For the crypt, the domain is divided into two distinct regions, the vertical crypt walls and the semi-circular crypt base. Hence, the spontaneous curvature takes the values

$$\kappa_S = \begin{cases} 1/R, & \text{if } (x_i, y_i) \in \Omega, \\ 0, & \text{otherwise} \,. \end{cases} \tag{5.8}$$

Here $1/R$ is the non-zero spontaneous curvature to be determined by numerical experiment, where R is the radius of curvature, (x_i, y_i) are the coordinates of cell centre i, and Ω corresponds to a region defined by the crypt base.

5.2 Model Implementation

The investigations presented in this chapter focus on the role of the basement membrane force, and the balance of forces that is required to maintain a stable configuration of cells, in order to achieve a realistic model of healthy cell division and migration within the epithelial monolayer. Subsequently it is possible to identify conditions under which the layer might buckle, and what drives this process. Two sets of simulation results are described, each characterised by different spontaneous curvatures being imposed on the basement membrane. In Section 5.3, a spontaneous curvature of zero is applied, which corresponds biologically to the portion of the basement membrane that sits beneath the vertical walls of the crypt. This is extended in Section 5.4 to consider a region of non-zero spontaneous curvature, to model the region of the epithelium at the crypt base. Firstly, however, an outline of the chosen model parameters is provided, in addition to a brief description of how the model simulations are implemented within Chaste.

5.2.1 Parameter Choices

Unless stated otherwise, the parameters used throughout all modelling stages are those listed in Table 5.1. The distances in the model are scaled with cell width (taken to be 10 μm [2, 109]), and time is measured in hours. The equilibrium area of each cell is calculated to be that when the cell population is at steady state, and there are no spring forces acting on the cells, which leads to the hexagonal pattern shown in Figure 4.3. Consequently, the equilibrium area of a cell is defined to be $\sqrt{3}/2\,\text{Cell width}^2$, which is equivalent to 86.6 μm^2.

To generate simulations of a cylindrical crypt using the cell-centre model, Meineke et al. [76] use a single parameter to describe the movement of cells, which is defined as the ratio of the spring strength to the drag coefficient: $\lambda = \mu/\eta$. The value of λ is chosen so as to generate realistic cell movement rates, as if the spring stiffness is too high or the damping too small, then oscillations arise in the springs. Conversely, if the damping is too high or the spring stiffness too small, then the crypt cannot maintain a quasi-steady state, as cell proliferation occurs faster than sloughing. Thus to maintain a steady, realistic flux of cells out of the crypt, within Chaste, $\lambda = 15\,\text{hour}^{-1}$ (equivalently, $\lambda = 1/240\,\text{s}^{-1}$, which corresponds to a mechanics timescale of 240 s).

Experimentally measured parameters have been applied within alternative cell-based models (*e.g.* [31, 47, 73]), but how to compare cell-based models, and thereby to compare the use of such parameter values remains an open question. One approach to this is to use

Parameter	Description	Value	Units	Ref.
μ	Spring strength	15	N Cell width^{-1}	[76]
η	Constant drag coefficient	1	N hours Cell width^{-1}	[76]
s	Equilibrium spring rest length	1	Cell width	[123]
Δt	Timestep	0.0042	Hours	
β	Basement membrane force parameter	see text	N Cell width^{-1}	
κ_S	Spontaneous curvature	see text	Cell width^{-1}	
$1/R$	Non-zero κ_S for crypt base	see text	Cell width^{-1}	
A_0	Equilibrium area of a cell	$\sqrt{3}/2$	Cell width^2	
A_T	Threshold area for cell division	0.5	Cell width^2	

Table 5.1: Unless stated otherwise, the model parameters assume the values given in this table.

a consistent computational implementation, such as Chaste, or alternatively, to compare specific coarse-grained models. Murray et al. [80] provide a method for relating different force laws in cell-based models via the derivation of diffusion coefficients on the continuum scale. By comparing the derived diffusion coefficients for the linear force law applied within the off-lattice cell-centre model and, for example, the Hertz force law that is used in the overlapping spheres model, it is possible to relate how these force laws measure against one another.

As described in Murray et al. [80], for cell number density, q, the diffusion coefficient derived from the linear force law defined by Equation (4.2) is given by

$$D_L(q) = \frac{\mu}{\eta q^2}\,. \tag{5.9}$$

For the Hertz force law (where s is the equilibrium length) the diffusion coefficient is given by

$$D_H(q) = \begin{cases} \frac{3k_H}{2\eta}\frac{(s-1/q)^{1/2}}{q^2}\,, & q > \frac{1}{s}\,, \\ 0\,, & q \leq \frac{1}{s}\,. \end{cases} \tag{5.10}$$

Here, at low cell density, $q \leq \frac{1}{s}$, the cells are at equilibrium and do not exert forces upon one another and correspondingly the diffusion coefficient is zero.

The diffusion coefficients can be used to compare the chosen parameter values in Table 5.1 with those of alternative models from the literature. Assuming sufficiently large cell densities, and by appealing to the binomial theorem, if $D_L = D_H$ in the continuum approximation, then

$$\mu \sim \frac{3k_H\sqrt{s}}{2}\,, \tag{5.11}$$

where the Hertz spring constant, $k_H = 15\,\text{Cell width}^{-1/2}\,\text{hours}^{-2}\,\text{Cell mass}$ [80]. By the values of μ and s in Table 5.1, k_H is a factor of 2/3 smaller than the spring constant applied in the crypt simulations. Differences in the typical cell densities between the models will

contribute towards the difference in these parameters, but overall, this is a reasonable relationship, given that the value of λ, and hence of μ, can be adjusted slightly to account for varying crypt size and cell turnover rates.

5.2.2 Creating Simulations in Chaste

Model simulations are defined in Chaste by creating new simulation, boundary condition, cell killer and force classes. Firstly, a `MutableMesh` is defined with the requisite number of nodes. Epithelial and stromal cells are assigned to these nodes to generate the setup shown in Figure 5.1. To distinguish between epithelial and stromal cells, the proliferative cells in the monolayer are assigned a `WildTypeMutationState`, while the tissue cells are assigned a `StromalCellMutationState` and are colour-coded appropriately in visualisations.

This collection of cells is used to define a `MeshBasedPopulationWithGhostNodes`, which is passed to the simulation class, `TissueSlabSimulation`. In addition to updating the correspondence between cells at each timestep, which necessitates a remeshing step to re-define cell-cell connectivity subject to the forces acting on individual cells, this class coordinates division and apoptosis events. Boundary conditions are specified on this cell population by defining a `TissueSlabRigidBoundaryCondition` and passing this to the simulation class. A new cell killer class, `SloughingAndAnoikisCellKiller`, instructs epithelial cells to undergo apoptosis according to the conditions outlined in Section 5.1.3. The basement membrane force described in Section 5.1.5 is defined in a new force class, `BasementMembraneForce`, while the adhesive and repulsive forces between cells are defined in a second force class, `CellCentreWithVariableCellInteractionForce`, which allows variable adhesion between different cell types. These force classes are passed to the simulation class in a test which compiles all of these elements. Results from simulations of the model described in Section 5.1 are now presented and discussed.

5.3 A Flat Layer: Zero Spontaneous Curvature

The effect of the basement membrane force applied to the initial configuration of cells shown in Figure 5.1(a) is examined when the spontaneous curvature, $\kappa_S = 0$, and so the membrane seeks to be uniformly flat. To produce plots that are indicative of the general behaviour of the model under different conditions, 100 simulations were run for each set of parameters values, and the average results taken. Each simulation was run for a duration of 125 cell hours (*i.e.* on the timescale of the cell cycle and not the computational simulation

runtime), and the results calculated at the final timestep. This ensures that a number of divisions will have occurred for each cell and enough simulations are run to produce results that are indicative of the general behaviour of the system (as averaging more than 100 sets of results does not change what is observed below).

The stochastic nature of the model is due to the cell division events in the proliferating layer, which are determined using the cell cycle model. The pseudo-random number generator used is re-seeded for each simulation to generate a new, independent set of birth events. More specifically, the seed used is unique to the simulation index from 0 to 99, and therefore 100 independent sequences of birth events are chosen and used throughout. This enables identical experiments to be run when varying the parameter of interest, thereby allowing accurate comparison of behaviour for different parameter values.

For $\kappa_S = 0$, the ideal state of the basement membrane is to be flat, and given the simple geometry applied here, the locus of the epithelial cell centres should lie parallel to the x-axis. The flatness of the epithelial layer is described by the metric α, measured as the average gradient of the lines connecting neighbouring cell pairs (the average gap ratio). That is, the modulus of the vertical and horizontal distance between each pair of neighbouring proliferating cell centres is found, the individual ratios calculated and then averaged over all the pairs. So for n cells in the layer, moving in order of increasing x-coordinate, α is given by:

$$\alpha = \frac{1}{(n-1)} \sum_{i=1}^{n-1} \left| \frac{y_{i+1} - y_i}{x_{i+1} - x_i} \right| . \tag{5.12}$$

This gives an indication of how wrinkled the layer is, and ensures that no cancelling occurs between consecutive positive and negative gradients.

5.3.1 Increasing the Basement Membrane Force

Firstly, results are presented that examine the effect of increasing the magnitude of the basement membrane force when the interactive forces between all cells are equal, and hence assigned a spring strength $\mu = 15$ as in Table 5.1. Given that the value of the basement membrane force changes for each cell at each timestep, as it depends on the local curvature, these plots indicate changes with β. To emphasise the quantitative behaviour of this system, the value of the basement membrane force is typically one quarter of the magnitude of the linear spring forces acting between cells.

Figure 5.4(a) plots the average horizontal (solid line) and vertical (dashed line) distance between neighbouring pairs of epithelial cells against β, which are combined to show the

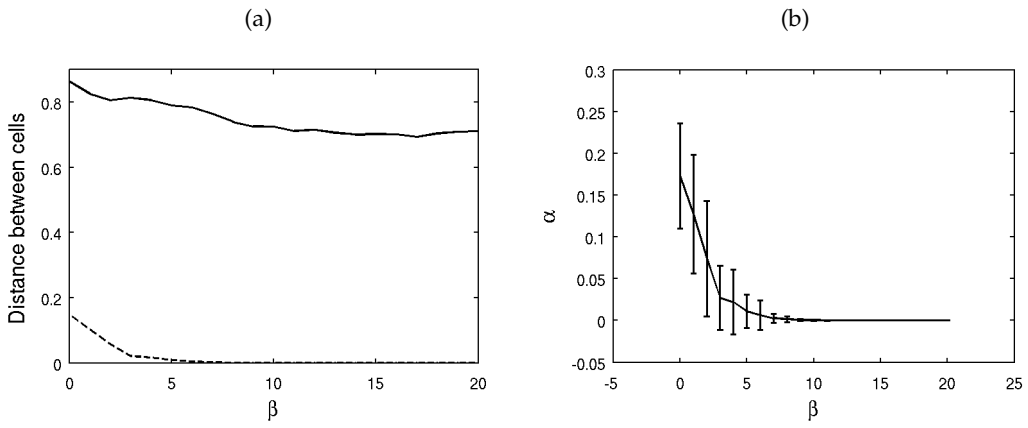

Figure 5.4: Two plots showing how increasing the basement membrane parameter, β, influences: (a) The average horizontal (solid line) and vertical (dashed line) distance between neighbouring epithelial cells. (b) The average gap ratio, α, between neighbouring epithelial cells, where the error bars indicate the standard deviation for each value of β. This ratio decreases as β increases, and for $\beta \geq 10$, $\alpha \approx 0$, because the vertical distance between neighbouring epithelial cells is approximately zero. Hence the layer can be described as flat.

change in the average gap ratio, α, in Figure 5.4(b). Note that these distances are scaled with the equilibrium cell width and hence are non-dimensional. These plots show that as β increases, both the horizontal and vertical distances between neighbouring epithelial cell centres decrease. The consequence of this is seen clearly in the decrease of α, which is approximately zero for $\beta \geq 10$, and hence the layer is flat when a sufficiently high basement membrane force is applied.

Figure 5.5 illustrates this behaviour by comparing two snapshots from simulations: Figure 5.5(a) corresponds to $\beta = 0$ and Figure 5.5(b) corresponds to $\beta = 15$. These snapshots show that the layer is completely flat for $\beta = 15$, whereas it is wrinkled and cells are being forced out of the layer when $\beta = 0$, eventually to undergo apoptosis by anoikis. (Simulation movies 1 and 2, provided on the attached CD, correspond to these two cases as described in Section 5.5.)

Figure 5.6(a) plots the total number of epithelial cells in the monolayer, which increases as β increases. This is in accordance with the decreasing horizontal gap between neighbouring cells shown in Figure 5.4(a). Figure 5.6(b) plots the total number of cells removed both by anoikis and by sloughing at the edges over the course of the simulation. When $\beta = 0$, the proliferating epithelial cells are quickly and easily pushed upwards, losing contact with the stromal cells below, and so are removed by anoikis. However, as β increases, the number of cells undergoing anoikis decreases from approximately 140 to less than 10. This result shows that the basement membrane force plays a key role in preventing detachment of the epithelial cells by correcting the bending in the layer that causes cells to move upwards.

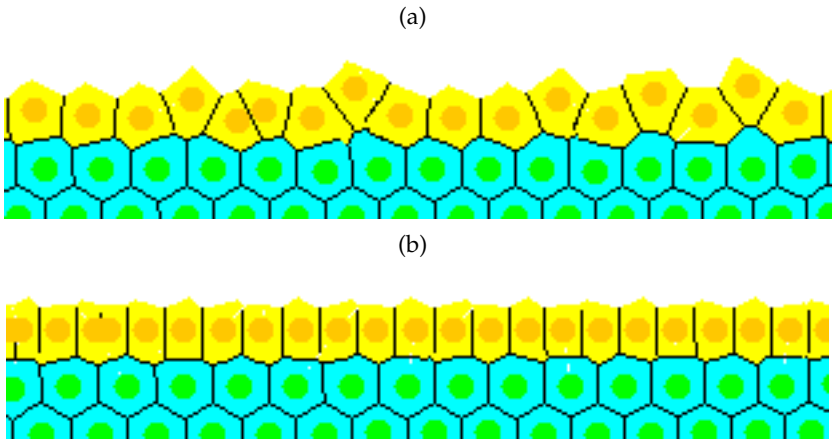

Figure 5.5: Snapshots taken from simulations to show the typical behaviour for (a) $\beta = 0$, (b) $\beta = 15$. The images have been cropped to highlight the behaviour of the monolayer.

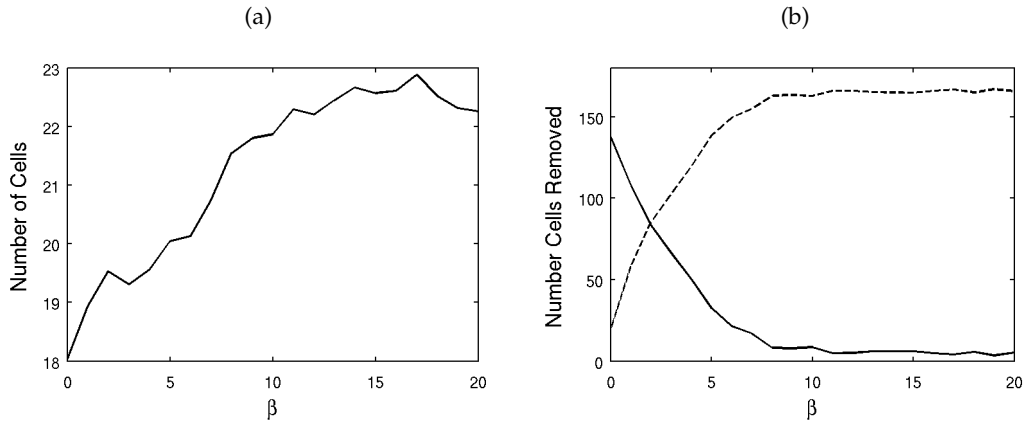

Figure 5.6: Increasing the basement membrane parameter, β: (a) The total number of epithelial cells at the final timestep, averaged over all simulations. (b) The total number of epithelial cells removed by the mechanisms of anoikis (solid line) and cell sloughing (dashed line), averaged over all simulations. This shows that as β increases, the number of cells removed by anoikis decreases, whilst the number removed by sloughing increases. The latter of these results is important with regards to migration along the epithelial layer.

The opposite behaviour is observed for the number of cells that are removed by sloughing at the edges – this total increases from approximately 20 to 160. This reveals a marked change in the dynamics of the system, whereby the extent of cell migration increases as β increases, rather than cells being simply forced upwards and out. The basement membrane force acts to keep the cells aligned horizontally in the monolayer, and the repulsion due to the interactive cell-cell forces causes the cells to push their neighbours outwards, whereupon sloughing occurs. Thus it is demonstrated that the basement membrane force plays a key role in the model, to favour horizontal migration of the proliferating cells, and to prevent cell detachment from the stromal layer by correcting unwanted bending. Together with Figure 5.4, these results indicate that a basement membrane force parameter of $\beta \geq 10$ is required to maintain such a stable, flat layer while epithelial cells migrate and few cells are removed by anoikis.

5.3.2 Varying Interactive Cell-Cell Forces

While the layer remains flat for $\beta \geq 10$, the average horizontal distance between epithelial cells decreases as β increases, so that the cells are positioned closer together. This is because increasing the strength of the basement membrane force increases the adhesion of epithelial cells to the virtual basement membrane, and above a particular threshold, this adhesion will impede migration. For the cells to move towards a state of equilibrium the springs should be at, or tending to, the natural rest length, which is 1 cell width. It is therefore important to investigate the effect of varying the spring strength parameters, to ascertain if it is possible to achieve a state closer to that of equilibrium.

For a fixed value of $\beta = 12$, the effect of increasing the ratio of spring strengths between neighbouring epithelial cells (E-E) to neighbouring stromal cells (S-S) is investigated, and this ratio (E-E / S-S) is now represented by the parameter μ_{ES}. For increasing μ_{ES}, Figure 5.7(a) shows the change in the average horizontal and vertical distance between neighbouring epithelial cells, Figure 5.7(b) shows how the average gap ratio α changes, Figure 5.7(c) shows how the total number of epithelial cells at the final timestep (125 hours) changes, and Figure 5.7(d) shows the number of cells that are removed by anoikis and sloughing. These results should be compared with those in Figures 5.4 and 5.6.

Firstly, from Figure 5.7(a), the horizontal distance between the epithelial cells increases as μ_{ES} increases, and the vertical distance remains close to zero. This coincides with a reduction in the total number of cells in the layer (see Figure 5.7(c)). As shown in Figure 5.7(b), when the strength of the E-E springs is weaker than that of the S-S springs

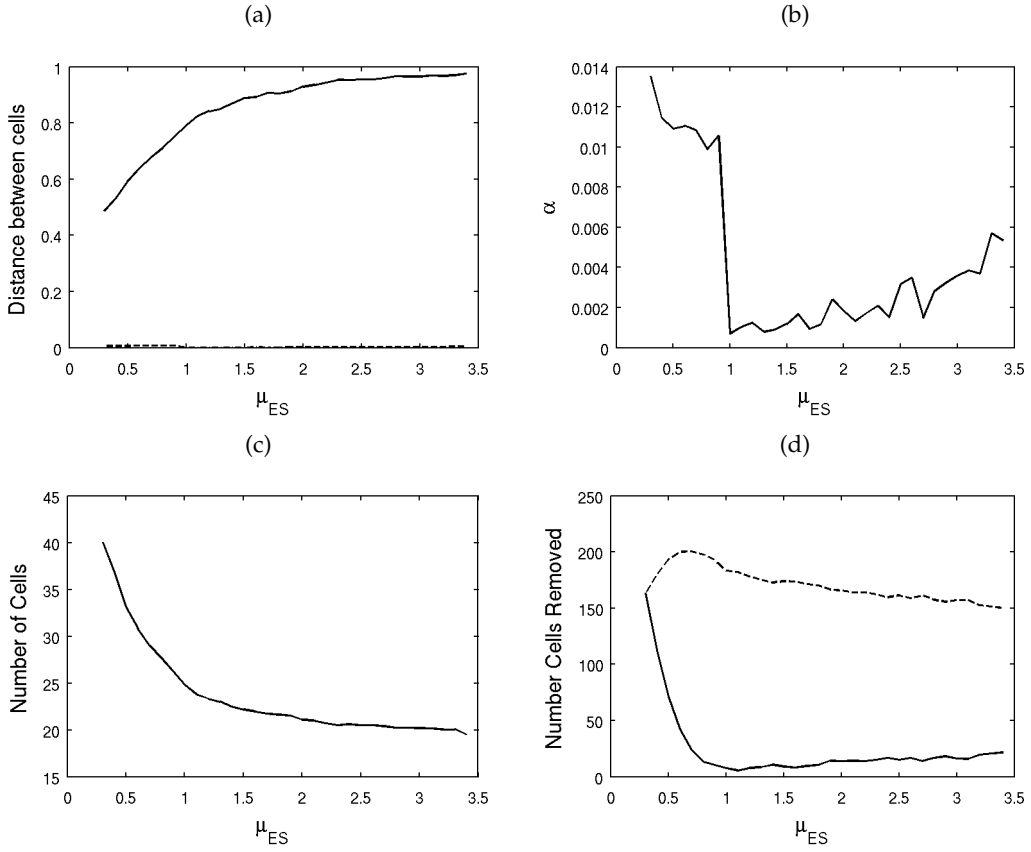

Figure 5.7: A series of plots that demonstrate the effect of increasing the E-E/S-S spring strength ratio, μ_{ES}: (a) The average horizontal distance (solid line) and vertical distance (dashed line) between neighbouring epithelial cells; (b) the average gap ratio, α; (c) the total number of epithelial cells at the end of the simulation; (d) the total number of epithelial cells removed by anoikis (solid line) and sloughing (dashed line) at the edges.

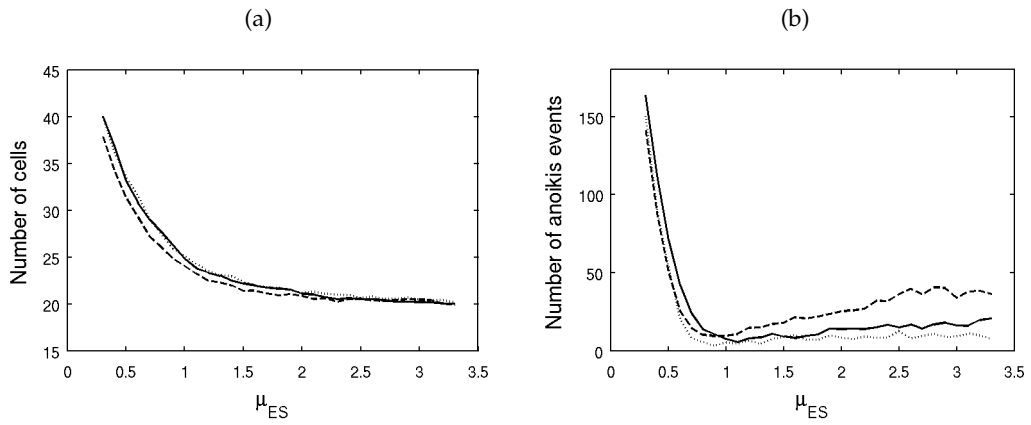

Figure 5.8: Increasing μ_{ES} and comparing increasing values of β: $\beta = 8$ (dashed line), $\beta = 12$ (solid line), $\beta = 16$ (dotted line). (a) The total number of epithelial cells at the end of the simulation; (b) the total number of epithelial cells removed by anoikis.

($\mu_{ES} < 1$), the average gap ratio α is larger than when the E-E springs are stronger. As the E-E spring strengths increase ($\mu_{ES} > 1$), the horizontal distance between cells increases due to the stronger repulsive force when cells are under compression.

However, given the results in Figure 5.7(d), when $\mu_{ES} > 2$, such that the springs are tending to the natural spring length, it is observed that sloughing is decreased while anoikis is increased. Hence, excessively strong interactive forces between epithelial cells hinders migration. Despite this, the results suggest that increasing the spring strength between pairs of epithelial cells to a factor of 2.5 times that of other springs will yield cells with natural sizes (such that the spring lengths are close to the equilibrium value), without overly compromising the extent of cell migration. (Movie 3, on the attached CD, corresponds to the case where $\beta = 12$ and $\mu_{ES} = 2.5$, as described in Section 5.5.)

The results shown in Figure 5.8 compare the total number of epithelial cells and anoikis events as μ_{ES} is increased, for $\beta = 8, 12, 16$. This shows that the results are consistent for different values of β.

The effect of varying the ratio of spring strengths between epithelial and stromal cells and those connecting neighbouring epithelial cells (E-S/E-E), represented by the parameter μ_{ESE}, is shown in Figure 5.9. From these results, it is clear that increasing μ_{ESE} has negligible effect on cell movement. Figure 5.9(a) shows that the horizontal and vertical separation between cells remains approximately constant, and Figure 5.9(b) shows that the change in α is negligible. Similarly, the change in the average number of cells in the layer is less than 2, and the total number of anoikis and sloughing events remain approximately constant. These results occur because the E-S springs only exert forces under repulsion.

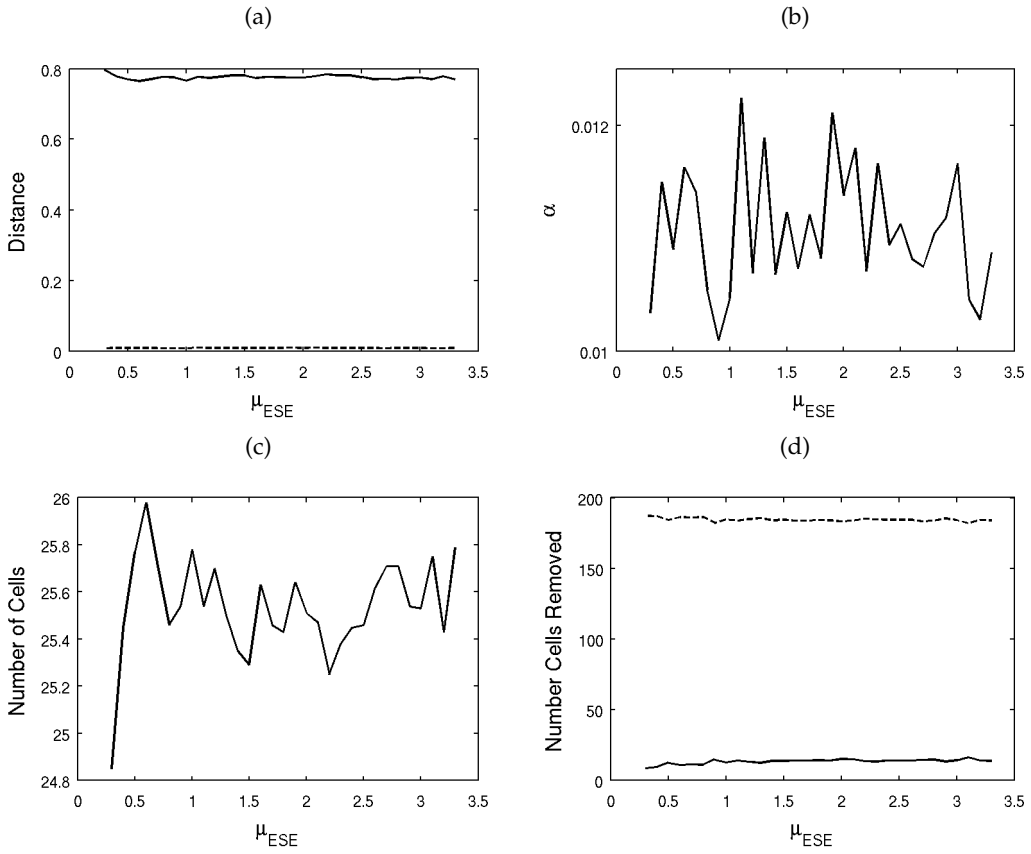

Figure 5.9: Increasing the E-S/E-E spring strength ratio, μ_{ESE}, where the results are calculated at the end of the simulation (t = 125 hours): (a) The horizontal gap (solid line) and vertical gap (dashed line), averaged over all pairs of neighbouring epithelial cells; (b) the average gap ratio, α; (c) the total number of epithelial cells at the final timestep; (d) the total number of epithelial cells removed by anoikis (solid line) and sloughing (dashed line) at the edges.

5.3.3 Hyperproliferation

As described in Section 2.2, inactivation of the APC tumour suppressor gene is one of the initiating events in CRC [17, 41, 55]. It is observed experimentally that one downstream effect of the loss of APC is an increase in proliferation, either through an increased proliferative capacity for individual cells, or an enlarged proliferative compartment [83, 104]. By reducing the cell cycle time for each cell in the monolayer, it is possible to investigate a form of hyperproliferation in this model and observe what effect, if any, this has on the integrity of the tissue structure. Figure 5.10 plots the corresponding results to Figures 5.4 and 5.6, where the duration of each phase of the cell cycle is reduced and now chosen from a Uniform $X \sim U(3, 5)$ distribution, such that on average cells divide three times as often as before. For comparison, the results for normal cell division conditions are also shown (in blue), where the cell cycle duration is sampled from a Uniform $X \sim U(11, 13)$ distribution.

Figure 5.10(a) shows that the horizontal distance separating neighbouring cells decreases as in Figure 5.4(a), but the decrease is greater under these new conditions, such that the cells are more closely packed in the monolayer and the average horizontal separation is approximately 0.5 for $\beta \geq 10$. Accordingly, the total number of epithelial cells in the layer increases to over 30, as shown in Figure 5.10(c), which is a marked increase over that for conditions of normal proliferation. The vertical separation also decreases, but at a slower rate than under normal conditions. When these results are combined in Figure 5.10(b), α does not decrease as sharply, and is always greater than in the regular case shown in Figure 5.4(b). This implies that the layer is more wrinkled, and never attains a purely flat state with this chosen rate of proliferation.

Figure 5.10(d) shows a major difference in the number of cells removed by anoikis and by sloughing – in each case the number of cells removed by each method has increased greatly from simulations run under normal conditions. As β increases, the total number of cells removed by anoikis decreases from approximately 400 to 350, while those removed by sloughing increases from approximately 50 to 450. A switch in behaviour has occurred; before, fewer cells were removed by anoikis as β increased. Now it is the case that the total number of anoikis events levels out at a much higher value, so that both cell removal mechanisms are employed as the layer seeks to attain a state of equilibrium. This behaviour is due to the increase in the number of cells in the layer, which leads to more birth events, and subsequently the need to remove a greater number of cells. These results could also indicate that increased cell death could be observed in early CRC.

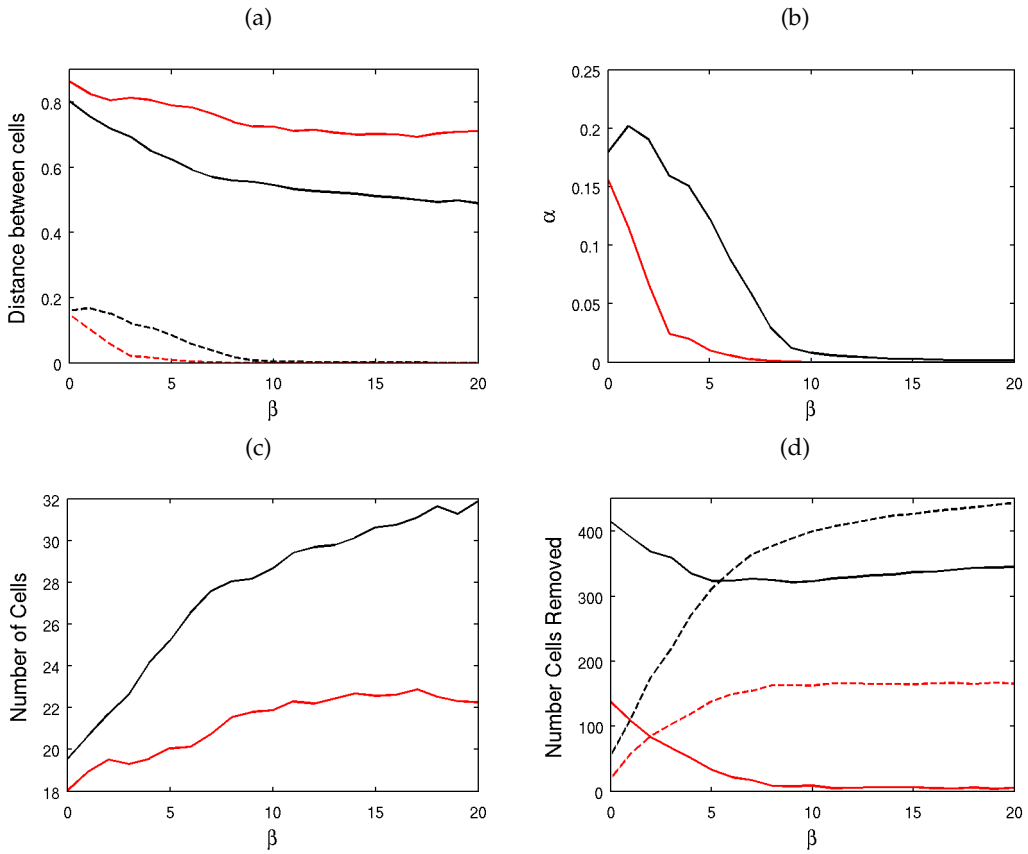

Figure 5.10: A series of plots comparing the results already shown for normal cell division, with those for hyperproliferative conditions. This is achieved by reducing the cell cycle duration from a Uniform $X \sim U(11, 13)$ distribution (red curves) to a $X \sim U(3, 5)$ distribution (black curves). (a) The average horizontal distance (solid line) and vertical distance (dashed line) between neighbouring epithelial cells; (b) the average gap ratio, α; (c) the total number of epithelial cells at the final timestep; (d) the total number of epithelial cells removed by anoikis (solid line) and sloughing (dashed line) at the edges.

The results presented above suggest that a simple increase in the rate of cell division within the crypt does not simply lead to an increase in migration, but rather increases the vulnerability of the layer to buckling due to the high number of cells in the layer, as found by Edwards and Chapman [35]. This is consistent with the predicted increase in anoikis events, the total number of which is greater than for normal cell division events. Consequently, should excessive cell division be coupled with failed apoptosis cues, then rapid hypertrophy would result, disrupting the tissue architecture. (Movie 4, on the attached CD, shows an example of the monolayer evolving under hyperproliferative conditions, as described in Section 5.5.)

5.3.4 Summary

The results presented thus far have examined the consequence of applying the basement membrane force with a zero spontaneous curvature. As such, the aim has been to consider a proliferating layer of epithelial cells constrained to lie on a bed of stromal cells, and under healthy conditions for cell division to stimulate in-plane migration to ensure that the monolayer remains flat. Thus result, the model outlined in Section 5.1 has been studied with $\kappa_S = 0$, and the following behaviour observed.

The results show that the basement membrane force is crucial in maintaining the stability of the monolayer of proliferating cells. As expected, the larger this force is, *i.e.* as β increases, the flatter the layer remains and fewer cells detach from the underlying stroma. This highlights the potential for exploiting anoikis as a complementary mechanism with which to control the system. Specifically, results show that $\alpha \approx 0$ for $\beta \geq 10$, which corresponds to the level of rigidity and adherence of epithelial cells to the basement membrane which is required to keep the monolayer flat and prevent wrinkling.

These results are in agreement with those found by Galle et al. [47], who proposed a biophysical 3D agent-based model to examine cell growth regulation and control for epithelial monolayers. The results of this 3D model found few anoikis events occurred when cell-substrate adhesion was high – this is equivalent to the lower incidence of anoikis events when the basement membrane force is strong for the model proposed in this chapter. Unlike Galle et al. [47], however, the role of density-dependent inhibition of mitosis, introduced in Section 2.1.3, has not yet been considered. This is addressed in Section 5.4.5.

In conjunction with the basement membrane force, the strength of the interactive forces between neighbouring proliferative cells influences the inter-cell spacing – these forces combine the attraction caused by adhesion molecules in the cell membranes, and the

repulsion caused by the limited compressibility of each cell. The Delaunay triangulation, and the implementation of anoikis, ensures that epithelial cells retain connections to the basement membrane, as well as to their immediate neighbours. The results show that for high values of the basement membrane force parameters, stronger forces between neighbouring cells are required to prevent overcrowding, and under these conditions the monolayer tends towards a state of equilibrium, where the cells tend towards their natural sizes. There is, however, a limit to the spring strength above which a higher number of cells are removed by anoikis, and the rate of cell migration decreases. Further, the results show that to prevent this and to maintain homeostatic dynamics, it is required that the spring strength ratio $\mu_{ES} \leq 2.5$ for a basement membrane parameter value $\beta = 12$. The high basement membrane parameter ensures that bending is counteracted to keep the layer flat, while the strength of the forces between neighbouring epithelial cells is increased enough to prevent overcrowding.

A simple experiment to investigate the consequences of increased cell proliferation shows that the layer is more likely to be corrupted under such conditions, as α does not decrease as sharply as under normal proliferative rates, and does not reach zero as before. This implies that the layer is wrinkled, and never attains a purely flat state with this chosen rate of proliferation. Results also show that both cell removal mechanisms are employed as the layer seeks to attain a state of equilibrium, and this is especially important in light of failed apoptotic cues that can characterise cancerous cells, prolonging survival in the absence of matrix attachment [52]. As shown by Galle et al. [47], loss of anoikis can lead to additional layers forming above the initial epithelial monolayer, particularly in conjunction with a loss of anchorage-dependent growth.

Given that the biological context for this work is a model of the crypt with a realistic geometry, and the basement membrane force has now been shown to be effective, the next step is to consider the region of the crypt where the basement membrane has a supported, positive curvature, *i.e.* the crypt base. Investigations concerning this portion of the basement membrane are considered below.

5.4 The Curved Base: Non-Zero Spontaneous Curvature

The results presented in Section 5.3 demonstrate the effect of the basement membrane force when the spontaneous curvature is defined to be zero, which is geometrically equivalent to the straight portions of the crypt walls. By increasing the spontaneous curvature, it is possible to define a curved region that corresponds to the base of the crypt. As described in

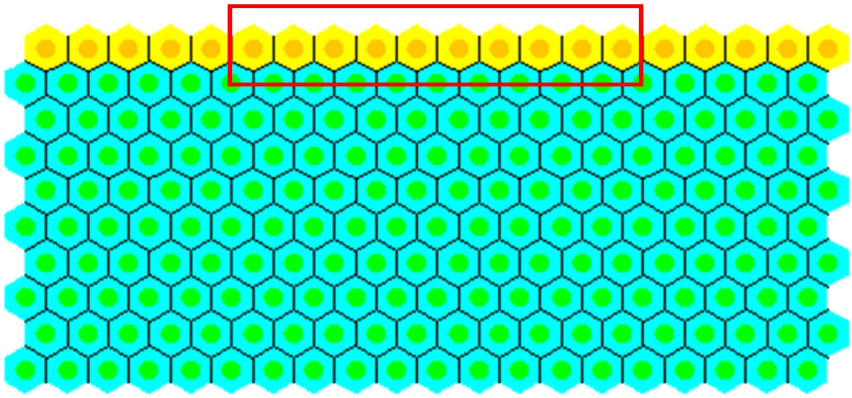

Figure 5.11: The top row of yellow cells are the proliferating epithelial cells, while the green cells are the non-proliferating stromal cells. The region of the basement membrane highlighted by the red rectangle is assigned a non-zero spontaneous curvature, $1/R$, and corresponds to Ω in Equation (5.8), while the remainder outside this region is assigned a zero spontaneous curvature.

Section 2.1.1, the muscularis mucosae sits directly beneath the epithelial layer of the crypt, separated by the basement membrane, and forms a continuous network that follows the contours of the crypt bases. The support provided is analogous to an egg box, where each crypt base assumes the role of an egg. Before describing simulation results for $\kappa_S > 0$, the changes to the model that are necessary for this extension are outlined.

A region of non-zero spontaneous curvature is defined in the centre of the basement membrane, equal to half the length of the epithelial monolayer, between two regions of zero spontaneous curvature, as shown in Figure 5.11. This is a 10 x 20 rectangular array of cells similar to the geometry shown in Figure 5.1, where the red rectangle encloses the central region where $\kappa_S = 1/R$ (see Equation (5.8)). The number of layers of stromal cells has increased to allow for deformation that will occur as the epithelial layer bends downwards.

Periodic boundary conditions are imposed on the vertical walls of the block to model the continuous epithelial layer that lines neighbouring crypts, such that the monolayer experiences a force that mimics epithelial cells meeting at the intercrypt table. In Chaste, this is modelled by defining a `Cylindrical2dMesh` instead of a `MutableMesh`. Consequently, cell sloughing no longer occurs beyond the edges of the stromal block. Rather, anoikis is implemented throughout the layer and is the only mechanism of cell death until random apoptosis is introduced in the outer regions of the epithelial layer in Section 5.4.6.

Simulations are run to determine the optimal parameter balance for the portion of the basement membrane that supports the base of each crypt. Unless stated otherwise, each

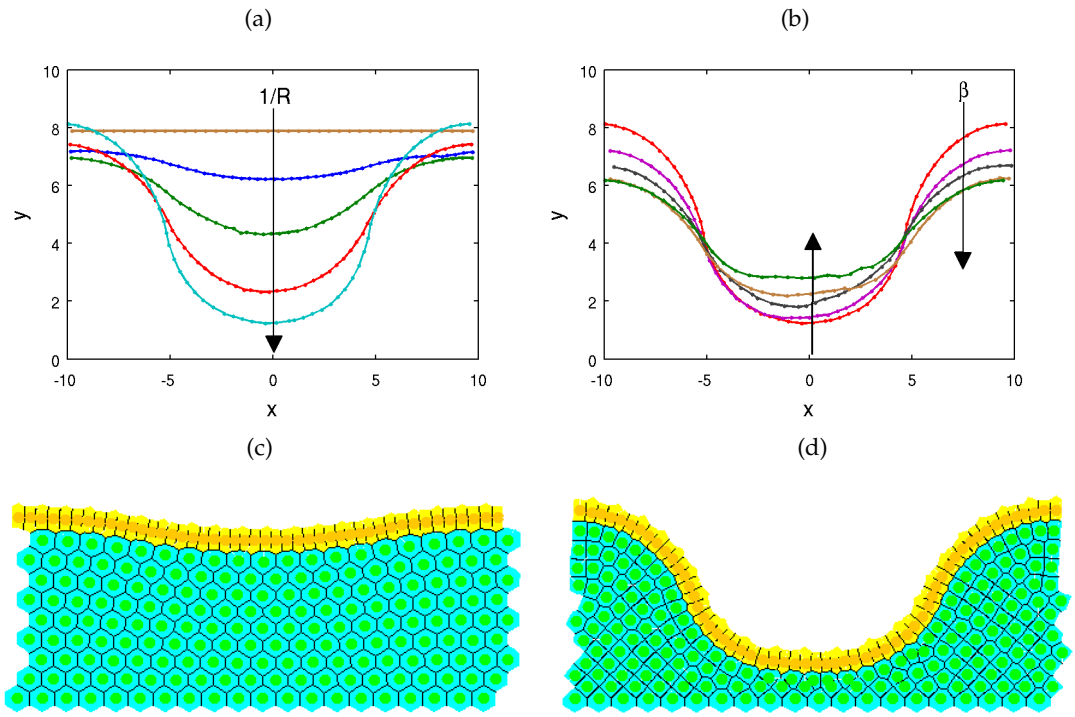

Figure 5.12: The evolution of the epithelial layer, where the (x, y)-coordinates of each epithelial cell are plotted after 60 hours. (a) $\beta = 12$, increasing $1/R = 0, 0.1, 0.2, 0.3, 0.4$ (indicated by the arrow); (b) a comparison of the final state of the epithelial layer when $1/R = 0.4$ for increasing $\beta = 12, 14, 16, 18, 20$ (indicated by the arrows). (c) A simulation snapshot showing the deformation of the epithelial monolayer and stromal cells when $\beta = 12$ and $1/R = 0.1$, (d) $\beta = 12$ and $1/R = 0.4$.

simulation is run for a total of 60 cell hours, beyond which the epithelial layer has reached a state of equilibrium and does not deform further. All parameters are given in Table 5.1.

5.4.1 Increasing the Spontaneous Curvature

Firstly, *in silico* experiments were run to determine the effect of increasing $1/R$, the spontaneous curvature in the central region, and β, the strength of the basement membrane force. The plots in Figure 5.12(a) and (b) illustrate the change in behaviour of the monolayer by plotting the (x, y)-coordinates of all epithelial cells at the final timestep ($t = 60$ hours) for typical simulations. Figure 5.12(c) and (d) are simulation snapshots that illustrate two different cases – firstly, for $1/R = 0.1$, and secondly for $1/R = 0.4$.

Model simulations reveal that as $1/R$ increases, the epithelial monolayer is pushed further down into the tissue stroma as the central portion of the monolayer bends. This behaviour is demonstrated clearly in Figure 5.12(a), where $\beta = 12$ and the arrow indicates the direction of increasing spontaneous curvature. It is also observed that increasing $1/R$ decreases the

radius of the circle that can be extrapolated from the arc length of the layer – this is as expected.

As the basement membrane force increases, a stronger force acts on the outer edges to maintain a zero curvature, preventing these regions from bending to compensate the deformation of the region of non-zero curvature. This is illustrated in Figure 5.12(b), where $1/R = 0.4$ and the effect of increasing β is indicated by the arrows. This plot shows that as β increases, the outer edges flatten and are pushed further down into the stroma. Accordingly, there is less distinction with the crypt base region, and the central portion of monolayer is not pushed down as much.

Figure 5.13 shows how, for a fixed value of $1/R$, the total number of epithelial cells in the layer at the final timestep changes as β varies, where these results are averaged over all 50 simulations for each β. This plot reveals that the number of epithelial cells in the layer decreases as β increases. This is in contrast to the result obtained when $\kappa_S = 0$ uniformly across the monolayer (see Section 5.3). In the simpler case, the number of epithelial cells increases as β increases, because the basement membrane force prevents detachment of the epithelial cells by correcting the bending in the layer that leads to cells moving upwards. However, by introducing a non-zero curvature region, cells are more vulnerable to moving out of the layer and so can be be removed by anoikis more easily. As β increases, the shape of the layer changes due to the junction between the regions of zero and non-zero spontaneous curvature (as shown in Figure 5.12(b)). It is this shape change, and the corresponding decrease in the overall arc length of the layer, which alters the total number of epithelial cells. To relate this to the biology of the layer, it is necessary to know more about the variability in the rigidity of, and the adhesion of epithelial cells to, the basement membrane.

5.4.2 Increasing Cell-Cell Interaction Forces

In Section 5.3, the strength of the adhesive and repulsive forces between cells, which increase and decrease as the spring constant μ is varied, are shown to be crucial to prevent overcrowding in the flat epithelial monolayer. Specifically, increasing the ratio of the spring constant between epithelial-epithelial connections to stromal-stromal connections (μ_{ES}) allows the cells to maintain natural sizes (the spring lengths are close to, or at, equilibrium) without compromising cell migration along the layer. This can be observed as the number of cells in the monolayer decreases. The effect of increasing this ratio is

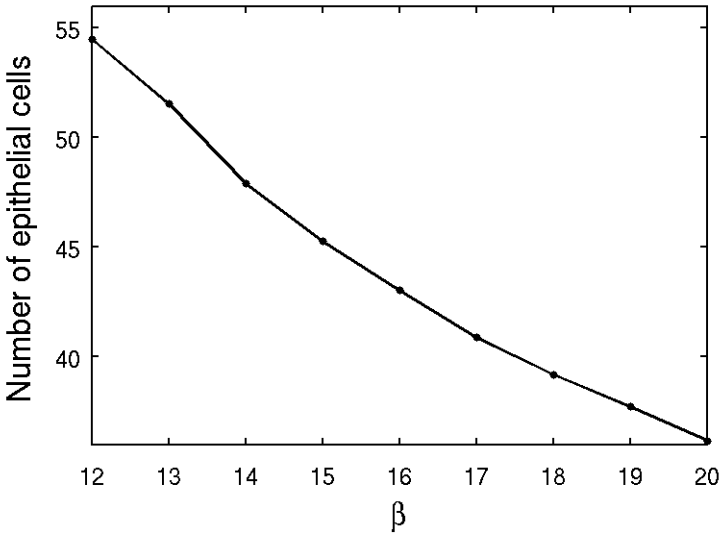

Figure 5.13: The total number of epithelial cells in the monolayer for $1/R = 0.4$, and increasing β.

investigated here under conditions of non-zero spontaneous curvature, and the results are shown in Figure 5.14(a) for $1/R = 0.4$, $\beta = 12$.

Increasing the spring strength between epithelial cells markedly reduces the extent to which the layer is deformed. This occurs because the cell-cell forces dominate over the basement membrane force, preventing full deformation to the spontaneous curvature. Further, the number of epithelial cells within the layer (which increases as the layer deforms from the initial flat state until reaching a steady state) is higher for larger μ. This is shown in Figure 5.14(b), which plots the number of epithelial cells at each time step for increasing μ, averaged over 50 simulations. This arises as a consequence of the reduced curvature of the layer, which in turn causes fewer anoikis events. The larger the curvature of the layer, the more vulnerable epithelial cells are to popping out of the layer, and so this effect is countered by the dominant cell-cell interaction forces.

5.4.3 Extending to the Crypt Geometry

Figure 5.15 illustrates how it is possible to deform an initially flat epithelial monolayer to adopt a configuration analogous to the test-tube shaped geometry of the crypt as viewed in cross-section. To achieve this, a non-zero spontaneous curvature region is defined in the centre of the monolayer, equal to 20% of the width of the tissue block. It is also necessary to increase the size of the stromal cell compartment, as well as define a sufficiently wide epithelial monolayer. The layer is fully deformed after approximately 100 cell hours. This

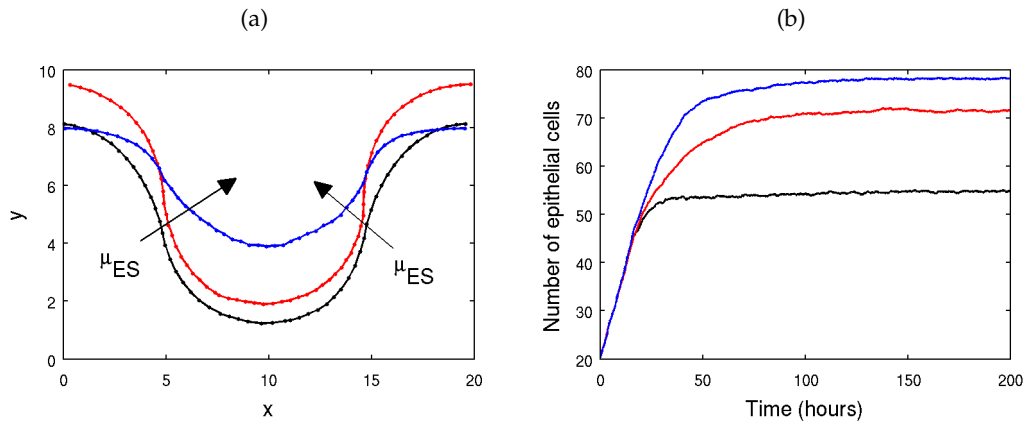

Figure 5.14: (a) Plotting the (x, y)-coordinates of the epithelial cells after 60 hours, where the arrow indicates the direction of increasing $\mu = 15, 30, 45$. (b) Plotting the number of epithelial cells in the layer over time, averaged over 50 simulations. In both plots $\mu = 15$ (black), 30 (red), and 45 (blue).

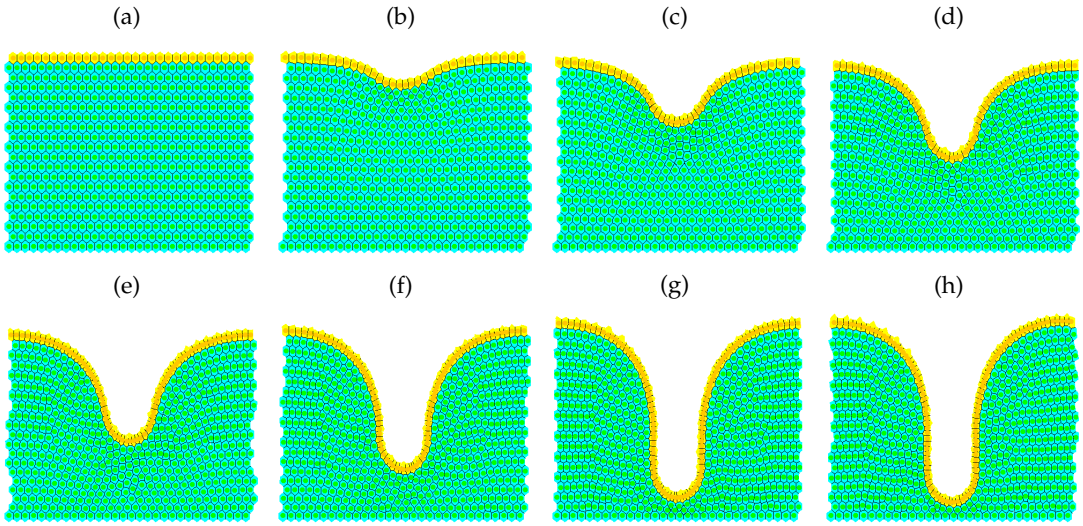

Figure 5.15: Deforming an epithelial layer to adopt the test-tube shape of the crypt, as viewed in a cross-section. To do this, it is necessary to define a wide enough epithelial monolayer, and include a sufficient number of layers of stromal cells.

is the discrete equivalent of the model proposed by Nelson et al. [85]. (Movie 6, on the attached CD, illustrates this as described in Section 5.5.)

The following investigations in Sections 5.4.4 – 5.4.6 focus on the geometry as it is presented in Figure 5.11, to investigate cell migration along a continuously growing epithelial monolayer from the non-zero spontaneous curvature region towards the zero spontaneous curvature region. This is chosen to increase the run time of simulations, as fewer cells are required, and the model behaviour is unchanged from the case shown in Figure 5.15. A cross-sectional crypt configuration is considered specifically in Chapter 6, but is instead started from an approximate test-tube geometry so that distinct proliferative compartments

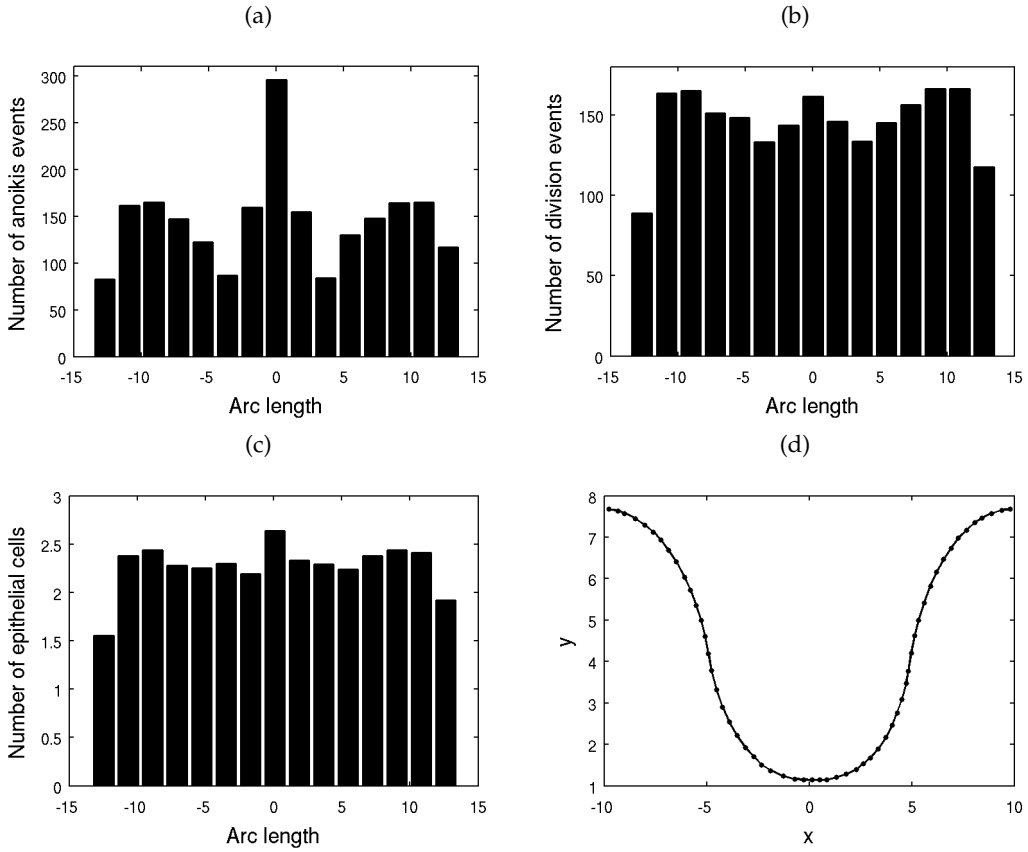

Figure 5.16: The spatial distribution of anoikis and division events, and epithelial cell locations. Here $\beta = 12$, $1/R = 0.4$, and anoikis is the only mechanism of cell removal. (a) Anoikis events, (b) division events, (c) epithelial cell locations at the final timestep, (d) a plot of the coordinates of epithelial cells in the layer at the final timestep.

can be defined as dependent on an imposed Wnt gradient. This is discussed in Section 6.2.1.

5.4.4 Anoikis and Cell Migration

It is crucial that the application of the basement membrane force does not inhibit migration, or induce excessive cell compression, causing cells immediately to be forced out of the monolayer following a cell division event, to be removed by anoikis. These constraints are imposed to investigate whether the model reproduces the migratory behaviour known to occur in the crypt in the absence of an explicitly known active migration force [53]. To examine the frequency and spatial distribution of anoikis events, 100 simulations of 500 hours of cell time were recorded, taken once the layer had deformed to a steady state. The anoikis and division events, as well as the number of cells, were counted from all simulations, and the frequency presented in each case is an average over the total 100. For these simulations, $\beta = 12$ and $1/R = 0.4$.

Figure 5.16(a) summarises the spatial distribution of anoikis events, where the frequency of events is plotted on the y-axes, and arc length along the epithelial layer is given on the x-axis, this being measured from the centre of the layer. There is a clear peak in this distribution, which coincides with the centre of the curved base, where the number of anoikis events is more than double that from other regions of the monolayer. The edge bins show a drop in frequency that is due to the bin size itself, which is larger than is strictly necessary for these regions, as only a small portion of the monolayer extends beyond the penultimate edge bins.

Figure 5.16(b) shows the corresponding spatial distribution of division events. This distribution is more uniform, with a slight increase towards the centre of the layer, and at the boundaries between the regions of zero and non-zero curvature. Similarly, the spatial distribution of epithelial cells at the end of each simulation, shown in Figure 5.16(c), is fairly uniform with a slight increase in the same regions (note that this represents a snapshot in time at the end of each simulation). A typical plot of the epithelial cell centres at the final timestep is shown in Figure 5.16(d).

The distribution of anoikis events does not correlate exactly with either the distribution of division events, nor the spatial distribution of epithelial cells. In particular, the sharp peak in anoikis events at the centre of the layer is much higher than the peak in epithelial cell density or cell division at this point would suggest. It is claimed here that the high number of anoikis events is a consequence of the high compression of cells in the curved region, which forces a perpendicular alignment of two neighbouring epithelial cell centres, such that one cell centre is positioned towards the lumen, and the other towards the basement membrane. Due to the Delaunay triangulation, the cell centre that moves out towards the lumen retains connections only to other epithelial cells, and not to the basement membrane, so it is removed by anoikis. It is likely that this effect is prevalent immediately following mitosis, where the two daughter cell centres are joined by a much shorter spring.

That anoikis is correlated with cell compression is in agreement with the behaviour shown in the 3D individual-based model of an epithelial monolayer proposed by Galle *et al.* [47], where it is also found that if proliferation is uninhibited, epithelial cells are forced out of the layer. Such results are common despite the difference in the models, and especially in the underlying force law (the spring law vs. the Hertz law).

The number of anoikis events also increases towards the boundary of the non-zero and zero spontaneous curvature regions, where the layer adopts a convex shape. These results suggest that the shape that the layer adopts around this boundary again renders epithelial cells vulnerable to popping out of the layer, leading to anoikis. Cells elsewhere in the layer

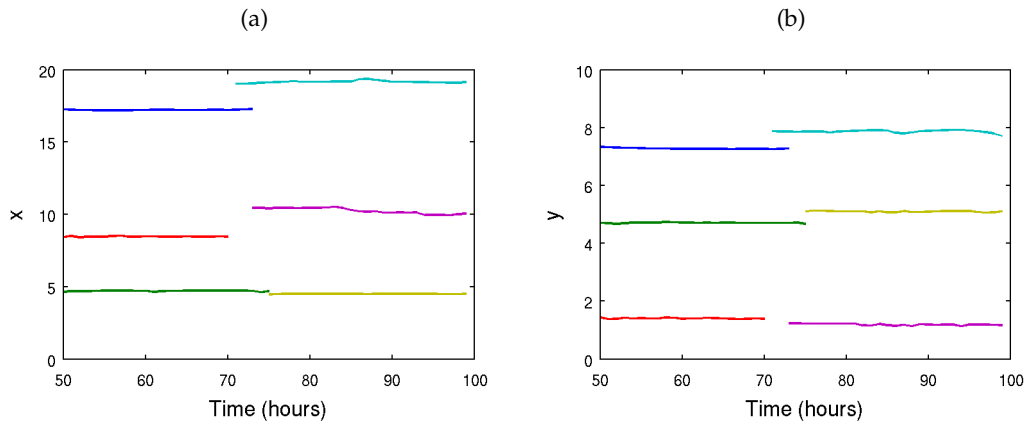

Figure 5.17: Typical cell migration in the epithelial layer. Each colour corresponds to a different cell and tracks the x and y-coordinates at each hour. In each case, the cells maintain a roughly constant position, showing that they do not migrate upwards: (a) x-coordinates, (b) y-coordinates. Results are shown from 50 hours to allow the layer sufficient time to equilibrate.

are under lower compression, and the curvature of the layer is closer to zero, so cells are more likely to remain in the monolayer following a division event.

The high incidence of anoikis events suggests that there is little, if any, migration occurring in the epithelial layer. This is confirmed by visualising simulations, and also by plotting the coordinates of the cells over time. Figure 5.17 shows six typical examples, chosen to illustrate the movement that occurs at the lowest point on the monolayer, and further up the y-axis towards the highest point (see Figure 5.16(d)). It is evident that, in each case, the cells do not migrate in either the x or y direction. Rather, the cells maintain a constant position in the layer, and are only removed due to an anoikis event. This emphasises that migration is not occurring in the model, but rather the cells have reached a state of stagnation due to excess compression and when a cell divides, it will typically undergo anoikis. This is not in agreement with known crypt dynamics, as it is established that upward migration occurs towards the crypt collar.

5.4.5 Density-Dependent Inhibition of Mitosis

The phenomenon of density-dependent inhibition of mitosis is well established, and arises as a consequence of the limited availability of mitogens, growth and survival factors for cells [2]. As discussed in Section 2.1.3, under normal circumstances, this prevents over-proliferation of cells, and experimental results indicate that growth arrest is actively induced in the G0/G1 phase of the cell cycle [67]. Thus far, density-dependent inhibition of mitosis has not been included in this model. The results presented in Figs. 5.16 and 5.17 indicate that, when it is neglected, the correct migration pattern is not observed as cells

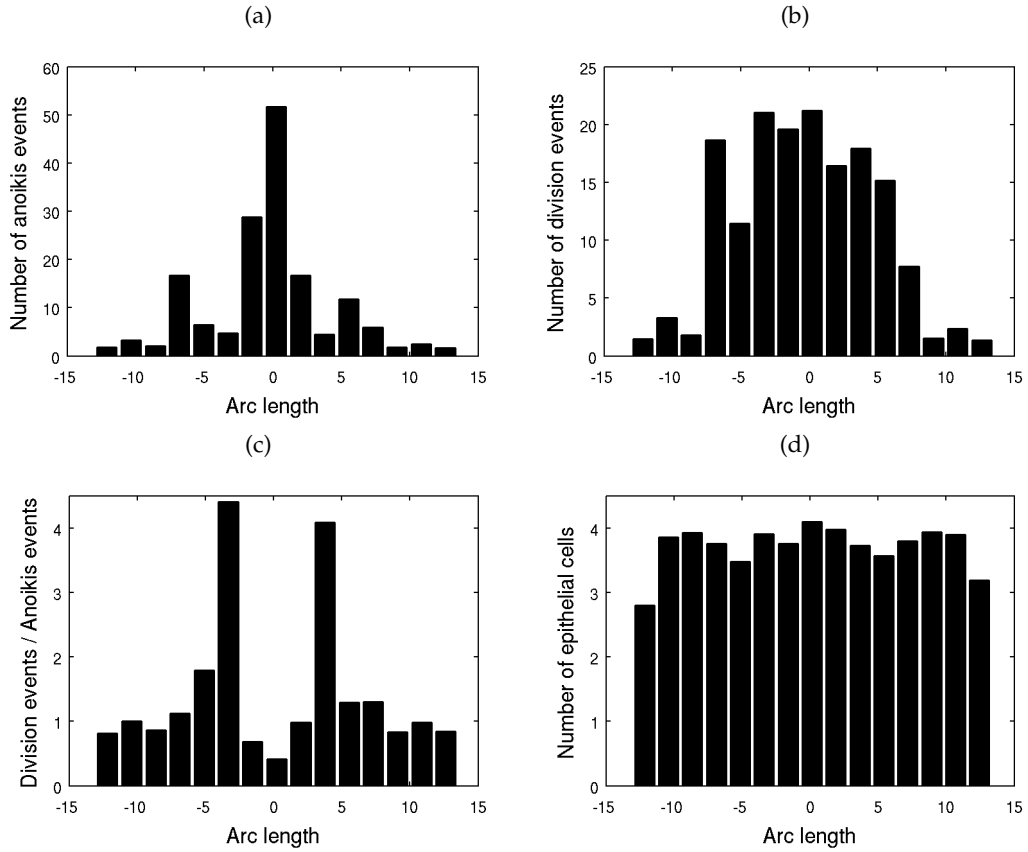

Figure 5.18: A series of plots which show the spatial distribution of anoikis and division events that occur in the epithelial layer when density-dependent inhibition of mitosis is implemented. (a) Anoikis events, (b) division events, (c) the ratio of division events to anoikis events, (d) epithelial cell locations at the final timestep.

divide despite excessive compression, and the newly created cells are forced out of the layer and removed from the simulation too quickly.

To model density-dependent inhibition of mitosis, a threshold area is defined below which a cell cannot divide. Specifically, should a cell have an area, $A < A_T$, where A_T is the minimum area at which cell division can occur, then this cell will not divide until its area grows to exceed this threshold. In these simulations, the equilibrium area for each cell is $A_0 = \sqrt{3}/2$ (≈ 0.86) as the non-dimensional equilibrium spring length is 1, and $A_T = 0.5$. Again, 100 simulations were run, each for 500 hours of cell time, with $\beta = 12$ and $1/R = 0.4$. The results are shown in Figure 5.18.

Firstly, Figure 5.18(a) shows that the spatial distribution of anoikis events still peaks at the centre of the monolayer. Comparison with Figure 5.16(a) reveals that while the frequency of anoikis events has reduced, the proportion of events happening at the centre of the monolayer has increased. Figure 5.18(b) shows that the pattern of cell division has changed,

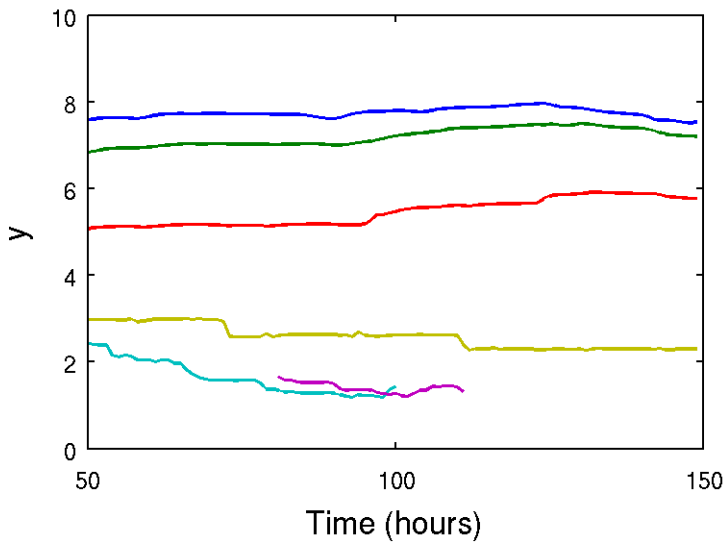

Figure 5.19: Six typical migratory tracks for epithelial cells in the monolayer, when anoikis and density-dependent inhibition of mitosis are implemented.

with fewer division events occurring towards the edges of the monolayer (where there are fewer cells), and the overall frequency of division events greatly reduced. This information is combined in Figure 5.18(c), which shows the spatial distribution of the ratio of division events / anoikis events. This shows that the ratio is close to one throughout the epithelial layer, save two regions which correspond to the most vertical regions of the epithelial monolayer – here division events exceed anoikis events. This demonstrates that anoikis is still dominant within the model, and occurs frequently immediately following cell division.

Overall, the distribution of epithelial cells at the end of the simulation is fairly uniform, as shown in Figure 5.18(d), and is unchanged from that presented in Figure 5.16(c).

Figure 5.19 tracks the y-coordinates of six epithelial cells, displaying typical behaviour from different initial positions in the monolayer. As in Figure 5.17, the epithelial cells are not migrating up the monolayer, but remain in approximately the same vertical position. Compared to cells near the crypt collar, those cells closest to the lowest point of the monolayer typically live for a shorter period before being removed by anoikis.

These results show that, with density-dependent inhibition of mitosis, cells are prevented from dividing when under compression so that once the layer has reached a state of equilibrium, migration does not occur as too few cells are introduced into the simulation. Thus, the model does not yet accurately reproduce the known dynamics of cells within the crypt.

5.4.6 Random Cell Death

The periodic boundaries that are implemented in this model mimic the continuous epithelial layer that lines neighbouring crypts. As the cells in individual crypts migrate up towards to the intercrypt table, apoptosis/sloughing occurs at the crypt collar. With no mechanism of cell loss other than anoikis, the results shown already indicate that cells are prevented from migrating and dividing as the layer is overly compressed. Now, to consider the effect of a second mechanism of cell loss to mimic that known to occur at the crypt collar and intercrypt table, random apoptosis events are assumed in the outer portions of the epithelial layer. Specifically, those epithelial cells in the region $|x| > 8$ have a probability $P = 0.1$ of starting apoptosis within each hour of the simulation. Again, 100 simulations were run, each for a period of 500 hours of cell time, with $\beta = 12$ and $1/R = 0.4$. If, at any time, the random cell death resulted in a hole in the layer, the simulation was disallowed and a new simulation run, because the basement membrane force is not defined when there is a hole in the layer. Increasing the probability of cell death increases the likelihood of a hole forming in the epithelial layer, but for the parameters chosen only approximately one out of ten simulations was discontinued. The results are shown in Figure 5.20, and the frequencies presented correspond to an average over all 100 simulations.

Figure 5.20(a) plots the spatial distribution of anoikis events under these conditions, and Figure 5.20(b) plots the spatial distribution of division events. When compared with Figure 5.16 there is a reduction in both the number of anoikis and division events, but these frequencies are higher than when density-dependent inhibition of mitosis is implemented solely with anoikis.

Figure 5.20(b) shows that the number of cell births increases moving out from the non-zero spontaneous curvature region towards the zero spontaneous curvature region, and this distribution of division events has changed from when only anoikis and density-dependent inhibition of mitosis were implemented. This highlights the fact that the cells at the crypt base are still compressed, but there is migration occurring in the layer which allows the epithelial cells to achieve a sufficiently large area to undergo cell division. Moreover, the spatial range of anoikis and division events, as well as the spatial range of epithelial cells as shown in Figure 5.20(d), has extended, which reveals that the monolayer has grown beyond the length observed in Figures 5.16 and 5.18. There is also a change in the distribution of epithelial cell density at the final timestep, which now decreases moving outwards from the centre of the monolayer.

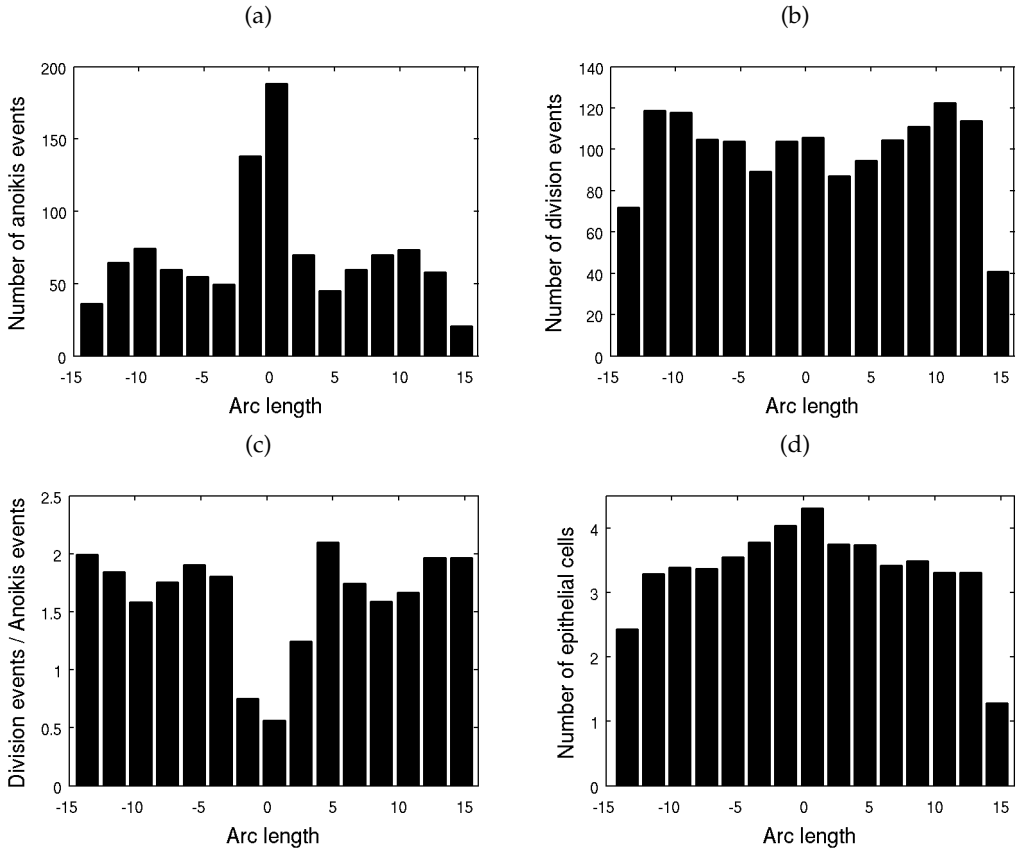

Figure 5.20: The spatial distribution of anoikis and division events that occur in the epithelial layer when density-dependent inhibition of mitosis and random cell death are implemented. (a) Anoikis events, (b) division events, (c) the ratio of division events to anoikis events, (d) epithelial cell locations at the final timestep.

As shown in Figure 5.20(c), overall, the ratio of division events to anoikis events has increased, when compared with Figure 5.18(c). Now it is shown that anoikis does not occur as frequently following division events, and the only region where this remains the case is at the very bottom of the crypt base. Here, cells are compressed and newly created cells are often forced out of the layer following division.

The growth of the epithelial monolayer is illustrated in Figure 5.21, which compares the typical final state of the epithelial layer for the three cases considered here: (i) anoikis only, (ii) anoikis and density-dependent inhibition of mitosis, and (iii) anoikis, density-dependent inhibition of mitosis and random cell death imposed at the edges of the monolayer. The arrows in the plot show that for the final case, the epithelial monolayer has extended and grown upwards.

These results are confirmed by examining the migratory patterns of epithelial cells. Figure 5.22 plots the y-coordinates of six typical epithelial cells over time. This plot reveals two

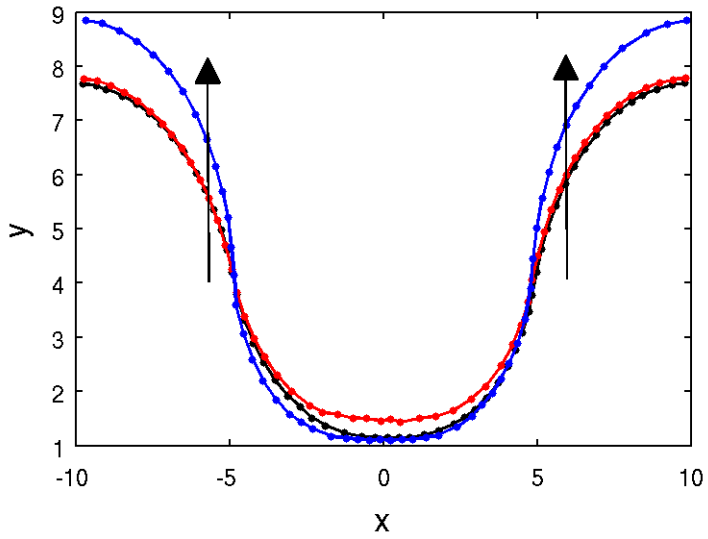

Figure 5.21: A comparison of the final state of the epithelial layer for the three cases considered. The direction of the arrows indicate the extension of the epithelial layer when random cell death is included at the edges (blue), compared to the two cases where this second form of apoptosis is not present (red and black).

distinct types of behaviour. Firstly, those cells sitting at the lowest point of the monolayer tend to remain in position, and do not migrate upwards. In contrast, those cells further up are shown to migrate upwards, before being removed either by anoikis, or by the random apoptosis at the edges. This is consistent with the known cell dynamics of the crypt – stem cells that sit at the base of the crypt do not migrate upwards, but rather maintain a steady population through asymmetric division events, despite not being fixed in position (as was the case in the model due to Meineke et al. [76]). However, both transit-amplifying cells and differentiated cells migrate towards the crypt collar. Therefore, including apoptosis towards the edges of the epithelial monolayer, as occurs in the crypt geometry itself, increases the rate of cell migration by establishing a feedback mechanism whereby apoptosis creates additional space for neighbouring epithelial cells to move into, thereby allowing the cells to equilibrate and then to divide – this is similar to the negative pressure hypothesis introduced in Section 2.1.2. From these results, it is concluded that for cell migration to occur, it is necessary to include a second mechanism of cell removal at the top of the crypt, in addition to density-dependent inhibition of cell division.

5.4.7 Summary

These results show that defining a region of non-zero spontaneous curvature causes the epithelial monolayer to adopt a localised semi-spherical shape, similar to the crypt base.

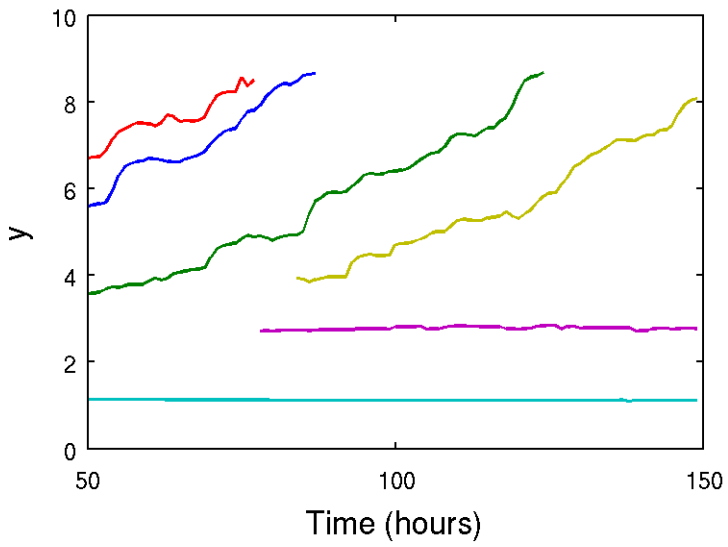

Figure 5.22: Six typical migratory tracks for epithelial cells in the monolayer, when anoikis, density-dependent inhibition of mitosis and random cell death at the edges are implemented.

The introduction of this non-zero spontaneous curvature region is motivated biologically by the presence of the crypt base and muscularis mucosae (described in Section 2.1.1), which appears to follow closely the outline of the individual crypt bases, affording structural support. To ensure that the radius of the semi-circle is not too large, a high spontaneous curvature should be chosen, but then to prevent excess deformation of the stromal tissue below, the ratio of the E-E/S-S spring strengths, μ_{ES}, should also be high. To prevent the horizontal, *i.e.* zero spontaneous curvature, portions of the layer from being pulled down, the minimum effective value of β should be chosen.

The results have also revealed insight into a possible mechanism behind the migration of cells in the epithelial monolayer. As outlined in Section 2.1.2, currently it is assumed that there is some form of active migration in the crypts, but it is not known what may drive this [63]. These results have shown that to ensure that cell migration occurs, and to avoid unrealistic numbers of cells being removed by anoikis, cell removal must be implemented to mimic the apoptosis / shedding that occurs at the crypt collar and intercrypt table. This is in addition to density-dependent inhibition of mitosis, which prevents the overproduction of cells in compressed regions. Indeed, these results indicate that it is possible that the cause of migration in the epithelial layer may not be solely due to an active force that pushes cells up the crypt, but that a feedback mechanism exists between cell birth and cell death, such that apoptosis at the crypt collar creates additional space for the neighbouring cells to move into. Subsequently, cells below are able to migrate upwards and barrier function is maintained. This is a plausible hypothesis generated via *in silico* experiments, which has

not been identified by any existing mathematical models. Discussion with our biological collaborators confirms that this is testable in a wet lab by using inhibitors to halt apoptosis in the crypt, and monitoring any changes to cell migration rates.

5.5 Computation

A typical simulation of 100 cell hours of the epithelial monolayer model presented in this chapter requires approximately 6 minutes of Central Processing Unit (CPU) time on a desktop Linux PC with two quad core 2.83GHz Intel(R) Xeon(R) processors. The numerical timestep parameter shown in Table 5.1 was chosen to ensure both temporal and spatial stability for the solutions, and simple investigations revealed that choosing a smaller timestep does not change the accuracy of the results. However, it is noted that the spatial mesh is defined by the biological problem itself, and changing the physical parameters from those implemented here will influence the choice of timestep.

Movies are provided on the attached CD which correspond to the following typical simulation examples.

- Movie 1: From Section 5.3, where the basement membrane has a zero spontaneous curvature, and $\beta = 0$. In this example, it is shown how the layer wrinkles in the absence of the basement membrane force, and many anoikis events occur as cells pop out of the layer.
- Movie 2: From Section 5.3, where the basement membrane has a zero spontaneous curvature, but now $\beta = 15$. In contrast to Movie 1, it is demonstrated here that the action of the basement membrane force maintains a flat monolayer throughout cell division events and fewer anoikis events occur.
- Movie 3: From Section 5.3.2, now the basement membrane force is applied with $\beta = 12$ and $\mu_{ES} = 2.5$. Compared with Movie 2, it is shown here that there are fewer cells in the epithelial monolayer, as increasing the magnitude of the interactive cell forces yields cells with natural sizes, without compromising the extent of cell migration.
- Movie 4: From Section 5.3.3, this is an example of the behaviour of the epithelial monolayer under hyperproliferative conditions. Here $\beta = 12$ and $\mu_{ES} = 2.5$, so that this simulation can be directly compared with Movie 3.
- Movie 5: From Section 5.4, this is an example of the behaviour of the epithelial monolayer when the central portion of the basement membrane is assigned a non-

zero spontaneous curvature, $1/R = 0.4$ and $\beta = 12$. In this example, both density-dependent inhibition of mitosis and random death at the edges of the monolayer are applied, generating cell migration.

- Movie 6: From Section 5.4.3, this is a movie showing how, by increasing the number of layers of stromal cells and defining a sufficiently wide monolayer, it is possible to deform an initially flat epithelial monolayer to adopt the shape of a crypt.

5.6 Discussion

The crypt epithelium maintains a test-tube shaped geometry throughout repeated division, migration and apoptosis events. As described in Chapter 2, this structural integrity is due to mechanical support provided by the surrounding tissue stroma, which incorporates the musculature and PCFS, and which is separated from the epithelium by the basement membrane. In particular, the PCFS, which sits subjacent to the basement membrane, comprises stromal cells that do not migrate with, or divide as often as the epithelial cells, but form a supporting "crypt outside the crypt" [84]. This chapter concerns the definition and subsequent investigation of a new model of a growing, deformable epithelial monolayer in light of the tissue structure of the crypt, and in particular, presents the first stage of development of a model for the colorectal crypt that accounts for support of the surrounding tissue stroma.

The basement membrane is incorporated as a component of an off-lattice cell centre model for a single epithelial monolayer, constrained to lie on a bed of stromal cells which approximate the tissue stroma and PCFS cells. The basement membrane force accounts for both the rigidity of the membrane, and the cell-substrate adhesion. Additional features of crypt dynamics that are considered include directed cell division which arises due to cell polarity, and cell death as a consequence of epithelial cell detachment from the basement membrane: anoikis. Aside from the unlimited proliferative capacity of the epithelial cells in the model, which is designed to allow a continuously growing layer, these features are included to follow the behaviour of the epithelial layer in the crypt, as described in Chapter 2.

In this chapter a simple geometry is employed, which permits quantitative analysis of the "wrinkled" or flat state of the epithelial layer, defined by the metric α, as well as quantification of division, anoikis and migration events. Utilising this framework, the results of Sections 5.3 and 5.4 have demonstrated the effect of the basement membrane force, and also informed appropriate parameter choices for the model.

Results show that the basement membrane force maintains the epithelial monolayer throughout repeated division events. Provided this force is large enough ($\beta \geq 10$), the virtual basement membrane is sufficiently rigid. Under these conditions, and for a uniform spontaneous curvature of zero, the epithelial monolayer remains flat and is prevented from wrinkling, and fewer cells are forced to detach from the basement membrane to be removed by anoikis. Consequently, the rate of cell migration increases. This is in agreement with results found in an earlier 3D monolayer model [47]. In conjunction with the basement membrane force, the strength of the interactive forces between neighbouring proliferative cells plays a role in controlling the inter-cell spacing. In particular, for high values of β, stronger forces between neighbouring cells are required to prevent overcrowding, and under these conditions the monolayer tends towards a state of dynamic equilibrium. Specifically, the results show that to prevent this and to maintain homeostasis, it is required that the ratio of spring strengths between epithelial and stromal cells be $1 < \mu_{ES} \leq 2.5$ for a basement membrane parameter value $\beta = 12$.

A simple experiment that examines the effect of hyperproliferation shows that the flat epithelial layer is more vulnerable to wrinkling under these conditions, and should this be coupled with failed apoptosis, hypertrophy could result. Overall, the results for $\kappa_S = 0$ demonstrate the effectiveness of the basement membrane force in a simple geometry, and it is clear that this model could easily be applied and extended to other biological epithelia, such as the interfollicular epidermis, or the olfactory mucus membrane.

By defining a region of positive spontaneous curvature in the epithelial monolayer, it is possible to investigate the role of the basement membrane force as it acts beneath the curved base of the crypt. Investigations are presented in Section 5.4 which again prove the effectiveness of this force, and show that to maintain the curved region and prevent excess deformation of the stromal cells below, the basement membrane force needs to be of equal magnitude as for the case when the spontaneous curvature is uniformly zero.

Moreover, simulations reveal a key feedback mechanism between density-dependent inhibition of cell division and cell apoptosis. Specifically, unless sufficient cell apoptosis is present towards the edges of the monolayer, epithelial cells reach a state of confluence, do not divide and migration is inhibited. These results suggest that cell migration in the crypt may not be due solely to proliferative pressure from below, but that the epithelial cells move into the space created by apoptosis events at the collar. This prevents holes forming in the layer so that barrier function is maintained – a theory that is in line with the extrusion process that occurs for apoptotic cells in epithelial layers [74, 102] – and subsequently, the

compression is eased, allowing cells to grow sufficiently to proceed through the cell cycle and undergo division. This is known as the negative pressure hypothesis [61].

In the model, a second form of apoptosis has been introduced explicitly, but is defined to be general – random apoptosis events – given that the cause of apoptosis at the crypt collar and intercrypt table is currently unknown. It is likely that programmed cell death acts in combination with anoikis events that may be induced by the crowding of cells at the crypt collar, where the layer has a negative curvature, to remove cells and ultimately enable cell migration. This is in agreement with studies that have shown that cell crowding and extrusion are closely linked [131], and that migration and mitosis are closely correlated [10, 65], which suggest that it is possible that migration stimulates mitosis. Discussion with our biological collaborators reveals this to be a testable hypothesis in the wet lab. Hence, this simple model has already yielded potential insight into an aspect of crypt dynamics which is currently not fully understood.

The next stage of model development is to apply this definition of the basement membrane force to a 2D cross-sectional crypt geometry. This work is presented in Chapter 6, which confirms the parameter balances found here, and which considers simple experiments in this extended geometric framework.

Chapter 6

A Two-Dimensional Cross-Sectional Model of the Crypt

In Chapter 5, the off-lattice cell centre model which was presented in Chapter 4 was extended to incorporate the mechanical influence of the basement membrane and surrounding musculature within a model for a single epithelial layer, constrained to lie on a block of stromal cells. The design of this model is motivated by the cellular dynamics of the colonic crypt epithelium, and so considers additional biological features such as cell polarity, anoikis and density-dependent inhibition of mitosis, which were introduced in Chapter 2. However, as outlined in Section 3.3.1, the colonic epithelium shares many common traits with other biological epithelia, and in its current form, the model is general enough to be applied to other epithelial tissues, including the interfollicular epidermis, or olfactory mucus membrane.

Investigations thus far have examined the impact of the basement membrane force, and have shown that sufficient adhesion to the basement membrane – modelled by increasing the force magnitude – reduces the incidence of anoikis events, favouring cell migration along the layer. Further, the role of the basement membrane is considered as it acts beneath the semicircular crypt base, and these investigations have informed understanding of a possible mechanism of cell migration in the crypt. Specifically, the results suggest that feedback may exist between density-dependent inhibition of mitosis and cell removal at the crypt collar. It is hypothesised that epithelial cells move into the additional space created by apoptosis events towards the crypt collar, which eases compression lower in the crypt, thereby allowing cells to grow sufficiently to proceed through the cell cycle and undergo division. This also prevents holes from appearing in the layer due to cell death – a theory that is consistent with the extrusion process that occurs for apoptotic cells in epithelial layers [74, 102]. To determine whether this negative pressure effect could

be the sole driver of migration, or one of a combination of mechanisms, requires further experimental insight.

The simple geometric framework employed for these investigations is currently a limiting factor preventing realistic modelling of the colonic epithelium, and so the next step is to implement a more realistic crypt geometry. This chapter is primarily concerned with the application of the current model within a 2D cross-sectional slice of the crypt, and the necessary model extensions are addressed in Section 6.1. As a consequence of the change in geometry, the cell cycle model is modified to account for an imposed concentration gradient of Wnt factors along the vertical crypt axis, which controls cell division and differentiation, as discussed in Section 6.1.2.

The goal of this work is to develop a predictive model that can suggest what emergent phenomena would arise from subcellular and cellular abnormalities. However, first, it is necessary to determine the appropriate parameter values that give rise to the expected cellular and tissue dynamics under healthy conditions. This is addressed in Section 6.2, where results from the simple rectangular geometry are translated to the cross-sectional geometry. It is necessary to balance the strength of the basement membrane force – which corresponds to the membrane rigidity, as well as adhesion of the epithelial cells to the basement membrane – with the adhesion and repulsion forces between neighbouring cells, to allow constant upward migration at a rate that is matched by cell removal at the collar. With these parameter values established, simulation results are presented to illustrate the typical migratory behaviour of epithelial cells in this crypt model. Where possible, in light of the restrictions of a 2D model, comparisons are made with experimental data.

With the stable system defined, simple experiments are conducted to investigate aberrant cell phenotypes in Section 6.3. These include *in silico* simulation of the 1986 experiments by Kaur and Potten [61], in which mitosis is arrested using irradiation and cytotoxic agents. These results have been cited as evidence that the pressure caused by proliferation in the lower half of the crypt is not the sole mechanism driving cell migration. In separate investigations, accumulated mutations are simulated by examining the consequences of failed differentiation, reduced migration and failed apoptosis, and the effect of these mutations on the system dynamics is reported.

The model definition and results presented in Sections 6.1 and 6.2 have been published in PLoS Computational Biology, along with the results in Section 5.4 [33].

6.1 Model Extensions

This section is concerned with extensions to the model of the epithelial monolayer introduced in Chapter 5. First, the new 2D geometry is defined. Second, a new cell cycle model is incorporated into the framework, which is dependent on an imposed gradient of Wnt factors mimicking that observed in the crypt, as described in Section 2.1.3.

6.1.1 Geometry

The new geometry represents a slice taken longitudinally from the apex of the crypt to the collar, as shown in Figure 6.1, which places the model in the context of an histological slice of a crypt. Characteristically, crypts have narrow lumens and more bulbous bases, which gives them shapes analogous to thermometers (visualising this in a histological slice depends on the angle at which the slice is made). Additionally, neighbouring crypts are separated by only a few cells. The epithelial layer is thus a 1D chain of cells (coloured yellow and pink) embedded in a 2D rectangle of stromal cells (coloured green). To maintain the hollow lumen of the crypt, this region is filled with ghost nodes, shown in Figure 6.1(c), and as explained in Section 4.1.2 the ghost nodes do not exert any forces on the real nodes. This prevents epithelial cells from opposite walls forming long connections in the Delaunay triangulation and exerting forces on one another, and keeps opposite walls of the crypt separate.

Figure 6.1(d) is an example of how the cross-sectional model can be defined to have a narrower lumen than that shown in Figure 6.1(c). This is obtained by defining a smaller width for the mesh of nodes, reducing the width of the lumen filled with ghost nodes, and reducing the spontaneous curvature that is defined for the crypt base region. However, the geometry implemented for the simulations described throughout this chapter is chosen to be that of Figure 6.1(c), to enable investigation of polyp formation (see Section 6.3.2) as mutant cells divide outwards towards the lumen.

As is the case biologically, non-proliferating epithelial cells are introduced into the epithelial monolayer to represent the terminally differentiated cells positioned towards the crypt collar, which are coloured pink in the visualisations. Cell proliferation is Wnt-dependent, as described in Section 6.1.2. Again, periodic boundary conditions are imposed on the vertical walls of the tissue block, to mimic the existence of neighbouring glands on either side of the crypt. Those cells lining the base of the stroma are pinned to model the presence

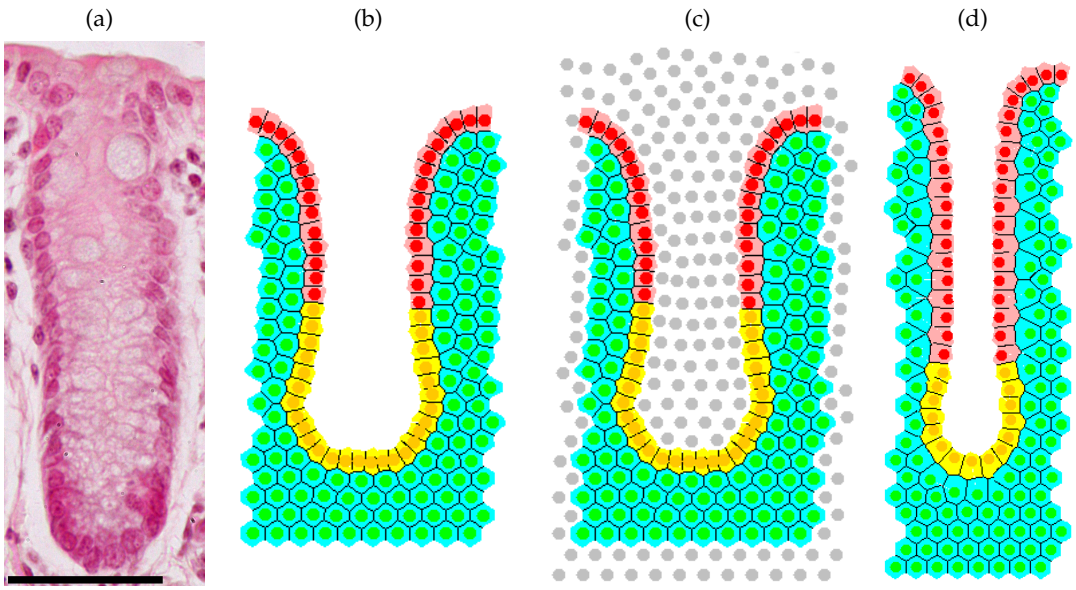

Figure 6.1: (a) A haematoxylin and eosin stained wax section of a murine colonic crypt. Scale bar = 50 microns. Reprinted from Dunn et al. [33]. (b) The cross-sectional crypt configuration. Proliferating and non-proliferating epithelial cells are indicated in yellow and pink respectively, whilst non-proliferating stromal cells are indicated in green. (c) Ghost nodes (grey), described in Section 4.1.2, are included to create and maintain the hollow lumen of the crypt. (d) An example of a crypt with a narrower lumen.

of the muscularis externa that sits beneath the muscularis mucosae, as shown in Figure 2.1. Otherwise, elements of the submucosa are not considered here.

In this new geometry, the region in which the basement membrane has non-zero spontaneous curvature, Ω, defines the crypt base. Specifically, the region of the basement membrane that sits below the bottom 20% of the crypt length (calculated as the difference between the y-coordinates of the lowest and highest positioned epithelial cells) is assigned a non-zero spontaneous curvature, and this evolves dynamically as the height of the crypt changes. The spontaneous curvature is defined to be zero everywhere else.

6.1.2 Cell Division

Now that a more realistic crypt geometry has been imposed, it is necessary to model the proliferating and non-proliferating regions of the epithelial monolayer. To achieve this, a linearly decreasing concentration gradient of Wnt factors is imposed along the vertical axis of the crypt, as illustrated in Figure 6.2: this normalised Wnt profile decays from 1 at the crypt base to 0 at the crypt collar. Each cell detects the Wnt level at its centre and a threshold is prescribed such that cells which are positioned in a region of sufficient Wnt proceed through the cell cycle and undergo division. Those cells that are positioned higher

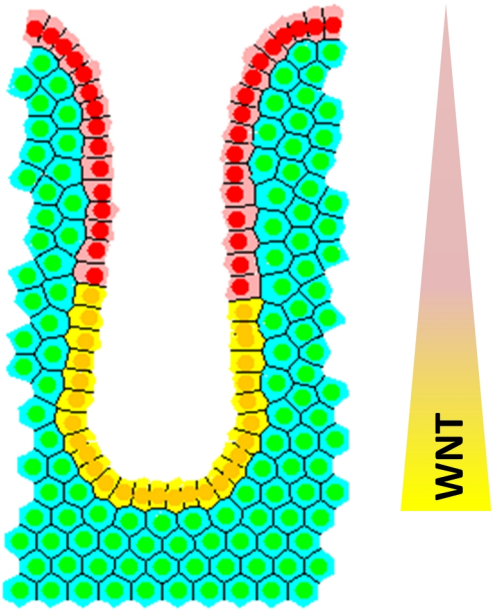

Figure 6.2: A linearly decreasing gradient of Wnt factors is imposed in the cross-sectional model, which is normalised to 1 at the base of the crypt, and 0 at the crypt collar. A threshold is prescribed such that cells in the region of insufficient Wnt factors are defined to be terminally differentiated.

up the crypt experience a lower level of Wnt that is below this threshold, and so are defined to be terminally differentiated and do not divide. This models a discrete point at which epithelial cells stop proliferating in the crypt. This method of defining the proliferative region has been implemented previously in other models, *e.g.* Van Leeuwen et al. [123], Osborne et al. [87] and Walter [125].

As in Section 5.1.2, the duration of the G_1 phase of the cell cycle is randomly drawn for each cell from a uniform distribution, while the duration of the remaining phases are held constant. Therefore each cell has a total cell cycle duration sampled from a Uniform $X \sim U(11, 13)$ distribution [8]. Directed cell division, which arises from the planar cell polarity exhibited by epithelial cells, is again applied for each dividing cell according to the relative position of the nearest epithelial neighbours, and using the approach outlined in Section 4.1.4.

6.2 Model Simulations

Under normal, healthy conditions, the crypt achieves a state of dynamic homeostasis, where cell birth and death are balanced to maintain a regular turnover of cells and allow the epithelium to be renewed every few days. The conditions required for this model to

exhibit homeostasis are sought, and are found to require that the basement membrane force must balance the adhesive and repulsive forces between neighbouring cells, while allowing constant upward migration at a rate that matches the rate of cell removal at the collar. Thus, the number of epithelial cells in the crypt should fluctuate only slightly around a constant value, the cells should not be overly compressed, and the structure should not buckle. The investigations detailed in Chapter 5 provide a basis for establishing the necessary parameter balances that should be used for the new geometry and cell cycle model. Subsequently, simulation results corresponding to healthy conditions are presented and discussed.

6.2.1 Parameter Choices

As shown in Section 5.4.3, it is possible to deform the epithelial monolayer from an initial horizontal configuration to adopt a test-tube crypt shape. However, in order to do so it is necessary to define the initial rectangular geometry to be sufficiently wide, which in turn increases the width of the tissue stroma surrounding the crypt once the layer has fully deformed. This is unrealistic, as the stroma between neighbouring crypts is only 2–3 cells thick. Further, at this stage, cell proliferation is defined to be dependent on a decreasing Wnt gradient, and so the starting point for the following simulations is an initial geometry that approximates the shape of the crypt, as shown in Figure 6.3. This also has the advantage of eliminating the time required to fully deform the flat layer. From the approximate geometry, the basement membrane force acts to maintain the test-tube shape within the tissue through local calculation of the discrete curvature. This is a key feature of the model, as the test-tube geometry emerges due to the action of the forces, rather than being fixed and imposed as in most earlier models.

The choice of the basement membrane force magnitude, as governed by the parameter β, is influenced by the new geometry as the force acts on the curve of the monolayer at the crypt collar where the vertical walls meet the horizontal intercrypt table. As the spontaneous curvature is zero everywhere save at the crypt base, the action of the basement membrane force will cause the corners to flatten, and in so doing, will lower the intercrypt table and cause the crypt to shrink in height. This behaviour is depicted in Figure 6.3, which reveals the changes that occur as the system relaxes from the initial, approximate geometry to the equilibrium state. To prevent the crypt from shrinking in height too much, a low value of β must be chosen, but one which still defines a large enough basement membrane force to keep the vertical walls of the crypt column flat. Thus it is sensible to choose $\beta = 12$. This is consistent with the results shown in Figure 5.12(b).

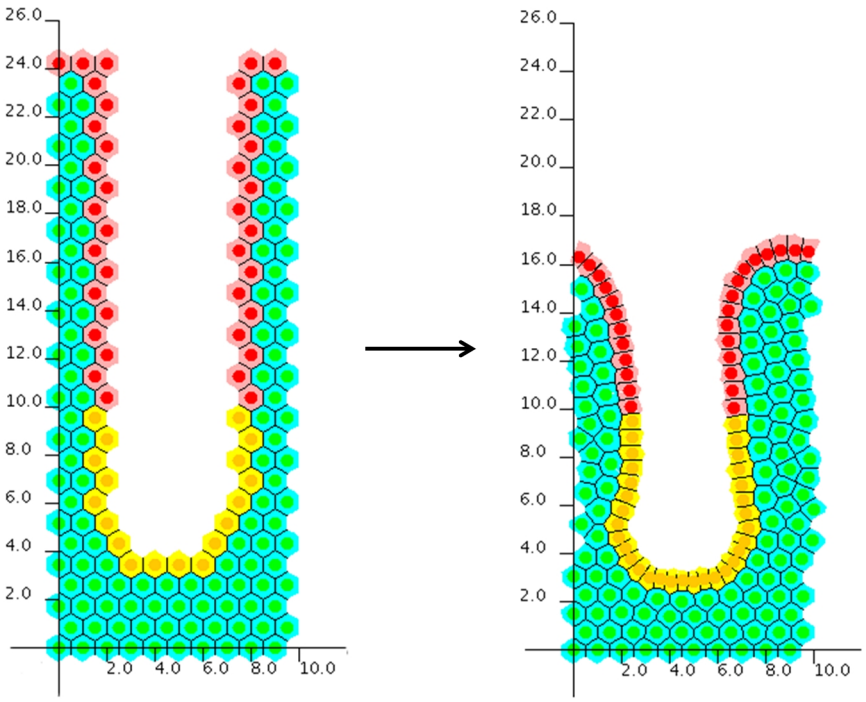

Figure 6.3: Starting from an initial approximate geometry (left), the action of the basement membrane force causes the corners to flatten, and in so doing, lowers the intercrypt table and causes the crypt to shrink in height until it reaches equilibrium (right). This action influences the choice of β. The axes shown here are those used to generate the results in this section, and the equilibrium geometry (right) is used as the starting point for all simulations.

The results from the simple rectangular geometry indicate that for $\beta = 12$, a spontaneous curvature of $1/R = 0.3$ or $1/R = 0.4$ is optimal for the crypt base, to ensure a sufficiently small radius for the semicircular region. Lastly, to prevent overcrowding of cells in the monolayer, a large enough spring constant, $\mu = 45$, must be chosen. As demonstrated in Section 5.4.4, density-dependent inhibition of cell division must be implemented, and random death events are included towards the crypt collar to model cell removal in this region.

6.2.2 Results

Simulations of the cross-sectional model were performed using the parameter values stated above ($\beta = 12$, $1/R = 0.3$, $\mu = 45$), with density-dependent inhibition of mitosis and random cell death occurring within the top 10% of the crypt length (calculated dynamically as the crypt height changes over time). With these parameters, the crypt achieves a state of dynamic homeostasis with repeated mitotic events and cell migration directed towards the crypt collar. The following results concern such simulations, and unless stated otherwise,

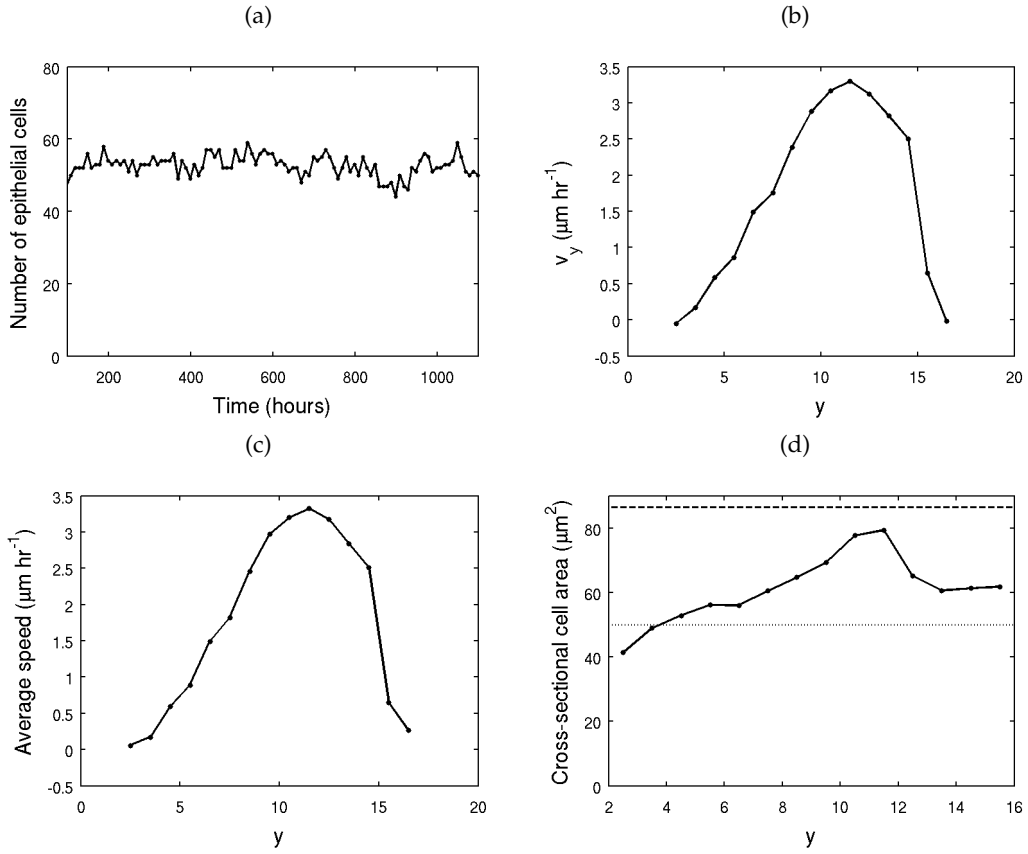

Figure 6.4: Results for a typical cross-sectional model simulation of 1000 hours. (a) The total number of epithelial cells in the crypt model over time, (b) the average vertical or y-component of velocity, v_y, for cells as a function of y, (c) the average speed, v, as it varies with y, (d) the average cross-sectional epithelial cell area as a function of y. Also shown on this plot is the equilibrium cell area (dashed line), and the threshold cell area below which cells do not divide under density-dependent inhibition of mitosis (dotted line).

demonstrate the behaviour of the model using these parameter values. The coordinate axes used to generate simulation statistics are those plotted against the crypt snapshots shown in Figure 6.3. This plot shows that the base of the crypt sits at $y \approx 3$, and hence result plots are shown for $y \geq 2$, and not $y \geq 0$. All simulations relate to the equilibrium crypt geometry, differing only due to the random seed used to determine cell birth and death events.

Model Stability

To demonstrate the evolution and stability of the cross-sectional model over long time periods, a typical simulation was run for 1000 crypt hours, and results for this are shown in Figure 6.4.

Figure 6.4(a) shows how the total number of epithelial cells in the crypt changes over time. The number remains approximately constant, and fluctuates between 50-60 cells due to the stochasticity of cell birth and cell death in the model. This shows that the average rate of cell turnover in the crypt is constant, and from this it is concluded that cell birth and death are matched. (In this plot, results from the first 100 hours are omitted to ensure that equilibrium has been reached.)

Figure 6.4(b) plots the vertical component of velocity, calculated as the average v_y of all epithelial cells within predefined horizontal bands of unit width: $2 \leq y < 3; 3 \leq y < 4; \ldots; 15 \leq y < 16$. These bands are defined according to the lowest and highest positions of epithelial cells throughout the simulation. Here, the units of velocity have been dimensionalised to μmhr^{-1}. This plot shows that v_y increases moving up the crypt axis, from zero at the crypt base to a maximum at the start of the differentiated cell zone. The upward velocity decreases upon reaching the top portion of the crypt, the differentiated cell compartment, to a minimum where cells instead move horizontally across the crypt collar and intercrypt table, located just above $y = 14$, before being removed by apoptosis. The average speed, $v = \sqrt{v_x^2 + v_y^2}$, is shown in Figure 6.4(c). Comparison with Figure 6.4(b) reveals that the overall cell speed is dominated by the vertical component of velocity.

Figure 6.4(d) plots the average cross-sectional area of the epithelial cells, again calculated within the horizontal bands specified above. Also marked on this plot is the equilibrium cross-sectional cell area ($86.6\mu\text{m}^2$, dashed line) and the threshold cell area above which cells can proceed through the cell cycle ($50\mu\text{m}^2$, dotted line). In the absence of experimental data which quantify cell volumes below which mitosis is inhibited, this parameter was chosen to produce behaviour that is in line with the proliferative patterns observed in the crypt. This plot shows that, on average, only cells at the very bottom of the crypt ($2 \leq y < 4$) tend to have a cross-sectional area below that of the threshold required for cell division to occur. It is also clear that cells do not attain the equilibrium area, but rather are continuously compressed within the crypt. This causes the cells to adopt a shape that is more columnar, which is in agreement with what is observed biologically.

Figure 6.5 shows the distribution of residence times for the epithelial cells in the crypt, generated from the 1000 hour-long simulation. Figure 6.5(a) shows that most of the cells remain in the crypt for under 100 hours, and focussing on this region, as shown in Figure 6.5(b), it is observed that that the majority of cells remain in the crypt for 30-50 hours, but a large proportion of cells remain in the crypt for longer. These results are consistent with cell turnover time for the crypt, which is estimated at 3-5 days for the murine small

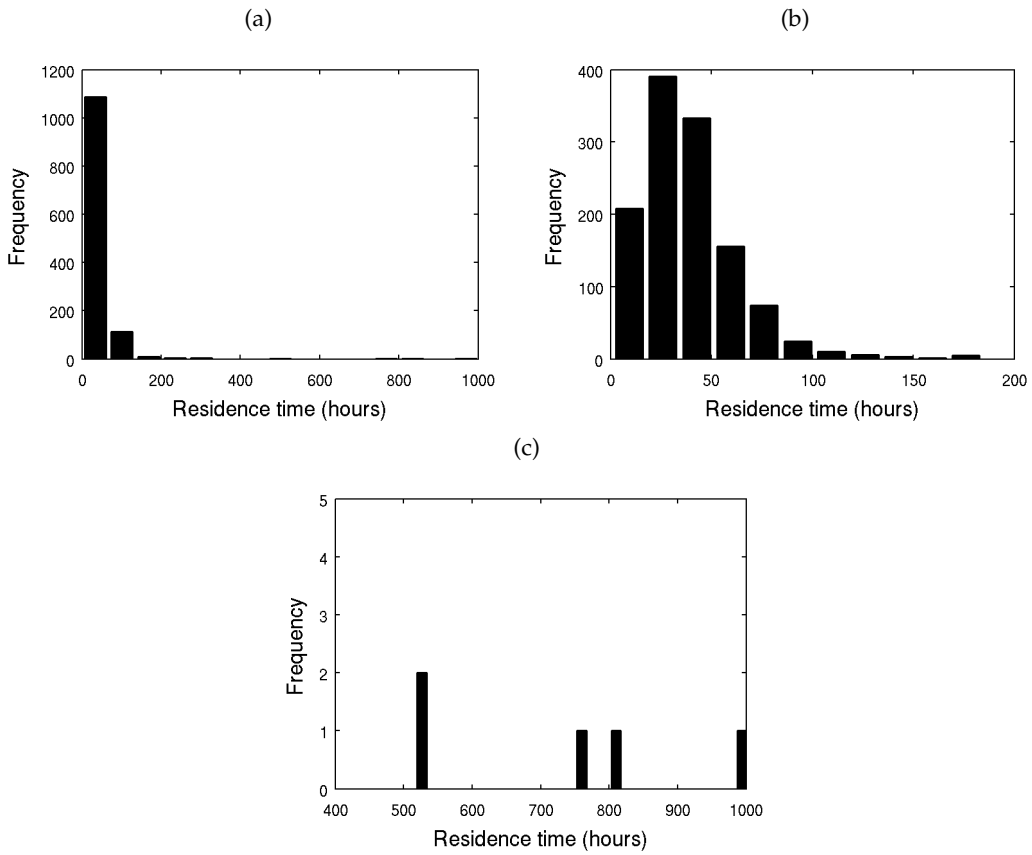

Figure 6.5: A series of histograms showing the residence times for epithelial cells in a typical cross-sectional model simulation of 1000 hours. (a) All epithelial cells, (b) focussing on those cells that remain in the crypt for under 200 hours, (c) focussing on those cells which remain in the crypt for over 500 hours.

intestine [97]. Figure 6.5(c) focuses on those cells which remain in the crypt for over 500 hours, and in one case, for the duration of the simulation. These cells are those at the very base of the crypt, residing in what is understood to be the stem cell region.

Comparison of Results – Cell Velocity

Figure 6.6 provides a comparison of the velocity data obtained from the 1000 hour-long simulation with independent numerical results generated by Osborne et al. [87], and with experimental results obtained by Kaur and Potten [61]. Figure 6.6(a) reproduces Figure 6.4(b), for ease of comparison.

Figure 6.6(b) plots v_y against y for three different cylindrical crypt models: a cell-vertex model (solid line), a cell-centre model (dashed line) and a continuum model (dashed-dotted line). In each case, it is observed that v_y increases linearly with distance moving up the crypt, before levelling out in the non-proliferating zone. Qualitatively, this result

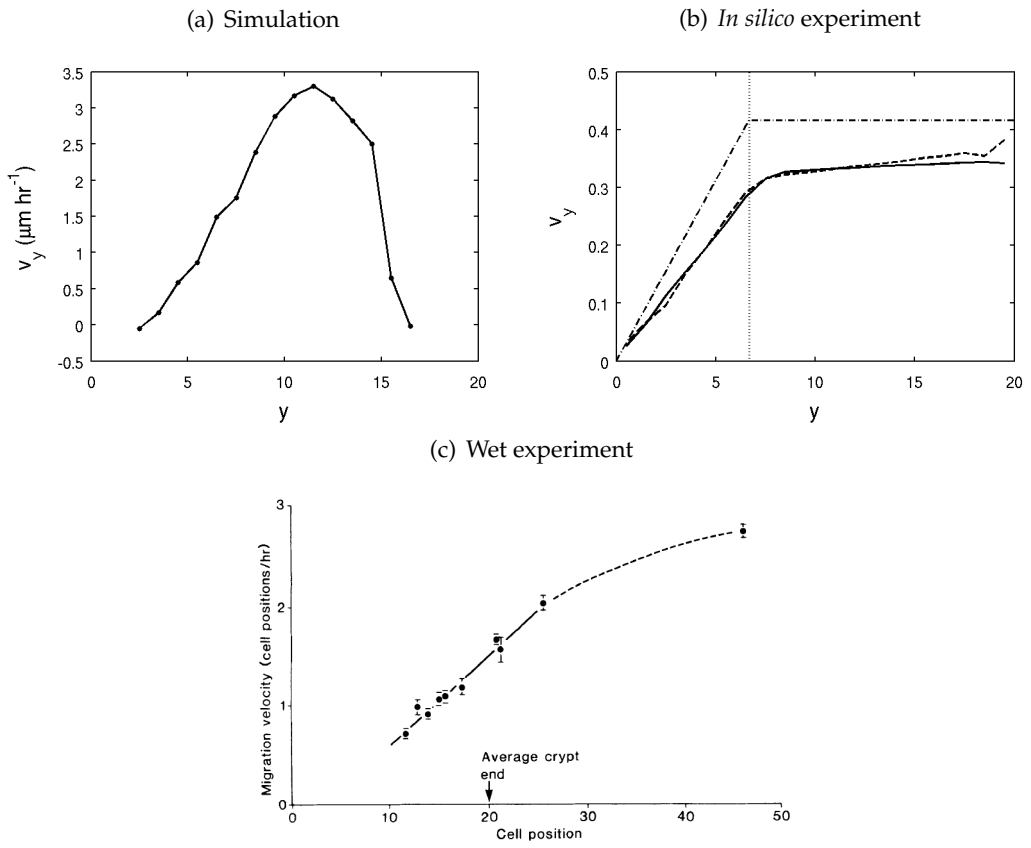

Figure 6.6: (a) Results for the cross-sectional model simulation of 1000 hours, (b) results reproduced from Osborne et al. [87] which plots v_y against y for the cylindrical crypt model using a cell-vertex model (solid line), a cell-centre model (dashed line) and a continuum model (dashed-dotted line), where v_y is measured in cell diameters hr^{-1}, (c) experimental results reprinted from Kaur and Potten [61], which plot the cell migration velocity against distance along the crypt-villus axis for small-intestinal crypt samples.

differs from that shown in Figure 6.6(a) in the upper portion of the crypt, and this is due to the difference in geometry used for the models. The cross-sectional model accounts for the intercrypt table, along which cells migrate horizontally, whereas the earlier cylindrical models impose a cut off point above which cells are assumed to be sloughed off and are no longer followed in the simulation. Also, in the cylindrical models, the proliferative pressure is dispersed moving up the crypt as the epithelial cells are free to move on a plane – this is in contrast to the 1D chain of epithelial cells in the cross-sectional model.

The plot shown in Figure 6.6(c) is reprinted from Kaur and Potten [61], and shows the change in migration velocity moving up the crypt-villus column from healthy small-intestinal samples. Given that cells in the small intestine move directly onto the villus upon reaching the crypt collar, the cell velocity continues to increase beyond the top of the crypt, which is marked on the figure. Therefore, this plot can only be used to compare

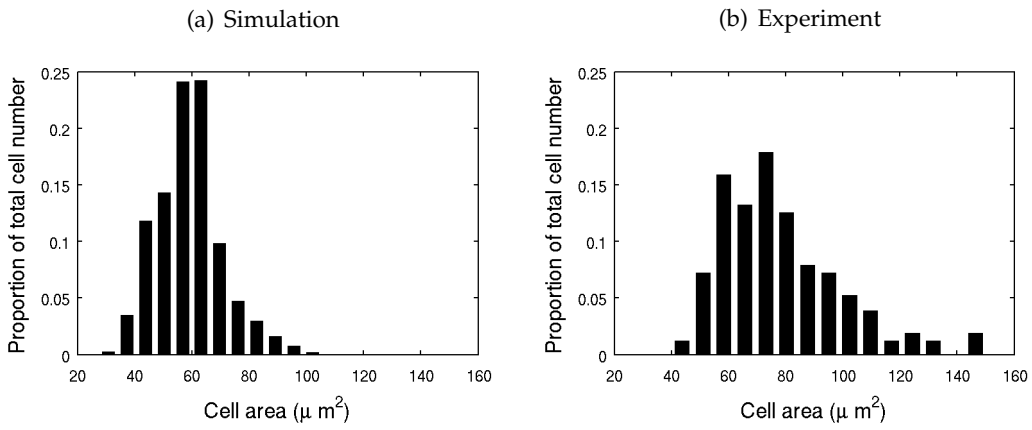

Figure 6.7: A comparison of model results with experimental cell area data for three healthy murine colonic epithelium samples. (a) A histogram of cross-sectional area data collected from the simulation of 1000 hours. These data have been dimensionalised to allow comparison with the experimental data (1 cell width corresponds to 10μm [2, 109]), and the frequency has been averaged over total cell number to show the proportion of cells. (b) Experimental data obtained from three wildtype murine tissue samples, taken from midway down the length of the colon. Data provided by Dr. Scott Nelson, University of Dundee.

the results shown in Figures 6.6(a) and (b) insofar as they correspond to the crypt region only. This supports the observed linear increase in cell velocity moving up towards the crypt collar, and contradicts the levelling out observed in Figure 6.6(b) for the cylindrical models. Further, this demonstrates that reproducing the shape of the crypt geometry has an impact on the accuracy of simulated cell dynamics.

Comparison of Results – Cell Area

Figure 6.7 provides a comparison of the cross-sectional cell area data obtained from the 1000 hour-long simulation with experimental data obtained from murine crypts, provided by our biological collaborators following the methods outlined in Dunn et al. [33]. Figure 6.7(a) is a histogram of cross-sectional cell areas taken from the simulation, where the frequency is averaged over the total cell number to indicate the proportion of cells within each bin. For this plot, the non-dimensional areas have been dimensionalised for comparison, scaled with a typical cell diameter of 10μm [2, 109].

Figure 6.7(b) is a histogram of cross-sectional cell area data obtained from colonic epithelium samples taken from midway down the length of the colon, the 50% region, in three wildtype (*i.e.* healthy) mice. These data were acquired using multiphoton fluorescence microscopy to generate 3D images of fixed whole-mount tissue, and measurements calculated using Volocity image analysis software[1]. Despite this being a small data set, it

[1] `http://www.perkinelmer.com/pages/020/cellularimaging/products/volocity.xhtml`

serves as a guide to what is found realistically in the murine crypt. This histogram shows that cross-sectional cell area can range from $40\mu m^2$-$150\mu m^2$, and there is a peak between 60-$80\mu m^2$. These results are qualitatively similar to those in Figure 6.7(a), where the range is approximately 30-$115\mu m^2$, and the peak is at approximately $60\mu m^2$. It is worth noting, however, that in the simulations distances have been scaled with a typical epithelial cell length of $10\mu m$, but an alternative scaling could be applied. These results indicate that despite only considering a cross section of the crypt, the turnover and cell numbers in the model lead to plausible and realistic cell areas.

6.2.3 Cell Migration

The results in Section 5.4 for the epithelial monolayer model show that outward migration occurs from the base of the non-zero spontaneous curvature region towards the edges (Figure 5.22). This pattern of cell movement away from the crypt base is also found in simulations of the cross-sectional model and is consistent with the upward migration that is observed biologically. As shown already, the average cell velocity increases linearly towards the crypt collar in agreement with experimental results. Typical example migration tracks that illustrate this are given in Figure 6.8, where three plots are presented showing cells moving upwards from one of three regions of the crypt: (a) at the crypt base, (b) in the central region, and (c) at the crypt collar.

Figure 6.8(a) shows that cells born at the base of the crypt tend to remain in that region, as is the case for stem cells in the crypt. It is possible, however, for these cells to migrate out of this zone and move up to the crypt collar, and examples of this are shown in the plot. The two examples that move from the base of the crypt to the crypt collar do so over the course of approximately 40 hours and 100 hours respectively, transit times which correlate with the renewal of the crypt epithelium every few days. Also shown in this plot is the track of one cell which migrates to $y \approx 7$, at which point it undergoes anoikis. This anoikis event coincides with a division event, in which the increased compression has caused the cell to pop out of the layer. The other cell born out of this division event will continue to move up the crypt.

Figures 6.8(b) and (c) both demonstrate the upward migration of cells from the middle of the crypt, and from the top of the proliferative compartment, towards the crypt collar. These cells, which are born higher up the vertical crypt axis, typically migrate to the crypt collar in approximately 20-40 hours.

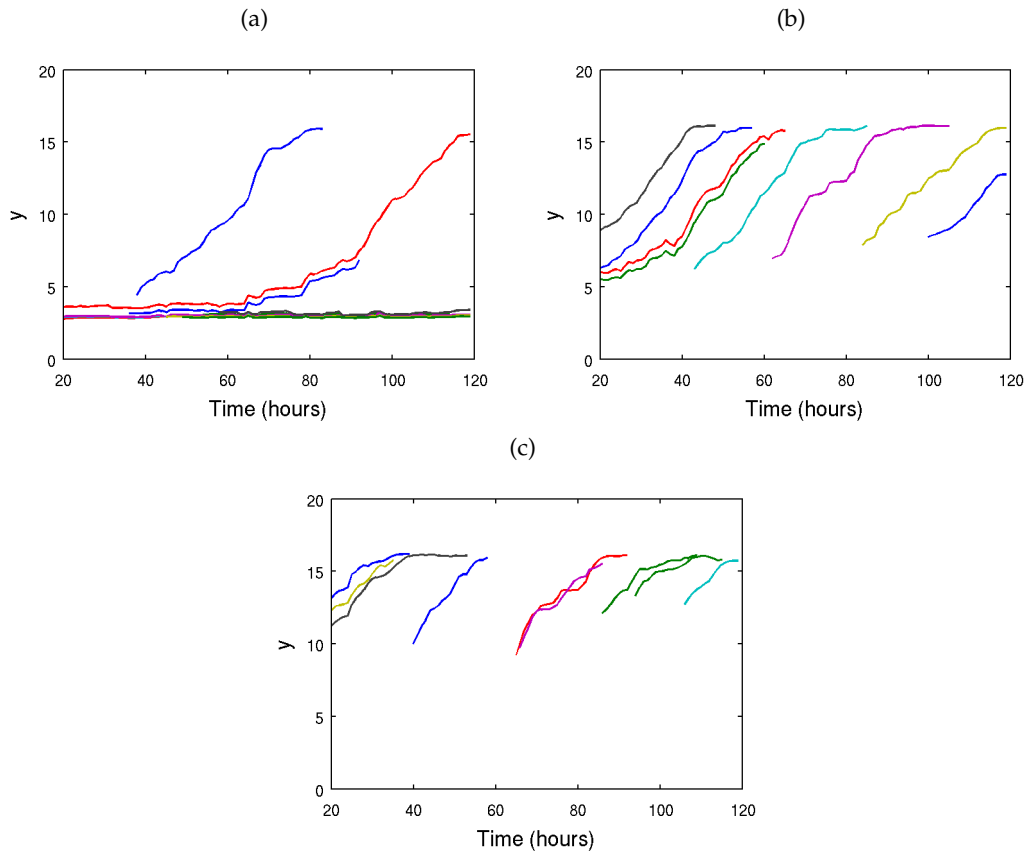

Figure 6.8: Typical migration tracks for cells that are born (a) at the base of the crypt, (b) in the central portion of the crypt, (c) at the top of the proliferative compartment.

Simulation Examples

The upward migration of epithelial cells can be observed by watching simulation movies (such as movie 7 on the attached CD, described in Section 6.4), and to emphasise this, individual cells and their progeny can be labelled and marked with a different colour (blue). To illustrate this here, Figure 6.9 shows snapshots taken at ten-hour intervals from a simulation where a single epithelial cell was labelled once the crypt had reached a state of equilibrium. This cell and its progeny steadily move up the crypt towards the collar before being removed by apoptosis. The y-coordinates of these cells are plotted in Figure 6.11(a), and the shape of this plot is similar to the single cell tracks made by cells shown in Figure 6.8(a). This arises because the epithelial cells form a 1D chain and so move upwards in tandem. In this case, it takes approximately 100 hours for the original cell and its progeny to all reach the crypt collar and be removed by apoptosis.

The snapshots shown in Figure 6.10 track the migration of a different epithelial cell, again taken at 10 hour intervals, and the y-coordinates of this cell and its progeny are plotted

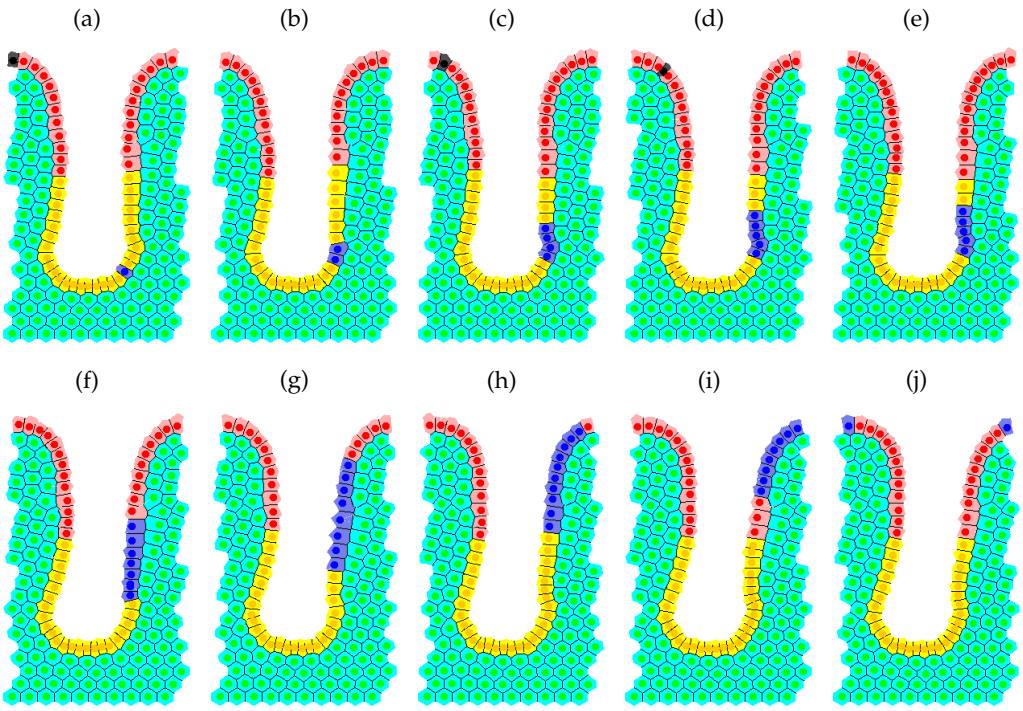

Figure 6.9: Simulation snapshots taken at 10 hour intervals, which track the migration of a labelled epithelial cell (coloured blue, indicated in (a)), and its lineage, which are subsequently labelled. Cells marked in grey are apoptotic.

in Figure 6.11(b). As in Figure 6.9, the labelled cells move up the crypt towards the collar. However, the migration of these cells differs from that shown in Figure 6.9. The initial labelled cell starts slightly lower in the crypt and takes longer to move out of the base region. In total, it takes approximately 170 hours for this cell and its progeny to be completely expelled from the crypt.

These examples illustrate the behaviour that can be observed in cells which originate in similar regions of the crypt. For reference, the initial cells that are labelled here are later assigned mutations (see Section 6.3.2), so it is possible to directly compare the change in behaviour caused by altering the cell properties.

6.2.4 Average Results for Multiple Simulations

The results presented thus far demonstrate that it is possible to maintain the crypt structure and healthy dynamics over a long time period – the rate of cell turnover is approximately constant, and cell migration occurs up the crypt axis towards the crypt collar. Due to the stochasticity of birth and death events, to generate a realistic representation of the behaviour of this model, 50 simulations of 500 crypt hours were run, and the results are

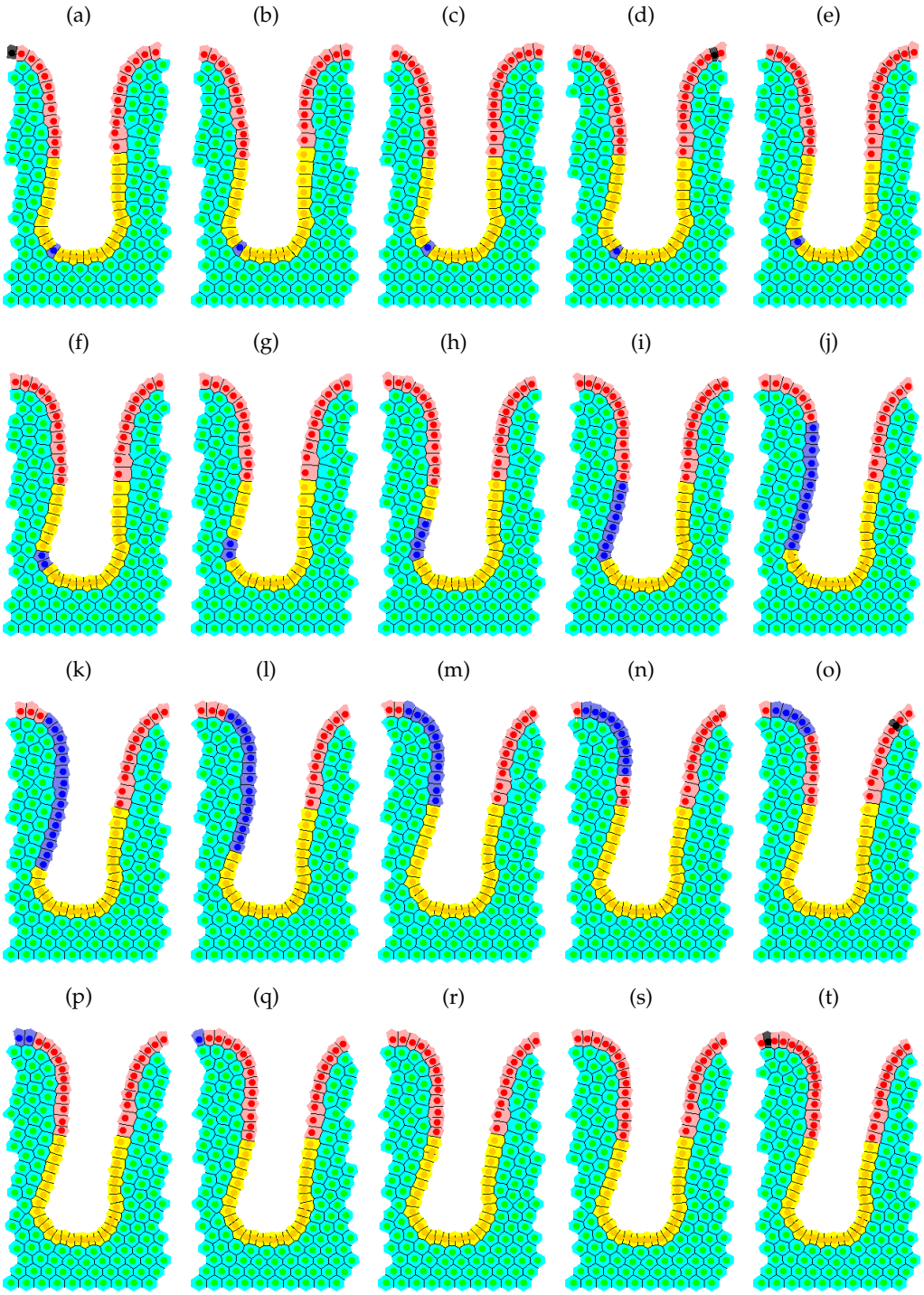

Figure 6.10: Simulation snapshots taken at 10 hour intervals, which track the migration of a labelled epithelial cell (coloured blue, indicated in (a)), and its lineage, which are also labelled in blue. Cells marked in grey are apoptotic.

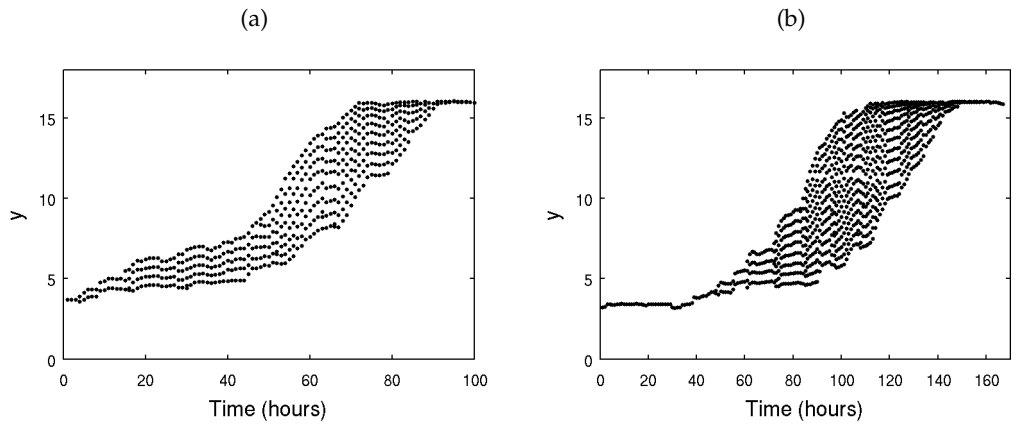

Figure 6.11: The y-coordinates of the cells that are labelled and shown in (a) Figure 6.9, and (b) Figure 6.10.

now shown. As explained in Section 5.3, the pseudo-random number generator used is re-seeded for each simulation to ensure independent realisations. To generate the series of plots in Figure 6.12, the frequencies were obtained for all 50 simulations, and subsequently averaged to represent typical results for a single simulation.

Figure 6.12(a) shows the distribution of anoikis events along the y-axis. The distribution peaks at the base of the crypt, and then decreases to approximately zero at the start of the differentiated cell zone. This reveals a correlation between the range of the proliferative compartment ($2 \leq y \leq 10$) and the incidence of anoikis events. Further, the plot shows that, typically, anoikis events do not occur in the differentiated cell zone, save at the curve of the crypt collar ($14 \leq y \leq 16$). This is in agreement with the results found for the epithelial monolayer model, shown in Section 5.4, where it is suggested that the negative curvature and overcrowding at the crypt collar render the epithelial cells vulnerable to losing contact with the basement membrane and popping out of the layer. Moreover, as the cells in this region are now differentiated, anoikis here is not a consequence of a cell division event.

The peak in anoikis events at the crypt base is not in agreement with experimental results: cell death is not commonly observed at the crypt base [131]. The correlation between division and anoikis suggests that, in the model, many anoikis events occur immediately following mitosis, particularly at the base. These events arise as a consequence of cell centres being forced towards the lumen, and once the cell centres are remeshed, the apically displaced cell centre retains connections only to neighbouring epithelial cells and so has lost contact with the basement membrane.

The process of asymmetric division, which occurs in the stem cell pool at the base of the crypt, involves a perpendicular alignment of the mitotic spindle, causing the apical

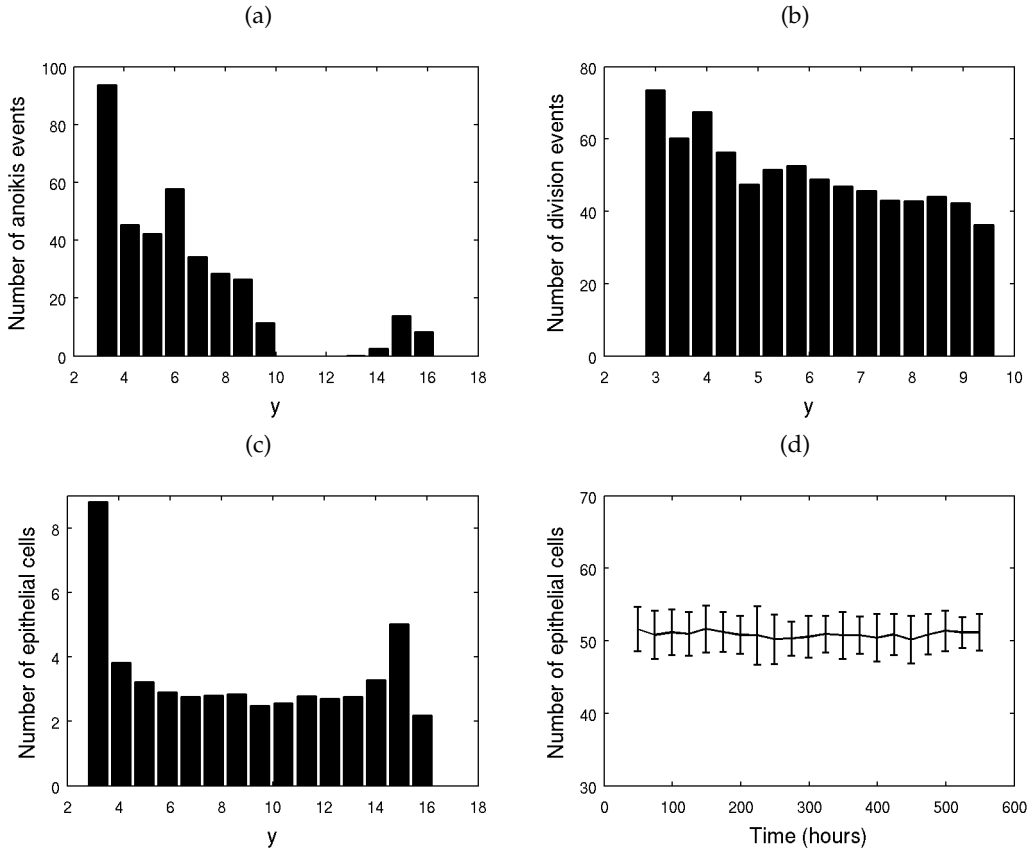

Figure 6.12: Simulation statistics for the cross-sectional model, obtained as the average of 50 simulations, each of 500 hours in duration. (a) The spatial distribution of anoikis events along the y-axis, (b) the spatial distribution of division events along the y-axis, (c) the spatial distribution of epithelial cells at the final timestep, (d) the average number of epithelial cells over time where the error bars indicate the standard deviation at each timestep.

displacement of one daughter nuclei, which later reinserts basally. An example of this is shown in Figure 6.13, where an Lgr5+ stem cell, imaged using green fluorescent protein, is undergoing division. Staining of the cell nuclei reveals that the nucleus of the dividing cell is apically displaced, and the cell body is tethered to the basement membrane by a thin stalk.

In the model there is currently no torque force applied to pull apically-displaced cell centres back into the monolayer, as biologically it is not known how this process occurs during division. However, these results suggest that mechanical compression of cells at the crypt base may play a role in causing asymmetric division by forcing the perpendicular alignment of the spindle. In contrast, those cells further up the crypt do not move out of the layer as often, and this correlates with the expected symmetric division for epithelial cells in the transit-amplifying compartment.

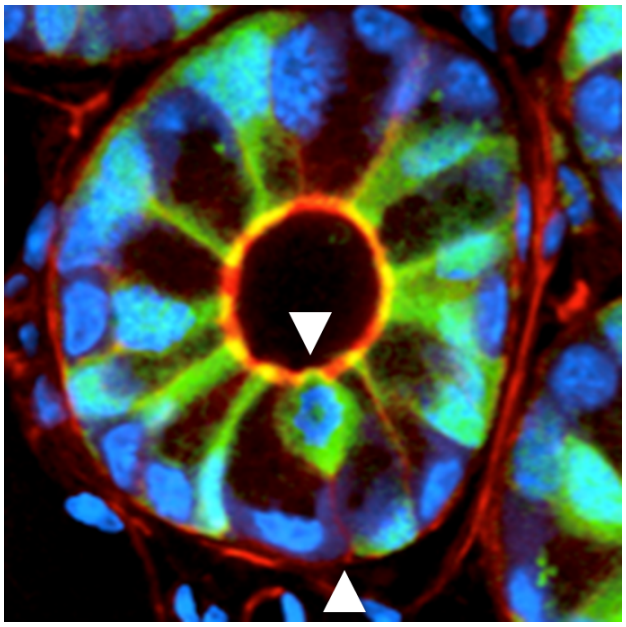

Figure 6.13: Cross section of an intestinal crypt. F-actin (red) marks the outline of cells and clearly shows the apical surface that lines the lumen of the crypt, while the cell nuclei are stained using DAPI (blue). An Lgr5+ cell (green) is dividing asymmetrically (the arrowheads point to the apical and basal regions of the dividing cell) as indicated by the apically displaced nucleus and the position of the cell body.

Figure 6.12(b) shows that the spatial distribution of division events is roughly constant throughout the proliferative compartment, with only a slight increase towards the crypt base. This coincides with the larger number of cells in this region, and the peak in anoikis events.

Figure 6.12(c) plots the spatial distribution of epithelial cells in the crypt at the final timestep (t = 500 hours). This plot indicates a higher density of cells at the base of the crypt, which is in part due to the shape of the epithelial layer for $y < 4$, as it takes account of the extra cells positioned along the flat base. The density of cells remains approximately constant moving up towards the crypt collar, save a slight increase at the junction between the crypt walls and the intercrypt table (which also takes into account the additional cells along this horizontal portion of the layer). The proportion of epithelial cells at the bottom of the crypt does not generate a number of division events proportionately higher than those further up the crypt due to the implementation of density-dependent inhibition of mitosis.

Figure 6.12(d) shows how the mean number of epithelial cells in the crypt changes over time, these results being obtained by averaging over all simulations. The error bars on this plot indicate the standard deviation at each timestep. This plot shows that the average number of epithelial cells remains approximately constant over time, at just over 50 cells.

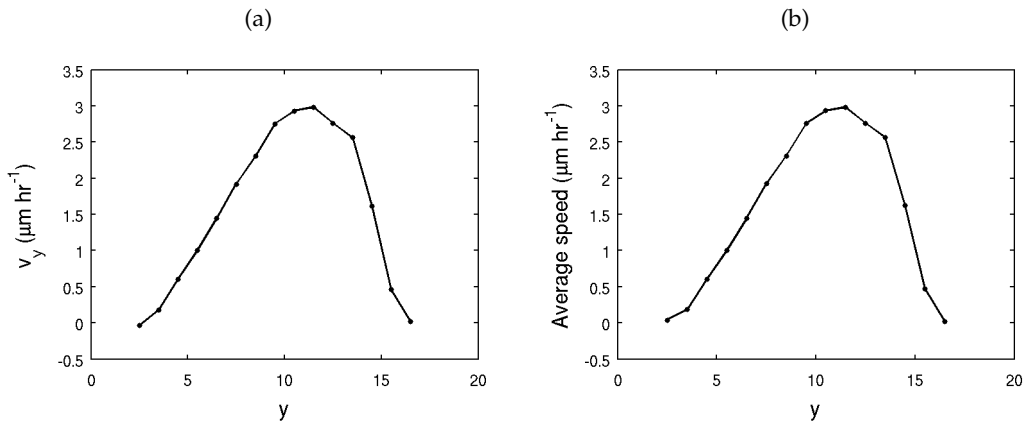

Figure 6.14: Average velocity results for multiple simulations of the cross-sectional model. (a) The vertical component of velocity, v_y, (b) the average speed, v.

The bounds of this average are less than 5 cells at each timestep, and these results correlate with the longer simulation shown in Figure 6.4.

Cell Velocity

The change in cell velocity moving up the crypt axis is also considered for these multiple simulations, and the averaged results are shown in Figure 6.14. Specifically, the y-component of the cell velocity, v_y, is given in Figure 6.14(a), and the average speed, $v = \sqrt{v_x^2 + v_y^2}$, is given in Figure 6.14(b). The results in these plots are similar to those in Figure 6.4, showing that the velocity increases moving up the crypt axis towards the collar, but then decreases on the intercrypt table, where migration is predominantly horizontal and random apoptosis events are frequent.

6.2.5 Summary

Thus far, the epithelial monolayer model proposed in Chapter 5 has been extended to represent the 2D cross-sectional geometry of the crypt, and simulation results have been presented which correspond to a typical 'healthy' crypt scenario. The proliferative compartment within the crypt is determined by a linearly decreasing Wnt profile, and all epithelial cells are assigned the same properties.

Simulation results show that a stable state of dynamic homeostasis can be achieved in this model, provided density-dependent inhibition of mitosis and a second mechanism of cell removal at the crypt collar are included. This facilitates the upward migration of epithelial cells from the crypt base, while cell numbers remain approximately constant (fluctuating

only due to the stochasticity inherent in the model). Qualitatively, these results are in agreement with what is known about the cellular behaviour in a healthy intestinal crypt. The change in cell velocity moving up the vertical crypt axis matches the linear increase towards the crypt collar found in the experimental results published by Kaur and Potten [61], and the cross-sectional cell areas are shown to agree with murine crypt data. Further, these velocity results are shown to be more accurate than those found for the earlier, cylindrical crypt models.

The cross-sectional model demonstrates a high incidence of anoikis events at the crypt base, in agreement with results found using the epithelial monolayer model described in Chapter 5. This is not commonly observed by experimentalists [131]. However, when these results are considered in light of the process of asymmetric division in stem cells, whereby one nuclei is positioned apically before reinserting basally by an as yet unknown mechanism (Figure 6.13), it is suggested that the crypt shape may play a role in forcing the alignment of the mitotic spindle for the compressed cells at the base. In the model, the compression of cells at the base forces one of the daughter cell centres to lose contact with the basement membrane, whereupon it is removed and this registers as an anoikis event. That a high incidence of anoikis events happen following division at the base of the crypt therefore indicates a mechanosensory cause for asymmetric division in the stem cells at the base of the crypt. This hypothesis is supported by experimental results outlined in Section 2.1.3, which demonstrate that cells do respond to their mechanical environment, and moreover that cytokinesis is a mechanical process [36]. It has also been suggested that the shape of cells and tissues can influence cell division via cortical tension heterogeneity which guides spindle orientation [117].

The simulation results also show that anoikis events occur at the curve of the crypt collar. As cells in this region are differentiated, it is hypothesised that such events arise due to the overcrowding of cells and negative curvature of the layer at this point, rendering cells vulnerable to extrusion. To test this, one could grow epithelial cells on curved substrates to examine the incidence of extrusion on negatively curved regions. Alternatively, cells could initially be grown on a flat substrate, which is bent once the cells reach confluence.

Now that a stable model has been defined, it is possible to investigate the consequences of changing the properties assigned to one or more cells, in order to consider the downstream effects of genetic mutations involved in the early stages of the adenoma-carcinoma sequence. Such experiments are now considered, beginning with an *in silico* investigation of the irradiation experiments carried out by Kaur and Potten [61].

6.3 *In silico* Experiments

The overall goal of this work is to develop a predictive model with which to conduct *in silico* experiments which investigate emergent phenomena that are the consequence of subcellular and cellular abnormalities. This section is concerned with simple experiments that examine the effects of abnormal cell behaviour, implemented by varying individual or collective cell properties. Starting with an *in silico* reproduction of Kaur and Potten's cell migration experiments [61], these investigations focus on gaps in the biological understanding of how cellular dynamics and tissue homeostasis are controlled, as well as how and when these processes break down.

As detailed in Section 2.2, the inactivation of the APC tumour suppressor gene is generally accepted to be the initiating event in CRC, and the breakdown of crypt dynamics follows a progression characterised by the adenoma-carcinoma sequence (Figure 2.9) [37]. It is known that loss of APC function leads to abnormal or even halted migration of a cell, increased proliferation and a failure to differentiate [104]. Such mutant cells then produce progeny that also exhibit these premalignant cell properties. By characterising abnormal properties in individual epithelial cells within the cross-sectional model, it is possible to track the downstream effects on the crypt structure, and these experiments are detailed here.

6.3.1 Eliminating Cell Division

The experiments of Kaur and Potten [61] are cited widely as proof that there is an active driving force regulating cell migration in the crypt, and that this movement is not solely due to mitotic pressure arising from cell division in the lower proliferative compartment. Despite this, no mechanism for cell migration in the crypt is yet known, but it is hypothesised that movement could occur due to the presence of signalling gradients along the vertical axis, or by active protein synthesis of 'motility molecules' [63].

In their study, they applied irradiation and cytotoxic agents to murine crypts, excised from mice aged between 10-13 weeks. Specifically, groups of four replicates were injected with tritiated thymidine (^{3}HTdR) to label dividing cells, and radiation was applied shortly after to reduce the mitotic index to zero rapidly, halting proliferation completely for at least 8 hours (cell death still occurred). It is shown that the mitotic activity did not return to the pre-irradiation level over the first 12 hours of treatment, but started to increase after 8 hours.

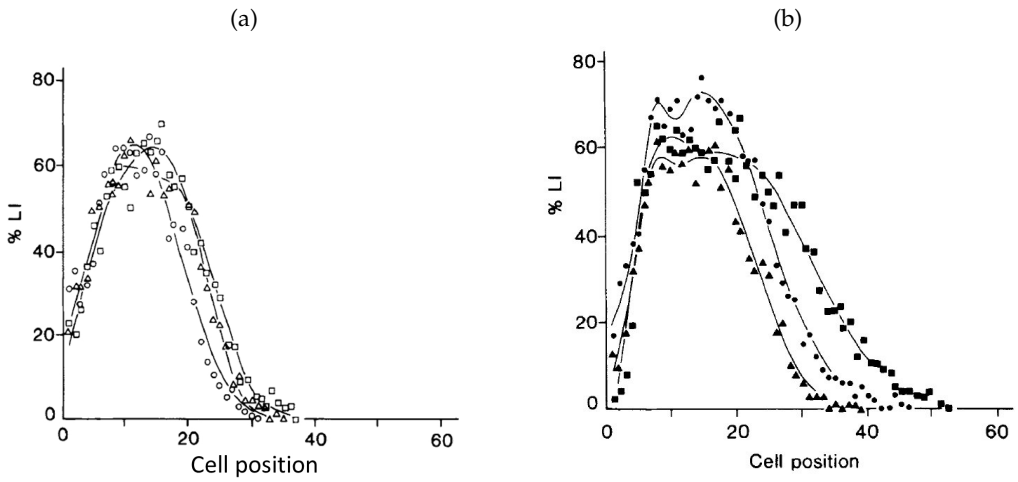

Figure 6.15: An example of the experimental results from Kaur and Potten [61] showing the labelled cell distributions at specific time intervals following irradiation (%LI corresponds to the percentage of labelled cells in the crypt): (a) (○) 1 hour, (△) 3 hours, (□) 6 hours. (b) (●) 9 hours, (▲) 12 hours, (■) 24 hours. These distributions indicate that the labelled cells are moving up the vertical crypt axis over time. Modified from Kaur and Potten [61].

Each replicate was examined at delay periods of 1, 3, 6, 9, 12 and 24 hours following interference, following the scoring technique detailed in the separate paper by the same authors that investigates the circadian changes in migration velocity [62]. Cell velocities were calculated from changes in the displacements of labelled cells, using the labelling index distributions at each timepoint shown in Figure 6.15. To obtain these distribution curves, 25 crypts were sampled per animal to give 100 crypts for each group of 4 mice, with crypts selected for scoring provided there were a sufficient number of cells (≥ 17) and the crypt was clearly longitudinally sectioned. Cells were numbered moving up from the base of the crypt along one side towards the crypt collar, such that each cell position along the x-axes in Figure 6.15 corresponds to a single cell location. In each crypt, whether the cell in each positioned was labelled or not was recorded, and the results collated over all crypt samples to give the average labelling index at each cell position for the group of mice.

The shift of the distribution curves up the longitudinal crypt axis demonstrates that the labelled cells are migrating upwards over time. That continued displacement following irradiation was observed in these cells indicates that cell division is not the sole mechanism regulating epithelial cell migration in the crypt.

This experiment is recreated here using the cross-sectional model, by eliminating cell division in the crypt entirely once a stable equilibrium has been achieved. This is illustrated in Figure 6.16. Fifty simulations were run, and the behaviour of the crypts monitored for a maximum of forty hours after mitosis was halted. Simulation results were recorded in

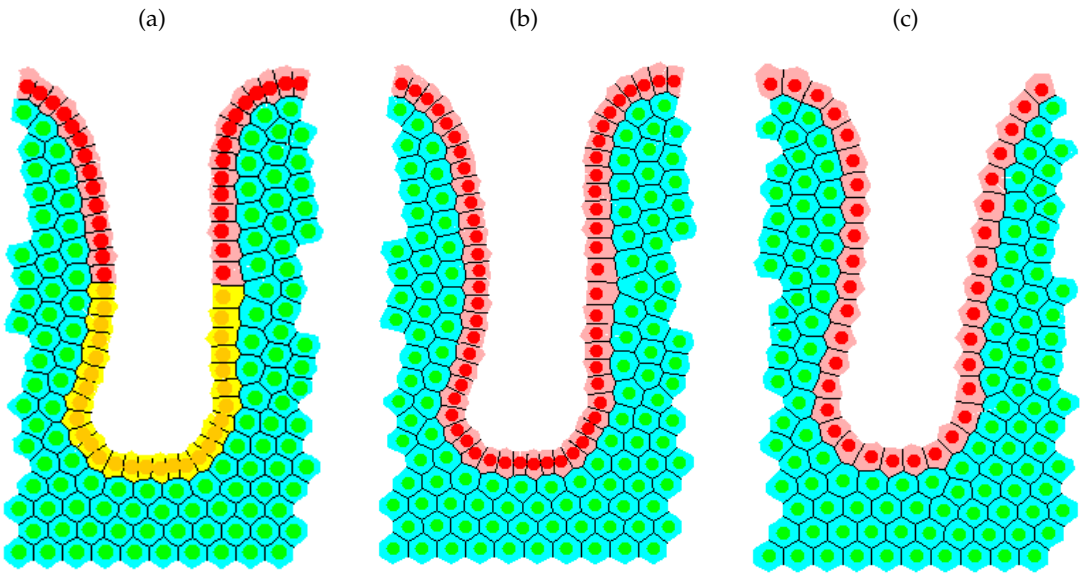

Figure 6.16: Snapshots of the crypt (a) before elimination of division, (b) immediately after elimination of division, (c) 24 hours after elimination of division.

each case up to the point at which cell death lead to the formation of a hole in the monolayer which could not be filled without cell division. In most simulations, the monolayer maintained its integrity for at least twenty hours following the simulated irradiation. In many cases it did so for longer, even up to the maximum of forty hours.

A typical snapshot of the crypt before and after elimination of mitosis, as well as 24 hours later, is shown in Figure 6.16. The averaged results for all 50 simulations are presented in Figure 6.17, where the cell velocities have been tracked for up to 24 hours following irradiation.

Figure 6.17(a) plots the change in epithelial cell number at each timestep for the 24 hours following irradiation. This shows that the epithelial cells steadily decrease in number, which is due to continued apoptosis events in the absence of proliferation.

Figure 6.17(b) plots the change in the average upward component of cell velocity, v_y, within defined horizontal bands of unit width, as described in Section 6.2.2. This plot suggests that, despite the decrease in total number, the cells are still migrating up the crypt. However, when compared with Figures 6.4(b) and 6.14(a) for the healthy crypt simulations, it is clear that stochastic apoptosis events are influencing the change in velocity. Despite this, there is still an increase in v_y moving up from the crypt base, and a decrease towards the crypt collar.

Figures 6.17(c) and (d) show how the distribution of the epithelial cell areas changes

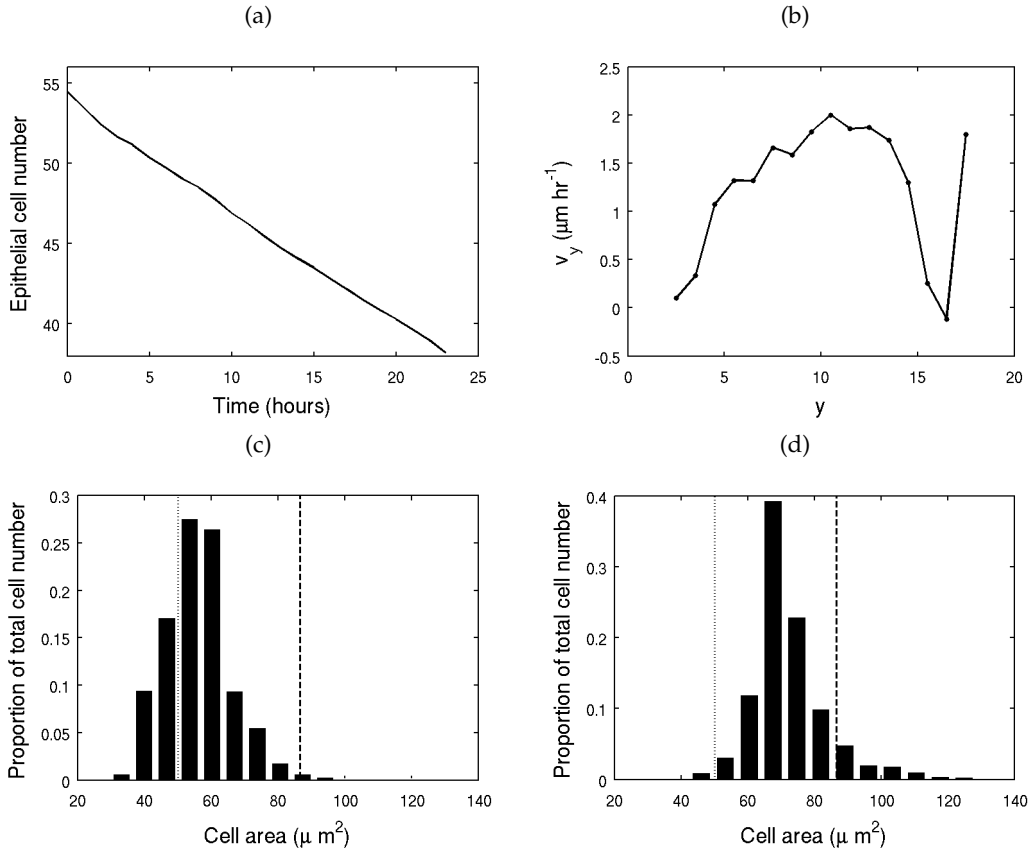

Figure 6.17: The change in cell velocity and area following elimination of cell proliferation. (a) The change epithelial cell number, averaged over all simulations, (b) the change in v_y with y, (c) a histogram of epithelial cell areas taken at equilibrium, before elimination of division, (d) a histogram of epithelial cell areas taken 24 hours after elimination of division.

when proliferation is halted. Figure 6.17(c) corresponds to an equilibrium crypt, while Figure 6.17(d) corresponds to a crypt 24 hours after irradiation. Also marked on these plots is the equilibrium cell area (86.6μm^2), which a cell will adopt if allowed to relax fully, and the threshold area above which cell division can occur (50μm^2). These plots illustrate that after 24 hours, the areas of the epithelial cells are larger, on average, because there is less compression in the layer and the crypt is relaxing. This behaviour is evident from snapshots of typical simulations (compare the results presented in Figures 6.16(b) and (c)).

To compare these results directly with the results presented by Kaur and Potten [61], Figure 6.18 plots the labelled cell distribution at different time points for a typical case, up to 24 hours post interference. In this example, those cells that were proliferative before eliminating mitosis are labelled, and the plots track the percentage of labelled cells within bands of unit width ($2 \leq y < 3$, $3 \leq y < 4$ etc.) after 1, 3, 6, 9, 12 and 24 hours. These results can be compared with those shown in Figure 6.15, and the same trend is revealed:

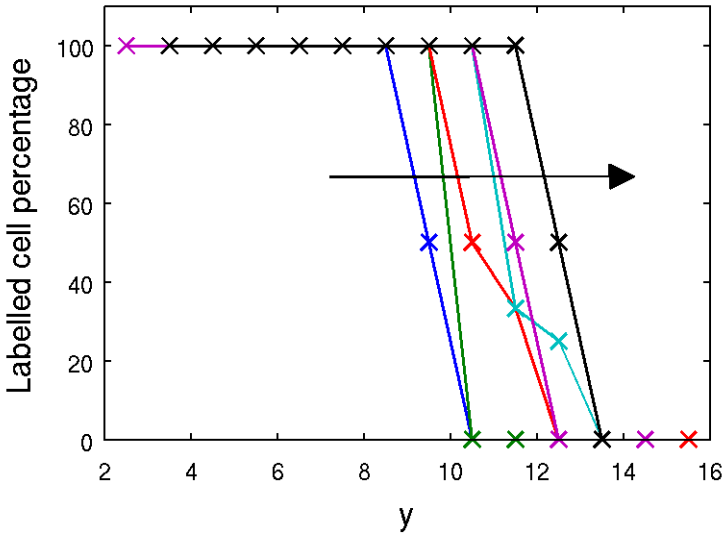

Figure 6.18: The change in the distribution of labelled cells following the elimination of cell division. Here, the arrow indicates the movement of the distribution with increasing time (after 1 hour, 3 hours, 6 hours, 9 hours, 12 hours and 24 hours).

the labelled cell distribution moves further up the crypt axis over time (indicated by the arrows). There is a difference in the shape of the distributions shown in Figure 6.18 with those found by Kaur and Potten [61], but this is due to the original locations of the labelled cells, which initially occupy $2 \leq y \leq 10$, compared with the experimental set-up, where only those cells in S-phase were labelled.

Summary

These *in silico* experiments reveal that epithelial cells in the crypt will continue to migrate in the absence of mitosis, in some cases for up to forty hours post irradiation, without any additional forces needed to propel their movement. The cause of this movement is the relaxation and growth afforded to cells by the space created by sloughing at the crypt collar. Additionally, in reality, migration may not only occur as the crypt relaxes, but as a consequence of the merging of cell columns, causing the crypt to narrow – a similar hypothesis was proposed by Loeffler et al. [71] as described in Section 3.1.1. It is not possible to investigate this hypothesis in the 2D model, but this would be possible in a 3D crypt model. Given that cell removal at the collar is modelled here as random and independent of other events, it is not possible to track simulations beyond the point at which a hole forms in the layer. However, it is arguable that, biologically, the cells will not continue to migrate indefinitely without further mitosis events as there would not be enough cells in the crypt to prevent loss of barrier function.

It should also be noted that in the experiments of Kaur and Potten [61], the mitotic index remained close to zero only for the first 12 hours of the experiment. It is likely, therefore, that mitotic events occurring after this time will have influenced the results of the investigation. Here, however, mitosis is completely eliminated, and migration is still observed. In combination with the results of Section 5.4.6, this suggests that cell division and apoptosis work together to generate cell migration in the crypt, but that it is the action of cell removal at the collar which makes it possible. Moreover, this movement has been found without imposing additional signalling gradients, or assuming an explicit active migration force. However, it is not possible here to rule out the presence and influence of such factors without further experimental work in a wet lab.

6.3.2 Aberrant Cell Properties

Inactivation of the APC tumour suppressor gene is one of the initiating events in CRC [17, 41, 55, 104], leading to abnormal or even halted cell migration, increased proliferation and a failure to differentiate. These premalignant properties are conferred onto mutant cell progeny. Further, cancerous cells from a range of tissues are able to resist apoptosis [2]. In particular, when the p53 gene is defective in malignant cells, proliferation continues and cells do not die. If a cell does not undergo apoptosis then hypertrophy can result, disrupting the tissue architecture.

The consequence of introducing mutant cells to the crypt population is now investigated by assigning to these cells the following aberrant phenotypes: arrested differentiation, reduced migration and failed apoptosis. Corresponding simulation movies are provided on the attached CD, as described in Section 6.4. The effects on the structure of the crypt are reported, and in particular the properties required to ensure persistence of mutated cells are identified, which is crucial to advancement in the adenoma-carcinoma sequence. In all simulations, unless otherwise stated, it is assumed that $\beta = 12$, $1/R = 0.3$ and $\mu = 45$.

Failure to Differentiate

To investigate the consequence of failed differentiation in the crypt, individual cells are assigned a single mutation that removes all dependence on the imposed Wnt gradient and are introduced to a simulation once dynamic equilibrium has been reached. These cells continue to divide irrespective of location, until being removed by apoptosis. Simulations reveal that despite a failure to differentiate, on average, such isolated mutant cells tend not to persist in the crypt. This depends on location, however, as if a mutant is introduced at

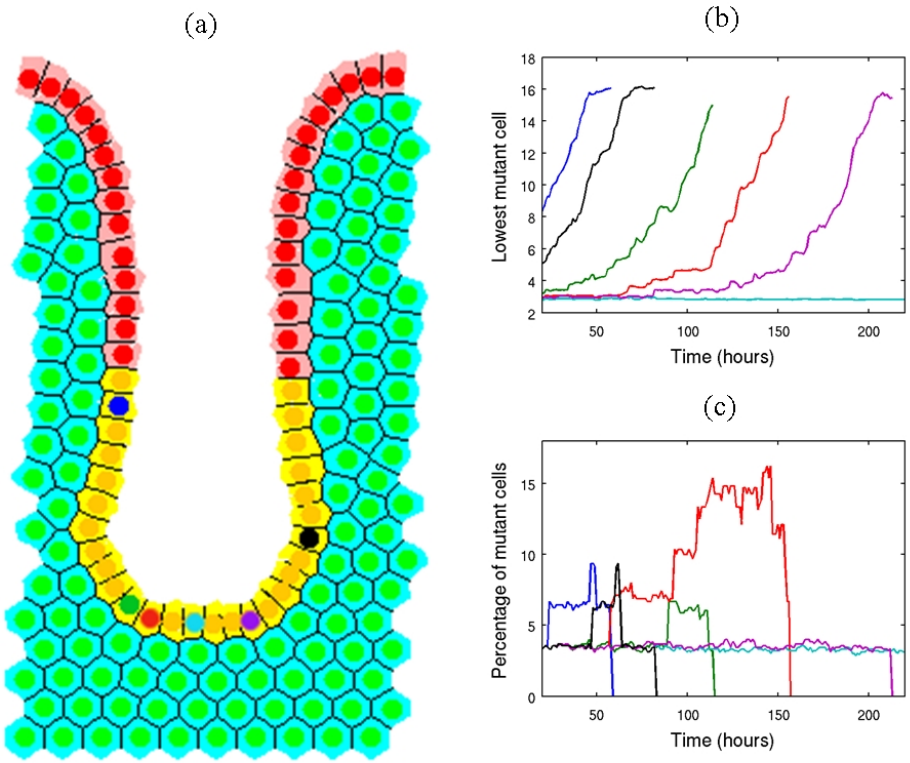

Figure 6.19: Tracking cells with a single mutation that arrests differentiation. (a) A snapshot of the crypt before mutant cells are introduced, where the nodes marked in different colours correspond to those shown in the plots. (b) Typical tracks of the lowest mutant cell originating from different locations up the vertical crypt axis, (c) the percentage of mutant epithelial cells over time.

the very bottom of the crypt base, it is more likely to be under compression and not divide due to density-dependent inhibition of mitosis, and so will remain in position. Moreover, if such a cell does divide, this compression will often lead to an anoikis event, as discussed in Section 5.4.1. Cells located slightly further up experience a lesser degree of compression, and so will divide more often, and the time afforded to generate mutant progeny is then dependent on how low the original mutant cell is in the crypt.

To illustrate behaviour that is typical across simulations, Figure 6.19(a) marks, by colour-coding cell centres, the location of mutant cells which are individually introduced to identical simulations, as controlled by seeding the random number generator. These colours correspond to the migration tracks which are plotted in Figure 6.19(b). In this plot, the y-coordinate of the mutant cell with the lowest y-coordinate is tracked, and Figure 6.19(c) plots the corresponding percentage of mutant cells at each timestep for each track. This demonstrates the difference in behaviour observed for mutations that originate in different locations, and the spread of mutant progeny. As can be observed from these

results, mutant cells do not persist indefinitely in the crypt, save for those cells positioned at the very bottom of the crypt base ($y \approx 2$). As outlined above, such cells are often too compressed to proceed through the cell cycle due to density-dependent inhibition of mitosis. Further, the time taken to expel these mutations is similar to that found for healthy cells.

From these results, it is concluded that a single mutation which arrests cell differentiation does not confer the ability for mutations to colonise the crypt – this is in line with the normal crypt dynamics, whereby the rapid turnover of cells in the crypt is understood to provide a frontline mechanism against sporadic mutations. This is in agreement with a similar experiment conducted using the cell-centre model in a cylindrical crypt framework, which found that a mutant population that has no Wnt dependence for proliferation is flushed out, and cannot colonise the crypt [125].

Reduced Migration

A further consequence of a mutation in the APC tumour suppressor gene is that such cells can exhibit reduced or halted migration in the crypt, and again, this characteristic will be conferred on any progeny. This second aberrant property is investigated here by increasing the drag acting on the mutant cells, by increasing the viscosity parameter, η, (see Section 4.1.3). As before, differentiation of mutant cells does not depend on the Wnt gradient, but rather such cells continue to divide up to the crypt collar and until being removed by apoptosis.

Figure 6.20(a) tracks the migration of mutant cells in the crypt by plotting the y-coordinate of the lowest mutant cell when $\eta = 5$ for mutant cells, and $\eta = 1$ for all healthy cells (see Table 5.1). These tracks correspond to the same initial mutant cell as shown in Figure 6.19. The plot demonstrates that the mutant cells persist in the crypt for longer time periods than when only a single mutation is applied, and can remain for over 500 hours, depending on the location of the initial mutation. Figure 6.20(b) indicates the percentage of mutant epithelial cells in each case, showing that in the cases where the mutation remains in a low position, the percentage of mutant epithelial cells also increases, and eventually colonises the crypt in some cases.

To emphasise the effect that this additional mutation has had over the single mutation that arrests cell differentiation, Figure 6.20(c) compares six specific tracks for when only a single mutation is applied (dashed lines) with that for when two mutations are applied (solid lines). Each colour corresponds to the same initial mutant cell. In each case, the mutant

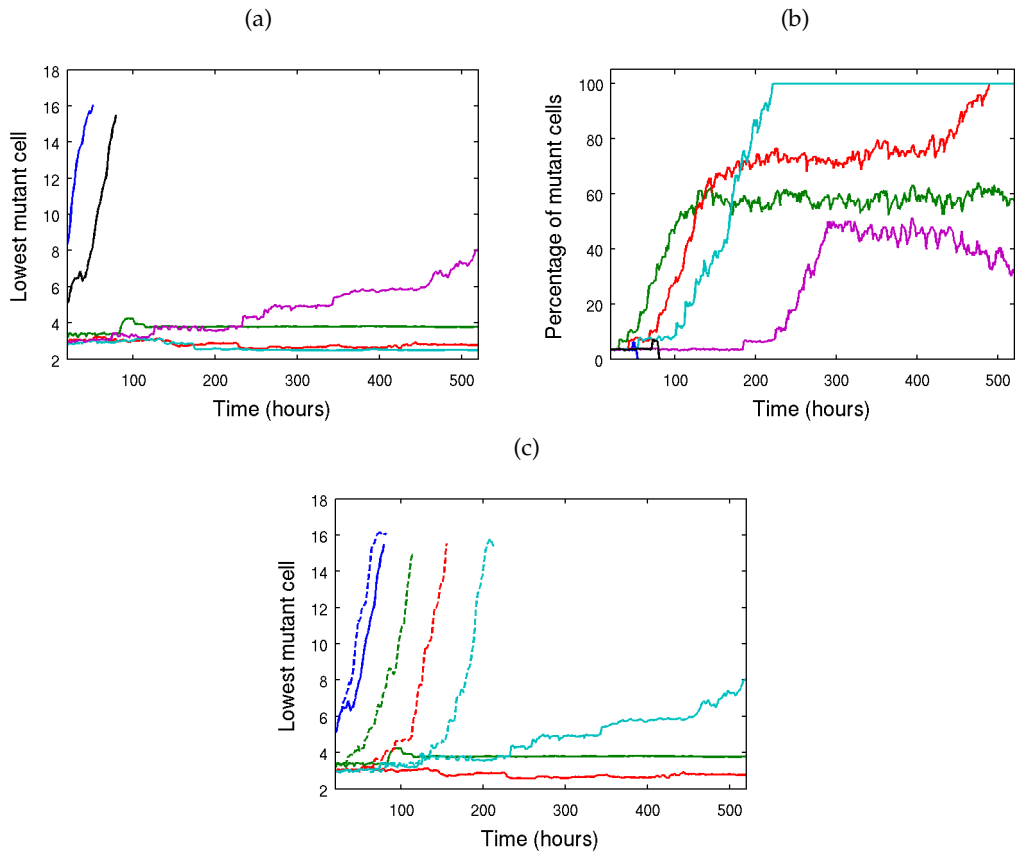

Figure 6.20: Tracking cells with two mutations: arrested differentiation and increased drag ($\eta = 5$ for mutant cells, $\eta = 1$ for healthy cells). (a) Typical examples of the y-coordinate of the lowest mutant cell originating from different locations up the vertical crypt axis. (b) The percentage of mutant epithelial cells over time. (c) Comparing the tracks of the lowest mutant cell with only one mutation (dashed lines) and with two mutations (solid lines). Tracks of the same colour correspond to the same initial mutant cell.

cells remain in the crypt for more than double the length of time, and moreover, this plot shows there are cases when a cell only persists in the crypt when the second mutation is applied.

Figure 6.21 contains snapshots taken at forty-hour intervals to illustrate an example where the mutant cell population is not completely expelled from the crypt, but also does not achieve total colonisation within 500 hours. These snapshots show that the mutations have spread throughout half of the monolayer, and as shown in Figure 6.20, this situation remains unchanged from 100 hours onwards. This example compares directly with the snapshots shown in Figure 6.10, where the same cell and progeny are labelled, but not mutated. The earlier snapshots show that the healthy, labelled cells are expelled from the crypt after 160 hours under healthy conditions. This example is important, because it reveals a case in which mutant cells can persist in the crypt over long time periods.

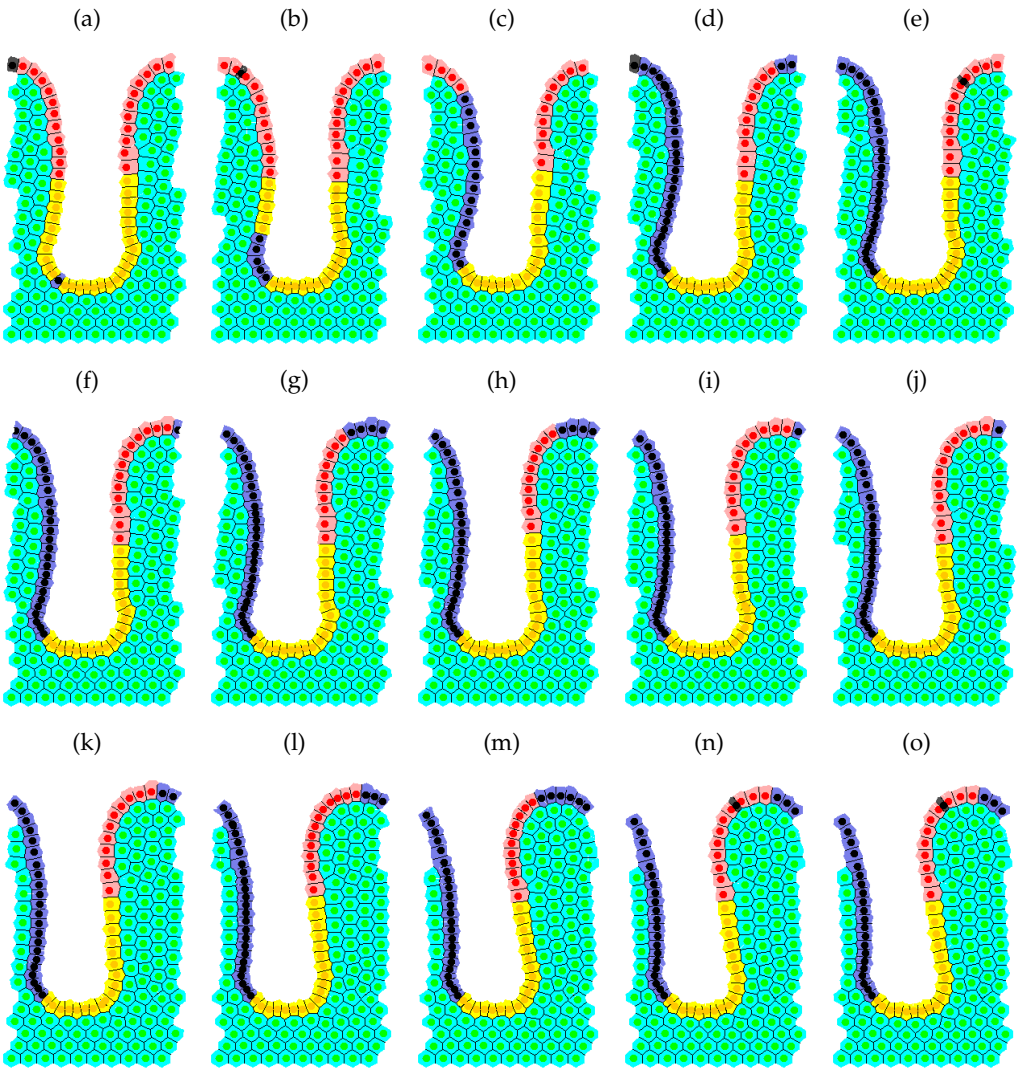

Figure 6.21: Simulation snapshots taken at 40 hour intervals, which track the migration of a mutant epithelial cell (coloured blue with a black cell centre, indicated in (a)), and its lineage, which are subsequently mutated. These mutant cells experience a larger drag term than healthy cells, $\eta = 5$, and so experience reduced migration. Cells marked in grey are apoptotic. These snapshots can be compared directly with those in Figure 6.10, in which the same initial cell and progeny are labelled, but no mutations are present. (As described in Section 4.1.5, for visualisation purposes, boundaries are assigned to each periodic mesh such that cells that move beyond the boundaries are transferred to the opposite edge. The consequence of this is seen in the snapshots from (d) onwards, as labelled cells start to appear at the opposite edge of the crypt collar.)

Further, to achieve this permanence, the initial mutation occurs in a cell close to the crypt base. Again, this is in agreement with results found from *in silico* experiments conducted using the cylindrical crypt model, whereby increased drag allows the mutant population to persist within the crypt [125].

Figure 6.22 reveals how the system dynamics change when the viscosity parameter for

mutant cells is increased: (a) and (b) correspond to $\eta = 10$; (c) and (d) correspond to $\eta = 15$. These plots show that increasing the drag (from $\eta = 5$ to $\eta = 10$) increases the average time spent in the crypt, but the effect is more pronounced on cells nearer the crypt base. However, increasing the drag to $\eta = 15$ causes a switch in the behaviour of some of these tracks, and cells that colonised the crypt under lower drag no longer do so within the same time frame. This is because increasing the drag to a very high value influences cell division via density-dependent inhibition of mitosis if the original mutant cell is positioned low enough in the crypt to be in a region of high compression. Simulations show that cells with a higher drag divide less often, as cells with a larger η are less likely to be able to move to increase area and enable cell division. With fewer mutant cells present, it is easier for the mutation to be expelled from the crypt – this is shown by comparing the red curves in Figures 6.22(a) and (c).

Another way in which the mutant cells can spread through and colonise the crypt is given in Figure 6.23, where snapshots are shown at forty hour intervals. In this case, which corresponds to the red curve in Figure 6.22(a), the mutant cells colonise the entire crypt, which is biologically equivalent to the monocryptal adenoma described in Section 2.2.1. The simulation shows that this mutation spreads in a "bottom-up" fashion. In this model, monoclonality is not observed as readily with only a single mutation which causes differentiation to fail, and this emphasises that a reduction in cell migration is key to enabling mutations to spread and persist in the crypt. This is in agreement with the hypothesis proposed by Näthke [83], who proposes that a change in migration is key to the persistence of a mutation.

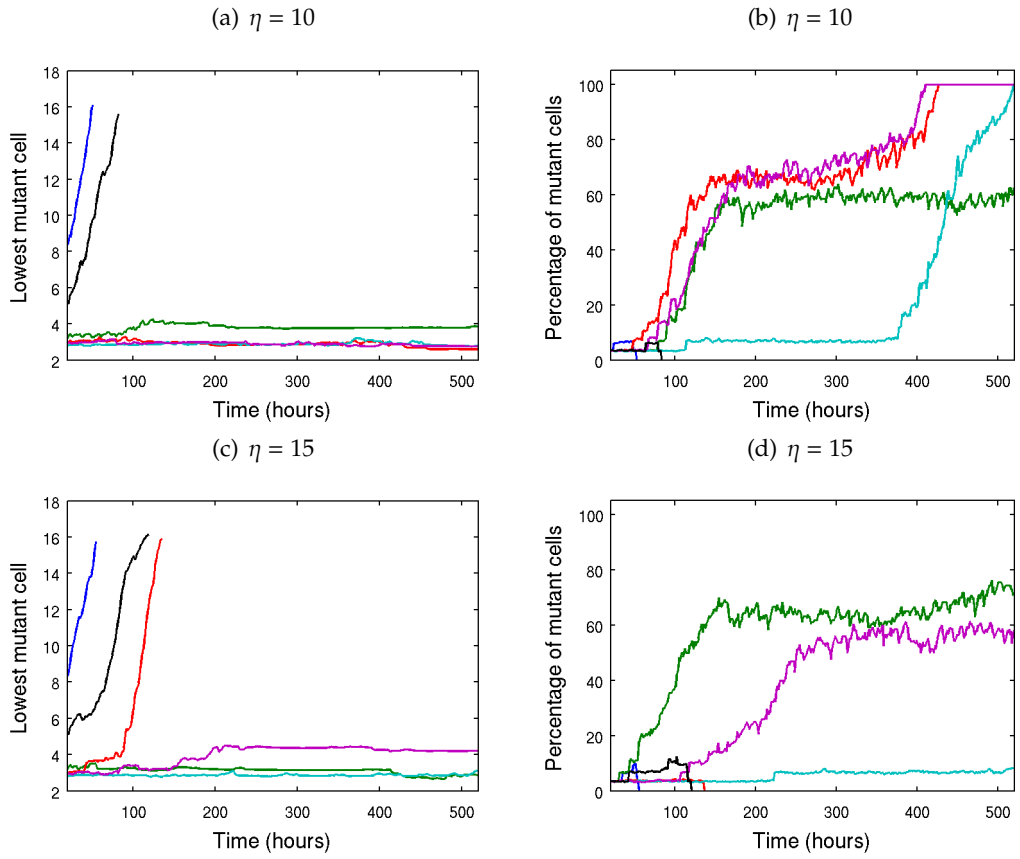

Figure 6.22: A series of plots showing how the tracks of mutant cells introduced into a normal crypt are affected by the position at which the mutation was initiated and the strength of viscous effects. (a) Tracking the mutant cells when the viscosity parameter is increased further, $\eta = 10$, (b) the percentage of mutant epithelial cells for $\eta = 10$. (c) Tracking the mutant cells when $\eta = 15$, (d) the percentage of mutant epithelial cells for $\eta = 15$.

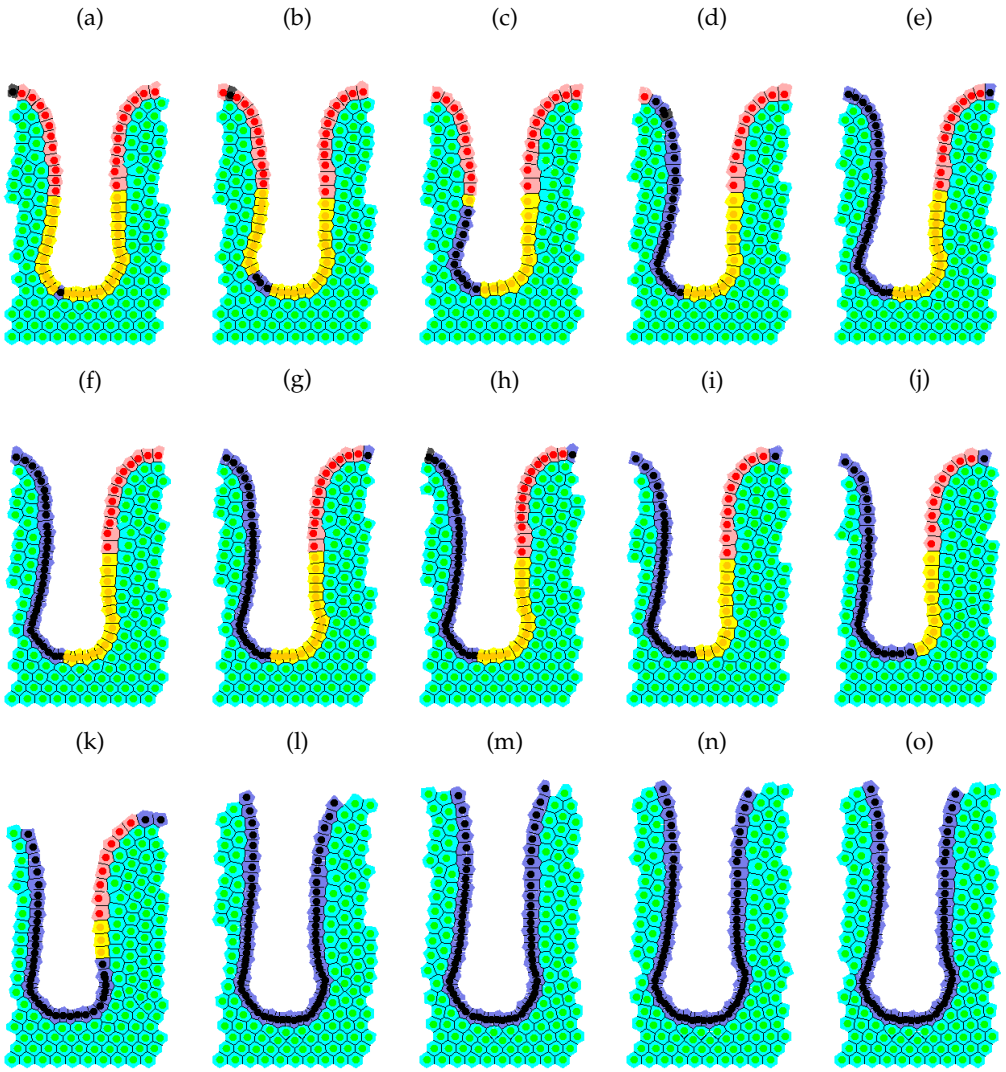

Figure 6.23: Simulation snapshots taken at 40 hour intervals, which track the migration of a mutant epithelial cell (coloured blue with a black cell centre, indicated in (a)), and its lineage. The mutant cells experience a drag term that is 10 times greater than that of the healthy cells, and as a result, experience reduced migration. Cells marked in grey are apoptotic. In this example, the mutant cells eventually colonise the entire crypt.

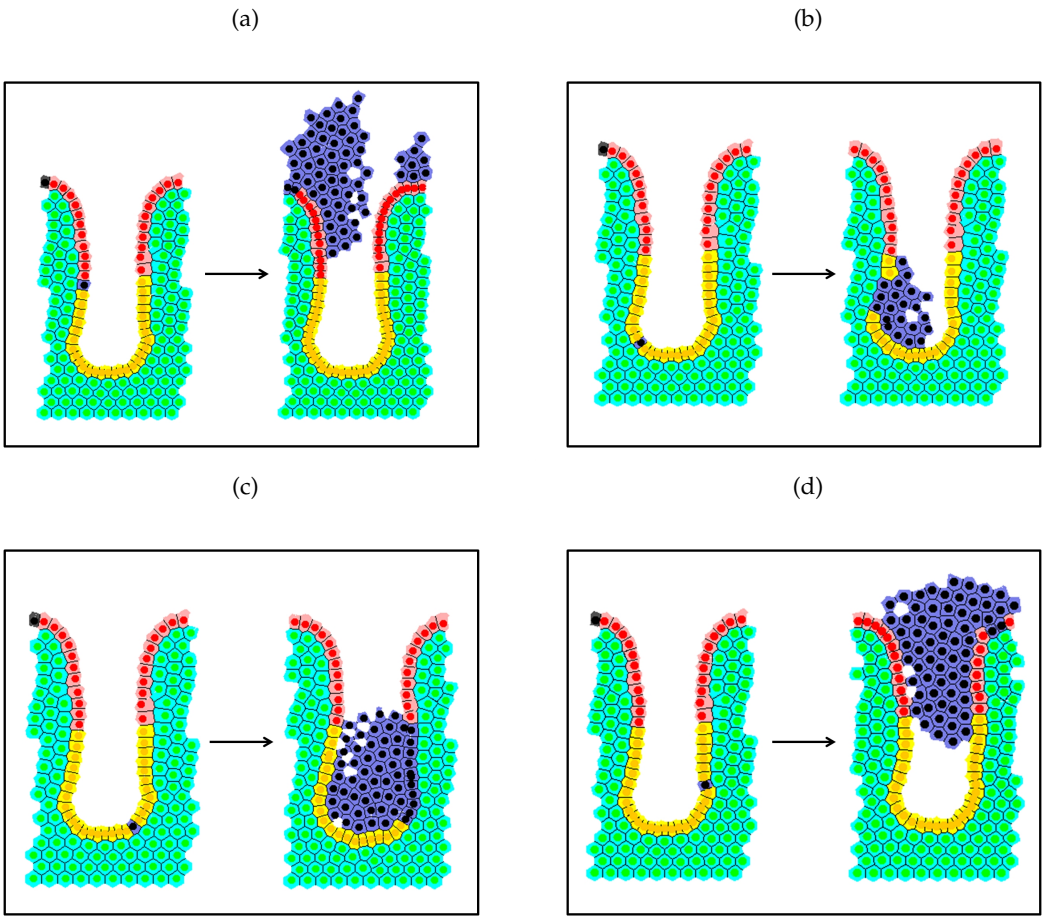

Figure 6.24: Simulation results showing the consequences of failed apoptosis in addition to arrested differentiation and reduced migration ($\eta = 5$ for mutant cells). Each box shows the different initial mutation position (left), and how this evolves and spreads throughout the crypt (right).

Failed Apoptosis

Apoptosis is crucial for maintaining normal cell turnover in the crypt, which requires that cell birth is balanced by cell loss due to anoikis and cell removal at the collar. Cancerous cells from a range of tissues may be able to resist apoptosis, and in particular, mutation of the p53 gene, which is the most common genetic change across all cancers [58], is implicated in the control of cell death [2]. When p53 is defective in malignant cells, proliferation continues and cells do not die. Further, resistance to anoikis can arise through a number of mechanisms: activated oncogenes such as Src and Ras, over-expression of the Focal Adhesion Kinase (FAK) protein and activation of growth factor receptors; many of these transformations occur during the growth of a colon tumour [128].

To investigate the consequences of failed apoptosis in the crypt model, a third mutation is introduced in addition to failed differentiation and reduced migration. This mutation

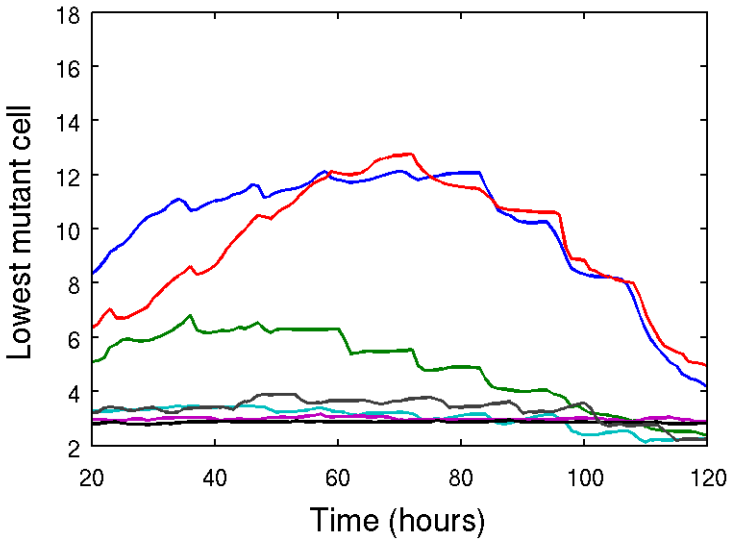

Figure 6.25: Tracking cells with three mutations: arrested differentiation, increased drag ($\eta = 5$) and failed apoptosis. Typical examples of the lowest mutated cell originating from different locations up the vertical crypt axis.

causes cells to ignore the cues for anoikis and apoptosis at the crypt collar. Simulations show that after a mutation is assigned to a single epithelial cell, the mutation quickly spreads and moves out towards the crypt lumen (displacing the ghost nodes), or upwards above the crypt collar. This behaviour is shown in the snapshots in Figure 6.24. Figure 6.25, which tracks the y-coordinate of the lowest mutation, shows that eventually the mutant cells spread downwards into the lumen. Such behaviour is relevant to understanding the formation of polyps, which occur as protrusions into the gut lumen. It is clear that should this be coupled with a loss of sensitivity to density-dependent inhibition of mitosis, as is known to be the case in cancerous cells [67], the effect would be expedited and compounded.

6.3.3 Summary

In this section, the results of *in silico* investigations using the cross-sectional model have been presented. The cell migration experiments performed by Kaur and Potten [61] have been replicated, and as they reported, cell migration is found to occur even in the absence of cell division, and over the same time period. However, as this is a mechanical model, the cause of migration under these conditions cannot be attributed to 'motility molecules' arising from protein synthesis, and no additional active forces are prescribed to push cells towards the crypt collar. Rather, the migration that occurs is due to relaxation of the

epithelial monolayer, which occurs in response to the sloughing of cells from the crypt collar. This creates space for the epithelial cells to both grow and move into.

This type of investigation is limited by the complete elimination of mitosis. In practice, a hole will eventually develop in the layer if cells continue to migrate towards the collar in the absence of cell division. This behaviour is replicated in the cross-sectional model. It is therefore possible that cell migration, death and mitosis are linked in such a way that cell death can stimulate cell division, rather than just enabling it, in the event that there are too few cells in the monolayer. This hypothesis fits with the concept of stem cell plasticity, introduced in Section 2.1.2, in which the stem cells are capable of regenerating the tissue following injury [19, 28].

The effect of introducing aberrant cell properties has also been investigated via the accumulation of mutations that affect cell differentiation, migration and apoptosis. The results indicate that a single mutation which halts differentiation in mutant cells does not confer persistence to these cells in the crypt, which are expelled from the crypt by the normal upward migration and sloughing at the collar. However, such persistence is observed in cells that combine failed differentiation with reduced migration. It is demonstrated that cells starting sufficiently low in the crypt can persist, proliferate and colonise the crypt over long time periods to produce the equivalent of a monocryptal adenoma. This is important in understanding the evolution of tumorigenesis, as accumulated mutations are required to progress through the adenoma-carcinoma sequence, and this happens over a timescale of months and years.

The introduction of a third mutation, representing resistance to apoptosis, demonstrates how quickly excess cell growth can affect the integrity of the crypt structure. Mutated cells quickly spread outwards into the lumen and upwards above the crypt collar. Combined with the initial two mutations, and without the normal cues for density-dependent inhibition of mitosis, such a change in cell behaviour later in tumorigenesis would be key to the formation of polyps.

6.4 Computation

A typical simulation of 100 cell hours of the cross-sectional model presented in this chapter requires approximately 15 minutes of CPU time on a desktop Linux PC with two quad core 2.83GHz Intel(R) Xeon(R) processors. Comparing this with the run time of the epithelial monolayer model presented in Chapter 5, the cross-sectional model runs approximately 2.5 times slower (see Section 5.5). This increase in run time is due to the increase in

cell number, and the additional model components that are considered along with the more realistic geometry, such as Wnt-dependent proliferation. The numerical timestep implemented for this model is identical to that used for the growing epithelial monolayer model in Chapter 5.

Movies are provided on the attached CD which correspond to the following typical simulation examples.

- Movie 7: From Section 6.2, this is a typical example of the cross-sectional model with parameters $\beta = 12$, $\mu = 45$, $1/R = 0.3$. In this simulation, cell migration occurs up the vertical crypt axis where epithelial cells undergo apoptosis randomly, or by anoikis upon losing contact with the basement membrane.
- Movie 8: From Section 6.3.2, this is an example of a simulation where a single mutant cell (coloured blue) is introduced to the epithelial monolayer which does not exhibit Wnt-dependent proliferation. Consequently the mutant cell, and its progeny, continue to divide irrespective of location in the crypt. As discussed in Section 6.3.2, however, this is not sufficient to confer persistence on the mutant population.
- Movie 9: From Section 6.3.2, in this example, a mutant cell is introduced to the epithelial monolayer which experiences increased viscosity ($\eta = 10$ compared with $\eta = 1$ for healthy cells), in addition to Wnt-independent proliferation. In this example, the mutant population eventually colonises the crypt after 220 hours.
- Movie 10: From Section 6.3.2, this is an example of a simulation where a mutant cell is introduced which divides independently of the imposed Wnt gradient, experiences increased viscosity and ignores all apoptosis cues. The mutant progeny also demonstrate these characteristics. In this simulation, it is shown that the mutant population divides outwards, into the crypt lumen.

6.5 Discussion

This chapter focuses on the application of the model of a growing, deformable epithelial monolayer, introduced in Chapter 5, to a new geometry: a 2D cross-sectional slice of the colonic crypt. The aim is to investigate how the geometry and tissue structure influence, and are influenced by, the cellular dynamics of the crypt. A linearly decreasing concentration gradient of Wnt factors is imposed along the vertical axis of the crypt, and a threshold is prescribed below which epithelial cells are defined to be differentiated. This is designed to mimic the known proliferative hierarchy in the crypt.

It is found that the application of the basement membrane force allows the shape of the crypt to evolve and deform, removing the need to impose a fixed geometry. This is a key aspect of this work, given that, with the exception of the work of Drasdo and Loeffler [31], all previous models have assumed a fixed geometry [21, 76, 87, 123], and this feature permits investigation of the destabilisation of the crypt structure.

Parameter values are identified in Chapter 5 for a sufficiently strong basement membrane force, which balances with the interactive cell forces that encapsulate cell-cell adhesion and limited compressibility. These parameters are found to generate a stable monolayer, and hence are applied to the extended geometry. Results are presented from stable simulations under typical, healthy conditions, which show that crypt homeostasis can be achieved, in which repeated mitotic events evolve to force consistent epithelial cell migration towards the crypt collar, without compromising the overall structure and architecture. This is characterised by a steady, constant turnover of cells, achieved in the presence of known constraints on the number of dividing cells, and with the application of two distinct mechanisms of cell death – anoikis, and cell removal at the crypt collar. The increase in cell velocity moving up the crypt axis is in agreement with experimental results found by Kaur and Potten [61], and differs from results found using the earlier cylindrical crypt model only insofar as the geometry changes at the crypt base and collar. Hence it is concluded that the geometric refinement has increased the accuracy of these results.

As for the epithelial monolayer model investigated in Chapter 5, the cross-sectional model demonstrates a high incidence of anoikis events at the crypt base. This is not commonly observed by experimentalists [131]. However, when these results are considered in light of the process of asymmetric division in stem cells (see Figure 6.13), whereby one daughter cell nucleus is positioned towards the lumen before being pulled back into the layer, the model results suggest that crypt shape may play a role in forcing the alignment of the mitotic spindle for the compressed cells at the base. This therefore indicates a mechanical cause for asymmetric division in the stem cells of the crypt. Again, anoikis events are found to occur at the curve of the crypt collar. As cells in this region are now differentiated, such cases arise due to the overcrowding of cells and the negative curvature of the layer at this point.

In the absence of extensive experimental data on cell forces to compare these results to (which is in part hindered by the simplified nature of the model), the model remains largely phenomenological, and so it is only possible to make qualitative inferences at this stage. Despite this, the hypothesis regarding the link between cell removal at the crypt collar and density-dependent inhibition of mitosis enabling cell migration is upheld

here, and remains a plausible, testable hypothesis. It is also possible to investigate the consequences of aberrant cell properties (see Section 6.3), to highlight the necessary and sufficient conditions for a permanent switch to abnormal crypt dynamics.

By imposing the same constraints on cell division, the behaviour of this model yields results which are similar to those found by Kaur and Potten [61] in their cell migration assays – namely, that cell migration can continue in the absence of mitosis. However, given that active migration is not imposed in this model, but rather emerges as a consequence of prescribing the known, basic mechanical constraints acting in the crypt, it is inferred that the observed migration may be a consequence of relaxation of the epithelial monolayer. Such relaxation occurs over the time frame considered by Kaur and Potten [61], and often over longer periods, extending to 40 hours. However, it is not possible to completely detach mitosis from cell migration in the crypt, simply because migration will not occur if the layer is not continually replenished to maintain barrier function. In contrast, as shown in Section 5.4.4, the model reveals that cell migration halts if cell removal at the collar is not imposed.

Simple experiments have been conducted to examine the effect of accumulated mutations within the crypt. These experiments show that, in addition to a failure to differentiate, mutated cells need to reduce migration in order to persist in the crypt. Further, mutations that originate lower in the crypt are more likely to persist and produce mutant progeny. These results are in agreement with those found by Walter [125], in which investigations conducted using both discrete cell-centre and cell-vertex models, as well as a continuum model, concluded that increasing the drag increases the likelihood of a mutant population persisting in the crypt. However, it was found in Section 6.3.2 that a very large drag acting on mutant cells, if the initial mutation starts very low in the crypt, can delay or prevent colonisation. This is because the mutant cell cannot migrate to increase its area sufficiently to overcome density-dependent inhibition of mitosis and divide. It is also shown here that arrested apoptosis subsequently allows mutated cells to grow and multiply out towards the crypt lumen, and above the crypt collar, and this process is expedited by the existing mutations.

When constructing a mathematical model of a biological system, it is wise to keep the model as simple as possible, focussing on the key components and understanding the impact of their interactions without over-complicating the description and analysis required [79]. With this in mind, the current 2D cross-sectional model has yielded insight into the biological system, but there are limiting factors which prevent full examination of the

destabilisation of the crypt structure that occurs in the progression from a healthy system to the growth of a malignant tumour.

As the 2D cross-sectional model consists of a 1D chain of cells, it is only possible for epithelial cells to move vertically or to displace the surrounding stroma. Consequently, if a mutant cell has inhibited migration, this will always affect those cells directly beneath it in the chain. In reality, these cells would be able to move around a blockage by moving laterally across the inner surface of the crypt. To correct this, it would not be sufficient simply to apply radial symmetry to the model, as this method would produce unrealistic results from the imposed symmetry, causing mutations to spread uniformly upwards as cells migrate. This would not be the case in a full 3D model which permits lateral movement of the cells around the inner surface of the crypt, and because of this, false positives observed in the 2D model could be eliminated. For example, a more detailed response of the system to the introduction of cell mutations could be obtained, and meaningful experiments to investigate the "top-down" and "bottom-up" theories could be conducted. In addition to this, it would be possible to define a stem cell compartment within the crypt, distinguished from the transit cell compartment by specific proliferative properties. This would enable investigation of stem cell number in the crypt, an open question within the field, and how this affects cell dynamics.

The additional degrees of freedom associated with cell movement introduced by a 3D model will increase the scope for accurately modelling the response of the system to different cellular events. For example, this extra freedom will influence the extent to which density-dependent inhibition of mitosis occurs. Also, it will be possible to model the merging or rearrangement of cell columns, causing the lumen to narrow or widen should the number of cells decrease or increase. This is likely to have a bearing on the persistence of mutations in the crypt. Therefore, extending this work to 3D will provide greater and more accurate insight into the spread of mutations and the subsequent effects at the tissue level. The initial steps towards a complete extension of this form are considered in the next chapter.

Chapter 7

A Three-Dimensional Model of a Growing, Deformable Epithelial Monolayer

Thus far a new 2D model of the colonic crypt has been proposed, which defines a deformable, cross-sectional geometry that evolves in response to interactive cell-cell forces and a novel basement membrane force. This new force captures the structural stability afforded to the epithelial monolayer by the extracellular tissue components, and is assumed to depend on the local curvature of the monolayer. By acting to maintain a prescribed curvature, which varies with cell position, the shape of the *in silico* crypt adapts and deforms according to local cell movements.

As already discussed, this simple model has afforded insight into the mechanisms at work in the crypt. Simulations suggest that crypt shape may influence cell death at the crypt collar and also the cellular decision relating to asymmetric or symmetric division. Further, these investigations support the negative pressure hypothesis [63] as a possible mechanism underlying cell migration in the crypt. It is suggested that feedback may exist between cell death towards the collar and density-dependent inhibition of mitosis, whereby cell loss generates a negative pressure on cells lower in the crypt which move upwards in response, thereby maintaining barrier function. *In silico* investigation reveal that this is a plausible mechanism to explain the cell migration patterns observed by Kaur and Potten [61] when mitosis is eliminated from the crypt.

Simple *in silico* experiments have also been conducted using the cross-sectional model to examine the consequences of accumulated genetic alterations. These results are in agreement with those generated from other discrete and continuous models [125], and confirm the hypothesis of Näthke [83], that a reduction in migration can confer persistence

on mutated cells, enabling them to colonise the epithelium, and ultimately, to accumulate further mutations over time.

Despite the insight that it provides, the 2D model represents a highly idealised description of what happens *in vivo*, as the movement of epithelial cells is restricted to a 1D chain. This precludes a realistic examination of cell migration, as well as the reproduction of deformation of the tissue structure under abnormal conditions, which has been observed experimentally in the form of crypt budding and fission. This chapter focuses on extending the model definition to 3D, considering a cuboid geometry and beginning with a definition of the basement membrane force in Section 7.1.2, analogous to that proposed for the 2D model in Section 5.1.5. This is redefined here due to the additional complexity of the 3D Delaunay triangulation. The results of *in silico* experiments are then presented in Section 7.2, to show how this extended force definition gives results which are consistent with those found for the 2D case.

Section 7.4 directly discusses the challenges and limitations associated with the computational implementation of the models presented in this thesis, both specifically to the integration of code written by a new user with the existing Chaste code base, and to the 3D model definition itself. Directions for future work are also discussed, which focus on the definition of a realistic crypt geometry in 3D, and the additional work that is required in order to produce a comprehensive model.

7.1 Model Extensions

This section is concerned with the extensions that are required to define a 3D model of a growing, deformable epithelial monolayer, equivalent to that proposed in Chapter 5 for a 2D monolayer. An off-lattice cell-centre framework is still employed, so that cell centres are represented by nodes which are connected using a Delaunay triangulation, with interactive forces defined along the lines of the triangulation according to Equations (4.2) and (4.3). The added complexity of the Delaunay triangulation in 3D space demands that the basement membrane force be updated, and this is described in Section 7.1.2.

7.1.1 Geometry

As in 2D, a simple geometry is defined to facilitate investigation of the effect of the basement membrane force, which is shown in Figure 7.1(a). A 7 x 7 x 5 cuboid of cells is considered, in which a monolayer of epithelial cells lies atop a block of quiescent, stromal cells. A

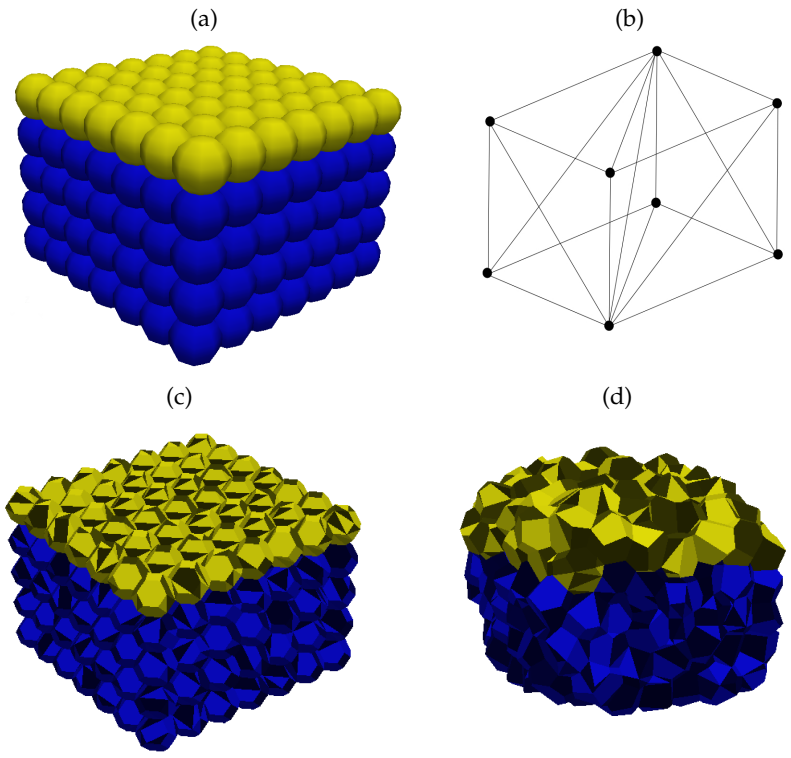

Figure 7.1: (a) The simple 3D configuration defined to investigate growth of a monolayer of proliferating epithelial cells (yellow) attached to a bed of non-proliferating stromal cells (blue). Here, cell centres are connected using the Delaunay triangulation and cells are visualised as regular spheres. (b) An example of the 3D Delaunay triangulation of four cell centres (indicated by the black circles at the vertices of the cuboid). Given that the Delaunay triangulation is more complicated than in 2D, only a small number of cells is shown here. Each cell centre belongs to at least one tetrahedral element, and these elements are used in the basement membrane force calculation described in Section 7.1.2. (c) An example of the cell configuration in (a) where instead ghost nodes have been included to enable visualisation of the cells by their Voronoi regions. (d) A snapshot of the cell configuration once it has relaxed, where cells are visualised by their Voronoi regions.

Delaunay triangulation is used to define cell-cell connectivity, and an example of this is shown in Figure 7.1(b) for four cell centres. As for the 2D model, the bottom row of stromal cells are pinned in position.

To prevent the model from becoming too computationally expensive, ghost nodes are not implemented in this framework. Rather, a cut-off length is imposed, beyond which there is no force acting along a particular spring. As explained in Section 4.1.2, without ghost nodes, it is not possible to visualise cell shapes from the corresponding Voronoi region, as there will be infinite tessellations on the boundaries. However, including a sufficient number of ghost nodes greatly increases the computational intensity of the simulation, due to the increase in the overall number of nodes. For this reason, cells are depicted as regular spheres, which also makes it easier to visualise what is happening throughout a

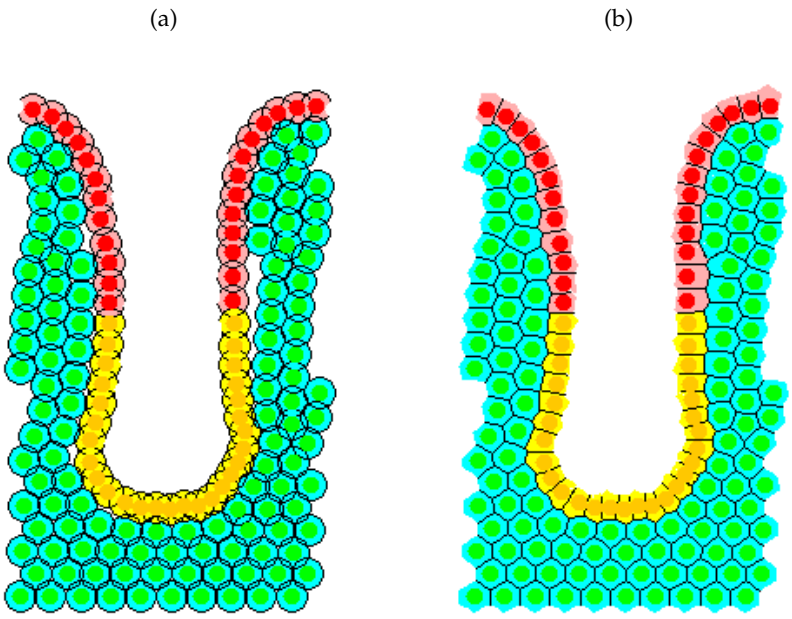

Figure 7.2: An example of how the cross-sectional model simulation can also be visualised with the cells as circles. The holes between cells here are just an artefact of the visualisation, and the radius of the circles that is used. (b) The cross-sectional model when cells are viewed as the Voronoi region.

simulation than when cell shapes are defined by a 3D Voronoi tessellation. This can be seen from Figure 7.1(c), which shows the same configuration of cells as in Figure 7.1(a) but with ghost nodes included to enable visualisation of the cells using the Voronoi tessellation, and Figure 7.1(d) which shows this cell configuration once it has relaxed. As can be seen from these two snapshots, the cells are harder to distinguish, when compared to the regular spherical shapes. This change is superficial as far as the model is concerned, and does not affect the cell-cell forces. For example, Figures 7.2(a) and (b) show how the cross-sectional model could be simulated with cells instead visualised using circles and how this compares to the 2D Voronoi regions. Choosing to represent cells as circles would not affect the mechanics of the system, nor the outcome of model simulations.

7.1.2 Three-Dimensional Basement Membrane Force

Determination of the basement membrane force in 3D is complicated by the added complexity of the geometry and subsequent triangulation. As in 2D, a discrete approximation of the curvature is calculated by considering the midpoints of the springs that connect epithelial and stromal cells. In 3D, however, the piecewise linear curve is superseded by a piecewise planar surface that passes through these points.

For each epithelial-stromal node pair, firstly, the tetrahedral elements to which the pair

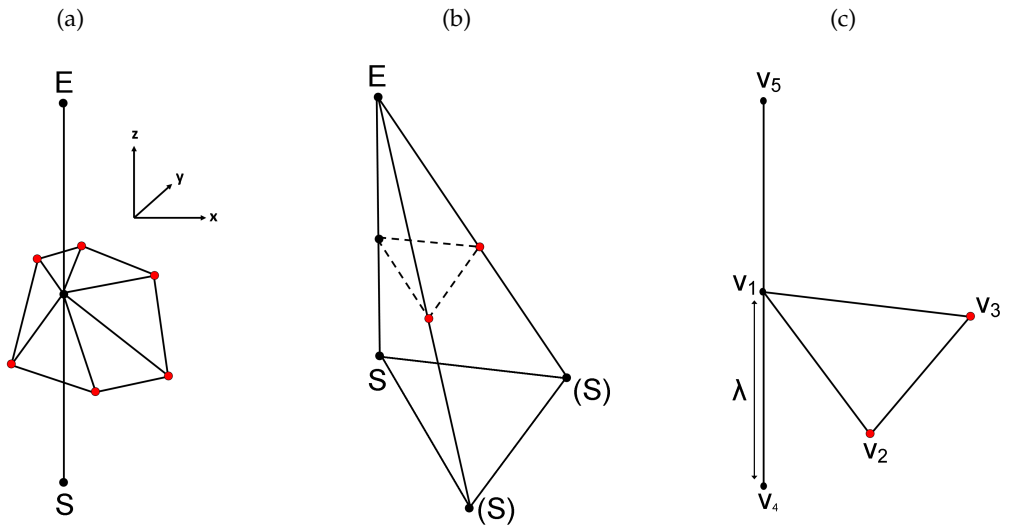

Figure 7.3: (a) An example of the local piecewise planar surface that passes through a point along the epithelial-stromal spring of interest, which connects the midpoints of epithelial-stromal springs that belong to common tetrahedral elements (indicated by the red circles). (b) An example of one of the tetrahedra to which an epithelial-stromal pair belongs. The triangular element is formed from the midpoints of the other epithelial-stromal pairs in that tetrahedron (red circles). (c) A single triangular face connected to the point $\mathbf{v_1}$ along the epithelial-stromal vector $\overrightarrow{\mathbf{v_5}\mathbf{v_4}}$.

belong are identified. The local basement membrane surface is then composed of a number of triangular faces, as shown in Figure 7.3(a). Each triangular face is unique to one of the tetrahedral elements to which this pair of nodes belongs, as illustrated in Figure 7.3(b), where the vertices of the triangle are taken as the midpoints of the other epithelial-stromal pairings in that tetrahedron (indicated by the red circles) and the midpoint of the epithelial-stromal spring of interest.

The discrete curvature for each epithelial-stromal pairing is found by examining how the summed area of each triangle in Figure 7.3(a) changes as the midpoint of the epithelial-stromal spring moves along the vector $\overrightarrow{\mathrm{ES}}$ (this corresponds to increasing or decreasing the distance parameter, λ; see Figure 7.3(c)). Details of the calculation are described below.

Consider the vector connecting an epithelial-stromal cell pair and the point, $\mathbf{v_1}$, which is a distance λ from the stromal node along the vector $\overrightarrow{\mathrm{ES}}$. Consider one of the triangles to which $\mathbf{v_1}$ belongs and define $\mathbf{v_2}$ and $\mathbf{v_3}$ as the other vertices (as in Figure 7.3(c)). Now $\mathbf{v_1}$ can be defined in terms of the points that correspond to the epithelial and stromal nodes, $\mathbf{v_5}$ and $\mathbf{v_4}$ respectively:

$$\mathbf{v_1} = \lambda \mathbf{v_5} + (1 - \lambda)\mathbf{v_4}\,. \tag{7.1}$$

If $\lambda = 0.5$, then $\mathbf{v_1}$ corresponds to the midpoint of $\overrightarrow{\mathrm{ES}}$. The area of the triangle $\mathbf{v_1}\mathbf{v_2}\mathbf{v_3}$ is

given by

$$A = \frac{1}{2}|(\mathbf{v_3} - \mathbf{v_1}) \times (\mathbf{v_2} - \mathbf{v_1})| \,. \tag{7.2}$$

To simplify this calculation, define $\mathbf{G} = (\mathbf{v_3} - \mathbf{v_1}) \times (\mathbf{v_2} - \mathbf{v_1})$, so that

$$\begin{aligned} 2A &= |\mathbf{G}| \\ &= \sqrt{G_1^2 + G_2^2 + G_3^2} \,, \end{aligned} \tag{7.3}$$

where G_1, G_2 and G_3 are the x, y and z components of $\mathbf{G}$ respectively. By appealing to Equation (7.1) for $\mathbf{v_1}$, and differentiating Equation (7.3) with respect to λ, it is possible to deduce how the area of the triangle changes as the distance parameter, λ, varies. This gives

$$\frac{dA}{d\lambda} = \frac{1}{2A} \sum_{i=1}^{3} G_i \frac{dG_i}{d\lambda} \,. \tag{7.4}$$

Equation (7.4) is evaluated at $\lambda = 0.5$ for each triangle τ in the set of triangles T to which $\mathbf{v_1}$ belongs, and the sum of these values calculated. This sum gives a discrete approximation of the signed curvature, κ, at the point $\mathbf{v_1}$:

$$\kappa = \sum_{\tau \in T} \frac{dA_\tau}{d\lambda} \,. \tag{7.5}$$

Here, A_τ is the area of the triangle τ.

The basement membrane force acts in the direction of the vector pointing from the stromal node towards the epithelial node, such that if the local piecewise planar surface area increases as λ increases (*i.e.* $\kappa > 0$) then the force acts to pull the epithelial node towards the stromal node. Conversely, if this area decreases as λ increases (*i.e.* $\kappa < 0$) then the epithelial node is pushed away from the stromal node. The total basement membrane force acting on each epithelial node i is evaluated for each stromal cell j that this epithelial cell is connected to according to the Delaunay triangulation. This gives

$$\mathbf{F_i} = -\beta \sum_{\forall j} \left(\sum_{\tau \in T} \frac{dA_\tau}{d\lambda} \right) \hat{\mathbf{u}}_{\mathbf{ij}} \,, \tag{7.6}$$

where $\mathbf{F_i}$ is the basement membrane force acting on epithelial node i, β is the basement membrane force parameter (as in the 2D model, but now scaled appropriately for the 3D model) and $\hat{\mathbf{u}}_{\mathbf{ij}}$ is the unit vector in the direction $(\mathbf{v_5} - \mathbf{v_4})$ (*i.e.* from stromal node j to epithelial node i). The force defined by Equation (7.6) acts to maintain a zero spontaneous curvature on the layer. Therefore, to maintain a pre-specified spontaneous curvature, κ_S, the force is updated so that

$$\mathbf{F_i} = -\beta \sum_{\forall j} \left(\sum_{\tau \in T} \frac{dA_\tau}{d\lambda} + \kappa_S \right) \hat{\mathbf{u}}_{\mathbf{ij}} \,. \tag{7.7}$$

The spontaneous curvature of the basement membrane, now scaled for the 3D model, depends on cell location in the crypt according to

$$\kappa_S = \begin{cases} 1/R, & \text{if } (x_i, y_i) \in \Omega, \\ 0, & \text{otherwise}. \end{cases} \tag{7.8}$$

Here $1/R$ is the constant, non-zero, positive spontaneous curvature to be determined by numerical experiment, (x_i, y_i) are the coordinates of cell centre i, and Ω is the region defined by the crypt base.

7.1.3 Periodic Boundary Conditions

To model the continuous epithelial layer and connective tissue between neighbouring crypts, periodic boundary conditions are imposed on all four vertical walls of the tissue block, for both stromal and epithelial cells. In 3D, this is no longer defined by the mesh class in Chaste, but rather by constructing periodic force classes for both the interactive cell forces and the basement membrane force: `PeriodicCryptModelInteractionForce` and `PeriodicBasementMembraneForce3d`. In each case, in both the x and y directions, the force class constructs an extended mesh, by mapping the real nodes from each half of the mesh to the opposite edge, as shown in Figure 7.4. The extended mesh is then used to calculate the forces, which are only exerted on the initial set of real nodes (indicated in black in Figure 7.4). This implementation is designed to increase the speed of simulations. For visualisation purposes, and to define a bounded domain as in 2D, cells that move beyond the periodic boundaries in the x and y planes are transferred to the opposite edge.

7.1.4 Cell Division

To model the directed cell division that arises from cell polarity, whereby daughter cells are positioned back within the epithelial monolayer following a division event, in 3D the cells are instructed to divide relative to the position of the basement membrane and surrounding stromal cells. For each given parent epithelial node, the neighbouring stromal cells are found using the Delaunay triangulation. The positions of these stromal nodes are averaged, and the vector connecting the epithelial cell to this averaged stromal position is found. The epithelial cell is then instructed to divide along a random vector which lies in the 2D surface which is perpendicular to that which connects it to the average stromal location. This ensures that cells divide parallel to the tissue stroma beneath.

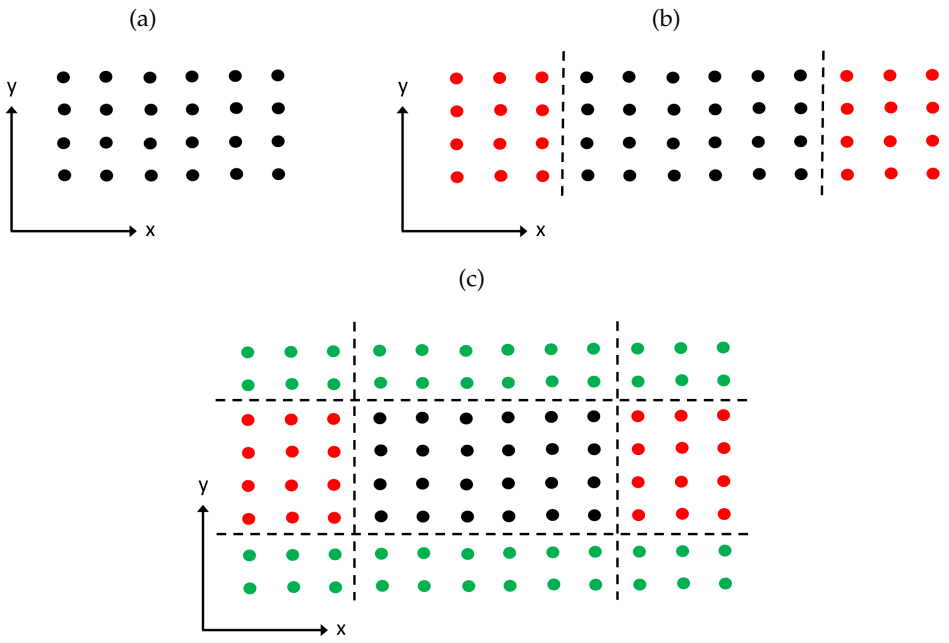

Figure 7.4: An illustration of how the mesh of nodes is extended within the periodic force classes. (a) The initial mesh of nodes, (b) copying each half of the original mesh to the opposite edge in the x-direction, where the new image nodes are indicated in red, (c) copying each half of this extended mesh to the opposite edge in the y-direction, where the new image nodes are indicated in green. The force class uses this final mesh to calculate the forces acting on only the real nodes (black).

As in Section 5.1.2, unless stated otherwise, cell division events are determined by a `StochasticDurationGenerationBasedCellCycleModel`, such that each cell has an overall cell cycle duration chosen from a Uniform $X \sim U(11, 13)$ distribution.

7.1.5 Anoikis

As in 2D, epithelial cells undergo anoikis if they lose contact with the basement membrane. This is implemented using the Delaunay triangulation, which determines epithelial-stromal cell connectivity. Epithelial cells with no stromal connections are defined to have lost contact with the substrate, and are immediately removed from the simulation.

7.2 The Action of the 3D Basement Membrane Force

In silico simulations are now conducted to illustrate the effect of the basement membrane force on a growing monolayer of epithelial cells. Analogous to the model development conducted in Chapter 5, two cases are considered which correspond to different spontaneous curvatures imposed on the basement membrane in Equation (7.7): firstly, $\kappa_S = 0$

everywhere, and secondly, where $\kappa_S = 1/R$ for $1/R > 0$ in a localised region. Unless stated otherwise, for the interactive cell forces defined by Equation (4.2), the spring constant, $\mu = 15$, and the drag coefficient, $\eta = 1$, are applied for all cells. Simulations are conducted within the Chaste environment, and results are visualised using Paraview, which is an open-source data analysis and visualisation tool[1].

Quantifying the Flatness of the Epithelial Layer

As described in Section 5.3, when a zero spontaneous curvature is applied, the flatness of the epithelial layer is described by a metric α. In 2D, this is defined to be the average gradient of the lines connecting neighbouring epithelial cell pairs (the average gap ratio). In 3D, this is generalised to account for the differences in the z-component of the vectors connecting neighbouring epithelial cell pairs. Let P be the set of neighbouring epithelial cell pairs i and j, such that $|P|$ is the size of the set. α is now defined as

$$\alpha = \frac{1}{|P|} \sum_{\forall \{i,j\} \in P} \frac{\left| z_i - z_j \right|}{\gamma_{ij}}, \tag{7.9}$$

where

$$\gamma_{ij} = \sqrt{(x_i - x_j)^2 + (y_i - y_j)^2}. \tag{7.10}$$

Here, (x_i, y_i, z_i) and (x_j, y_j, z_j) are the coordinates of the individual epithelial cells in each pair.

7.2.1 A Flat Layer: Zero Spontaneous Curvature

The effect of the 3D basement membrane force, defined by Equations (7.4) and (7.7), is examined firstly when the spontaneous curvature is zero, such that the force acts to maintain a uniformly flat epithelial monolayer. To determine the general behaviour of the model under different conditions, 50 simulations were run for each set of parameter values, and average results taken. The pseudo-random number generator used was re-seeded for each simulation to generate a new, independent set of birth events. Each simulation was run for 60 cell hours, and the results calculated at the final timestep. This ensures that (on average) each cell will have divided several times during each simulation and, therefore, that the results are indicative of the general behaviour of the system. In these results, anoikis is the only mechanism of cell apoptosis that is implemented.

[1] `http://www.paraview.org/`

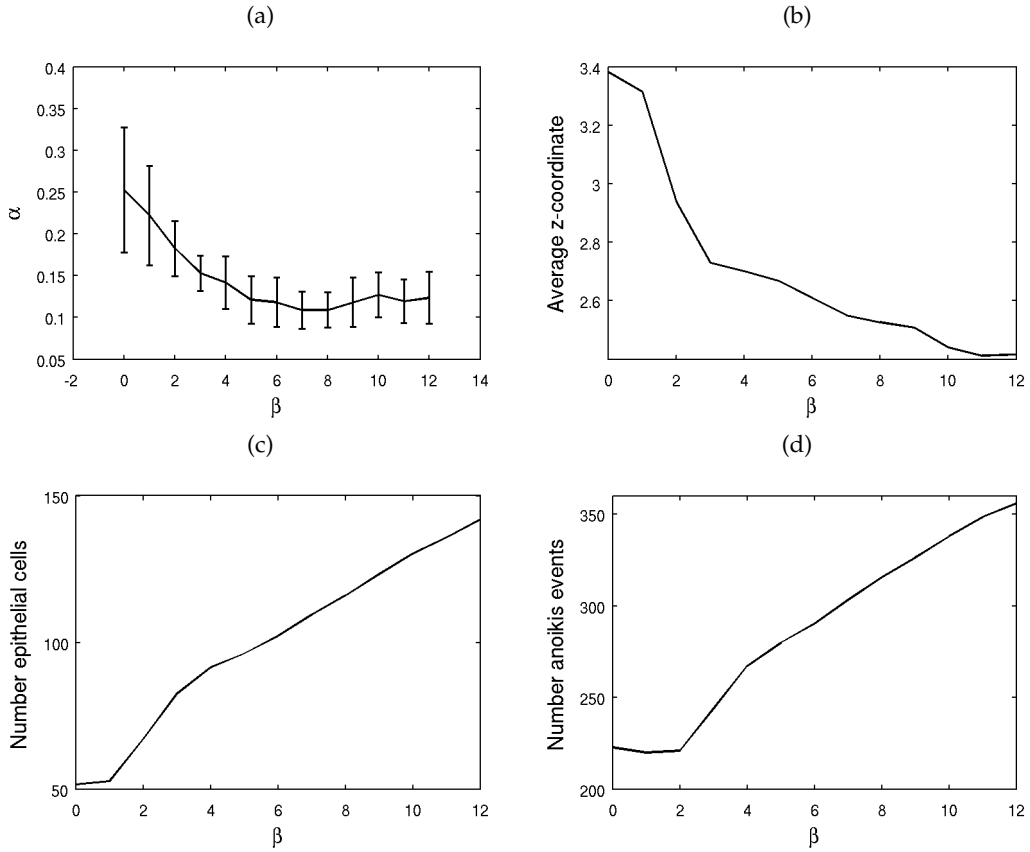

Figure 7.5: The effect of increasing the magnitude of the basement membrane force when $\kappa_S = 0$, as characterised by the basement membrane parameter β. (a) The flatness of the epithelial layer at the final timestep ($t = 60$ hours), characterised by α. The error bars indicate the standard deviation for each value of β. (b) The average z-coordinate of all epithelial cells at the final timestep. (c) The total number of epithelial cells in the layer at the final timestep (not summed over the entire simulation). (d) The total number of anoikis events that occur throughout the simulation. All of these results are averaged over a total of 50 simulations.

Figure 7.5(a) plots the change in α as the basement membrane parameter β is increased, with error bars indicating the standard deviation for each value of β, while Figure 7.5(b) shows how the average z-coordinate of the epithelial cells in the monolayer at the final timestep changes as β varies. Taken together, these two results describe how wrinkled the layer is, and whether there is any bulk movement of the layer. Figure 7.5(c) shows how the total number of epithelial cells in the monolayer at the final timestep ($t = 60$ hours) varies with β, while Figure 7.5(d) reveals how the total number of anoikis events that occur throughout the course of the simulation depends on β.

The results presented in Figure 7.5 show that as the magnitude of the basement membrane force increases, α decreases, which indicates that the layer becomes less wrinkled. As the layer flattens, it is also pushed downwards, compressing the tissue stroma beneath (see

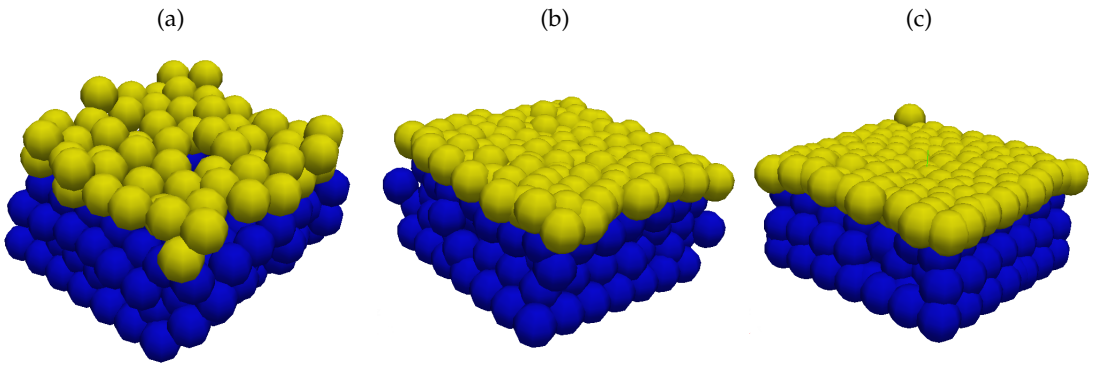

Figure 7.6: Typical simulation snapshots showing the model after 60 hours, when (a) $\beta = 0$, (b) $\beta = 6$, and (c) $\beta = 12$. From these snapshots, it is demonstrated that as β is increased, there are a greater number of epithelial cells in the layer, and the layer is flatter. It is also shown that the cells are more compressed.

Figure 7.5(b)). Further, as the magnitude of the force increases, adhesion to the basement membrane increases, which holds more epithelial cells in the monolayer – this is shown in Figure 7.5(c). As the number of cells increases, the extent of compression of the cells in the layer increases, and as these cells divide (indeed there are more division events as the cell number increases) the newly created cells are more likely to be quickly pushed out of the layer. This leads to an increase in the number of anoikis events. Illustrative snapshots from a typical simulation are presented in Figure 7.6, which show how the profile of the epithelial monolayer differs after 60 hours for three cases ($\beta = 0, 6, 12$).

Introducing Cell Sloughing

The results shown in Section 5.4.6 for the 2D model indicate that, unless a secondary form of cell death is imposed at the edges of the monolayer, migration is inhibited due to excessive cell compression. This behaviour is also replicated in the results for the 3D model, in that both epithelial cell number and the number of anoikis events increase as β increases (see Figures 7.5(c) and (d)).

To stimulate migration within the 3D model, a second form of apoptosis is introduced, as in Section 5.3: epithelial cell sloughing is assumed to occur beyond the edges of the tissue stroma. Specifically, from this point onwards, periodic boundary conditions are applied only to the stromal cells, but should an epithelial cell move beyond the periodic domain boundaries, it undergoes apoptosis, replicating the cell loss that occurs at the crypt collar and intercrypt table. The results presented in Figure 7.7 reveal how the results shown in Figure 7.5 change when cell sloughing is included.

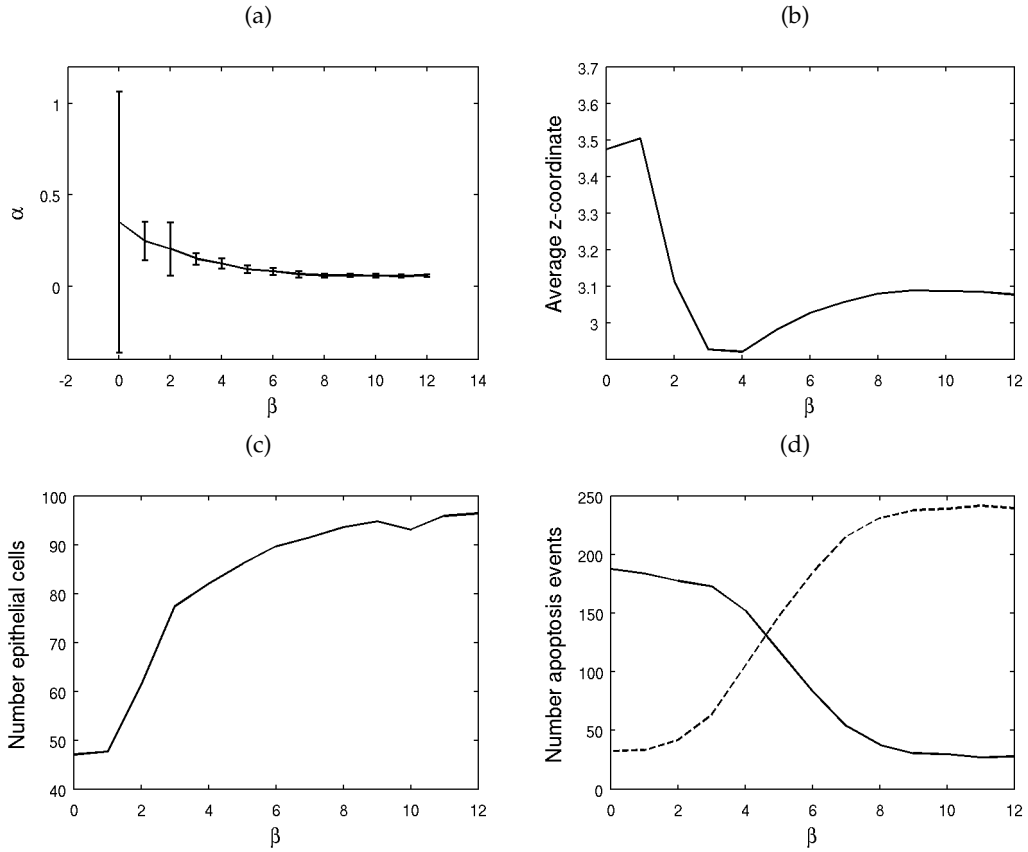

Figure 7.7: The effect of increasing the magnitude of the basement membrane force when $\kappa_S = 0$, and epithelial sloughing is active at the edges of the tissue stroma. (a) The flatness of the epithelial layer at the final timestep ($t = 60$ hours), is characterised by α. The error bars indicate the standard deviation for each value of β. (b) The average z-coordinate of the epithelial cells at the final timestep. (c) The total number of epithelial cells in the layer at the final timestep. (d) The total number of anoikis events (solid line) and sloughing events (dashed line) that occur throughout the simulation. All of these results are averaged over a total of 50 simulations.

The trends observed in Figures 7.7(a), (b) and (c) are similar to those observed in Figure 7.5. Figure 7.7(a) reveals that α decreases as β increases, indicating that the layer is flattening. However, this plot shows that the standard deviation is larger for $\beta = 0$ than for the case when cell sloughing is not implemented. This is because the number of cells decreases due to sloughing at the edges, which means that fewer anoikis events occur immediately following division and the layer is, correspondingly, more wrinkled. Figure 7.7(b) shows that the stromal cells become increasingly compressed, as for the case without cell sloughing, but that this compression eases for $\beta \geq 5$. In Figure 7.7(c), the number of epithelial cells in the layer increases with β, and plateaus for $\beta \geq 5$. Further, the maximum number of epithelial cells in the layer is lower than when sloughing is neglected (see Figure 7.7(c) compared with Figure 7.5(c)). The change in behaviour that occurs as β increases through $\beta = 5$ occurs because the number of cells that are removed by sloughing starts to exceed

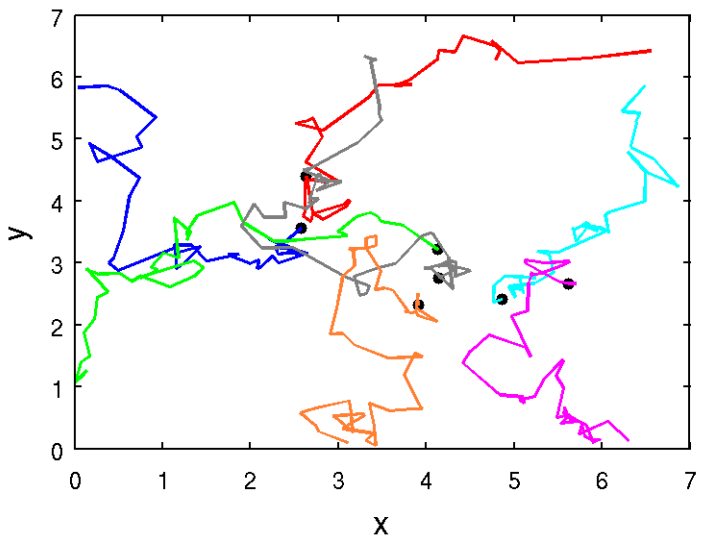

Figure 7.8: Typical migration tracks of individual cells in the 3D model when $\beta = 8$, $\kappa_S = 0$ and both anoikis and cell sloughing are implemented. Each colour corresponds to a different cell over time, and the initial location of each cell is marked with a •. Here the z-coordinates are omitted to emphasise the migration from the centre of the layer outwards to the edges, and the centre of the monolayer is at (3.5, 3.5).

the number removed by anoikis. This situation is depicted in Figure 7.7(d), and parallels the result found for the 2D case (see Figure 5.6(b)).

As β increases, cells are more tightly adherent to the basement membrane and the layer flattens due to the fact that $\kappa_S = 0$ uniformly across the layer. Now that cell sloughing is introduced, the removal of cells at the edges of the domain creates additional space for the epithelial cells to move into as a consequence of the repulsive effects of the interactive cell-cell forces. This is a non-local effect, which causes cells to move horizontally across the layer, and is similar to the results shown for the 2D models, whereby cell migration is enabled by the removal of cells towards the crypt collar. Thus, for sufficiently large values of β, cell migration is favoured over anoikis, and the layer is relatively flat.

To illustrate the migration that can be observed for this model, Figure 7.8 plots typical migration tracks for six different cells. In each case, over time, the cells migrate out towards the edges of the epithelial monolayer. This is consistent with the result shown in Figure 7.7(d), where for large values of β, the cells can migrate along the flat layer, rather than being removed by anoikis.

The above results indicate that, when cell sloughing is imposed as a secondary mechanism of cell removal from the layer, fixing $\beta \geq 8$ is optimal both to maintain a relatively flat layer, and also to enable cell migration rather than anoikis events arising due to an overly

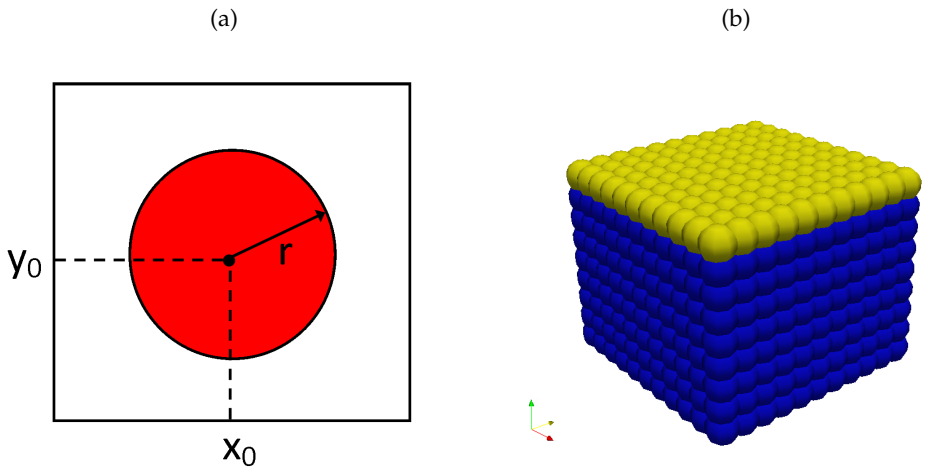

Figure 7.9: (a) A schematic diagram indicating the regions in which $\kappa_S = 1/R$ (red), and the region $\kappa_S = 0$ (white). In this diagram, (x_0, y_0) marks the centre of the tissue block and r is the radius of the non-zero spontaneous curvature region, defined to be 3/10 of the width of the tissue block. (b) The initial configuration of cells used to investigate a region of non-zero spontaneous curvature – epithelial cells are coloured yellow and stromal cells are coloured blue. The number of layers of stromal cells has increased to allow for deformation of the epithelial layer.

compressed layer. These results are taken into consideration when the case for $\kappa_S = 1/R$ for a specified region of the epithelial monolayer is considered, in order to investigate the semi-spherical domain which characterises the crypt base.

7.2.2 The Curved Base: Non-Zero Spontaneous Curvature

By introducing a localised domain of positive spontaneous curvature for the basement membrane it is possible to investigate cell movement within the semi-spherical region that corresponds to the crypt base, which is supported by the muscularis mucosae, basement membrane and pericryptal fibroblast sheath. In this model, the region of the basement membrane with a non-zero spontaneous curvature is a circular domain centred in the middle of the epithelial monolayer, as illustrated in Figure 7.9(a). This circle has a fixed radius, r, equal to 0.3 of the width of the layer of epithelial cells. The number of layers of stromal cells is increased to allow for the deformation that will occur as the epithelial layer bends downwards, and the new initial cell configuration is a cuboid of 11 x 11 x 9 cells, as shown in Figure 7.9(b).

Results

The increase in deformation of the epithelial monolayer caused by increasing the non-zero spontaneous curvature, $1/R$, in the central, circular region indicated in Figure 7.9(a) is

now considered. Figure 7.10 contains typical surface plots of the epithelial layer, plotted at $t = 100$ hours, and demonstrates the degree of deformation of the layer as $1/R$ is increased, and $\beta = 8$. Next to each surface plot is a contour plot that indicates the degree of deformation as defined by the z-coordinates of the epithelial cells in the monolayer at the final timestep. From these plots, it is clear that increasing $1/R$ increases the extent to which the epithelial layer deforms downwards into the tissue stroma. These results are consistent with those presented for the 2D model in Section 5.4. Results from a typical simulation (with $\beta = 8$ and $1/R = 0.15$) are presented in Figure 7.11, which contains three snapshots of just the epithelial layer, viewed from different angles. The stromal cells are omitted from these snapshots to facilitate visualisation of the deformation.

Figure 7.12 illustrates the change in behaviour when β is increased and $1/R = 0.15$: simulation snapshots of the epithelial monolayer are presented alongside the corresponding surface plot. Comparison with Figure 7.10 reveals that increasing $1/R$ has a stronger effect on the surface than increasing β, but there is an observable increase in the extent of deformation of the curved region. Again, this result is consistent with that found for the 2D model (see Figure 5.12 in Section 5.4.1).

The value of $1/R$ that is implemented for further investigations is chosen to give a sufficiently deformed semi-spherical region to represent the crypt base region, while β is chosen to prevent excess deformation of the stromal cells beneath the epithelial layer. Guided by the results in Figure 7.10, $1/R = 0.15$ is fixed. Figure 7.5 indicates that for $\beta \geq 8$ there is no significant further change in α, the total number of epithelial cells in the layer, or the number of anoikis and sloughing events. Therefore, in future simulations, $\beta = 8$ and $1/R = 0.15$.

7.2.3 Multiple Simulations

To investigate the behaviour of the epithelial monolayer during repeated division events, 50 simulations were run for a period of 100 hours from the time at which the deformation of the layer had reached an equilibrium state, that is, once the non-zero spontaneous curvature region had fully developed. Each simulation had an independent set of birth events, achieved by re-seeding the random number generator in each case. As stated above, these simulations were performed with a basement membrane force parameter, $\beta = 8$, and the non-zero spontaneous curvature in the central region fixed at $1/R = 0.15$.

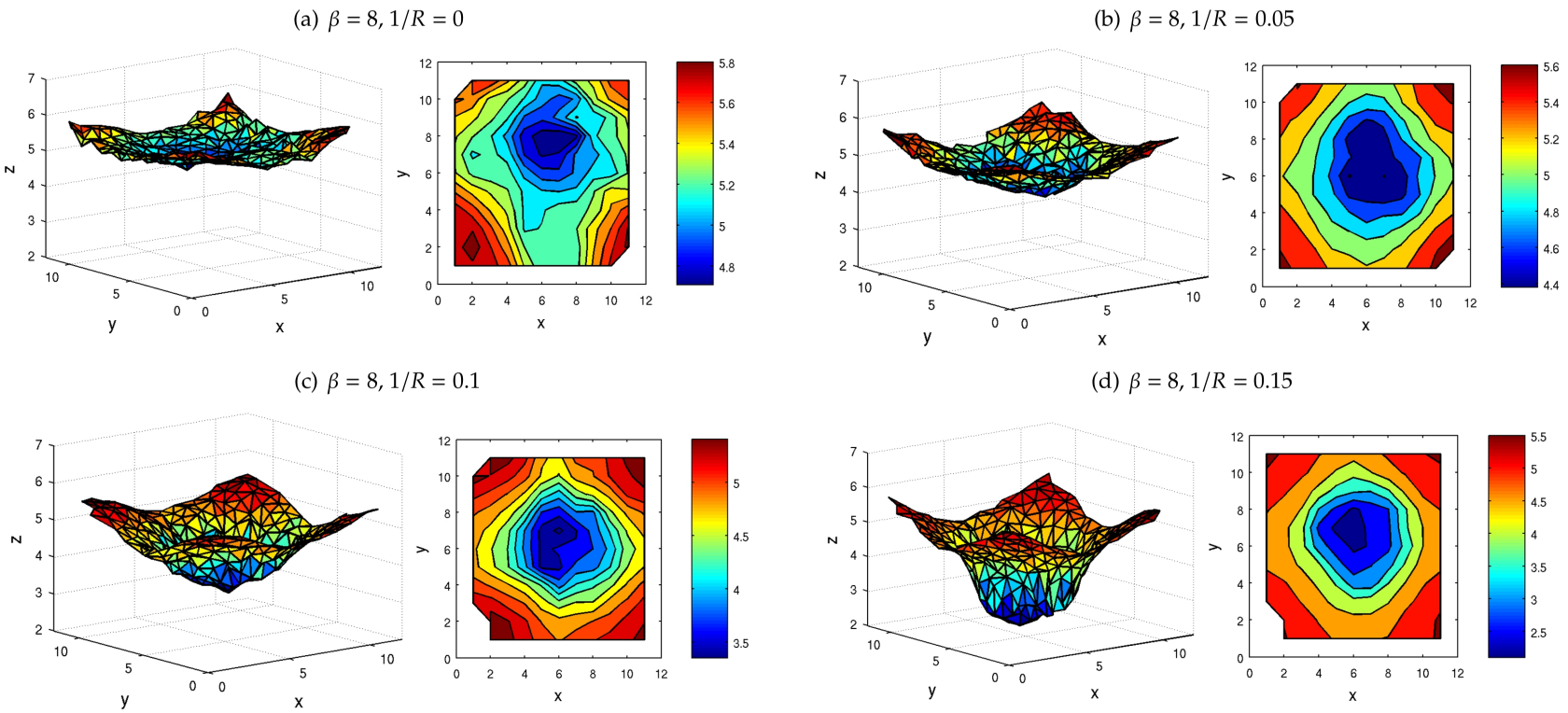

Figure 7.10: The effect on the epithelial monolayer of increasing the spontaneous curvature, $1/R$, in the central region (described in Figure 7.9(a)), where results are taken after 100 hours and the layer is fully deformed. The plots on the left are surface plots of the epithelial monolayer, and the plots on the right are contour plots that indicate the extent of deformation according to the z-coordinates of the epithelial cells, indicated by the colour bar next to each plot. Here $\beta = 8$ and (a) $1/R = 0.0$, (b) $1/R = 0.05$, (c) $1/R = 0.1$ and (d) $1/R = 0.15$.

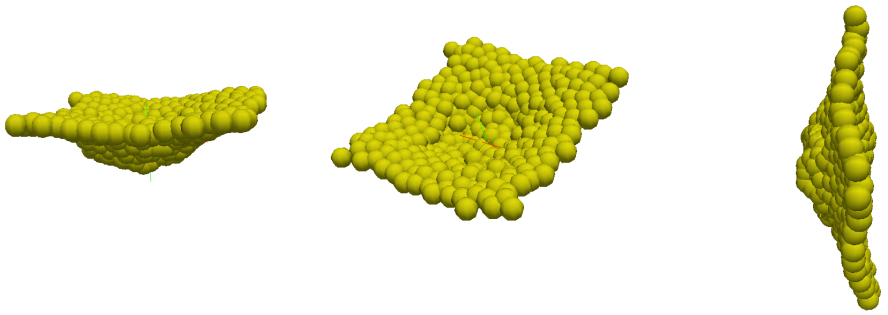

Figure 7.11: Snapshots that illustrate a fully deformed epithelial layer when $\beta = 8$ and $1/R = 0.15$ in the central circular region defined by Figure 7.9(a). These are shown from different angles to highlight the deformed region that corresponds to the crypt base.

Epithelial Cell Distribution and Anoikis Events

The plots shown in Figure 7.13 are histograms that illustrate the ratio of anoikis events to epithelial cell number along each of the coordinate axes individually. Events and cells are counted for all simulations, and the frequencies presented represent the average over all 50 examples. Given that, in this simple cuboid geometry, all epithelial cells are assumed to be proliferative, and given that density-dependent inhibition of mitosis is not applied, the distribution of epithelial cells correlates with the distribution of cell division events.

As can be seen from Figures 7.13(a) and (b), within the (x, y)-plane, the incidence of anoikis events increases towards the centre of the monolayer, which corresponds to the bowl of the deformed, semi-spherical region. As such, these results suggest that anoikis occurs more frequently following cell division in the semi-spherical crypt base region, and that this must arise due to the concave shape and high compression of cells, which forces them out of the layer more easily. In contrast, anoikis events are relatively infrequent in relation to the number of epithelial cells in the zero spontaneous curvature region of the basement membrane, where the monolayer is flatter.

Figure 7.13(c) shows that, relative to the density of epithelial cells along the z-axis, the number of anoikis events increases from the base of the semi-spherical region, reaching a maximum for $3 < z < 4$. This corresponds to the curved ridge between the non-zero and zero spontaneous curvature domains, analogous to the crypt collar. Anoikis events subsequently decrease for higher values of z, which corresponds to the flat, zero spontaneous curvature region. This again shows that the shape of the semi-spherical region plays a role in determining cell fate, and that cells are more easily pushed out of the monolayer in the curved, rather than flat, region.

(a) $\beta = 6$, $1/R = 0.15$

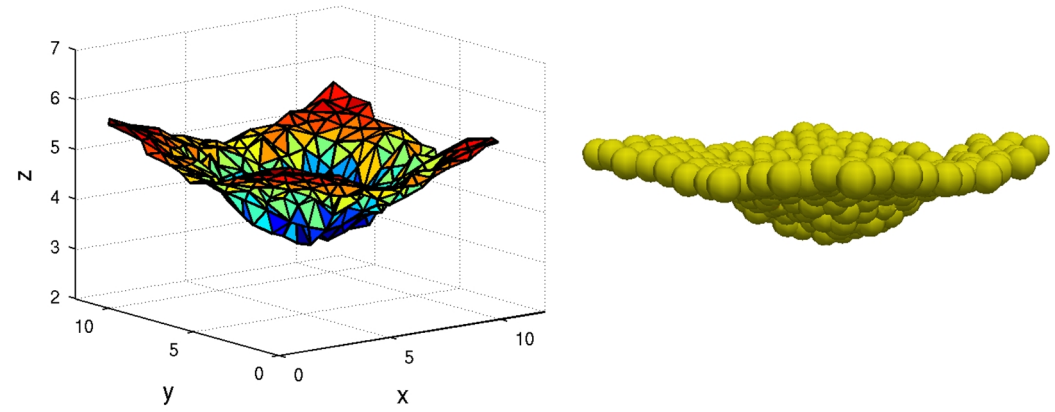

(b) $\beta = 8$, $1/R = 0.15$

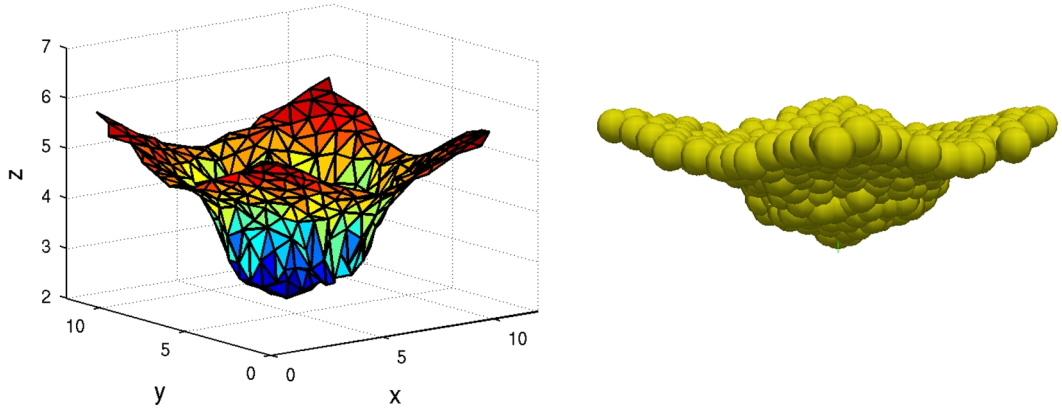

(c) $\beta = 10$, $1/R = 0.15$

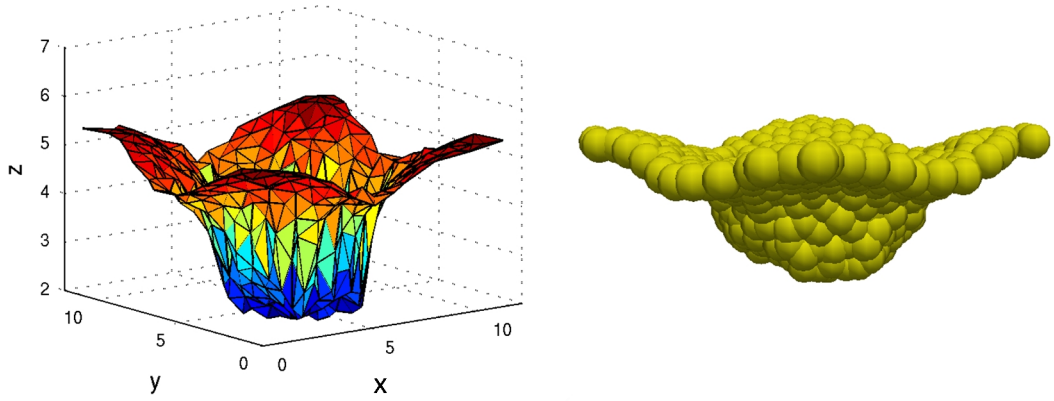

Figure 7.12: Increasing the basement membrane parameter, β, when $1/R = 0.15$. The left column is a surface plot of the epithelial cell centres, and the right column is the corresponding simulation snapshot, showing only the epithelial layer. These plots illustrate that for constant $1/R$, increasing β increases the extent of deformation of the curved region, but overall that increasing β does not have as dominant an effect on the deformation of the layer as increasing $1/R$.

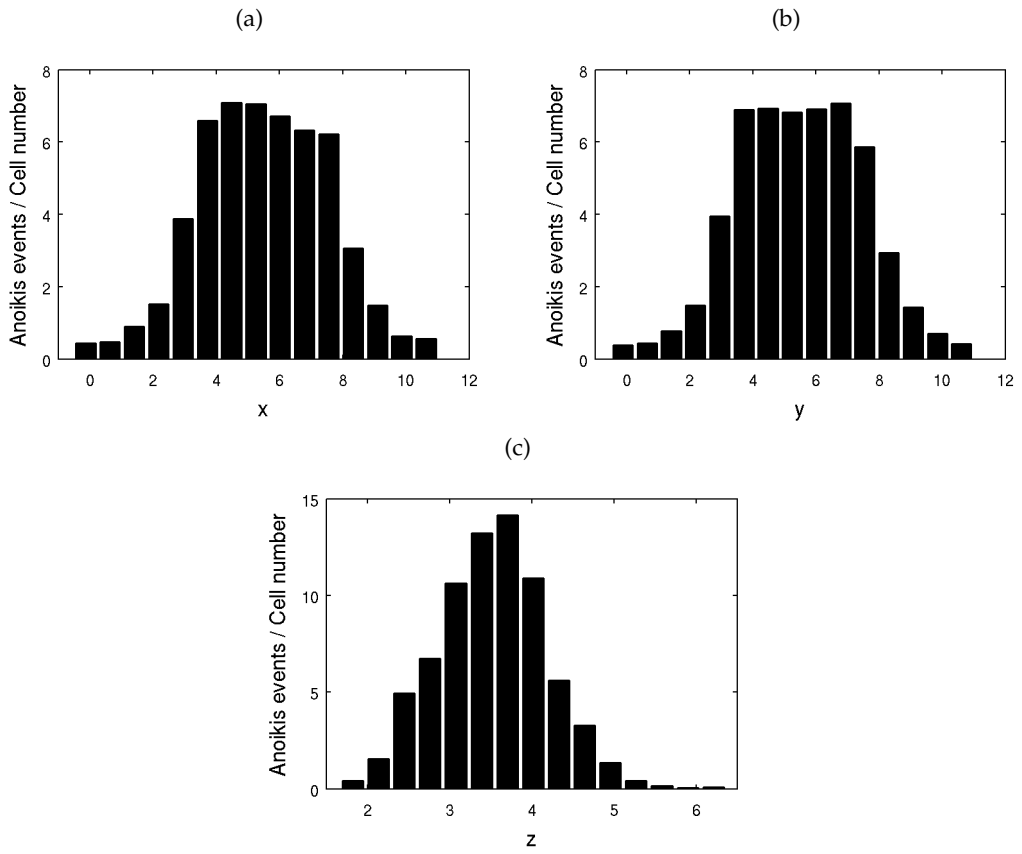

Figure 7.13: Histograms that show the ratio of anoikis events to epithelial cell number along each of the coordinate axes: a) x-axis, (b) y-axis, (c) z-axis. These results represent the average taken over 50 simulations, each run for a period of 100 cell hours.

These results are similar to those found for the 2D model. Firstly, they suggest that the shape of the monolayer at the crypt base renders cells vulnerable to popping out of the layer (to be removed by anoikis) immediately following cell division. This emphasises once more that the shape of the crypt may play a role in the choice between asymmetric and symmetric division, given than anoikis is not commonly observed at the crypt base [131], and the mechanical effect that is being observed mirrors the mechanism of asymmetric cell division. Secondly, the results suggest that, due to the high number of anoikis events occurring at the interface between the zero and non-zero spontaneous curvature regions, cell sloughing at the crypt collar may be due to anoikis events that arise as a consequence of a decrease in the cell-substrate contact area, causing cells to detach from the basement membrane.

The next stage of model development would be to extend this geometry to represent that of the test tube shape of the crypt. By considering a realistic crypt geometry, it would be possible to perform *in silico* experiments similar to those conducted in Section 6.3.2, which

track the movement of mutant cell populations introduced into the crypt, and their effects on the tissue composition and structure. However, currently, computational limitations prevent this advancement, and these are discussed in detail in Section 7.4.

7.3 Computation

A typical simulation of 100 cell hours of the 3D model presented in this chapter requires approximately 2 hours of CPU time on a desktop Linux PC with two quad core 2.83GHz Intel(R) Xeon(R) processors. This is 8 times slower to run for a simulation of the cross-sectional model of the same period of cell time. The increase in CPU time is due to the increased number of cells, and the additional complexity of the Delaunay triangulation in 3D, which is remeshed at every timestep and is used in both the interactive cell-cell and basement membrane force calculations. Hence, the 3D model is very much more computationally intensive than the 2D model. This is discussed further in Section 7.4.

Movie 11, provided on the attached CD, corresponds to a typical simulation example of the 3D model where $\beta = 8$, $1/R = 0.15$ and sloughing of epithelial cells occurs beyond the edges of the tissue domain.

7.4 Model Implementation

As described in Chapter 4, the simulations presented in Chapters 5, 6 and 7 are constructed within a single user project which inherits functionality from the main trunk of cell-based code in Chaste. In this section, the implementation of the models is discussed with regards to the issues inherent in this style of code development, as well as computational limitations that are associated with the model definition. Lastly, factors which influence the direction of future work are considered and possible options are proposed.

7.4.1 Inheriting Functionality From Chaste

The code developed to run simulations of the crypt models presented in this thesis was implemented in Chaste. For the first time, code was constructed by a single new user who had not been involved in the development of the Chaste project from the outset. As the new code was designed to inherit functionality from the existing cell-based trunk, this represents the first example of a new user interfacing individual work with the Chaste project, and the associated challenges are discussed below. An awareness of such issues is

important for the ongoing development of extensible software such as Chaste, especially as the number of users increases.

The practice of establishing user projects represents one of the advantages of the Chaste structure (discussed in Section 4.2.3) as it enables individuals to work on independent projects, and to build upon a tested code-base that is written and structured according to good software engineering principles. This is in contrast to inheriting hand-me-down code that typically is passed down to new researchers, which may not be robust or well documented. However, it is still a challenge to the single user to build new code around the existing framework and code structure, which may introduce an element of inflexibility. In particular, there is the time required to acquire a thorough understanding of the core functionality, which currently comprises approximately 500,000 lines of code, as it may be necessary to modify the core code in order to implement aspects of the code in the user project. Participation in group development sessions, which focus solely on the cell-based trunk of code, and which was undertaken in tandem with this project, is necessary to acquire a better understanding of the code structure. These sessions ensure that all new users eventually become developers, and contribute to and extend the main code base.

Each user project must integrate accurately with the main trunk firstly to compile and generate simulations, but also to avoid errors in numerical output, maximise efficiency and avoid repetition. Should debugging be necessary, it is not always obvious whether errors arise as a consequence of the new simulation code being incorrect, whether it conflicts with the cell-based structure, or whether a new weakness has been found within Chaste. Ultimately, the test-driven approach that is applied to develop Chaste suggests that problems are unlikely to be due to the core code base. However, solving such problems is not always trivial, and moreover, often time-consuming. Should an issue with the main code be found then the user informs the main developers who usually assist with fixing the problem. It is to the user's benefit to follow the style of code development established in Chaste to reduce the potential for the introduction of errors. This lays the foundation for future researchers to repeat this process and further extend the code, but this can only happen if the user project code is successfully transferred to the Chaste trunk. Two examples of how this process evolves, which are unique to the model development for this thesis are now described.

Specific Examples

For the 2D model presented in Chapter 5, an issue associated with code development arose from the need to define a new cell cycle model to incorporate density-dependent inhibition of mitosis, which at the time, did not exist within the cell-based framework. As for all new functionality, the challenge in this instance was to construct the code for the cell cycle model so as to link with the structure of a general cell-based simulation, and in particular, how each cell is defined to progress through the cell cycle at each timestep. In the new cell cycle model, a cell is prevented from dividing at any stage unless its volume exceeds a given threshold value (see Section 2.1.3). However, simply incrementing the length of the G_1-phase of the cell cycle for a particular compressed cell is not sufficient to prevent it from dividing, as within Chaste, if a cell becomes compressed during the G_2 or S-phases then it will still divide. Due to this, density-dependent inhibition of mitosis was, initially, not implemented in the desired manner for all cells. To solve this problem, and prevent all small cells from dividing, an explicit volume check was introduced directly before any cell birth event could happen. As an example of a challenging problem, the solution in this case was fairly simple, but not very elegant, and it was necessary to track firstly whether the cell division events that were occurring in cells under the threshold area was due to the new code or within the main cell-based trunk, which was time-consuming and not intuitive to a new user.

As described in Section 4.1.5, periodic boundary conditions are implemented in 2D using a method already defined in the Chaste framework: by defining a cylindrical geometry. In this method, each half of the set of real nodes are copied as image nodes to the opposite side of the boundary, before the meshing algorithm defines cell-cell connectivity. Subsequently, the edges of the periodic boundaries are stitched together by removing elements that contain more than one image node, and then replacing connections to the remaining image nodes in the extended triangulation by their real counterparts. This process of extending the number of nodes and defining the periodic connections is non-trivial in 3D, as the mesh is much more complicated, and the potential for introducing errors is high. Further, it is computationally intensive to carry out this method for such large numbers of nodes. It was therefore decided to implement periodicity in 3D at the force level (see Section 7.1.3). This functionality has now been incorporated in the cell-based trunk of code.

7.4.2 Computational Limitations of a Three-Dimensional Mesh-Based Framework

The model proposed thus far in this chapter is the 3D analogue of that investigated in Chapter 5: a growing, deformable epithelial monolayer constrained to lie on a block of stromal cells that approximate the surrounding tissue, and with a defined basement membrane. Sections 7.1 and 7.2 define the 3D basement membrane force, and simulations illustrate that similar behaviour is observed for the monolayer with regards to cell division, migration and death. At this stage, however, it is recognised that without substantial work it is not possible to extend this model to a 3D test-tube crypt geometry, or to incorporate more detailed subcellular behaviour, such as Wnt dependent proliferation. The computational limitations that currently prevent these steps being taken are now discussed, along with suggestions for as how they could be resolved or circumvented.

As explained in Section 7.3, the time taken to run the 3D simulations is much greater than that for the 2D models. This is due to the increase in the number of cells, and moreover, the recalculation of the Delaunay mesh which is required at every timestep. Currently, this prevents multiple simulations of a significant duration from being performed, to investigate the long-term behaviour of the model, and so it is not possible as yet to investigate the consequences of introducing a mutant cell population. For the simulations implemented in Section 7.2, to keep the cell number, and hence run time, at a minimum, ghost nodes were not included and consequently, density-dependent inhibition of mitosis could not be incorporated. Without including a surrounding layer of ghost nodes to prevent infinite tessellations from forming (see Section 4.1.2), it is not possible to calculate the Voronoi region of boundary cells in 3D and so determine whether their volume is above the prescribed threshold for division to occur. This currently prevents direct comparison of the 2D and 3D models.

Figure 7.14 illustrates the complexity of the Delaunay triangulation for a 3D mesh of nodes, and how this mesh evolves over time, subject to the interactive cell-cell and basement membrane forces. These snapshots correspond to a simulation where $\kappa_S = 0$ across the entire domain, and $\beta = 8$ (see Section 7.2.1). As can be seen from the images, the mesh is very complicated, and as a consequence, mesh-handling becomes very difficult throughout multiple cell division, migration and death events. Subsequently, tracing errors is complicated (even for an initially small mesh: 7 x 7 x 5) and as the 3D mesh-based components of the cell-based Chaste framework have not been tested or implemented by any users beyond basic unit and acceptance tests, building new code in a user project to integrate with the main code base is more challenging than for the 2D case. In particular, simulations run

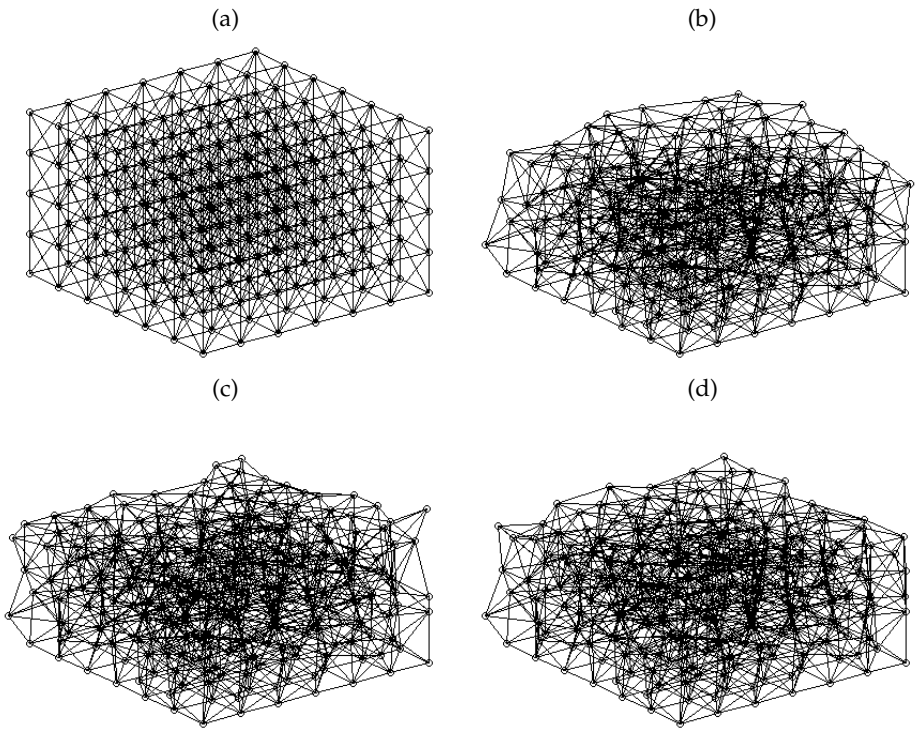

Figure 7.14: Snapshots that illustrate the complexity of the Delaunay triangulation for a 3D mesh of nodes, and how this mesh evolves over time. Here, the initial mesh is composed of 245 nodes, and the mesh snapshots correspond to an example of a simulation where $\kappa_S = 0$ across the whole domain, equivalent to the results shown in Section 7.2.1. (a) The initial mesh of nodes, (b) after 10 hours, (c) after 20 hours, (d) after 30 hours.

using specific parameters suggest that there may be a conflict of the simulation code with the external meshing algorithm that is employed, but this conflict is not yet understood. Extending this mesh to represent the 3D test tube geometry, and incorporating the hollow lumen of ghost nodes, would increase the complexity further still.

Parallelisation

To extend the 3D geometry to a realistic crypt shape and then conduct meaningful *in silico* investigations necessitates sufficiently fast, reliable and robust code. As outlined above, the mesh-based framework upon which the model depends increases the complexity of computation, as well as the time taken to run simulations, and currently is not sufficiently robust. One option to increase the speed of simulations is to parallelise the code framework. This would permit the extension to a test tube crypt geometry, and also enable the inclusion of ghost nodes in the model, to calculate boundary cell volumes and implement density-dependent inhibition of mitosis. Consequently, comparison of the 3D model with the 2D model proposed in Chapter 5 would be feasible.

Currently, the cell-based Chaste framework is written for serial computation, whereby it is run on one core of a single computer and each component of the code is executed sequentially. Parallel computing, in contrast, employs multiple cores or stand-alone computers to implement the components of the code concurrently and simultaneously, which greatly reduces the time to solve. However, this necessitates redesigning the code in parallel, which is non-trivial and time-consuming. Firstly, the user must decide how to decompose the structure into independently solvable tasks – a process known as partitioning – and to determine what level of communication is needed between the decomposed problems, such communication having a computational cost. Problems which decompose into similar tasks that require little or no communication are known as embarrassingly parallel, and can be sped up easily by utilising multiple processors. In contrast, some problems may be non-parallelisable, or communication-intensive, and one of the main difficulties associated with designing a parallelised version of the code is to maximise the efficiency of the communications between the independent tasks. This can involve subtle decisions between model implementation and types of communication operations. It is also important to achieve a load balance in the distribution of tasks to maximise the speed of solution, and ultimately it is understood that the extent to which the code can be sped up depends on the extent to which it is parallelisable. In addition to the complexity of designing parallel code, the difficulties associated with debugging the code typically increase.

There is one specific barrier to parallelisation which is associated with the model definition itself. The mesh-based framework that is used to define cell-cell connectivity according to a Delaunay triangulation, as described in Section 5.2.2, necessitates a remeshing operation at each timestep. This is an example of how communications would need to be parallelised for this problem, due to the dependency of neighbouring cells on one another because of the interactive cell forces which determine adhesion, repulsion and cell size. In serial, this is computationally intensive for large numbers of cells, and more so when the connectivity is defined in 3D space. Currently, Chaste employs an external meshing algorithm, TetGen[2], which is called at each timestep and which is not currently set up to run in parallel. Thus, to overcome this problem, it would be necessary to generate a parallel meshing tool specifically for Chaste, or to restructure the code to allow the use of an existing parallel mesh generation software, such as Centaur[3].

Further, implementing a parallel remeshing algorithm would not be sufficient in itself, as the dependencies of the separate classes within Chaste (as illustrated in Figures 4.6 and 4.7) would necessitate parallelisation of further components according to the chosen

[2] http://tetgen.berlios.de/

[3] http://www.centaursoft.com/parallel-mesh-generation

partitioning scheme. In particular, the methodology of the cell-based simulation class, and the child simulation classes used to run different simulations like those contained within this thesis, integrates functionality such as the cell killers and forces, and applies them to the cell population. Thus, parallelised versions of these classes will be needed, in addition to the parallelised solvers. Such work is non-trivial, and currently is the focus of a separate D.Phil. project.

7.5 Discussion

The intestinal epithelium forms a continuous surface that folds into the closely packed and regularly spaced crypts of Lieberkühn, which are individually surrounded and supported by muscle and connective tissue. A 2D approximation to this system is considered in Chapter 6, in which epithelial cell movement is restricted to a 1D cell chain, and the structure itself is viewed in a cross-section. The work contained within Chapter 7 is motivated by the assertion that a 3D model can characterise better the spatial freedom afforded to crypt cells than a 2D model, and it is necessary to employ such a framework to investigate accurately the migration of epithelial cells as well as the spread of mutant populations. To that end, the basement membrane force, first introduced in Chapter 5, was generalised for application to a 3D surface. The influence of this force was demonstrated for a flat layer with zero spontaneous curvature and for a layer that includes a region with non-zero spontaneous curvature to model the shape and arrangement of cells at the crypt base. Cell death due to anoikis and via sloughing at the edges of the monolayer were both incorporated. The simple cell dynamics proposed here produce cell migration out towards the edges of the tissue block.

Simulations of the model show that anoikis events occur frequently in the crypt base region, and at the interface that separates the zero and non-zero spontaneous curvature regions. This emphasises once again the role that the shape of the structure may play in controlling cell death and cell fate, via mechanical restrictions that influence cell movement during, or immediately following, division. This behaviour is also exhibited by the 2D model. However, having demonstrated the effectiveness of this modelling concept in 3D, it is clear that a 3D model of the crypt with a realistic, deformable geometry is necessary to investigate the consequences of sporadic and accumulated cell mutations which occur throughout the progression of CRC. Currently, this is limited by the computational intensity of the simulations, which are not sufficiently robust or quick enough to run multiple experiments

that examine the long term behaviour of the system following the introduction of a mutant population.

Section 7.4 highlights the problems that currently limit further development of this model to a test-tube geometry, and more generally, discusses the difficulties associated with coding within the Chaste framework as a new user. It is identified that the mesh-based framework upon which the models in this thesis are based, while being suitable in 2D, becomes a hindrance in 3D due to the additional complexity of the triangulation and the remeshing operation that must be conducted at each timestep. One way to resolve this issue would be to redesign the code to run in parallel, but due to the inherent complexity of writing parallel code, and the structural hierarchy of the Chaste framework, this is not simple and cannot be achieved quickly. An alternative approach, rather than tackling this issue computationally, would be to reconsider the model definition and investigate different cell models to which the basement membrane force could be applied. This is discussed further in Section 8.2.1.

Ideally, once a realistic 3D model of the test-tube crypt geometry has been developed, that incorporates both proliferative and non-proliferative cells, it should be possible to use it to conduct *in silico* experiments similar to those in Section 6.3, which investigate the spread of mutant populations that exhibit different cell properties. The behaviour and predictions of the model can then be considered alongside wet experiments designed to validate or debunk new hypotheses, and ultimately, to initiate a feedback loop between computational and biological experiments to advance understanding of the system.

Chapter 8

Discussion and Conclusions

Understanding the normal function and dynamics of the crypts of Lieberkühn, and more importantly, how and when this function breaks down, is crucial to distinguish and correctly interpret the initiation and development of colorectal cancer. As a disease, it is both prevalent and deadly, so there is ample reason to dedicate a significant research effort to this area, whether this leads to the development of new and more efficient drugs to prevent, halt or reverse the cancer, or to novel ways to identify it at earlier stages.

Theoretical modelling can provide valuable insight into the progression of CRC, given the potential to perform mathematical analysis, or repeat *in silico* experiments that may not be feasible in a wet lab. However, to realise this potential, mathematical models should account accurately for the key features of crypt behaviour. This presents a significant challenge, because the crypt is not fully understood as a biological system, and there remain many unanswered questions. For example, the number and position of the stem cells are unknown, as is the cause of cell migration, and the precise mechanism that leads to cell death at the crypt collar. These knowledge gaps underscore the need for modellers to work in collaboration with biologists – an approach which has been undertaken within this DPhil research – to define key system characteristics, influences and behaviours, and importantly, to form well-posed questions.

Existing mathematical models of the crypt, as discussed in Chapter 3, have focused on questions about cell clonality, addressed the assumption of a pedigree concept of cell division (whereby cell age dictates cell positioning following division), and investigated the existence and location of a motile stem cell population. These earlier models (for example, [123], [21], [31]) have not fully linked subcellular and cellular behaviour with tissue-level properties. Given that the onset of CRC is marked by macroscopic changes in the tissue structure of the crypt – crypt budding, aberrant crypt foci and polyps – it

is important to extend the multiscale concept to the next spatial level. Even before such large changes can be observed, there is benefit to be derived from linking the stability and structure afforded by the surrounding tissue stroma and crypt geometry, to their mechanical influence on cell behaviour. For example, the results presented in Chapters 5 to 7 suggest that the negative curvature of the epithelial layer at the crypt collar may play a key role in cell death events in this region due to the decreased basal surface in contact with the basement membrane. The incidence of anoikis events at the crypt collar found in simulations of the 2D cross-sectional model illustrate how such a mechanical model can generate hypotheses and predict functional processes.

8.1 Summary of Work Contained Within This Thesis

The aim of this D.Phil. work was to develop a new computational model of the colorectal crypt which defines a realistic geometry and also accounts for the tissue structure which surrounds the epithelium. The key challenge in the model was to link the stability afforded to the epithelial monolayer by the surrounding musculature, basement membrane and pericryptal fibroblast sheath to the geometry in such a way as to enable cell growth, division, migration and death to occur in a biologically realistic manner. The work contained in Chapters 5 to 7 details this model development, firstly through the definition of a simple 2D geometry (which enables the model to be easily translated to other biological epithelia such as the interfollicular epidermis or olfactory mucus membrane) to investigate the growth of a deformable epithelial monolayer, which is subsequently extended to a 2D cross-sectional crypt geometry, and then further to 3D, where the monolayer overlies a 3D tissue stroma. The 3D model is the foundation for a more comprehensive, multiscale crypt model, which could include detailed subcellular models, and which will be achieved by extending the geometry and tackling computational limitations. These challenges and directions for future work are considered in Section 8.2.1.

The biological background for this modelling work is provided in Chapter 2, which contains a detailed description of the tissue structure of the intestinal crypt, supported by highly detailed fluorescent microscopy images generated by our biological collaborators. Image analysis identifies the role of the different components of the tissue stroma and, in particular, reveals new insight into the support provided to individual crypts by the muscularis mucosae. Specifically, the muscularis mucosae is shown to form a network that follows the contours of the crypt bases, analogous to the support of an egg box, with each crypt as a single egg. In addition to the presence of the basement membrane and PCFS, the

supporting role of the muscularis mucosae is key to the model definition presented in this thesis. In addition, Chapter 2 also describes those elements of crypt dynamics, such as the Wnt and Notch signalling pathways, cell polarity and anoikis, which were also included in the model.

Chapter 3 contains a review of existing mathematical models of the colorectal crypt. The different modelling approaches are described, and the outcome of analytic and *in silico* investigations which have already provided insight into crypt dynamics are summarised. Emphasis is given to models that track the spatial location of cells and, in light of the focus of this thesis, a detailed investigation of subcellular and cell cycle models is not included. Rather, attention focuses on three models that consider buckling of the epithelial monolayer lining the crypt [31, 35, 85]. It is noted, however, that these models are not suited to a full investigation of the breakdown in normal crypt structure that accompanies the onset of carcinogenesis. For example, the 2D crypt model proposed by Drasdo and Loeffler [31], while considering a realistic geometry with a deformable structure, does not link behaviour at the cellular level with subcellular influences, such as Wnt signalling, and further, this model does not account for neighbouring crypts or deformation of the tissue stroma. The continuum models due to Edwards and Chapman [35] and Nelson et al. [85] focus on behaviour at the tissue level, and as such, neglect cell heterogeneity. Thus, it is not possible to track individual cell behaviours, or investigate whether there are mechanical causes for events such as anoikis at the crypt collar.

Chapter 4, the final introductory chapter, describes in detail the off-lattice cell-centre model that is the basis of the new crypt model that is developed in the later chapters. Chaste, the computational framework used for model development, is introduced. The Chaste ethos, described in Section 4.2, is key to ensuring long-term maintenance and extensibility for the modelling work that is undertaken, and is designed specifically to facilitate comparison of different modelling paradigms. Involvement in the Chaste project was an important part of this D.Phil. work, as it encouraged code development according to the principles of eXtreme Programming, through implementing a test-driven framework. This leads to high-quality code that challenges the current convention which typically involves code being written by an individual researcher, often without employing good software engineering principles, and which is not published alongside journal articles or available as an open-source tool to the research community.

Chapter 5 introduces a new discrete model for a growing epithelium, designed to investigate the support given to the epithelial monolayer by the tissue stroma, and simultaneously to prescribe a deformable geometry. Within this model, a new force is defined to model the

presence of the basement membrane as well as cell-substrate adhesion, and the support provided by the surrounding musculature. A spontaneous curvature is assigned to the virtual basement membrane, which varies with cell position to distinguish the crypt base region from the flat regions of the epithelial monolayer which are equivalent to the vertical walls of the crypt. Investigations are conducted to identify values for the force parameter, β, and the spontaneous curvature, κ_S, for the crypt base that give rise to realistic patterns of cell movement, and these results are translated to a 2D cross-sectional geometry in Chapter 6. Moreover, the imposition of the basement membrane force allows the geometry of the structure to evolve over time, rather than being fixed, as in earlier models [21, 87].

In comparison to earlier theoretical models of the crypt, the main advances of the work presented in this thesis (the epithelial monolayer model, the cross-sectional model and the 3D model) is that the models enable investigation of the mechanical forces acting between epithelial cells and the surrounding tissue stroma in a deformable environment, while investigating the role of cell death and cell migration. There are clear distinctions between this work and those models which are based on the cylindrical crypt framework, as the latter do not couple cell behaviour to the crypt geometry. By considering a deformable geometry, it is possible to study the destabilisation of the epithelial monolayer, which is not possible using the 3D crypt model proposed by Buske et al. [21]. Further, by explicitly modelling the surrounding tissue stroma, and accounting for cell death via anoikis, the cross-sectional model extends the work proposed by Drasdo and Loeffler [31]. In summary, the models presented in this thesis enable investigation of the role that mechanical forces play in regulating tissue homeostasis, and may underpin future work designed to study the onset of crypt deformation under pre-cancerous conditions. The outcome of the model investigations are now summarised.

8.1.1 Cross-Sectional Model Predictions

The behaviour of the cross-sectional model is found to be in agreement with experimental information about the crypt – epithelial cells migrate upwards towards the crypt collar, generating a steady turnover while maintaining a stable structure. It is shown that the average cell velocity increases with distance along the vertical crypt axis from the crypt base and that this correlates well with experimental data [61]. Further, by comparing model simulation data with experimental data recorded by our collaborators, it is shown that, despite being a simple model, the cell numbers and turnover generate realistic cell cross-sectional areas (see Section 6.2.2).

As a consequence of the test-tube shaped geometry of the crypt, simulation results have afforded insight into how the crypt shape may influence cell division, death and proliferation. Specifically, results show that epithelial cells are forced out of the layer more often in two regions of the crypt: differentiated cells at the crypt collar and proliferating cells at the crypt base, whereupon they undergo anoikis. At the crypt collar, these events are likely to be the consequence of overcrowding, as well as the negative curvature of the layer and the concurrent decrease in cell-substrate contact area, which renders the cells vulnerable to detachment. These results are in agreement with observations that apoptosis follows extrusion for epithelial cells at the villus tip in the small intestine, and along the surface epithelium of the colon, where epithelial cells have reduced contact with the basement membrane [64]. Whether this is due to the tissue geometry directly, as predicted by the cross-sectional model, could be investigated by growing epithelial cells to confluence on a flat substrate, which is subsequently bent, and extrusion events monitored.

Stem cells are known to divide asymmetrically preferentially [99]. As outlined in Section 2.1.3, it is thought that cell shape may play a role in restricting the possible spindle alignment, such that the more compressed apical region of stem cells at the crypt base forces the spindles to align perpendicular to the tissue stroma. Subsequently, the apically-positioned daughter nuclei is pulled back into the monolayer by some as yet unknown mechanism before cytokinesis. In contrast, the transit cells further up the crypt are less compressed, which allows their spindles to align parallel to the tissue stroma. Mechanisms regulating symmetric and asymmetric cell division are not explicitly included in the cross-sectional model, yet *in silico* simulation results show that newly created cell centres at the crypt base are forced to grow out of the layer, and consequently are removed by anoikis. Anoikis events are not commonly observed in this region [131]. Yet, as cells pop out of the layer on purely mechanical grounds, when considered with the known division mechanism of stem cells, which are thought to reside in the curved base of the crypt, these results support the hypothesis that crypt shape influences whether a cell undergoes asymmetric or symmetric division. Until now, no theoretical model has linked crypt shape with cell division and anoikis, and hence these inferences are key results of this work.

Simulations conducted in 2D using both the simple rectangular geometry and the cross-sectional model have revealed a possible mechanism by which epithelial cells migrate in the monolayer. Currently within the field it is assumed that cell migration in the crypts is active, but it is not known what force may drive this movement [63]. Simulations of the 2D epithelial monolayer model reveal that unless sufficient cell apoptosis is present towards edges of the layer (and correspondingly, the top of the crypt in the cross-sectional

model), epithelial cells reach a state of confluence, do not divide and migration is inhibited. These results suggest that cell migration in the crypt may not be due solely to proliferative pressure from below, but that a non-local mechanical effect occurs as a consequence of cell loss toward the crypt collar, which creates additional space for the epithelial cells move into. This subsequently allows the cells to grow sufficiently to proceed through the cell cycle and undergo division, and also ensures that holes do not form in the layer, such that barrier function is maintained. This negative pressure hypothesis is a theory which is in line with the extrusion process that occurs for apoptotic cells in epithelial layers, whereby the dead cell is squeezed out of the layer by its neighbours, and the resulting gap is simultaneously closed [102]. Determining whether this mechanism alone could generate the observed patterns of cell migration, or whether it is one of a combination of mechanisms, requires further experimental insight. Discussion with biological collaborators suggests that it is possible to conduct such investigations in a wet lab by using inhibitors to stop apoptosis and marking any change to the typical migratory pattern.

By reproducing the cell migration experiments performed by Kaur and Potten [61], it is demonstrated that cell migration will occur in the cross-sectional model in the absence of cell division, and over the same time period. However, the cause of migration is the relaxation of the epithelial monolayer, which occurs in response to the sloughing of cells from the crypt collar. This creates additional space into which the epithelial cells can expand and move. If cell death continues, holes may form in the layer, disrupting barrier function. Therefore it is suggested that migration, cell death and mitosis are coupled so that cell death can stimulate cell division, rather than just enabling it, in the event that there are too few cells in the monolayer. This is in agreement with the capability of stem cells to regulate the rate of cell division to maintain tissue homeostasis [28].

Further *in silico* experiments conducted using the 2D cross-sectional model agree with existing biological hypotheses which suggest that an accumulation of mutations, which correspond to different aberrant cell properties, are needed to convey persistence to mutant cells and their progeny, rather than a single sporadic mutation which is easily flushed out. The cross-sectional model results are also in line with those found from similar theoretical experiments conducted using the cylindrical crypt model [125]. However, the inclusion of anoikis and density-dependent inhibition of mitosis in the new model prevents the simulation breakdown that can occur for the cylindrical model when the proliferation rate of the mutant population exceeds the rate at which cells are sloughed, leading to high numbers of cells in the simulations. However, these investigations can only make tentative inferences, due to the restrictions placed on cell movement by the definition of

the epithelial monolayer as a 1D chain of cells. In the 2D modelling framework, should a mutant cell reduce or halt migration, it immediately restricts the movement of those cells directly beneath it. In 3D, cells can move laterally around the inner surface of the crypt, and potentially circumvent this problem. Hence, a model extension to three dimensions is considered.

8.1.2 Three-Dimensional Model

Motivated by the spatial limitations imposed on cell movement in 2D, the crypt model is extended to 3D in Chapter 7. A cuboid structure, which consists of a monolayer of epithelial cells atop a block of stromal cells (analogous to the geometry considered in Chapter 5) is used to conduct simple investigations into the response of the epithelium to repeated division events and cell migration.

The additional complexity of the Delaunay triangulation in 3D necessitates a redefinition of the basement membrane force, via the definition of a piecewise planar surface that passes through the midpoints of the connections between epithelial and stromal cells. Simulations reveal that the 3D basement membrane force behaves in the same way as for the 2D case. In particular, the layer deforms as the basement membrane seeks to attain the predefined spontaneous curvature. Moreover, by incorporating a mechanism of cell sloughing at the edges of the stromal cell block, the basement membrane force and interactive cell-cell forces act to promote directed cell migration across the layer and a corresponding reduction in anoikis is observed.

Comparison of the spatial distribution of epithelial cells within the monolayer and the spatial distribution of anoikis events again suggests that the shape of the monolayer may play a role in determining cell fate. Specifically, the concave shape of the crypt base, and the high compression of cells in this region, forces cells out of the layer soon after a division event. Even though asymmetric division is not explicitly modelled, it is observed that cells are forced into the lumen following mitosis in a manner consistent with the perpendicular alignment of the mitotic spindle during asymmetric division. This is in agreement with the results found for the 2D model. It is also found, as for the 2D model, that the convex shape assumed by the layer at the boundary between the zero and non-zero spontaneous curvature regions (which is analogous to the crypt collar) renders cells vulnerable to detachment from the underlying stroma. This suggests that cell loss at the top of the crypt may be due, in part, to anoikis following cell extrusion.

In its current form, the 3D model supports the hypotheses generated using the cross-sectional model regarding migration, division and cell death in the epithelial monolayer, but cannot yet afford any further insight into crypt dynamics. It is suggested that a 3D model provides a more realistic representation of cell movement throughout the crypt, by removing the restrictions imposed by a 1D cell chain, and that this has relevance when considering the growth and spread of a mutant population. However, investigation of this requires that a realistic geometry be defined, which is currently limited by the computational intensity of the simulations, as described in Section 7.4.2. One option to address this problem is to develop parallelised code, but this is a difficult and time-consuming project. A possible alternative approach is discussed in Section 8.2.

8.2 Future Work

The preliminary results demonstrate that the 3D model proposed in Chapter 7 can be used to define a deformable geometry for the crypt structure and to investigate cell movement in a more biologically realistic manner. One of the obvious next steps of this work is an extension of the 3D model presented in Chapter 7 to a more realistic crypt geometry. This can be made even more accurate by employing data that characterises typical cell numbers and sizes within a specific region of the colon. Crypt sizes and dimensions vary from the end of the colon closest to the appendix to the end closest to the rectum. Typically, the 50% region, which is halfway between the two extreme ends of the intestine, is the easiest to image and is the most consistent region of tissue. Data that characterises cell size, number and distribution is already available, but existing crypt models do not reference this detail and are not specialised for a specific region of the intestine, even though this is of relevance to biologists. Most existing models (including the cross-sectional model contained in Chapter 6) are too simplistic to reproduce the crypt dimensions accurately – for example, the cylindrical crypt models consistently overestimate the number of cells at the crypt base, and the lumen of the cross-sectional model is larger than in reality, in order to prevent epithelial cells from opposite walls forming long connections in the triangulation, and to enable investigation of the outward growth of mutant cell populations and the possible formation of polyps. A 3D model will improve the accuracy of the spatial dimensions considered in modelling work.

In the same manner that extra detail was added to the 2D model in Chapter 6 to accompany the cross-sectional crypt geometry, in a 3D test-tube geometry, it will be possible to consider the distinct proliferative regions of the crypt – the stem, transit and terminally-differentiated

compartments – as well as realistic cell cycle models that control cell division. Such a model of the crypt would also be amenable to comparison with biological data that quantifies model parameters, such as interactive cell forces and the strength of cell-substrate adhesion, which can be obtained experimentally. A further extension is to develop a discrete model of multiple neighbouring crypts, and investigate the spread of mutations from one gland to another.

With regards to cell-cell adhesion, extracellular signalling gradients and, as mentioned above, the cell cycle, the modelling approach considered in this work is simple in terms of being multiscale. Thus, in addition to extending the existing 3D model to a realistic geometry, a comprehensive, multiscale model will be achieved through the inclusion of more detailed subcellular models. For example, sophisticated models of cell-cell adhesion could be linked to the spring constant, μ, such as that proposed by Ramis-Conde et al. [100], which captures the interaction between E-cadherin and β-catenin at the cell membrane. In this case, μ would depend on the density of surface adhesion molecules, which is calculated using the E-cadherin / β-catenin model (described in Section 3.3), which evaluates the state of the E-cadherins via cell-cell connectivity and determines when E-cadherin-β-catenin bonds form at the cell membrane. In addition, one could implement a deterministic continuum cell cycle model which is dependent on Wnt, such as that proposed by Swat et al. [114] and implemented by Van Leeuwen et al. [123].

As outlined already, the main improvement of a 3D model over the 2D cross-sectional model proposed in Chapter 6 is the replication of cell migration across the inner surface of the crypt, in comparison to cell migration in a 1D chain of cells. Further, in a test-tube geometry, it will be possible to model the merging or rearrangement of cell columns, causing the lumen to narrow or widen should the number of cells decrease or increase. This would permit investigation of the hypothesis proposed by Loeffler et al. [71], that contracting forces dominate in the absence of mitosis, causing the vertical columns of cells to merge, which ultimately forces upward migration. This would also have a bearing on investigations similar to those conducted in Section 6.3.1, which reproduce the Kaur and Potten [61] experiments and examine possible mechanisms behind cell migration. Moreover, *in silico* experiments could be conducted akin to those described in Section 6.3, in which mutant cell populations are introduced and their ability to persist monitored, in addition to observation of downstream tissue effects such as buckling or crypt fission. The improved accuracy of cell movement throughout the crypt (across the inner surface) would translate to a greater level of confidence over the predictions formed by the results.

However, to achieve such a comprehensive model involves addressing the speed of the computational simulations, and two possible directions for this are described below.

8.2.1 Future Challenges

Currently the cell-based Chaste framework is written to run in serial, such that each component of the code is executed sequentially. In contrast, by employing a parallelised structure, multiple cores or stand-alone computers could be utilised to implement the components of the code concurrently and simultaneously, thereby decreasing run times. This represents one possible direction of future work for this model, but as outlined in Section 7.4.2, parallelisation of the code in Chaste is non-trivial and so would require significant effort and a high level of expertise.

An alternative direction for future work would be instead to implement a different off-lattice framework, such as an overlapping spheres model, similar to the cell-based framework in the models developed by Drasdo and Loeffler [31] and Buske et al. [21]. OS-based models do not derive cell-cell connectivity from a mesh such as a Delaunay triangulation, but rather cells interact via distance functions which circumvents the mesh-based problems such as those described in Section 7.4.2, and eliminates the need to remesh the nodes at every timestep, greatly simplifying parallelisation.

The challenge associated with adopting an OS-based model would be to determine how to characterise the basement membrane itself in the absence of predefined cell connections. The mesh-based framework provides a natural definition for the basement membrane as spanning the midpoints of the connections between the epithelial and stromal cells, defined by the triangulation. Indeed, this was the motivation for employing a mesh-based cell population from the outset, and has been shown to be effective, and sufficiently fast, in 2D. Once a suitable method for defining the basement membrane has been determined, it will be possible to implement a basement membrane force in a similar manner. The work contained within this thesis then provides a basis for such a model and should enable future researchers to achieve a 3D crypt model more quickly. In addition, parallelisation of an OS-based framework is much simpler than for a mesh-based framework, as no remeshing algorithm is required. This modification is currently being undertaken within Chaste. Thus, it is expected that an OS model, which employs an equivalent model of the basement membrane and defines a realistic crypt geometry, would be an efficient tool to investigate crypt dynamics.

8.2.2 Summary

Despite the limitations addressed above, the 2D and 3D models presented in this thesis enable investigation of the role of mechanical forces in maintaining tissue homeostasis within the crypt, and have identified possible mechanical causes for asymmetric division, epithelial cell migration and cell death at the crypt collar. Moreover, this work lays the foundation for a comprehensive 3D model of the crypt which could be used to conduct new *in silico* experiments, focussing on the deformation of the structure that could arise due to the persistence and proliferation of a mutant cell population. It is suggested that to achieve the most accurate predictions, it will be necessary to extend the multiscale aspects of the model – in particular at the subcellular level – in addition to defining the test-tube shaped geometry.

In order to generate such a 3D model with a realistic, deformable geometry similar to the work presented here, it is necessary to address the speed of computation. To retain the mesh-based framework requires that a parallel remeshing algorithm is developed for Chaste, but this is not a trivial task. Rather, it is suggested that redefining the basement membrane force within a OS framework is a simpler task, though such a definition is still an open problem.

The outcome of investigations using a comprehensive 3D model can, ideally, be used to suggest new experiments in a wet lab, to test hypotheses and further the understanding of the crypt system. Further uses include drug delivery applications, where it is key to manage dosage timing, and to prevent the drug from being expelled from the system as the epithelial layer is renewed. As was the initial motivation of this work, ultimately it will be possible to perform meaningful *in silico* experiments that examine the migration and colonisation of mutant cell populations, and the subsequent destabilisation of the crypt structure at the onset of carcinogenesis. In this way, and in collaboration with experimental work carried out by biologists to test hypotheses and refine model definitions, such work will contribute towards understanding of the development of colorectal cancer.

References

[1] Adra, S., Sun, T., MacNeil, S., Holcombe, M., and Smallwood, R. (2010). Development of a three dimensional multiscale computational model of the human epidermis. *PLOS ONE*, 5:e8511.

[2] Alberts, B., Johnson, A., Lewis, J., Raff, M., Roberts, K., and Walter, P. (2002). *Molecular Biology of the Cell*. Garland Science, New York, 4th edition.

[3] Allen, M. P. and Tildesley, D. J. (1987). *Computer simulation of liquids*. Oxford University Press, Oxford.

[4] Andersson, E. R., Sandberg, R., and Lendahl, U. (2011). Notch signaling: simplicity in design, versatility in function. *Development*, 138:3593–3612.

[5] Appleton, P., Quyn, A., Swift, S., and Näthke, I. (2009). Preparation of wholemount mouse intestine for high-resolution three-dimensional imaging using two-photon microscopy. *J. Microsc.*, 234:196–204.

[6] Araujo, R. P. and McElwain, D. L. S. (2004). A history of the study of solid tumour growth: the contribution of mathematical modelling. *Bull. Math. Biol.*, 66:1039–1091.

[7] Ascher, U. and Petzold, L. (1998). *Computer Methods for Ordinary Differential Equations and Differential-Algebraic Equations*. SIAM, Philadelphia.

[8] Barker, N., Ridgway, R. A., van Es, J. H., van de Wetering, M., Begthel, H., van den Born, M., Danenberg, E., Clarke, A. R., Sansom, O. J., and Clevers, H. (2009). Crypt stem cells as the cells-of-origin of intestinal cancer. *Nature*, 457:608–612.

[9] Barker, N., van Es, J., Kuipers, J., Kujala, P., van den Born, M., Cozijnsen, M., Haegebarth, A., Korving, J., Begthel, H., Peters, P., and Clevers, H. (2007). Identification of stem cells in small intestine and colon by marker gene Lgr5. *Nature*, 449:1003–1007.

[10] Barthold, S. W. (1979). Autoradiographic cytokinetics of colonic mucosal hyperplasia in mice. *Cancer Res.*, 39:24–29.

[11] Beck, K. and Andres, C. (2004). *Extreme Programming Explained: Embrace Change*. Addison-Wesley, Boston.

[12] Beysens, D. A., Forgacs, G., and Glazier, J. A. (2000). Cell sorting is analogous to phase ordering in fluids. *PNAS*, 97:9467–9471.

[13] Bienz, M. (2005). β-catenin: A pivot between cell adhesion and wnt signalling. *Curr. Biol.*, 15(2):R64–R67.

[14] Bird, R. (1987). Observation and quantification of aberrant crypts in the murine colon treated with a colon carcinogen: preliminary findings. *Cancer Lett.*, 37:147–151.

[15] Bjerknes, M. and Cheng, H. (1999). Clonal analysis of mouse intestinal epithelial progenitors. *Gastroenterol.*, 116(1):7–14.

[16] Boman, B. M., Fields, J., Bonham-Carter, O., and Runquist, O. (2001). Computer modeling implicates stem cell overproduction in colon cancer initiation. *Cancer Res.*, 61:8408–8411.

[17] Boman, B. M., Fields, J. Z., Cavanaugh, K. L., Guetter, A., and Runquist, O. A. (2008). How dysregulated colonic crypt dynamics cause stem cell overpopulation and initiate colon cancer. *Cancer Res.*, 68:3304–3313.

[18] Boman, B. M., Walters, R., Fields, J., Kovatich, A., Zhang, T., Isenberg, G., Goldstein, S., and Palazzo, J. (2004). Colonic crypt changes during adenoma development in familial adenomatous polyposis. *Am. J. Pathol.*, 165(5):1489–1498.

[19] Booth, C. and Potten, C. (2000). Gut instincts: thoughts on intestinal epithelial stem cells. *J. Clin. Invest.*, 105(11):1493–1499.

[20] Bryant, D. and Mostov, K. (2008). From cells to organs: building polarized tissue. *Nat. Rev. Mol. Cell Bio.*, 9:887–901.

[21] Buske, P., Galle, J., Barker, N., Aust, G., Clevers, H., and Leoffler, M. (2011). A comprehensive model of the spatio-temporal stem cell and tissue organisation in the intestinal crypt. *PLOS Comput. Biol.*, 7:1–13.

[22] Cairns, J. (1975). Mutation selection and the natural history of cancer. *Nature*, 255:197–200.

[23] Cancer Research, U. K. (2011). Bowel (colorectal) cancer - uk incidence statistics.

[24] Cheng, L. and Lai, M.-D. (2003). Aberrant crypt foci as microscopic precursors of colorectal cancer. *World J. Gastroenterol.*, 9(12):2642–2649.

[25] Clayton, E., Doupé, D. P., Klein, A. M., Winton, D. J., Simons, B. D., and Jones, P. H. (2007). A single type of progenitor cell maintains normal epidermis. *Nature*, 446(7132):185–189.

[26] Crosnier, C., Stamataki, D., and Lewis, J. (2006). Organizing cell renewal in the intestine: stem cells, signals and combinatorial control. *Nat. Rev. Genet.*, 7:349–359.

[27] Dallon, J. and Othmer, H. (2004). How cellular movement determines the collective force generated by the dictyostelium discoideum slug. *J. Theor. Biol.*, 231:203–222.

[28] Deheragoda, M. and Wright, N. (2006). An update on the pathophysiology of the intestinal crypt. *Diagn. Pathol.*, 12:268–278.

[29] Drasdo, D. and Forgacs, G. (2000). Modeling the interplay of generic and genetic mechanisms in cleavage, blastulation, and gastrulation. *Dev. Dynam.*, 219:182–191.

[30] Drasdo, D., Hoehme, S., and Block, M. (2007). On the role of physics in the growth and pattern formation of multi-cellular systems: what can we learn from individual-cell based models? *J. Stat. Phys.*, 128:287–345.

[31] Drasdo, D. and Loeffler, M. (2001). Individual-based models to growth and folding in one-layered tissues: intestinal crypts and early development. *Nonlinear Anal.*, 47:245–256.

[32] Duggan, C. D. and Ngai, J. (2007). Scent of a stem cell. *Nat. Neurosci.*, 10(6):673–674.

[33] Dunn, S. J., Appleton, P. L., Nelson, S. A., Näthke, I. S., Gavaghan, D. J., and Osborne, J. M. (2012a). A two-dimensional model of the colonic crypt accounting for the role of the basement membrane and pericryptal fibroblast sheath. *PLOS Comput. Biol.*, 8:e1002515.

[34] Dunn, S. J., Fletcher, A., Chapman, S., Gavaghan, D. J., and Osborne, J. M. (2012b). Modelling the role of the basement membrane beneath a growing epithelial monolayer. *J. Theor. Biol.*, 298:82–91.

[35] Edwards, C. M. and Chapman, S. J. (2007). Biomechanical modelling of colorectal crypt budding and fission. *Bull. Math. Biol.*, 69:1927–1942.

[36] Effler, J. C., Kee, Y.-S., Berk, J. M., Tran, M. N., Iglesias, P. A., and Robinson, D. N. (2006). Mitosis-specific mechanosensing and contractile-protein redistribution control cell shape. *Curr. Biol.*, 16:1962–1967.

[37] Fearon, E. R. and Vogelstein, B. (1990). A genetic model for colorectal tumorigenesis. *Cell*, 61:759–767.

[38] Fenn, R. (2001). *Geometry*. Springer-Verlag, London.

[39] Finney, K., Appleton, D., Ince, P., Sunter, J., and Watson, A. (1989). Proliferative status of colonic mucosa in organ culture: 3H-thymidine-labelling studies and computer modelling. *Virchows Arch. B Cell Pathol. Incl. Mol. Pathol.*, 56:397–405.

[40] Fleming, E. S., Zajac, M., Moschenross, D. M., Montrose, D. C., Rosenberg, D. W., Cowan, A. E., and Tirnauer, J. S. (2007). Planar spindle orientation and asymmetric cytokinesis in the mouse small intestine. *J. Histochem. Cytochem.*, 55:1173–1180.

[41] Fodde, R. and Brabletz, T. (2007). Wnt/β-catenin signalling in cancer stemness and malignant behaviour. *Curr. Opin. Cell Biol.*, 19:150–158.

[42] Fodde, R. and Tomlinson, I. (2010). Nuclear β-catenin expression and wnt signalling: in defence of the dogma. *J. Pathol.*, 221:239–241.

[43] Fre, S., Huyghe, M., Mourikis, P., Robine, S., Louvard, D., and Artavanis-Tsakonas, S. (2005). Notch signals control the fate of immature progenitor cells in the intestine. *Nature*, 435:964–968.

[44] Frisch, S. M. and Francis, H. (1994). Disruption of epithelial cell-matrix interaction induces apoptosis. *J. Cell. Biol.*, 124:619–626.

[45] Gallacher, M., Mackenna, B. R., and McKirdy, H. C. (1973). Effects of drugs and of electrical stimulation on the muscularis mucosae of rabbit large intestine. *Br. J. Pharmac.*, 47:760–764.

[46] Galle, J., Hoffmann, M., and Aust, G. (2009). From single cells to tissue architecture – a bottom-up approach to modelling the spatio-temporal organisation of complex multi-cellular systems. *J. Math. Biol.*, 58:261–283.

[47] Galle, J., Loeffler, M., and Drasdo, D. (2005). Modeling the effect of deregulated proliferation and apoptosis on the growth dynamics of epithelial cell populations in vitro. *Biophys. J.*, 88:62–75.

[48] Gaspar, C. and Fodde, R. (2004). Apc dosage effects in tumorigenesis and stem cell differentiation. *Int. J. Dev. Biol.*, 48:377–386.

[49] Gatenby, R. A. and Maini, P. K. (2003). Cancer summed up. *Nature*, 421:321.

[50] Gemin, A., Sweet, S., Preston, T. J., and Singh, G. (2005). Regulation of the cell cycle in response to inhibition of mitochondrial generated energy. *Biochem. Biophys. Res. Comm.*, 332:1122–1132.

[51] Graner, F. and Glazier, J. A. (1992). Simulation of biological cell sorting using a two-dimensional extended Potts model. *Phys. Rev. Lett.*, 69:2013–2017.

[52] Grossman, J. (2002). Molecular mechanisms of "detachment-induced apoptosis – Anoikis". *Apoptosis*, 7:247–260.

[53] Heath, J. P. (1996). Epithelial cell migration in the intestine. *Cell Biol. Int.*, 20(2):139–146.

[54] Honda, H. (1983). Geometrical models for cells in tissues. *Int. Rev. Cystol.*, 81:191–248.

[55] Humphries, A. and Wright, N. A. (2008). Colonic crypt organization and tumorigenesis. *Nat. Rev. Cancer*, 8:415–424.

[56] Ilyas, M. (2005). Wnt signalling and the mechanistic basis of tumour development. *J. Pathol.*, 205:130–144.

[57] Isele, W. and Meinzer, H. (1998). Applying computer modeling to examine complex dynamics and pattern formation of tissue growth. *Comput. Biomed. Res.*, 31:476–494.

[58] Joerger, A. C. and Fersht, A. R. (2007). Structure-function-rescue: the diverse nature of common p53 cancer mutants. *Oncogene*, 26:2226–2242.

[59] Kaplan, K., Burds, A., Swedlow, J., Bekir, S., Sorger, P., and Näthke, I. (2001). A role for the adenomatous polyposis coli protein in chromosome segregation. *Nat. Cell Biol.*, 3:429–432.

[60] Katoh, M. and Katoh, M. (2007). Notch signaling in gastrointestinal tract (review). *Int. J. Oncol.*, 30:247–251.

[61] Kaur, P. and Potten, C. S. (1986a). Cell migration velocities in the crypts of the small intestine after cytotoxic insult are not dependent on mitotic activity. *Cell Tissue Kinet.*, 19:601–610.

[62] Kaur, P. and Potten, C. S. (1986b). Circadian variation in migration velocity in small intestinal epithelium. *Cell Tissue Kinet.*, 19(6):591–599.

[63] Kaur, P. and Potten, C. S. (1986c). Effects of puromycin, cycloheximide and noradrenaline on cell migration within the crypts and on the villi of the small intestine. *Cell Tissue Kinet.*, 19(6):611–625.

[64] Kiesslich, R., Goetz, M., Angus, E. M., Hu, Q., Guan, Y., Potten, C., Allen, T., Neurath, M. F., Shroyer, N. F., Montrose, M. H., and Watson, A. J. M. (2007). Identification of epithelial gaps in human small and large intestine by confocal endomicroscopy. *Gastroenterol.*, 133:1769–1778.

[65] Klein, R. M. and Torres, J. (1978). Analysis of intestinal cell proliferation after guanethidine-induced sympathectomy. *Cell Tiss. Res.*, 195:239–250.

[66] Korinek, V., Barker, N., Moerer, P., van Donselaar, E., Huls, G., Peters, P., and Clevers, H. (1998). Depletion of epithelial stem-cell compartments in the small intestine of mice lacking tcf-4. *Nature*, 19:379–383.

[67] Küppers, M., Ittrich, C., Faust, D., and Dietrich, C. (2010). The transcriptional programme of contact-inhibition. *J. Cell Biochem.*, 110:1234–1243.

[68] Landau, L. D. and Lifschitz, E. M. (1986). *Theory of Elasticity*. Pergamon Press, Oxford, 3rd edition.

[69] Lander, A. D., Gokoffski, K. K., Wan, F. Y. M., Nie, Q., and Calof, A. L. (2009). Cell lineages and the logic of proliferative control. *PLOS Biol.*, 7(1):84–100.

[70] Lewis, J. R. and Cafiso, D. S. (1999). Correlation between the free energy of a channel-forming voltage-gated peptide and the spontaneous curvature of bilayer lipids. *Biochemistry*, 38:5932–5938.

[71] Loeffler, M., Potten, C. S., Paulus, U., Glatzer, J., and Chwalinkski, S. (1988). Intestinal cell proliferation II. Computer modelling of mitotic index data provides further evidence for lateral and vertical cell migration in the absence of mitotic activity. *Cell Tissue Kinet.*, 21:247–258.

[72] Loeffler, M., Stein, R., Wichmann, H. E., Potten, C. S., Kaur, C., and Chwalinski, S. (1986). Intestinal cell proliferation I. A comprehensive model of steady-state proliferation in the crypt. *Cell Tissue Kinet.*, 19:627.

[73] Macklin, P., Edgerton, M. E., Thompson, A. M., and Cristini, V. (2012). Patient-calibrated agent-based modelling of ductal carcinoma in situ (dcis): from microscopic measurements to macroscopic predictions of clinical progression. *J. Theor. Biol.*, 301:122–140.

[74] Marchiando, A. M., Shen, L., Vallen Graham, W., Edelblum, K. L., Duckworth, C. A., Guan, Y., Montrose, M. H., Turner, J. R., and Watson, A. J. M. (2011). The epithelial barrier is maintained by in vivo tight junction expansion during pathologic intestinal epithelial shedding. *Gastroenterol.*, 140:1208–1218.

[75] McDonald, S. A. C., Preston, S. L., Lovell, M. J., Wright, N. A., and Jankowski, J. A. Z. (2006). Mechanisms of disease: from stem cells to colorectal cancer. *Nat. Clin. Pract. Gastr.*, 3(5):267–274.

[76] Meineke, F. A., Potten, C. S., and Loeffler, M. (2001). Cell migration and organization in the intestinal crypt using a lattice-free model. *Cell Prolif.*, 34:253–266.

[77] Meinzer, H., Sandblad, B., and Baur, H. (1992). Generation-dependent control mechanisms in cell proliferation and differentiation – the power of two. *Cell Prolif.*, 25:125–140.

[78] Mirams, G. R. (2008). *Subcellular phenomena in colorectal cancer*. PhD thesis, University of Nottingham.

[79] Murray, J. D. (2002). *Mathematical Biology*, volume 1. Springer, New York, 3rd edition.

[80] Murray, P. J., Edwards, C. M., Tindall, M. J., and Maini, P. K. (2012). Classifying general nonlinear force laws in cell-based models via the continuum limit. *Phys. Rev. E.*, 85:021921.

[81] Mutoh, H., Sakurai, S., Osawa, H., Tomiyama, T., Kita, H., Yoshida, T., Tamada, K., Yamamoto, H., Isoda, N., and Sugano, K. (2005). Pericryptal fibroblast sheath in intestinal metaplasia and gastric carcinoma. *Gut*, 54:33–39.

[82] Nagai, T. and Honda, H. (2001). A dynamic cell model for the formation of epithelial tissues. *Philos. Mag. B*, 81(7):699–719.

[83] Näthke, I. (2004). The adenomatous polyposis coli protein: the achilles heel of the gut epithelium. *Annu. Rev. Cell Dev. Biol.*, 20:337–366.

[84] Neal, J. and Potten, C. (1981). Description and basic cell kinetics of the murine pericryptal fibroblast sheath. *Gut*, 149(22):19–24.

[85] Nelson, M. R., Howard, D., Jensen, O. E., King, J. R., Rose, F. R. A. J., and Waters, S. L. (2011). Growth-induced buckling of an epithelial layer. *Biomech. Model Mechanobiol.*, 10:883–900.

[86] O'Rourke, J. (1998). *Computational Geometry*. Cambridge University Press, Cambridge, 2 edition.

[87] Osborne, J. M., Walter, A., Kershaw, S. K., Mirams, G. R., Fletcher, A. G., Pathmanathan, P., Gavaghan, D., Jensen, O. E., Maini, P. K., and Byrne, H. M. (2010). A hybrid approach to multi-scale modelling of cancer. *Phil. Trans. R. Soc. A*, 368:5013–5028.

[88] Pascal, R., Kaye, G., and Lane, N. (1968). Colonic pericryptal fibroblast sheath: replication, migration and cytodifferentiation of a mesenchymal cell system in adult tissue. i. autoradiographic studies of normal rabbit colon. *Gastroenterol.*, 54:835–851.

[89] Pathmanathan, P., Cooper, J., Fletcher, A., Mirams, G., Murray, P., Osborne, J., Pitt-Francis, J., Walter, A., and Chapman, S. J. (2009). A computational study of discrete mechanical tissue models. *Phys. Biol.*, 6:1–14.

[90] Paulus, U., Loeffler, M., Zeidler, J., Owen, G., and Potten, C. S. (1993). The differentiation and lineage development of goblet cells in the murine small intestinal crypt: experimental and modelling studies. *J. Cell Sci.*, 106(2):473.

[91] Paulus, U., Potten, C. S., and Loeffler, M. (1992). A model of the control of cellular regeneration in the intestinal crypt after perturbation based solely on local stem cell regulation. *Cell Prolif.*, 25:559–578.

[92] Phelps, R., Chidester, S., Dehghanizadeh, S., Phelps, J., Sandoval, I., Rai, K., Broadbent, T., Sarkar, S., Burt, R., and Jones, D. (2009). A two-step model for colon adenoma initiation and progression caused by apc loss. *Cell*, 137:623–634.

[93] Pitt-Francis, J., Bernabeu, M., Cooper, J., Garny, A., Momtahan, L., Osborne, J., Pathmanathan, P., Rodriquez, B., Whiteley, J., and Gavaghan, D. (2008). Chaste: using agile programming techniques to develop computational biology software. *Phil. Trans. R. Soc.*, 366:3111–3136.

[94] Pitt-Francis, J., Pathmanathan, P., Bernabeu, M. O., Bordas, R., Cooper, J., Fletcher, A. G., Mirams, G. R., Murray, P., Osborne, J. M., Walter, A., Chapman, S. J., Garny, A., van Leeuwen, I., Maini, P. K., Rodrguez, B., Waters, S. L., Whiteley, J. P., Byrne, H. M., and Gavaghan, D. G. (2009). Chaste: A test-driven approach to software development for biological modelling. *Comput. Phys. Commun.*, 180(12):2452–2471.

[95] Polyak, K., Hamilton, S., Vogelstein, B., and Kinzler, K. (1996). Early alteration of cell-cycle-regulated gene expression in colorectal neoplasia. *Am. J. Pathol.*, 149(2):381–387.

[96] Potten, C. S., Booth, C., and Hargreaves, D. (2003). The small intestine as a model for evaluating adult tissue stem cell drug targets. *Cell Prolif.*, 36:115–129.

[97] Potten, C. S. and Loeffler, M. (1987). A comprehensive model of the crypts of the small intestine of the mouse provides insight into the mechanisms of cell migration and the proliferation hierarchy. *J. Theor. Biol.*, 127:381–391.

[98] Preston, S. L., Wong, W., Chan, A. O., Poulsom, R., Jeffery, R., Goodlad, R. A., Mandir, N., Elia, G., Novelli, M., Bodmer, W. F., Tomlinson, I. P., and Wright, N. A. (2003). Bottom-up histogenesis of colorectal adenomas: Origin in the monocryptal adenoma and initial expansion by crypt fission. *Cancer Res.*, 63:3819–3825.

[99] Quyn, A., Appleton, P., Carey, F., Steele, R., Barker, N., Clevers, H., Ridgway, R., Sansom, O., and Näthke, I. (2010). Spindle orientation bias in gut epithelial stem cell compartments is lost in precancerous tissue. *Cell Stem Cell*, 6:175–181.

[100] Ramis-Conde, I., Drasdo, D., Anderson, A. R. A., and Chaplain, M. A. J. (2008). Modeling the influence of the E-Cadherin-β-Catenin pathway in cancer cell invasion: a multiscale approach. *Biophys. J.*, 95:155–165.

[101] Riccio, O., van Gijn, M. E., Bezdek, A. C., Pellegrinet, L., van Es, J. H., Zimber-Strobl, U., Strobl, L. J., Honjo, T., Clevers, H., and Radtke, F. (2008). Loss of intestinal crypt progenitor cells owing to inactivation of both notch1 and notch2 is accompanied by derepression of cdk inhibitors $p27^{Kip1}$ and $p57^{Kip2}$. *EMBO*, 9(4):377–383.

[102] Rosenblatt, J., Raff, M., and Cramer, L. (2001). An epithelial cell destined for apoptosis signals its neighbors to extrude it by an actin- and myosin-dependent mechanism. *Curr. Biol.*, 11:1847–1857.

[103] Sangiorgi, E. and Capecchi, M. (2008). Bmi1 is expressed in vivo in intestinal stem cells. *Nat. Genet.*, 40(7):915–920.

[104] Sansom, O., Reed, K., Hayes, A., Ireland, H., Brinkmann, H., Newton, I., Batlle, E., Simon-Assmann, P., Clevers, H., Näthke, I., Clarke, A., and Winton, D. (2004). Loss of Apc in vivo immediately perturbs Wnt signaling, differentiation, and migration. *Genes Dev.*, 18:1385–1390.

[105] Sato, T., Vries, R. G., Snippert, H. J., van de Wetering, M., Barker, N., Stange, D. E., van Es, J. H., Abo, A., Kujala, P., Peters, P. J., and Clevers, H. (2009). Single lgr5 stem cells build crypt-villus structures in vitro without a mesenchymal niche. *Nature*, 459:262–266.

[106] Schaller, G. and Meyer-Hermann, M. (2005). Multicellular tumor spheroid in an off-lattice voronoi-delaunay cell model. *Phys. Rev. E*, 71:051910.

[107] Shanmugathasan, M. and Jothy, S. (2000). Apoptosis, anoikis and their relevance to the pathobiology of colon cancer. *Path. Int.*, 50:273–279.

[108] Shih, I.-M., Wang, T.-L., Traverso, G., Romans, K., Hamilton, S. R., Ben-Sasson, S., Kinzler, K. W., and Vogelstein, B. (2001). Top-down morphogenesis of colorectal tumors. *PNAS*, 98(5):2640–2645.

[109] Smallwood, R. (2009). Computational modelling of epithelial tissues. *WIREs Syst. Biol. Med.*, 1:191–201.

[110] Snippert, H. and Clevers, H. (2011). Tracking adult stem cells. *EMBO Rep.*, 12(2):113–122.

[111] Sträter, J., Koretz, K., Güthert, A., and Möller, P. (1995). In situ detection of enterocytic apoptosis in normal colonic mucosa and in familial adenomatous polyposis. *Gut*, 37:819–825.

[112] Süli, E. and Mayers, D. (2003). *An Introduction to Numerical Analysis*. Cambridge University Press.

[113] Sun, T., Adra, S., Smallwood, R., Holcombe, M., and MacNeil, S. (2010). Exploring hypotheses of the actions of tgf-β1 in epidermal wound healing using a 3d computational multiscale model of the human epidermis. *PLOS ONE*, 4:e8515.

[114] Swat, M., Kel, A., and Herzel, H. (2004). Bifurcation analysis of the regulatory modules of the mammalian G_1/S transition. *Bioinformatics*, 20:1506–1511.

[115] Takayama, T., Katsuki, S., Takahasi, Y., Ohi, M., Nojiri, S., Sakamaki, S., Kato, J., Kogawa, K., Miyake, H., and Niitsu, Y. (1998). Aberrant crypt foci of the colon as precursors of adenoma and cancer. *New Engl. J. Med.*, 339(18):1277–1284.

[116] Tetsu, O. and McCormick, F. (1999). β-catenin regulates expression of cyclin D1 in colon carcinoma cells. *Nature*, 398:422–426.

[117] Théry, M. and Bornens, M. (2006). Cell shape and cell division. *Curr. Opin. Cell Biol.*, 18:648–657.

[118] Tomlinson, I. and Fodde, R. (2010). Nuclear β-catenin expression and wnt signalling: in defence of the dogma. *J. Pathol.*, 221:239–241.

[119] Trier, J. S., Allan, C. H., Abrahamson, D. R., and Hagen, S. J. (1990). Epithelial basement membrane of mouse jejunum. *J. Clin. Invest.*, 86:87–95.

[120] van de Wetering, M., Sancho, E., Verweij, C., de Lau, W., Oving, I., Hurlstone, A., van der Horn, K., Batlle, E., Coudreuse, D., Haramis, A.-P., Tjon-Pon-Fong, M., Moerer, P., van den Born, M., Soete, G., Pals, S., Eilers, M., Medema, R., and Clevers, H. (2002). The β-catenin/tcf-4 complex imposes a crypt progenitor phenotype on colorectal cancer cells. *Cell*, 111:241–250.

[121] van Es, J., Barker, N., and Clevers, H. (2003). You wnt some, you lose some: oncogenes in the wnt signaling pathway. *Curr. Opin. Genet. Devel.*, 13:28–33.

[122] Van Leeuwen, I. M. M., Edwards, C. M., Ilyas, M., and Byrne, H. M. (2007). Towards a multiscale model of colorectal cancer. *World J. Gastroenterol.*, 13:1399–1407.

[123] Van Leeuwen, I. M. M., Mirams, G. R., Walter, A., Fletcher, A., Murray, P., Osborne, J., Varma, S., Young, S. J., Cooper, J., Pitt-Francis, J., Momtahan, L., Pathmanathan, P., Whiteley, J. P., Chapman, S. J., Gavaghan, D. J., Jensen, O. E., King, J. R., Maini, P. K., Waters, S. L., and Byrne, H. M. (2009). An integrative computational model for intestinal tissue renewal. *Cell Prolif.*, 42:617–636.

[124] Walker, D. C., Southgate, J. S., Hill, G., Holcombe, M., Hose, D. R., Wood, S. M., MacNeil, S., and Smallwood, R. H. (2004). The epitheliome: modelling the social behaviour of cells. *Biosystems*, 76:89–100.

[125] Walter, A. (2009). *A Comparison of Continuum and Cell-based Models of Colorectal Cancer*. PhD thesis, University of Nottingham.

[126] Wargovich, M., Brown, V., and Morris, J. (2010). Aberrant crypt foci: the case for inclusion as a biomarker for colon cancer. *Cancers*, 2:1705–1716.

[127] Weliky, M. and Oster, G. (1990). The mechanical basis of cell rearrangement, i. epithelial morphogenesis during fundulus epiboly. *Development*, 109:373–386.

[128] Windham, T. C., Parikh, N. U., Siwak, D. R., Summy, J. M., McConkey, D. J., Kraker, A. J., and Gallick, G. E. (2002). Src activation regulates anoikis in human colon tumor cell lines. *Oncogene*, 21:7797–7807.

[129] Wodarz, D. and Komarova, N. (2005). *Computational Biology of Cancer: Lecture Notes and Mathematical Modelling*. World Scientific Publishing, Singapore.

[130] Wong, S. Y., Chiam, K. H., Lim, C. T., and Matsudaira, P. (2010). Computational model of cell positioning: directed and collective migration in the intestinal crypt epithelium. *J. R. Soc. Interface*, 7:S351–S363.

[131] Wright, N. and Alison, M. (1984). *The biology of epithelial cell populations*. Oxford University Press, Oxford.

[132] Yeung, T. M., Chia, L. A., Kosinski, C. M., and Kuo, C. J. (2011). Regulation of self-renewal and differentiation by the intestinal stem cell niche. *Cell. Mol. Life Sci.*, 68:2513–2523.